Ultracold Molecules: The Effect of Electromagnetic Fields

WALLIS, ALISDAIR,OWEN,GARNETT

Ultracold Molecules: The Effect of Electromagnetic Fields

Alisdair Owen Garnett Wallis

A thesis submitted in partial fulfillment of the requirements for the degree of Ph.D.

Department of Chemistry
University of Durham

2010

Ultracold Molecules: The Effect of Electromagnetic Fields

Alisdair Owen Garnett Wallis

Submitted for the degree of Doctor of Philosophy
March 2010

Abstract

There is great interest within the physics and chemistry communities in the properties of ultracold molecules. Electromagnetic fields can be used to create, trap, and modify the collisional dynamics of ultracold molecules, and thus the properties of ultracold molecules in electromagnetic fields is of growing importance.

This thesis examines some of the effects of externally applied electromagnetic fields on ultracold molecules. Initially, magnetic Feshbach resonances in combined electric and magnetic fields are examined in the collisions of He(^1S)+SO($^3\Sigma^-$). Through detailed quantum scattering calculations, it is then shown that the sympathetic cooling of NH($^3\Sigma^-$) molecules with Mg atoms has a good prospect of success, a first for a neutral molecular system. Detailed quantum scattering calculations are performed for a wide range of collision energies and magnetic field strengths and it is found that the ratio of elastic to inelastic collisions is large for temperatures below 10 mK, and increases as the collision energy and magnetic field strength decrease. The near threshold collision properties of Mg+NH have been examined using a multichannel quantum defect theory approach.

A new type of conical intersection, that is a function of applied electromagnetic fields only, is also demonstrated. For states of opposite parity, brought into degeneracy with a magnetic field, the degeneracy can be resolved by the addition of an electric field, forming a conical intersection. A suitable arrangement of fields could thus be used to create a conical intersection in laboratory coordinates within an ultracold trapped gas. For a Bose-Einstein condensate, in the mean-field approximation, the resultant geometric phase effect induces stable states of persistent superfluid flow that are characterized by half-integer quantized angular momentum.

Declaration

The material contained within this thesis has not previously been submitted for a degree at the University of Durham or any other university. The research reported within this thesis has been conducted by the author unless indicated otherwise.

Acknowledgements

I would like to thank my supervisor Jeremy Hutson for all of his support and guidance throughout my Ph.D. I would also like to thank Simon Gardiner for all his help during the induced conical intersection work, Paul Julienne for his help navigating through multi-channel quantum defect theory, and the group of Roman Krems for their warm hospitality in Vancouver.

I am grateful to all the members of the Hutson group; Jesus Aldegunde, Musie Beyene, James Croft, Subhas Ghosal, Maykel Leonardo González-Martínez, Hong Ran, Ruth Le Sueur, Piotr Żuchowski, and all else in CG200 and the Department of Chemistry who have helped me during my time in Durham, especially to Lisa Murphy whose support has been invaluable.

Finally, I am grateful the EPSRC for funding and to all the support staff at Durham University who made this Ph.D. possible

Contents

List of Figures

List of Tables

Chapter 1

Introduction

Since the creation of the first gaseous Bose-Einstein condensates (BECs) in 1995 [1, 2] the ability to cool, trap, and control atoms and more recently molecules has increased dramatically, producing some spectacular experimental results. On cooling a sample of atoms, we can say that the sample is cold when it has a temperature below one Kelvin, and ultracold at temperatures below one milliKelvin. To put these temperatures into context the coldest temperature ever recorded on earth was 184 K (-89°C), the temperature of liquid nitrogen is 77 K (-196 °C), and the temperature of cosmic background radiation, left over from the big bang is approximately 3 K [3]. In terms of velocities, a helium atom at room temperature (298K) has a translational velocity of $\sim$1300 ms^{-1} while at 1 mK the translational velocity is only $\sim$2.5 ms^{-1}.

At such low temperatures the thermal de Broglie wavelength $\lambda_{\mathrm{dB}} = 2\pi/k$ that characterizes the spatial extent of a particle starts to become comparable to the inter-particle separation, and we enter a fully quantum mechanical regime. For a trapped gas of bosons, a significant fraction of the gas exists in the lowest quantum state of the trap forming a BEC, in which the wavefunctions of all the individual particles overlap creating a macroscopic quantum state [4, 5]. The first BEC was created with a gas of rubidium-87 atoms [1], and since then the field has exploded and many other ultracold atomic species have been produced. More recently attention has turned to ultracold molecules. With their complex energy structure, molecules open up many new possibilities in the study of quantum matter. However, this extra complexity comes at a price with the extra structure making molecules harder to cool and then to trap.

The high degree of control possible over cold and ultracold matter provides the ideal test-bed for fundamental atomic and molecular physics. Optical lattices formed from counter-propagating laser beams can be used to create artificial crystals of ultracold particles, providing powerful models of quantum many-body systems [6]. At ultracold temperatures the Doppler broadening of spectral lines caused by translational motion of particles is drastically reduced allowing high precision spectroscopic measurements to be performed on molecules [7]. Current experiments are underway to test the time-dependence of fundamental physical constants [8, 9], and the possibility of an electron dipole moment [10].

Perhaps the most interesting area for the chemically minded is the control obtainable over the dynamics of ultracold atoms and molecules with externally applied electromagnetic fields, allowing the investigation of fundamental collisional processes and ultracold chemistry. This is all possible at cold and ultracold temperatures as the perturbation of the energy levels caused by electromagnetic fields is similar to the translational energy at these temperatures [11].

Before any experiment can be performed with ultracold matter, it must first be created and then stored. The next few sections therefore discuss some of the basic features of cooling and trapping atoms and molecules.

1.1 Cooling and Trapping Molecules

The most basic method of cooling atoms is via laser cooling, which works via the transfer of momentum that occurs when an atom absorbs a photon. A laser beam is applied to oppose the direction of an atomic beam, the photon is absorbed by an atom slowing the atom by $\hbar k/m$. The atom then re-radiates the photon in a random direction, resulting in an average slowing of the atom, as shown schematically in figure 1.1 [12]. Combining magnetic and optical fields a magneto-optical trap (MOT) can be created, in which six intersecting laser beams propagating and counter propagating along X, Y, and Z are applied to a sample of atoms inside a magnetic quadrupole field created by two opposing Helmholtz coils. The laser frequencies are detuned such that as particles in high-field seeking (HFS) states (the energy of the state decreases with increasing field strength)

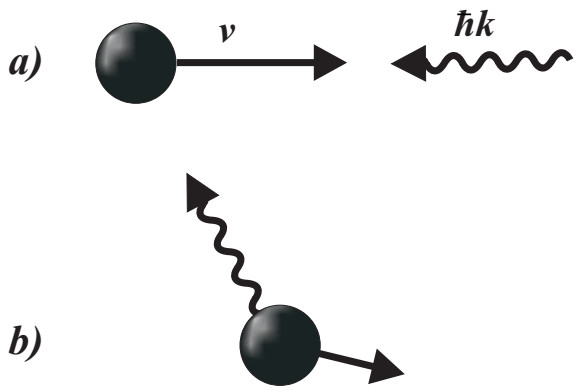

Figure 1.1: The two-step process of laser cooling, a) an atom moving with a velocity v absorbs a photon with momentum $\hbar k$ and is slowed to $v - \hbar k/m$. b) the atom then re-radiates the photon in a random direction on average slowing the atom.

are pushed out of the trap by the magnetic field gradient the probability of absorbing a photon and being pushed back towards the trap center is increased [13]. Using a MOT allows atoms to be laser cooled and accumulated, however the temperatures obtainable by laser cooling alone are not low enough to obtain Bose-Einstein condensation and another cooling process is required. The laser cooled atoms can be transferred into a conservative potential trap such as a magnetic trap or a far off resonant optical dipole trap [14] in which the atoms can be further cooled to degeneracy by an evaporative cooling scheme. In the evaporative cooling scheme the trap depth is lowered allowing the most energetic atoms to escape with the remaining atoms thermalizing at a lower temperature.

Laser cooling is the predominate method for atom cooling, however for laser cooling to work a two-level (absorbtion/emission) system is required and the extra complexity present in molecular energy levels drastically reduces its effectiveness. The failure of laser cooling for molecules means that many alternative methods to cool molecules have been developed.

The many methods for cooling molecules can be categorized into two distinct types, direct and indirect methods. Direct methods take samples of warm molecules and cool them down to cold and ultracold temperatures, whereas indirect methods involve formation of cold and ultracold molecules from samples of precooled ultracold atoms.

1.1.1 Direct Methods

Buffer-Gas and Sympathetic Cooling

The principle behind buffer-gas and sympathetic cooling is simply taking something hot and cooling it by putting it into something cold. The method of buffer gas cooling has been pioneered by the group of John Doyle at Harvard University from 1995 onwards [15–17]. Paramagnetic molecules are loaded into a cryogenic cell containing the buffer gas and are thermalized to hundreds of milliKelvin via collisions with the buffer gas, allowing the molecules to be magnetically trapped. As buffer gas cooling is independent of the energy level structure of a particular atom or molecule, in principle any trappable atom or molecule can be cooled in this way.

To thermalize and trap the atom or molecule before it collides with the walls of the cryogenic cell, the density of the buffer gas needs to be high enough to allow thermalization to occur on a length scale smaller than that of the cell. However, the density of the buffer gas decreases with decreasing temperature, thus there is a lower limit to the thermalization temperature attainable. For ^{3}He in a cell with a size on the order of 1 cm, a temperature as low as 240 mK can be attained. The first molecule to be cooled in this way was the calcium monohydride radical CaH [16]. The radical was prepared in the cell by laser ablation of a solid lump of CaH_2 and then thermalized with ^{3}He ($\approx$ 300 mK), producing 10^8 trapped molecules at a temperature of 400 mK.

A major problem with the method is the number of magnetically trapped molecules produced which is limited by the number of molecules that can be introduced into the cryogenic cell. Laser ablation only produces 10^8-10^{13} molecules with each laser pulse and introducing molecules through a capillary tube from a room temperature source only works for stable molecules with high vapor pressures. A method developed to get around this is the *buffer gas cooled beam* method, in which a molecular beam is used to transport the molecules into the cell through a hole. A thermalized sample of 10^{12} NH molecules has been produced using this method [18], a significant increase from using laser ablation or a capillary tube. A further advantage of using the cooled beam method is that the molecules can be pre-cooled before the beam is created [19].

Buffer gas cooling uses only a gas of cold He as the coolant, whereas sympathetic

cooling refers to using any pre-cooled gas to cool down a warm sample of atoms or molecules. Buffer gas cooling is limited to the mK temperature range, however sympathetic cooling offers the hope of going further, cooling molecules down into the μK range.

The most easily available coolants are the alkali-metal atoms which can be cooled to ultracold temperatures almost on demand [12]. However, the interaction potentials between alkali-metal atoms and heteronuclear diatomic molecules tend to be highly anisotropic, which couples different spin-substates increasing the rate spin-changing collisions that lead to trap loss reducing the effectiveness of sympathetic cooling, this is discussed further from chapter 5 onwards.

Stark Deceleration

A supersonic expansion of a high-pressure gas out of a small hole creates a molecular beam with a small velocity distribution and hence cold molecules with low relative velocities but with a high center of mass velocity in the laboratory frame. The beam can now be decelerated to produce molecules with a low center of mass velocity that can be trapped.

The technique of Stark deceleration is based upon the fact that a molecule with a permanent dipole moment will gain or lose energy when entering an electric field [20–22]. For a molecule in a low-field seeking quantum state (a state with an energy that increases with increasing field) moves into an electric field it gains a Stark energy, the gain in potential energy is compensated by a loss in kinetic energy thus if the field is removed the molecule will retain its lower velocity.

To allow continuous deceleration a series of stages consisting of two parallel metal rods is constructed, one of the rods is connected to a positive and the other a negative high voltage. As a molecule moves into the stage it is decelerated by the electric field, as the molecule reaches the point of maximum Stark energy the field is turned off and the field of the next stage is turned on. Alternating this process between each stage effectively forces the molecule to constantly move uphill against the field, and thereby allowing the continuous slowing of the molecule.

To examine the situation in more detail, let each stage be separated by a distance L

and the electric field switched after a time interval, ΔT. A phase angle ϕ can be defined to denote the position of the molecule at the time the electric field is switched, taking ϕ_0 to be the equilibrium situation when the molecule's velocity matches the frequency of the electric field, i.e. traveling the distance L in time ΔT. ΔT is gradually increased to account for the deceleration, so that a molecule with a phase ϕ_0 still moves a distance L in time ΔT. For molecules with a slightly larger phase than ϕ_0 it will lose more energy and be slowed relative to a molecule with ϕ_0 hence the phase will decrease until it is lower than ϕ_0, at which point the reverse happens and the molecule and it will lose less energy. Thus molecules with phases different from ϕ_0 will oscillate in phase and velocity about the equilibrium value, broadening the velocity distribution of the final packet of slowed molecules.

1.1.2 Indirect Methods

Feshbach Resonance Association

If two ultracold atoms are paramagnetic their potential can be influenced by external magnetic fields, a Feshbach resonance occurs when the collision energy of a pair of atoms exactly matches that of a bound molecular state [21–24]. Thus by varying the magnetic field to tune the atomic collision threshold across a molecular bound states a Feshbach resonance can be induced. Varying the magnetic field slowly enough across resonance the pair of colliding atoms can be adiabatically transferred into a bound molecular state. Figure 1.2 shows a schematic diagram of a magnetic Feshbach resonance.

The molecules formed via Feshbach resonances tend to be in highly excited vibrational states. However for fermionic atoms the molecules formed had surprisingly long lifetimes, attributed to Pauli suppression of the quenching process, where by a weakly bound molecular state couples to more tightly bound lower vibrationally lying molecular states and thereby stabilizing the weakly bound state [23, 25, 26]. These extended molecular lifetimes may allow the detailed experimental study of rovibrational states, relaxation processes, low temperature chemical reactivity [23] and also studying the close connections between molecular Bose-Einstein condensates and Cooper pairing in the BCS theory [25].

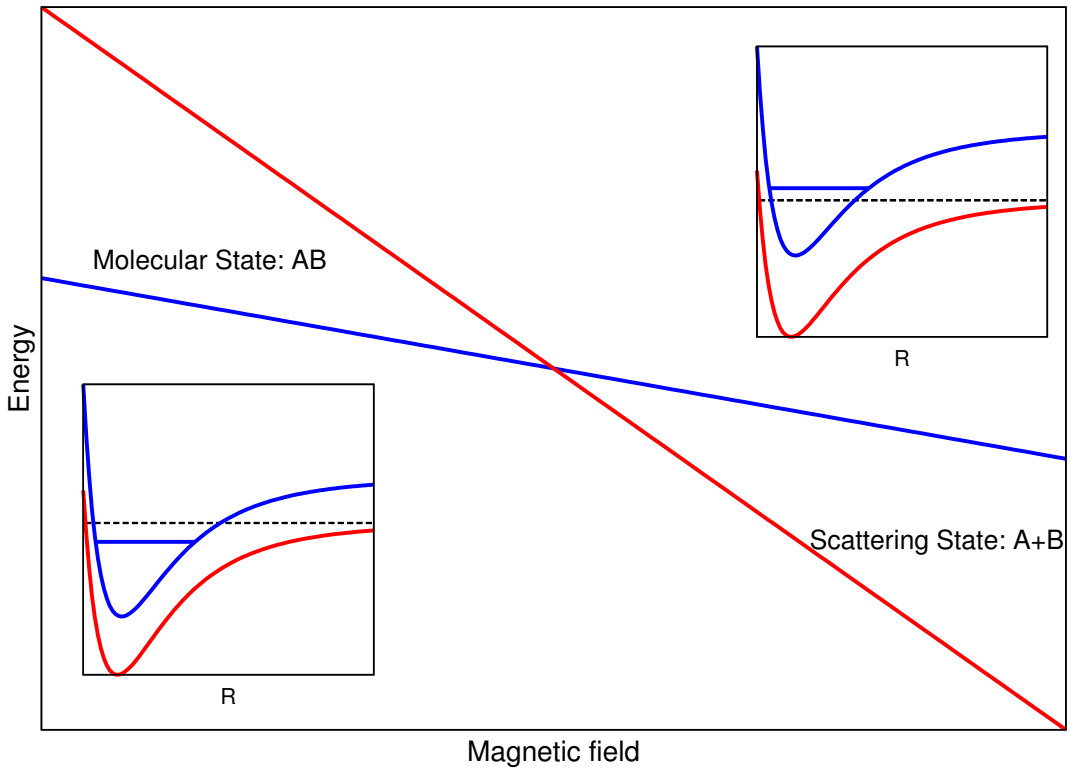

Figure 1.2: A magnetic Feshbach resonance occurs when a bound molecular state (blue) is tuned across a scattering threshold (red) as a function of magnetic field. The insets show the bound molecular state below/above the scattering threshold (dashed black) on the left/right of the resonance. The scattering threshold and the bound molecular state weakly avoided cross and thus by slowly ramping the field down, the colliding atoms on the right of the resonance can be adiabatically transferred into the molecular bound state on the left of the resonance.

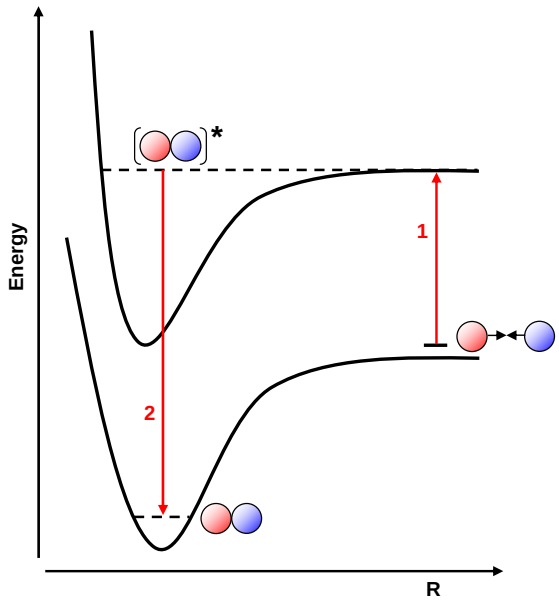

Figure 1.3: A basic photo-association scheme; (1) a pair of colliding atoms is excited to a weakly bound excited state, (2) a second photon is applied after a delay to transfer the excited state into a deeply bound molecular state.

Taking lithium as an example Strecker et al. [27] tuned an ultracold fermi gas of ^{6}Li atoms across a narrow magnetic Feshbach resonance formed an ultracold gas of $^6Li_2$ ($X^1\Sigma_g^+(v = 38)$) molecules with an efficiency of approximately 50%. Using a different Feshbach resonance Zwierlein et al. [25] created a gas of $^6Li_2$ molecules and by changing the trap depth evaporatively cooled the gas further to form a molecular Bose-Einstein condensate.

Photo-association

In the method of photoassociation, two atoms absorb a photon to form a molecule in a highly excited ro-vibrational state [21,23,24], the lifetime of the molecule formed is short due to spontaneous emission back to an unbound atomic state. However it is possible to use a two-photon process, as shown in figure 1.3, to produce molecules in their electronic ground state, with the second delayed photon used to stimulate emission to the molecular ground state. This was first achieved for Cs_2 in 1998 by Fiorettii et al. [28] who loaded a vapor-cell magneto-optical trap with Cs atoms with an approximate temperature of 200

μK and illuminated it with a diode laser. Detection of the Cs_2 molecules was by a pulsed photoionization laser producing Cs^+ and Cs_2^+ ions that were then detected by a time of flight spectrometer.

Using a multi-photon photoassociation process Sage et al. [29] produced ultracold RbCs molecules in their $X^1\Sigma^+$ vibrational ground states. The colliding Rb and Cs atoms were excited to an electronically excited molecular level, which rapidly decayed into the the metastable $a^3\Sigma^+(v = 37)$ state. A pump laser pulse was then used to excite the $a^3\Sigma^+$ molecules to an intermediate state, from which a dump laser pulse was used to transfer the RbCs molecules into the $X^1\Sigma^+$ ground state. The final translational temperature was $\sim 100\,\mu$K.

More recently deeply bound and absolute ground state molecules have been formed from weakly bound Feshbach molecules, created at magnetic Feshbach resonances in atomic gases, which are then transferred to the absolute ground state using a STIRAP (STImulated Raman Adiabatic Passage) scheme [30–33]. The STIRAP scheme transfers population from the weakly bound Feshbach state $|a\rangle$ to the ground state $|b\rangle$ through two overlapping laser pulses coupled to an excited state $|e\rangle$, in which the laser pulse that couples $|a\rangle$ to $|e\rangle$ is preceded by the pulse that couples $|b\rangle$ to $|e\rangle$.

1.1.3 Trapping

A basic magnetic quadrupole trap consists of a pair of opposed Helmholtz coils that create a magnetic field that vanishes at a point and increases linearly in all directions from that point, using this method it is possible to create traps that are multiple Kelvin deep. However, only low-field seeking (LFS) states (the energy of the state increase with field strength) are trapped and high-field seeking (HFS) states (the energy of the state decreases with field strength) are expelled from the trap, therefore relaxation from the low-field seeking to the high-field seeking state limits the lifetime of the trapped molecules. Despite these limitations success has been achieved notably with samples of $CaH(^2\Sigma)$ [16] and $NH(^3\Sigma^-)$ [34].

Transitions from the low-field to the high-field seeking states, can occur via collision relaxation or non-adiabatic spin-flip (Majorana) transitions. The trapped molecules will remain in the same quantum state adiabatically following the magnetic field if the mag-

netic field experienced by the molecule varies slowly with time. However near magnetic field zero at the center of the trap the rate of change of magnetic field becomes comparable to the transition frequency between the LFS and HFS states and thus trap loss occurs. A simple method to reduce the Majorana transitions is to remove the magnetic field zero and *plug the hole* in the trap. Various methods have been used to remove the hole, in one such method an oscillating bias field can be superimposed on the quadrupole trap creating a time-averaged orbiting potential (TOP) which removes the hole in the trap [35].

In an analogous way to magnetic field traps, molecules with an electric dipole moment in a LFS state can be trapped in a quadrupole electric field [36–38]. The creation of an electric field maximum to trap molecules in HFS states in three dimensional free space is impossible. However using a suitable arrangement of electrodes an electric field saddle point can be created with a field maximum a defocusing forces in the radial direction and a field minimum a focusing force in the axial direction. Reversing the current changes the saddle point creating a focusing force in the radial direction and a defocusing force in the axial direction. Connecting the electrodes to an AC current thus creates a trapping potential for both HFS and LFS states [39].

1.2 Outline

The broad aims of the work presented in this thesis are to explore some of the effects externally applied electromagnetic fields have on ultracold molecules. The structure of this thesis is as follows, Chapters 2 and 3 outline some of the basic scattering theory required to understand ultracold collisions in externally applied fields. There is a need for methods to cool molecules to below the milliKelvin temperature range and the effect of zero-energy magnetic Feshbach resonances on cross-section profiles is examined in chapter 4. The prospect of using magnesium atoms for the sympathetic cooling of NH molecules is accessed in chapters 5 to 8, in which a multichannel quantum-defect theory approach is used to examine the near threshold cross section properties. Finally a new type of conical intersection, formed purely by electromagnetic fields, and some of the consequences of such an intersection in a BEC is examined in chapters 9 to 13.

Chapter 2

Scattering Theory

Scattering theory provides the theoretical framework to describe collisions between particles, and unless otherwise stated the scattering theory presented in this chapter broadly follows the theory presented by Taylor [40], Joachin [41], Atkins and Friedman [42], and Manolopoulos [43]. The theory presented in this chapter is not a complete treatment of the subject and more can be found in the respective references.

2.1 Scattering Cross Sections

Consider a beam of particles directed at a target with a detector at a distance r from the target. The detector presents an area $r^2 d\Omega$, at an orientation (θ, ϕ), where $d\Omega = sin\theta d\theta d\phi$ is the solid angle subtended by the detector. For an incident flux of particles J_i in a state i, the detection frequency of particles in a state j, $dZ_j^{\text{det}}(\theta, \phi)$ is given by

$$dZ_j^{\text{det}}(\theta, \phi) = \sigma_{i\to j}^{\text{diff}}(\theta, \phi) J_i d\Omega, \tag{2.1}$$

where $\sigma_{i\to j}^{\text{diff}}(\theta, \phi)$ is the *differential cross-section* and like the detection frequency is dependent on the system orientation. Integrating the differential cross-section over all deflection angles,

$$\sigma_{i\to j}^{\text{tot}} = \int_0^{\pi} \int_0^{2\pi} \sigma_{i\to j}^{\text{diff}}(\theta, \phi) \sin\theta d\theta d\phi, \tag{2.2}$$

gives the integral scattering cross-section $\sigma_{i\to j}^{\text{tot}}$, which is the total cross-section for scattering over all angles. The total detection frequency is thus

$$Z^{\text{det}} = \sigma_{i\to j}^{\text{tot}} J_i. \tag{2.3}$$

It can be seen from this equation that the units of $\sigma^{\text{tot}}_{i\to j}$ are those of area, and it can be thought to represent an effective area presented by the scattering target. The rate of the process $i \to j$ is given by the rate coefficient $k_{i\to j} = v\sigma^{\text{tot}}_{i\to j}$, where v is the relative collision velocity.

To develop the theory further and show how cross sections can be calculated, the treatment will be initially confined to elastic scattering in which the initial kinetic energy of the system is equal to the kinetic energy of the system after the collision and thus the system remains in its initial state (single channel scattering). Before moving onto inelastic scattering in which the kinetic energy after a collision is not equal to the initial kinetic energy and the system changes its state (multichannel scattering).

2.2 Stationary Scattering Wavefunctions

The scattering dynamics of two particles interacting through a potential $V(\boldsymbol{R})$ are governed by the time-dependent Schrödinger equation,

$$\left(-\frac{\hbar^2}{2\mu}\nabla^2 + V(\boldsymbol{R})\right)\Psi(\boldsymbol{R},t) = i\hbar\frac{\partial}{\partial t}\Psi(\boldsymbol{R},t), \tag{2.4}$$

where μ is the reduced mass of the colliding system. The potential is time-independent and the wavefunction can be separated as

$$\Psi(\boldsymbol{R},t) = \psi(\boldsymbol{R})e^{-iEt/\hbar}, \tag{2.5}$$

where $\psi(\boldsymbol{R})$ is a solution of the time-independent Schrödinger equation

$$\left(-\frac{\hbar^2}{2\mu}\nabla^2 + V(\boldsymbol{R})\right)\psi(\boldsymbol{R}) = E\psi(\boldsymbol{R}), \tag{2.6}$$

which allows an infinite number of time-independent, *stationary* solutions for which the kinetic energy of the system has the definite value

$$E = \frac{p^2}{2\mu} = \frac{\hbar^2k^2}{2\mu} = \frac{\mu v^2}{2}. \tag{2.7}$$

Introducing a reduced potential $U(\boldsymbol{R}) = 2\mu V(\boldsymbol{R})/\hbar$, allows (2.6) to be rewritten as

$$\left[\nabla^2 + k^2 - U(\boldsymbol{R})\right]\psi(\boldsymbol{R}) = 0. \tag{2.8}$$

At large distances the stationary solution will be a superposition of an incident plane wave and an outgoing spherical wave with an amplitude dependent on θ and ϕ. Defining the incident plane wave along Z, the stationary scattering wavefunction that satisfies (2.8) must therefore have the asymptotic form

$$\psi(\boldsymbol{R}) \xrightarrow[R\to\infty]{} A\left(e^{ikZ} + f(\theta,\phi)\frac{e^{ikR}}{R}\right), \tag{2.9}$$

where $f(\theta,\phi)$ is the scattering amplitude. The scattering amplitude can be related to the particle flux density and thus to the differential and integral cross-sections to give

$$\sigma^{\text{diff}}(\theta,\phi) = |f(\theta,\phi)|^2 \tag{2.10}$$

$$\sigma^{\text{tot}} = \int_0^{\pi}\int_0^{2\pi} |f(\theta,\phi)|^2 \sin\theta d\theta d\phi. \tag{2.11}$$

For spherically symmetric (atom-atom) and cylindrically symmetric (atom-diatom) interaction potentials the definition of the incident plane wave along Z removes the azimuthal ϕ dependence from the scattering in the center of mass frame and thus the asymptotic form of the scattering wave function reduces to

$$\psi(\boldsymbol{R}) \xrightarrow[R\to\infty]{} A\left(e^{ikZ} + f(\theta)\frac{e^{ikR}}{R}\right). \tag{2.12}$$

Given that the problems treated in the thesis and that most scattering problems encountered in the ultracold regime are all cylindrically symmetric, we shall confine the follow treatment to potentials of the form $V(R,\theta)$.

2.3 Partial Wave Expansion

The scattering Hamiltonian written in spherical polar coordinates,

$$\begin{aligned}\hat{H} &= -\frac{\hbar^2}{2\mu}\nabla^2 + V(R,\theta) \\ &= -\frac{\hbar^2}{2\mu}\left[\frac{1}{R^2}\frac{\partial}{\partial R}\left(R^2\frac{\partial}{\partial R}\right) + \frac{1}{R^2\sin\theta}\frac{\partial}{\partial\theta}\left(\sin\theta\frac{\partial}{\partial\theta}\right) + \frac{1}{R^2\sin^2\theta}\frac{\partial^2}{\partial\phi^2}\right] + V(R,\theta),\end{aligned} \tag{2.13}$$

can be simplified by considering the *orbital angular momentum* operator

$$\boldsymbol{L} = \boldsymbol{R}\times\boldsymbol{p}. \tag{2.14}$$

Quantum mechanically the linear momentum operator is $\hat{\boldsymbol{p}} = -i\hbar\nabla$ and thus

$$\hat{L}_X = -i\hbar\left(Y\frac{\partial}{\partial Z} - Z\frac{\partial}{\partial Y}\right) = i\hbar\left(\sin\phi\frac{\partial}{\partial\theta} + \cot\theta\cos\phi\frac{\partial}{\partial\phi}\right) \tag{2.15}$$

$$\hat{L}_Y = -i\hbar\left(Z\frac{\partial}{\partial X} - X\frac{\partial}{\partial Z}\right) = i\hbar\left(-\cos\phi\frac{\partial}{\partial\theta} + \cot\theta\sin\phi\frac{\partial}{\partial\phi}\right) \tag{2.16}$$

$$\hat{L}_Z = -i\hbar\left(X\frac{\partial}{\partial Y} - Y\frac{\partial}{\partial X}\right) = -i\hbar\frac{\partial}{\partial\phi}, \tag{2.17}$$

and

$$\hat{L}^2 = \hat{L}_X^2 + \hat{L}_Y^2 + \hat{L}_Z^2 = -\hbar^2\left[\frac{1}{\sin\theta}\frac{\partial}{\partial\theta}\left(\sin\theta\frac{\partial}{\partial\theta}\right) + \frac{1}{\sin^2\theta}\frac{\partial^2}{\partial\phi^2}\right], \tag{2.18}$$

the Hamiltonian can therefore be rewritten as

$$\hat{H} = -\frac{\hbar^2}{2\mu}\left[\frac{1}{R^2}\frac{\partial}{\partial R}\left(R^2\frac{\partial}{\partial R}\right) - \frac{\hat{L}^2}{\hbar^2R^2}\right] + V(R,\theta). \tag{2.19}$$

It is easily verified that $\hat{H}$, $\hat{L}^2$, and $\hat{L}_Z$ commute

$$[\hat{L}^2, \hat{L}_Z] = [\hat{H}, \hat{L}^2] = [\hat{H}, \hat{L}_Z] = 0, \tag{2.20}$$

and the eigenfunctions common to $\hat{L}^2$ and $\hat{L}_Z$ are the spherical harmonics $Y_{LM}(\theta,\phi)$, defined such that

$$\hat{L}^2 Y_{LM}(\theta,\phi) = \hbar^2 L(L+1)Y_{LM}(\theta,\phi) \tag{2.21}$$

$$\hat{L}_Z Y_{LM}(\theta,\phi) = \hbar M Y_{LM}(\theta,\phi). \tag{2.22}$$

Thus eigenfunctions common to the three operators can be found and the cylindrically symmetric scattering wavefunction can thus be expanded in partial-waves corresponding to given values of L in terms of Legendre polynomials,

$$\psi(k,\boldsymbol{R}) = R^{-1}\sum_{L=0}^{\infty}\psi_L(k,R)P_L(\cos\theta). \tag{2.23}$$

Substituting the partial-wave expansion of the stationary scattering wavefunction into the time-independent Schrödinger equation, results in the following radial equation

$$\left[-\frac{\hbar^2}{2\mu}\frac{d^2}{dR^2} + \frac{\hbar^2L(L+1)}{2\mu R^2} + V(R,\theta)\right]\psi_L(k,R) = E\psi_L(k,R), \tag{2.24}$$

which can be rewritten in the simpler form using the reduced potential as

$$\left[\frac{d^2}{dR^2} + k^2 - \frac{L(L+1)}{R^2} - U(R,\theta)\right]\psi_L(k,R) = 0. \tag{2.25}$$

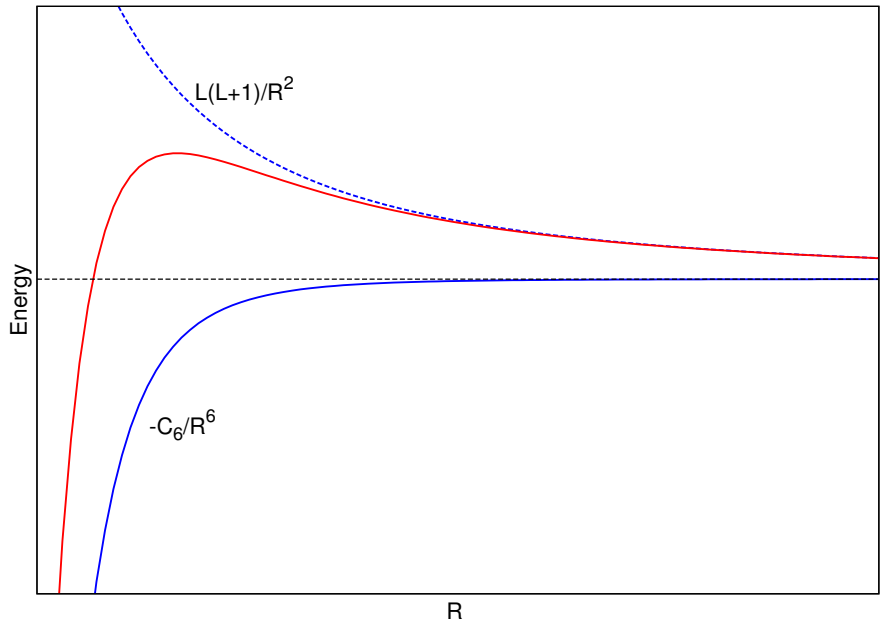

Figure 2.1: Effective potential (red) showing a centrifugal barrier, resulting from a potential that has an asymptotic form $-C_6/R^6$ (blue, solid) and a centrifugal term $L(L+1)/\mu R^2$ (blue, dashed).

It is worth noting that the centrifugal term resulting from orbital angular momentum term $L(L+1)/R^2$ results in an effective potential with centrifugal barrier, as shown in figure 2.1. For a potential that decays as $-C_6/R^6$ at long-range the height of the centrifugal barrier is approximately $E_{\rm cf}^L = (\hbar L(L+1)/\mu)^{\frac{3}{2}}(54C_6)^{-\frac{1}{2}}$.

2.4 Scattering Boundary Conditions

To solve the radial scattering equation (2.25), boundary conditions are required at $R = 0$ and ∞. ψ_L must be regular at the origin and thus

$$\psi_L(k,R) \xrightarrow[R\to 0]{} 0. \tag{2.26}$$

In the absence of a potential ($V(R) = 0$), (2.25) reduces to the *free radial equation*

$$\left[\frac{d^2}{dR^2} + k^2 - \frac{L(L+1)}{R^2}\right]\psi_L^{\rm free}(k,R) = 0, \tag{2.27}$$

which is the *spherical Bessel differential equation* in kR. Particular pairs of linear independent solutions are the spherical Bessel $j_l(kR)$ and spherical Neumann $n_L(kR)$ functions,

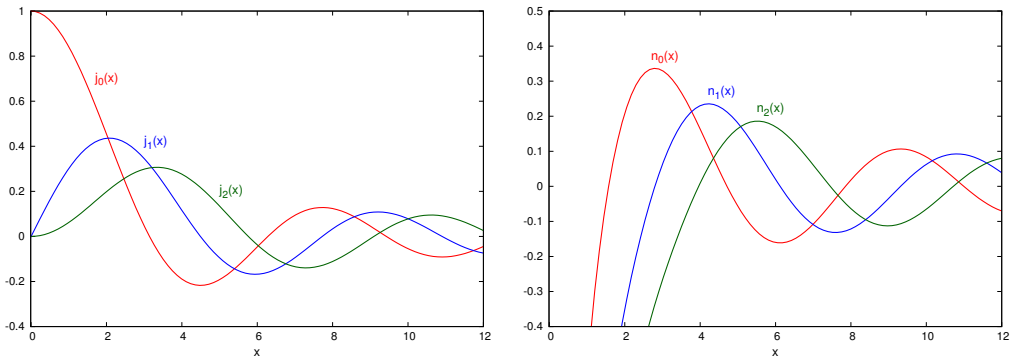

Figure 2.2: The first few spherical Bessel $j_L(x)$ and spherical Neumann $n_L(x)$ functions.

shown in figure 2.2, and the spherical Hankel functions $h_L^{(1)}(kR) = j_L(kR) + in_L(kR)$ and $h_L^{(2)}(kR) = j_L(kR) - in_L(kR)$ [44]. Which have the asymptotic form

$$j_L(x) \xrightarrow[x\to\infty]{} \frac{1}{x}\sin(x - L\pi/2) \tag{2.28}$$

$$n_L(x) \xrightarrow[x\to\infty]{} -\frac{1}{x}\cos(x - L\pi/2) \tag{2.29}$$

$$h_L^{(1)}(x) \xrightarrow[x\to\infty]{} -i\frac{e^{i(x-L\pi/2)}}{x} \tag{2.30}$$

$$h_L^{(2)}(x) \xrightarrow[x\to\infty]{} i\frac{e^{-i(x-L\pi/2)}}{x}. \tag{2.31}$$

Therefore asymptotically ψ_L is a linear combination of sine and cosine functions or equivalently a linear combination of incoming e^{-ikR} and outgoing e^{+ikR} radial waves, and two possible general solutions of (2.27) are

$$\psi_L^{\text{free}}(k,R) = kR\left[C_L^{(1)}(k)j_L(kR) + C_L^{(2)}n_L(kR)\right] \tag{2.32}$$

$$\psi_L^{\text{free}}(k,R) = kR\left[D_L^{(1)}(k)h_L^{(1)}(kR) + D_L^{(2)}h_L^{(2)}(kR)\right], \tag{2.33}$$

where $C_L^{(i)}$ and $D_L^{(i)}$ are pairs of integration constants depending on k.

Returning to the case of a non-zero potential $U(R) \neq 0$, and assuming that $U(R)$ goes to zero faster than $1/R$ as $R \to \infty$, beyond some distance $U(R)$ and $L(L+1)/R^2$ can be neglected, and the general solutions to (2.25) will be the same as those of the free radial equation (2.28). The asymptotic boundary condition can thus be expressed as

$$\psi_L(k,R) \xrightarrow[R\to\infty]{} RkC_L^{(1)}(k)\left[j_L(kR) - \tan\delta_L(k)n_L(kR)\right] \tag{2.34}$$

or

$$\psi_L(k,R) \xrightarrow[R\to\infty]{} A_L(k)\sin(kR - L\pi/2 + \delta_L), \tag{2.35}$$

where

$$A_L(k) = \sqrt{\left[C_L^{(1)}(k)\right]^2 + \left[C_L^{(2)}(k)\right]^2}, \tag{2.36}$$

and δ_L is the scattering phase shift, given by

$$\tan\delta_L(k) = -\frac{C_L^{(2)}(k)}{C_L^{(1)}(k)}. \tag{2.37}$$

It is also useful to express the boundary condition (2.35) in terms of incoming (e^{-ikR}) and outgoing (e^{+ikR}) waves

$$\begin{aligned}\psi_L(k,R) &\xrightarrow[R\to\infty]{} A_L(k)\frac{e^{-i\delta_L}}{2i}\left(e^{-i(kR-L\pi/2)} - e^{i(kR-L\pi/2+2\delta_L)}\right)\\ &\xrightarrow[R\to\infty]{} A_L(k)(-1)^L i^L \frac{e^{-i\delta_L}}{2i}\left(e^{-ikR} - S_L(k)e^{ikR}\right)\\ &\xrightarrow[R\to\infty]{} \tilde{A}_L(k)\left(e^{-ikR} - S_L(k)e^{ikR}\right),\end{aligned} \tag{2.38}$$

where the coefficient of outgoing wave $S_L(k)$ is an S-matrix element given by

$$S_L(k) = e^{2i\delta_L(k)}. \tag{2.39}$$

With the partial wave scattering boundary conditions we can now relate the scattering phase-shift and similarly the S-matrix element to the scattering amplitude $f(\theta)$, defined by (2.12). Using the plane wave partial wave expansion

$$e^{ikZ} = \sum_{L=0}^{\infty} i^L(2L+1)j_L(kR)P_L(\cos\theta), \tag{2.40}$$

and the asymptotic form of $j_L(kR)$, (2.12) can be rewritten as

$$\psi(k,R) \xrightarrow[R\to\infty]{} A\left[\sum_{L=0}^{\infty}(2L+1)i^L\frac{\sin(kR-L\pi/2)}{kR}P_L(\cos\theta) + f(\theta)\frac{e^{ikR}}{R}\right], \tag{2.41}$$

which can be compared to the asymptotic form of the partial wave expansion,

$$\psi(k,R) \xrightarrow[R\to\infty]{} \sum_{L=0}^{\infty}\frac{A_L(k)\sin(kR-L\pi/2+\delta_L)}{R}P_L(\cos\theta). \tag{2.42}$$

Expanding sine terms in (2.41) and (2.42) in terms of exponentials and equating coefficients of e^{ikR}/R it can be easily shown that

$$f(\theta) = \frac{1}{2ik}\sum_{L=0}^{\infty}(2L+1)P_L(\cos\theta)\,(S_L - 1) = \frac{1}{2k}\sum_{L=0}^{\infty}(2L+1)P_L(\cos\theta)\left(e^{i\delta_L}\sin\delta_L\right). \tag{2.43}$$

The integral cross section is thus

$$\sigma^{\text{tot}}(k) = \sum_{L=0}^{\infty}\sigma_L(k) = \frac{\pi}{k^2}\sum_{L=0}^{\infty}(2L+1)|S_L - 1|^2 = \frac{4\pi}{k^2}\sum_{L=0}^{\infty}(2L+1)\sin^2\delta_L(k). \tag{2.44}$$

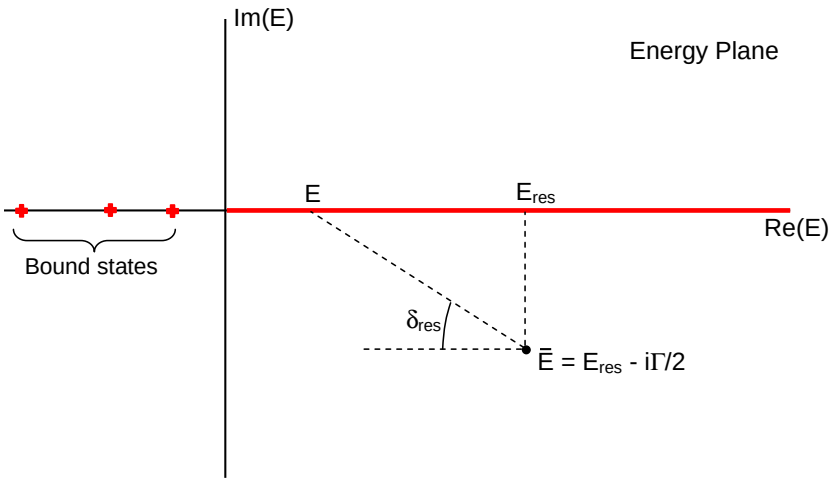

Figure 2.3: The resonant phase-shift δ_{res} forms an angle between the collision energy and the location of a pole in the S-matrix at a complex energy $\bar{E}$. The physically allowed regions are shown in red.

2.5 Scattering Resonances

Phase shifts and therefore cross-sections are usually slowly varying functions of the collision energy. However near scattering resonances the phase shift and thus the cross section undergo a rapid variation. To analyze this behaviour further the phase shift can be split into

$$\delta(E) = \delta_{\text{bg}}(E) + \delta_{\text{res}}(E), \tag{2.45}$$

where $\delta_{\text{bg}}(E)$ is a slowly varying background contribution and $\delta_{\text{res}}(E)$ is a resonance contribution to the total phase shift. Using this formulation the total cross section is thus

$$\sigma^{\text{tot}}(E) = \frac{4\pi}{k^2} \sin^2(\delta_{\text{bg}}(E) + \delta_{\text{res}}(E)). \tag{2.46}$$

The effect of a resonance on the phase shift can be visualized by noting that the S-matrix $S(E)$ is a complex quantity and by expanding our treatment into the complex plane, the S-matrix can be regarded as a function of a complex energy $\bar{E}$. A resonance corresponds to a pole in the scattering matrix, occurring at the location of bound states in either an asymptotically open channel (shape resonance) or an asymptotically closed channel (Feshbach resonance). In general the pole exists at the complex energy

$$\bar{E} = E_{\text{res}} - \frac{i\Gamma}{2}. \tag{2.47}$$

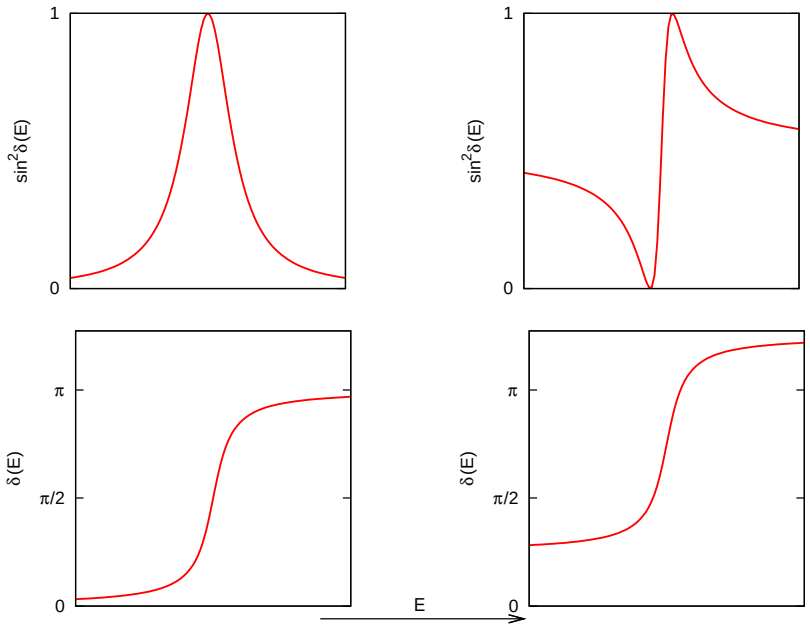

Figure 2.4: Across a resonance the Breit-Wigner form shows that the phase-shift changes by π, the form of the cross section which is proportional to $\sin^2\delta(E)$ is shown for a zero and a non-zero background phase-shift; $\delta_{\rm bg} = 0$ (left) and $\delta_{\rm bg} = \pi/4$ (right).

and $\delta_{\rm res}$ is the angle between a collision energy E and the location of the pole $\bar{E}$ in the complex plane, as shown in figure 2.3, from which it follows from simple geometric arguments that

$$\tan\delta_{\rm res}(E) = \frac{\Gamma/2}{E_{\rm res} - E}, \tag{2.48}$$

and thus

$$\delta(E) = \delta_{\rm bg}(E) + \tan^{-1}\left[\frac{\Gamma/2}{E_{\rm res} - E}\right], \tag{2.49}$$

which is known as the *Breit-Wigner* form of the phase-shift, where $E_{\rm res}$ is the resonance location and Γ is the width of the resonance.

As the collision energy is varied across resonance, the Breit-Wigner form shows that $\delta(E)$ varies by π and thus the single-channel S-matrix element $e^{2i\delta(E)} = \cos 2\delta(E) + i\sin 2\delta(E)$ corresponds to a circle of radius 1 in the complex plane. However the form of the cross section over a resonance $\propto \sin^2\delta$, will be determined by the value of the slowly varying background phase shift. Figure 2.4, shows the form of the cross section for the background phase shifts 0 and $\pi/4$.

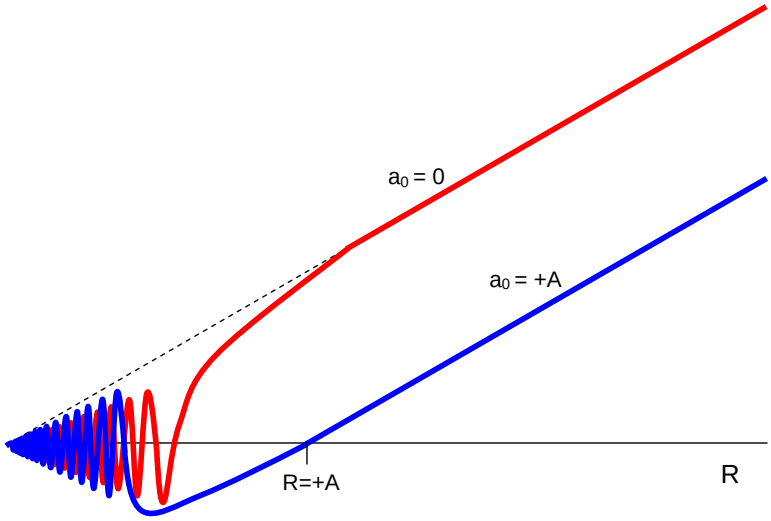

Figure 2.5: Schematic diagram of the short-range extrapolation of the long range wavefunction $\sim \sin(k(R - a_s))/\sqrt{k}$ to zero at zero energy, for $a_0 = 0$ and $a_0 = +A$.

2.6 Scattering at low temperatures

In the low temperature regime all partial wave cross section σ_L vanish as k^{4L}, and thus σ^{tot} becomes isotropic approaching a constant characterized the $L = 0$, s-wave partial cross section σ_0. It becomes useful to define the scattering length a_0,

$$a_0 = -\lim_{k\to 0} \frac{\tan \delta_0}{k}, \tag{2.50}$$

such that the scattering amplitude approaches,

$$f \xrightarrow[k\to 0]{} a_0, \tag{2.51}$$

and the cross section becomes,

$$\sigma^{\text{tot}} = 4\pi a_0^2. \tag{2.52}$$

The physical meaning of a_0 can be understood by considering the scattering from a hard sphere potential

$$U(R) = \begin{cases} +\infty & R < a \\ 0 & R > a. \end{cases} \tag{2.53}$$

The wavefunction outside a given by (2.34) must vanish at $R = a$, and thus

$$\tan \delta_L(k) = \frac{j_L(ka)}{n_L(ka)}. \tag{2.54}$$

Which in the low-energy limit ($ka \ll 1$) [44] becomes

$$\tan \delta_L(k) = -\frac{(ka)^{2L+1}}{(2L+1)!!(2L-1)!!}, \tag{2.55}$$

from which it becomes apparent that the low-energy scattering is dominated by $L = 0$. Using the small argument limit; $\tan^{-1}(x) \simeq x$ for $x \ll 1$, the phase shift becomes

$$\delta_0 = -ka, \tag{2.56}$$

and thus the zero-energy cross section is

$$\sigma^{\text{tot}} = 4\pi a^2. \tag{2.57}$$

For a real atom-atom or atom-molecule potential the wavefunction oscillates rapidly in the vicinity of the potential well, approaching its asymptotic form $\sim \sin(k(R - a_s))/\sqrt{k}$ well beyond the range of the potential. However this asymptotic form is equivalent to the wavefunction from a hard-sphere potential with the infinite wall at a_s. Physically this equates to the extrapolation of the long-range sine function to zero which occurs at the point $R = a_s$, as schematically shown in figure 2.5. For negative scattering lengths this equates to a virtual node in the wavefunction as $R \geq 0$.

2.7 Inelastic Scattering

If the colliding products can finish in multiple asymptotic states inelastic scattering becomes possible and the cross section now becomes

$$\sigma^{\text{tot}}_{\alpha\to\alpha'}(k) = \sum_{L,M}\sum_{L',M'} \frac{\pi}{k^2_\alpha}|S_{ij} - 1|^2 \tag{2.58}$$

where i and j are any two channels of the form; $i = (\alpha, L, M)$, $j = (\alpha', L', M')$, and α is a set of asymptotic quantum numbers describing the collision system. The S-matrix is no-longer just $e^{2i\delta_L}$ rather an $(N_{\text{open}} \times N_{\text{open}})$ matrix for N_{open} asymptotically open channels, with diagonal matrix elements

$$S_{ii} = e^{2i\delta_L}. \tag{2.59}$$

The general S-matrix element $\langle \alpha, L, M \mid S \mid \alpha', L', M' \rangle$ physically represents the probability amplitude of finding the system that originates in channel (α, L, M) at $t \to -\infty$, in the channel (α', L', M') at $t \to +\infty$.

Over a resonance the phase-shift no longer follows the Breit-Wigner form and the quantity that follows the Breit-Wigner form is the S-matrix eigenphase sum which is the sum of the phases of the eigenvalues of the S-matrix. However, the individual S-matrix elements still describe circles in the complex plane,

$$S_{ii'}(E) = S_{\mathrm{bg},ii'}(E) - \frac{ig_i g_{i'}}{E - E_{\mathrm{res}} + i\Gamma/2}, \tag{2.60}$$

where g_i is complex and is defined from the partial width of channel i, $\Gamma_i = |g_i|^2$. The radius of the circle $S_{ii'}$ is $|g_i g_{i'}|/\Gamma$. The effect of magnetic fields on the cross-section profile at a Feshbach resonance is examined in chapter 4.

2.8 Coupled Channel Methods: BOUND and MOLSCAT

For most scattering problems numerical propagation of the wavefunctions is required and in multichannel scattering problems numerical techniques are essential. Expressing the total Hamiltonian for a general system of colliding particles in Jacobi coordinates (R, θ)

$$\hat{H} = -\frac{\hbar^2}{2\mu} R^{-1} \frac{d^2}{dR^2} R + \frac{\hat{L}^2}{2\mu R^2} + \hat{H}_{\mathrm{int}} + V(R, \theta), \tag{2.61}$$

where R is the radial separation coordinate, and $\hat{H}_{\mathrm{int}} = \hat{H}_A + \hat{H}_B$ represents the internal Hamiltonians of the two particles A and B.

In the coupled channel approach, R is handled by direct numerical propagation on a grid, with all other coordinates included in the basis set [45, 46]. The total wavefunction for the n^{th} state of the system is expanded as

$$\Psi_n(R, \theta) = \sum_j \psi_j(\theta) F_{jn}(R)/R, \tag{2.62}$$

where $\psi_j(\theta)$ form a complete orthonormal channel basis and $F_{jn}(R)$ is a radial channel function describing the wave function in each channel j. Substituting the expansion into the total Schrödinger equation yields a set of coupled equations for the radial functions $F_{jn}(R)$

$$\frac{d^2}{dR^2} F_{jn}(R) = \sum_k W_{jk}(R) F_{kn}, \tag{2.63}$$

where

$$W_{jk}(R) = \langle \psi_j \mid \frac{2\mu}{\hbar^2} \{\hat{H}_{\mathrm{int}} + V(R, \theta)\} + \frac{\hat{L}^2}{R^2} - k^2 \mid \psi_k \rangle, \tag{2.64}$$

and $k^2 = 2\mu E/\hbar^2$. Expressing in matrix notation

$$\frac{d^2}{dR^2}\mathbf{F_n}(R) = \mathbf{W}(R)\mathbf{F_n}(R), \tag{2.65}$$

where for an N channel problem $\mathbf{F_n}(R)$ is a column vector of order N with elements F_{kn}, $\mathbf{W}(R)$ is the $N \times N$ interaction matrix with elements W_{jk}.

The BOUND [47] and MOLSCAT [48] packages solve the set of coupled channel equations for N channels by propagating solutions over a grid in R, with bound state and scattering state boundary conditions applied at R_{min} and R_{max}. One of the primary methods used for propagating solutions and solving the coupled channel equations is using the log-derivative method.

2.8.1 The Log Derivative Method

Rather than propagate N, $\mathbf{F_n}(R)$ column vectors the whole $(N \times N)$ matrix $\mathbf{F}(R)$ can be propagated, in which each column of $\mathbf{F}(R)$ is a linearly independent solution to (2.65). However, directly numerically propagating $\mathbf{F}(R)$ becomes unstable in the classically forbidden region as any channel functions in locally a closed channel can explode exponentially.

A more numerically stable method is to propagate the log-derivative matrix $\mathbf{Y}(R)$ which is stable in the presence of closed channels. The log-derivative matrix is defined to be

$$\mathbf{Y}(R) = \frac{d}{dR}\ln\mathbf{F}(R) = \mathbf{F}'(R)\mathbf{F}^{-1}(R), \tag{2.66}$$

which reduces (2.65) to the first-order matrix Ricatti equation

$$\mathbf{Y}'(R) = \mathbf{W}(R) - \mathbf{Y}^2(R). \tag{2.67}$$

For bound state solutions the object is to locate energies E_n for which solutions of equation (2.65) that satisfy bound-state boundary conditions in which $\mathbf{F}(R) \rightarrow 0$ as $R \rightarrow 0$ or ∞. The log-derivative matrix is propagated outwards from a point R_{min} in the inner-classically forbidden region and inwards from a point R_{max} in the outer classically-forbidden region to a matching point R_{mid} in the classically allowed region. If E is an eigenvalue of the coupled equations, there must exist a wavefunction vector

$\mathbf{F_n}(R_{\rm mid}) = \mathbf{F_n}^+(R_{\rm mid}) = \mathbf{F_n}^-(R_{\rm mid})$ for which $[\mathbf{F_n}^+]'(R_{\rm mid}) = [\mathbf{F_n}^-]'(R_{\rm mid})$ so that

$$\mathbf{Y}^+(R_{\rm mid})\mathbf{F_n}(R) = \mathbf{Y}^-(R_{\rm mid})\mathbf{F_n}(R_{\rm mid}), \tag{2.68}$$

or

$$\left[\mathbf{Y}^+(R_{\rm mid}) - \mathbf{Y}^-(R_{\rm mid})\right]\mathbf{F_n}(R_{\rm mid}) = 0. \tag{2.69}$$

A non-trivial solution of this equation exists only if the determinant $|\mathbf{Y}^+ - \mathbf{Y}^-|$ at $R_{\rm mid}$ is zero. The eigenvalues E_n can thus be located by searching for zeroes in $|\mathbf{Y}^+ - \mathbf{Y}^-|$ as a function of energy and this method was used in the early versions of BOUND. If there are multiple boundstates supported in multiple channels the behaviour of the matching determinant $|\mathbf{Y}^+(R_{\rm mid}) - \mathbf{Y}^-(R_{\rm mid})|$ away from zeros is strongly dependent on $R_{\rm mid}$ and the matching determinant can diverge in either direction with non-monotonic poles. A better method can be obtained by noting from (2.69), that $\mathbf{F_n}(R_{\rm mid})$ is an eigenvector of $\mathbf{Y}^+ - \mathbf{Y}^-$ with a zero eigenvalue. We can thus search for zeros in the eigenvalues [45] and this is the method used by version 5 of BOUND onwards.

If a bound state wavefunction is propagated at a trial energy $E_{\rm trial}$ from $R_{\rm min}$ to $R_{\rm max}$ and n nodes are encounter, n eigenvalues must lie below the trial energy. The log-derivative method provides a node count, with a zero of $\mathbf{F}$ corresponding to a pole in $|\mathbf{Y}|$, thus a bisection method is used to determine a range of energy in which a bound state occurs, a secant method is then used to determine the eigenvalue zero.

For scattering solutions the log-derivative matrix is propagated from $R_{\rm min}$ inside the classically forbidden region, in which $\mathbf{F}(R) \to 0$ as $R \to 0$, outwards to long-range beyond the range of the potential to $R_{\rm max}$ at which point the scattering boundary condition

$$\mathbf{F}(R) \underset{R\to\infty}{\longrightarrow} \mathbf{J}(R) + \mathbf{N}(R)\mathbf{K}, \tag{2.70}$$

can be applied. Where $\mathbf{K}$ is defined by the asymptotic behaviour of the wavefunction and the diagonal matrices $\mathbf{J}(R)$ and $\mathbf{N}(R)$ are made up of Ricatti-Bessel functions for open channels and modified spherical Bessel functions of the first and third kind for closed channels [49]. By differentiating (2.70) and multiplying it the inverse of (2.70) allows the log-derivative matrix to be related to $\mathbf{K}$ resulting in

$$\mathbf{K} = -\left[\mathbf{Y}(R_{\rm max})\mathbf{N}(R_{\rm max}) - \mathbf{N}'(R_{\rm max})\right]^{-1}\left[\mathbf{Y}(R_{\rm max})\mathbf{J}(R_{\rm max}) - \mathbf{J}'(R_{\rm max})\right]. \tag{2.71}$$

The **K** matrix can be written in the form of open-open (oo), open-closed (oc), closed-open (co), and closed-closed (cc) submatrices for N_o open and N_c closed channels

$$\mathbf{K} = \begin{pmatrix} \mathbf{K}_{oo} & \mathbf{K}_{oc} \\ \mathbf{K}_{co} & \mathbf{K}_{cc} \end{pmatrix} \tag{2.72}$$

with the S-matrix related to the open-open submatrix by

$$\mathbf{S} = [\mathbf{I} + i\mathbf{K}_{oo}]^{-1} [\mathbf{I} - i\mathbf{K}_{oo}] . \tag{2.73}$$

For most of the calculations performed in this work the hybrid modified log-derivative propagator of Alexander and Manolopoulos [50] has been used in which a fixed step-size log-derivative propagator is used in the short range from R_{min} to R_{mid} and a variable step size propagator based on the Airy function is used at long range R_{mid} to R_{max}. BOUND propagates the log-derivative matrix inward from R_{max} to R_{mid} and MOLSCAT propagates outwards from R_{mid} to R_{max}. Using the Airy propagator in the long-range region significantly reduces the computational time required in propagating to large values of R_{max}.

Chapter 3

Collisions of ^1S Atoms with $^3\Sigma$ Molecules

The Hamiltonian, in Jacobi coordinates (R, θ) shown in figure 3.1, for a structureless ^1S atom colliding with a $^3\Sigma$ diatomic molecule with a fixed bond length r_{mon}, can be written as

$$\hat{H} = -\frac{\hbar^2}{2\mu} R^{-1} \frac{d^2}{dR^2} + \frac{\hat{L}^2}{2\mu R^2} + \hat{H}_{\text{mon}} + \hat{H}_{\text{Z}} + \hat{H}_{\text{Stark}} + V(R, \theta). \tag{3.1}$$

$\hat{L}^2$ is the space fixed end-over-end rotation operator for the triatomic complex, $\hat{H}_{\text{mon}}$ is the field free diatomic monomer Hamiltonian, $\hat{H}_{\text{Z}}$ and $\hat{H}_{\text{Stark}}$ are the Zeeman and Stark Hamiltonians for magnetic and electric field interactions respectively, and $V(R, \theta)$ is the intermolecular potential term. μ is the reduced mass of the colliding system.

The monomer Hamiltonian for a $^3\Sigma$ diatomic molecule with rotational $\hat{n}$ and spin $\hat{s}$ angular momenta operators, can be written as

$$\hat{H}_{\text{mon}} = b_{\text{rot}} \hat{n}^2 + \hat{H}_{\text{sn}} + \hat{H}_{\text{ss}}, \tag{3.2}$$

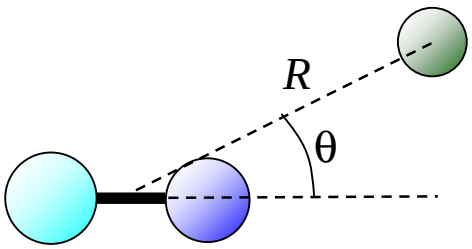

Figure 3.1: Jacobi coordinates (R, θ) of a atom + fixed bond length diatom system.

where $b_{\text{rot}} = \hbar^2/2\mu r_{\text{mon}}^2$ is the rotational constant of the monomer, $\hat{H}_{\text{sn}}$ is the spin-rotation operator and $\hat{H}_{\text{ss}}$ is the spin-spin interaction operator. If the collision of a ^1S atom with a $^2\Sigma$ molecule was being considered the spin-spin interaction is absent from (3.2) and the remaining terms would stay the same.

In the following sections matrix elements for each of the terms in the Hamiltonian will be present in the uncoupled $|nm_n\rangle|sm_s\rangle|LM_L\rangle$, coupled $|nsjm_j\rangle|LM\rangle$, and the fully coupled $|(ns)jLJM\rangle$ angular momentum basis sets, where $j = n + s$ and $J = j + L$ and m_i is the projections of the operator i onto the space-fixed Z-axis. The monomer Hamiltonian and Zeeman Hamiltonian terms, were first formalized by in the uncoupled $|nm_n\rangle|sm_s\rangle|LM_L\rangle$ representation by Krems and Dalgarno [51] and in the coupled $|nsjm_j\rangle$ $|LM_L\rangle$ representation by González-Martínez and Hutson [52]. The Stark Hamiltonian was first presented in the uncoupled basis for parallel fields by Tschberbul and Krems [53] and for non-parallel fields by Abrahamsson et al. [54]. All other terms unless otherwise specified have been derived by the author. Derivations of non-trivial terms are presented in Appendix B.

3.1 Matrix Elements of the Hamiltonian

3.1.1 The Spin-Rotation Interaction

The electron spin magnetic moment interacts with the magnetic moment caused by molecular rotation, the interaction is given by

$$\hat{H}_{\text{sn}} = \gamma_{\text{sn}}\hat{n}\cdot\hat{s} = \gamma_{\text{sn}}\left[n_z s_z + \frac{1}{2}(n_+ s_- + n_- s_+)\right] = \frac{\gamma_{\text{sn}}}{2}\left[\hat{j}^2 - \hat{n}^2 - \hat{s}^2\right] \tag{3.3}$$

where γ_{sn} is the spin-rotation coupling constant, $n_\pm$ and $s_\pm$ are ladder operators and $\hat{j} = \hat{n} + \hat{s}$.

Decoupled Basis

$$\begin{aligned}\langle nm_n \mid \langle sm_s \mid \hat{H}_{\text{sn}} \mid n'm_n'\rangle \mid sm_s'\rangle &= \delta_{nn'}\delta_{m_n m_n'}\delta_{m_s m_s'}\gamma_{\text{sn}} m_n m_s \\ &+ \delta_{nn'}\delta_{m_n m_n'\pm 1}\delta_{m_s m_s'\mp 1}\frac{\gamma_{\text{sn}}}{2}\left[n(n+1) - m_n'(m_n' \pm 1)\right]^{1/2}\left[s(s+1) - m_s'(m_s' \mp 1)\right]^{1/2}\end{aligned} \tag{3.4}$$

Coupled Basis

$$\langle nsjm_j \mid \hat{H}_{\rm sn} \mid n'sj'm'_j\rangle = \delta_{nn'}\delta_{jj'}\delta_{m_jm'_j}\gamma_{\rm sn}(-1)^{n+j+s} \times [n(n+1)(2n+1)s(s+1)(2s+1)]^{\frac{1}{2}} \begin{Bmatrix} s & n & j \\ n & s & 1 \end{Bmatrix}, \tag{3.5}$$

Fully-coupled Basis

$$\langle (ns)jLJM \mid \hat{H}_{\rm sn} \mid (n's)j'L'J'M'\rangle = \delta_{JJ'}\delta_{MM'}\delta_{LL'}\delta_{jj'}\delta_{nn'}\frac{\gamma_{\rm sn}}{2}\left[j(j+1)-n(n+1)-s(s+1)\right] \tag{3.6}$$

3.1.2 The Spin-Spin Interaction

The electron spin-spin interaction arises from the interaction between the two unpaired electrons in a $^3\Sigma$ molecule and can be expressed as

$$\hat{H}_{\rm ss} = \lambda_{\rm ss}\left[\frac{4\pi}{5}\right]^{\frac{1}{2}}\sqrt{6}\sum_q (-1)^q Y_{2-q}(\boldsymbol{r})\,[s\otimes s]^{(2)}_q\,, \tag{3.7}$$

where $\lambda_{\rm ss}$ is the electron spin-spin coupling constant and $[s\otimes s]^{(2)}_q$ is a second order tensor product.

Decoupled Basis

$$\langle nm_n \mid \langle sm_s \mid \hat{H}_{\rm ss} \mid n'm'_n\rangle \mid sm'_s\rangle = \frac{2\sqrt{30}}{3}\lambda_{\rm ss}(-1)^{s-m_s-m_n}\left[(2n+1)(2n'+1)\right]^{1/2}\left[s(s+1)(2s+1)\right]^{1/2} \times \begin{pmatrix} n & 2 & n' \\ 0 & 0 & 0 \end{pmatrix}\begin{Bmatrix} 1 & 1 & 2 \\ s & s & s \end{Bmatrix}\sum_q (-1)^q \begin{pmatrix} n & 2 & n' \\ -m_n & -q & m'_n \end{pmatrix}\begin{pmatrix} s & 2 & s \\ -m_s & q & m'_s \end{pmatrix} \tag{3.8}$$

Coupled Basis

$$\langle nsjm_j \mid \hat{H}_{\rm ss} \mid n'sj'm'_j\rangle = \delta_{jj'}\delta_{m_jm'_j}\frac{2\sqrt{30}}{3}\lambda_{\rm ss}(-1)^{j+n'+n+s}\left[s(s+1)(2s+1)\right]\left[(2n+1)(2n'+1)\right]^{\frac{1}{2}} \times \begin{pmatrix} n & 2 & n' \\ 0 & 0 & 0 \end{pmatrix}\begin{Bmatrix} 1 & 1 & 2 \\ s & s & s \end{Bmatrix}\begin{Bmatrix} s & n' & j \\ n & s & 2 \end{Bmatrix} \tag{3.9}$$

Fully-coupled Basis

$$\langle (ns)jLJM \mid \hat{H}_{\rm ss} \mid (n's)j'L'J'M' \rangle = \delta_{JJ'}\delta_{MM'}\delta_{LL'}(-1)^{n'+j+n+s}\frac{2\sqrt{30}}{3}\lambda_{\rm ss}$$
$$\times \left[s(s+1)(2s+1)\right]\left[(2n+1)(2n'+1)\right]^{1/2}\begin{pmatrix} n & 2 & n' \\ 0 & 0 & 0 \end{pmatrix}\begin{Bmatrix} 1 & 1 & 2 \\ s & s & s \end{Bmatrix}\begin{Bmatrix} s & n' & j \\ n & s & 2 \end{Bmatrix} \tag{3.10}$$

3.1.3 The Zeeman Effect

The introduction of a magnetic field removes the isotropy of free space, lifting the degeneracy of different m_s states. Neglecting rotational and spin anisotropy the Zeeman Hamiltonian for magnetic field orientated along the space-fixed Z-axis is given by

$$\hat{H}_{\rm Z} = g_e\mu_B\hat{B}\cdot\hat{s}, \tag{3.11}$$

where μ_B is the Bohr magneton and g_e is the electron g-factor.

Decoupled Basis

$$\langle nm_n \mid \langle sm_s \mid \langle LM_L \mid \hat{H}_Z \mid n'm_n' \rangle \mid sm_s' \rangle \mid L'M_L' \rangle = \delta_{nn'}\delta_{m_nm_n'}\delta_{m_sm_s'}\delta_{LL'}\delta_{M_LM_L'}g_e\mu_B Bm_s \tag{3.12}$$

Coupled Basis

$$\langle nsjm_j \mid \langle LM_L \mid \hat{H}_Z \mid n'sj'm_j' \rangle \mid L'M_L' \rangle = \delta_{nn'}\delta_{m_jm_j'}\delta_{LL'}\delta_{M_LM_L'}g_e\mu_B B(-1)^{n+s-m_j+1}$$
$$\times \left[s(s+1)(2s+1)(2j+1)(2j'+1)\right]^{\frac{1}{2}}\begin{pmatrix} j & 1 & j' \\ -m_j & 0 & m_j \end{pmatrix}\begin{Bmatrix} s & j' & n \\ j & s & 1 \end{Bmatrix} \tag{3.13}$$

Fully-coupled Basis

$$\langle (ns)jLJM \mid \hat{H}_Z \mid (n's')j'L'J'M' \rangle = \delta_{LL'}\delta_{nn'}\delta_{ss'}\delta_{MM'}g_e\mu_B B(-1)^{J'-M}$$
$$\times\left[(2J'+1)(2J+1)(2j'+1)(2j+1)(2s+1)s(s+1)\right]^{\frac{1}{2}}$$
$$\times\begin{pmatrix} J & 1 & J' \\ -M & 0 & M \end{pmatrix}\begin{Bmatrix} j & J & L \\ J' & j' & 1 \end{Bmatrix}\begin{Bmatrix} s & j & n \\ j' & s & 1 \end{Bmatrix} \tag{3.14}$$

3.1.4 The Stark Effect

If the quantization axis is oriented along the magnetic field Z-axis the interaction is given by [54]

$$\hat{H}_{\text{Stark}} = \hat{E} \cdot \hat{d} = -Ed\cos\chi = Ed\frac{4\pi}{3}\sum_{q} Y^{*}_{1q}(\boldsymbol{r})Y_{1q}(\boldsymbol{E}) \tag{3.15}$$

where χ is the angle between the magnetic and electric fields, $\boldsymbol{r}$ and $\boldsymbol{E}$ define the directions of the interatomic axis and the electric field with respect to the magnetic field axis, and d is the dipole moment. However the situation is greatly simplified when the magnetic and electric fields are parallel,

$$\hat{E} \cdot \hat{d} = Ed\cos\theta = EdC_{10}(\theta,\phi), \tag{3.16}$$

where θ is the space-fixed angle of $\boldsymbol{r}$ with the field axis (the z-direction), and

$$Y_{kq} = \left(\frac{2k+1}{4\pi}\right)^{\frac{1}{2}} C_{kq}. \tag{3.17}$$

The matrix elements for parallel fields are:

Decoupled Basis

$$\langle nm_n \mid \langle sm_s \mid \langle LM_L \mid \hat{H}_{\text{Stark}} \mid n'm'_n\rangle \mid sm'_s\rangle \mid L'M'_L\rangle = \delta_{LL'}\delta_{M_LM'_L}\delta_{ss'}\delta_{m_sm'_s}Ed(-1)^{m_n}$$
$$\times\left[(2n+1)(2n'+1)\right]^{1/2}\begin{pmatrix} n & 1 & n' \\ 0 & 0 & 0 \end{pmatrix}\begin{pmatrix} n & 1 & n' \\ -m_n & 0 & m'_n \end{pmatrix} \tag{3.18}$$

Coupled Basis

$$\langle nsjm_j \mid \langle LM_L \mid \hat{H}_{\text{Stark}} \mid n'sj'm'_j\rangle \mid L'M'_L\rangle = -\delta_{LL'}\delta_{M_LM'_L}Ed(-1)^{j+j'-m_j+s+1}$$
$$\times\left[(2j'+1)(2j+1)(2n+1)(2n'+1)\right]^{\frac{1}{2}}\begin{pmatrix} n & 1 & n' \\ 0 & 0 & 0 \end{pmatrix}\begin{pmatrix} j & 1 & j' \\ -m_j & 0 & m'_j \end{pmatrix}\begin{Bmatrix} n & j & s \\ j' & n' & 1 \end{Bmatrix} \tag{3.19}$$

Fully-coupled Basis

$$\langle (ns)jLJM \mid \hat{H}_{\text{Stark}} \mid (n's)j'L'J'M'\rangle = -\delta_{LL'}\delta_{MM'}Ed(-1)^{J+J'+j+j'-M+L+s}$$
$$\times\left[(2J'+1)(2J+1)(2j'+1)(2j+1)(2n+1)(2n'+1)\right]^{\frac{1}{2}}$$
$$\times\begin{pmatrix} J & 1 & J' \\ -M & 0 & M \end{pmatrix}\begin{pmatrix} n & 1 & n' \\ 0 & 0 & 0 \end{pmatrix}\begin{Bmatrix} j & J & L \\ J' & j' & 1 \end{Bmatrix}\begin{Bmatrix} n & j & s \\ j' & n' & 1 \end{Bmatrix} \tag{3.20}$$

The matrix elements for non-parallel fields are:

Decoupled Basis

$$\langle sm_s \mid \langle nm_n \mid -Ed\cos\chi \mid n'm_n' \rangle \mid sm_s' \rangle =$$
$$-\delta_{m_s m_s'} Ed(-1)^{m_n} \sqrt{\frac{4\pi}{3}} Y_{1,m_n'-m_n}(\hat{E}) \left[(2n+1)(2n'+1)\right]^{\frac{1}{2}}$$
$$\times \begin{pmatrix} n' & 1 & n \\ 0 & 0 & 0 \end{pmatrix} \begin{pmatrix} n' & 1 & n \\ m_n' & m_n - m_n' & -m_n \end{pmatrix} \tag{3.21}$$

3.1.5 Expansion of the Potential

The calculation of intermolecular potential matrix elements between angular-momentum eigenfunctions can be done by expanding the potential in terms of Legendre polynomials

$$V(R,\theta) = \sum_{\lambda} V_\lambda(R) P_\lambda(\cos\theta), \tag{3.22}$$

where $V_\lambda(R)$ are known as the radial strength coefficients. Inverting the Legendre expansion

$$V_\lambda(R) = \left(\lambda + \frac{1}{2}\right) \int_0^\pi V(R,\theta) P_\lambda(\cos\theta) \sin\theta d\theta, \tag{3.23}$$

allows $V_\lambda(R)$ to be numerically evaluated using Gaussian quadrature [55], with a minimum of $(\lambda + 1)$ quadrature points required to evaluate $V_\lambda(R)$. The matrix elements of the Legendre polynomials follow, the fully coupled $|(ns)jLJM\rangle$ matrix elements were first presented by Corey and McCourt [56].

Decoupled Basis

$$\langle nm_n \mid \langle sm_s \mid \langle LM_L \mid P_\lambda(\cos\theta) \mid m'm_n' \rangle \mid s'm_s' \rangle \mid L'M_L' \rangle =$$
$$\delta_{m_s m_s'} \left[(2n+1)(2n'+1)(2L+1)(2L'+1)\right]^{\frac{1}{2}}$$
$$\times \begin{pmatrix} n & \lambda & n' \\ 0 & 0 & 0 \end{pmatrix} \begin{pmatrix} L & \lambda & L' \\ 0 & 0 & 0 \end{pmatrix} \sum_{m_\lambda} (-1)^{m_\lambda - M_L - m_n} \begin{pmatrix} L & \lambda & L' \\ -M_L & -m_\lambda & M_L' \end{pmatrix} \begin{pmatrix} n & \lambda & n' \\ -m_n & m_\lambda & m_n' \end{pmatrix} \tag{3.24}$$

Coupled Basis

$$\langle LM_L \mid \langle nsjm_j \mid P_\lambda(\cos\theta) \mid n's'j'm'_j\rangle \mid L'M'_L\rangle =$$
$$[(2n+1)(2n'+1)(2j+1)(2j'+1)(2L+1)(2L'+1)]^{\frac{1}{2}} \begin{pmatrix} n & \lambda & n' \\ 0 & 0 & 0 \end{pmatrix} \begin{pmatrix} L & \lambda & L' \\ 0 & 0 & 0 \end{pmatrix}$$
$$\times \sum_{m_\lambda} (-1)^{s+j+j'+\lambda+m_\lambda-M_L-m_j} \begin{pmatrix} L & \lambda & L' \\ -M_L & -m_\lambda & M'_L \end{pmatrix} \begin{pmatrix} j & \lambda & j' \\ -m_j & -m_\lambda & m'_j \end{pmatrix} \begin{Bmatrix} j & j' & \lambda \\ n' & n & s \end{Bmatrix}. \tag{3.25}$$

Fully-coupled Basis

$$\langle (ns)jLJM \mid P_\lambda(\cos\theta) \mid (n's)j'L'JM\rangle =$$
$$(-1)^{s-\lambda-J} [(2n+1)(2n'+1)(2j+1)(2j'+1)(2L+1)(2L'+1)]^{\frac{1}{2}}$$
$$\times \begin{pmatrix} n & \lambda & n' \\ 0 & 0 & 0 \end{pmatrix} \begin{pmatrix} L & \lambda & L' \\ 0 & 0 & 0 \end{pmatrix} \begin{Bmatrix} j' & j & \lambda \\ L & L' & J \end{Bmatrix} \begin{Bmatrix} j' & j & \lambda \\ n & n' & s \end{Bmatrix}. \tag{3.26}$$

3.2 The Mechanism of Spin-Relaxation

An important collision process at cold and ultracold temperature is that of spin-relaxation. In the $n = 0$ rovibrational ground state of a $^3\Sigma$ molecule the important process is collisions that cause the molecule to go from the magnetically trappable low-field seeking $m_s = +1$ state to the untrappable $m_s = 0, -1$ states. Due to the conservation of the total angular momentum projection M in a magnetic field the $m_s \rightarrow m'_s$ transition must be accompanied by a change in the total orbital angular momentum L, i.e. $\mid m_s = +1, L = 0\rangle \rightarrow \mid m_s = -1, L = 2\rangle$. The mechanism for this process was derived by Krems and Dalgarno [51].

In a Hund's case b $^3\Sigma$ molecule the spin-spin interaction constant $\lambda_{\rm ss}$ is much greater than the spin-rotation interaction constant $\gamma_{\rm sn}$. Thus the spin-relaxation mechanism will be dominated by terms involving the spin-spin interaction, which mixes states with $\Delta n = 0, \pm 2$, resulting in states that can be written as

$$\mid \nu : sjm_j\rangle = a^\nu_j \mid (n,s)jm_j\rangle + b^\nu_j \mid (n+2,s)jm_j\rangle \quad j > n \tag{3.27}$$
$$\mid \nu : sjm_j\rangle = a^\nu_j \mid (n,s)jm_j\rangle - b^\nu_j \mid (n-2,s)jm_j\rangle \quad j > n \tag{3.28}$$
$$\mid \nu : sjm_j\rangle = \mid (n,s)jm_j\rangle \quad j = n, \tag{3.29}$$

where ν is a phenomenological quantum number and a_j^ν and b_j^ν are mixing coefficients. The ground state $n = 0$, $j = 1$ is therefore

$$| \nu = 0 : sj = 1m_j\rangle = a_j^{\nu=0} | (n = 0, s)j = 1m_j\rangle + b_j^{\nu=0} | (n = 2, s)j = 1m_j\rangle \tag{3.30}$$

where $m_j = m_s$. Spin-relaxation from $| \nu = 0 : sj = 1m_j\rangle \rightarrow | \nu = 0 : sj = 1m'_j\rangle$ where $m_s = m_j$, is driven by the spin-spin interaction, which is diagonal in $| \nu = 0 : sj = 1m_j\rangle$, and the $\lambda = 2$ anisotropic part of the interaction potential

$$\begin{aligned}\langle \nu = 0 : sj = 1m_j | V | \nu = 0 : sj = 1m'_j\rangle \\ &= (a_j^{\nu=0})^2\langle (n = 0, s)j = 1m_j | V | (n = 0, s)j = 1m'_j\rangle \\ &+ a_j^{\nu=0}b_j^{\nu=0}\langle (n = 0, s)j = 1m_j | V | (n = 2, s)j = 1m'_j\rangle \\ &+ a_j^{\nu=0}b_j^{\nu=0}\langle (n = 2, s)j = 1m_j | V | (n = 0, s)j = 1m'_j\rangle \\ &+ (b_j^{\nu=0})^2\langle (n = 2, s)j = 1m_j | V | (n = 2, s)j = 1m'_j\rangle. \end{aligned} \tag{3.31}$$

The first term in (3.31) is zero and thus

$$\begin{aligned}\langle \nu = 0 : sj = 1m_j | V | \nu = 0 : sj = 1m'_j\rangle = \\ &+ a_j^{\nu=0}b_j^{\nu=0}\langle (n = 0, s)j = 1m_j | V | (n = 2, s)j = 1m'_j\rangle \\ &+ a_j^{\nu=0}b_j^{\nu=0}\langle (n = 2, s)j = 1m_j | V | (n = 0, s)j = 1m'_j\rangle \\ &+ (b_j^{\nu=0})^2\langle (n = 2, s)j = 1m'_j | V | (n = 2, s)j = 1m'_j\rangle. \end{aligned} \tag{3.32}$$

The relative magnitudes of $a_j^{\nu=0}$ and $b_j^{\nu=0}$ depend on the ratio of the spin-spin interaction to the energy separation of the $n = 0$ and 2 levels

$$\frac{\lambda_{\rm ss}}{E_{n=2} - E_{n=0}}. \tag{3.33}$$

The cross-section is therefore predicted to scale as $\lambda_{\rm ss}^2/b_{\rm rot}^2$ [57]. Recently this scaling law was confirmed by Campbell et al. [58] who measured spin-relaxation cross sections for different isotopologues of He+NH($^3\Sigma^-$). Spin-relaxation thus occurs because during the collision the relative population of the $n = 0$ and $n = 2$ states is changed by the interaction potential and thus so is m_j.

The magnetic field induces couplings between states with different values of j but doesn't couple states with different m_j projections. The ground state $| \nu = 0 : sj = 1m_j\rangle$

is coupled to the excited states $\mid \nu : sj = 1m_j\rangle$ and $\mid \nu' : sj = 2m_j\rangle$ where

$$\mid \nu : sj = 1m_j\rangle = a_j^{\nu} \mid (n = 2s)j = 1m_j\rangle - b_j^{\nu} \mid (n = 0, s)jm_j\rangle \tag{3.34}$$

$$\mid \nu' : sj = 2m_j\rangle = \mid (n = 2, s)j = 2m_j\rangle. \tag{3.35}$$

The ground state can thus be written as

$$\mid m_j\rangle = a \mid \mu = 0 : sj = 1m_j\rangle + b \mid \nu : sj = 1m_j\rangle + c \mid (n = 2, s)j = 2m_j\rangle, \tag{3.36}$$

where a, b, and c are mixing coefficients that depend on B. The matrix elements of the interaction potential between the states $\mid m_j\rangle$ and $\mid m_j'\rangle$ are thus

$$\begin{aligned}\langle m_j \mid V \mid m_j'\rangle =& aa'\langle \nu = 0 : sj = 1m_j \mid V \mid \nu = 0 : sj = 1m_j'\rangle \\ &+ bb'\langle \nu : sj = 1m_j \mid V \mid \nu : sj = 1m_j'\rangle \\ &+ cc'\langle (n = 2, s)j = 2m_j \mid V \mid (n = 2, s)j = 2m_j'\rangle \\ &+ (ab' + a'b)\langle \mu = 0 : sj = 1m_j \mid V \mid \nu : sj = 1m_j'\rangle \\ &+ (ac' + a'c)\langle \mu = 0 : sj = 1m_j \mid V \mid (n = 2, s)j = 2m_j'\rangle \\ &+ (bc' + b'c)\langle \nu : sj = 1m_j \mid V \mid (n = 2, s)j = 2m_j'\rangle. \end{aligned} \tag{3.37}$$

In the limit of zero magnetic field, $a \to 1, b \to 0, c \to 0$ and (3.37) reduces to (3.32). The spin-relaxation in a magnetic field are thus induced by the same couplings as the field free case however the relative contribution of the $\langle n = 0 \mid V \mid n = 2\rangle$ and $\langle n = 2 \mid V \mid n = 2\rangle$ terms now depend on the magnetic field strength.

If the spin-rotation interaction constant γ_{sn} is comparable to λ_{ss}, then effects from the spin-rotation may need to be considered. The spin-rotation interaction is diagonal in m_s and thus spin-relaxation via the spin-rotation interaction occurs via the interplay of the coupling between $n = 0$ and $n > 0$ state and the interaction potential.

Chapter 4

Tuning Zero-Energy Feshbach Resonances in Electromagnetic Fields

In 2007 the BOUND and MOLSCAT [47, 48] packages were generalized by González-Martínez and Hutson [52] to allow calculations to be performed in the presence of external magnetic fields. BOUND and MOLSCAT have been further generalized to allow calculations to be performed in parallel electric and magnetic fields. What follows is a summary of the cross-section profiles over magnetic Feshbach resonances in He+NH($^3\Sigma^-$) [52, 59] and He+O_2($^3\Sigma_g^-$) [60], and the theory of which developed by Hutson [61]. Zero-energy magnetic Feshbach resonances in He+SO($^3\Sigma^-$) are then examined in combined electric and magnetic fields.

4.1 Tuning Zero Energy Magnetic Feshbach Resonances

Using the potential of Cybulski et al. [62], BOUND was used to calculate the bound-states of HeNH($^3\Sigma^-$) as a function of magnetic field predicting the location of zero-energy magnetic Feshbach resonances at fields at which a bound state crossed threshold. Figure 4.1 shows the ^{3}He-NH bound-states as a function of magnetic field for $M = 0$ and -1, the arrows indicate the locations of zero energy s-wave Feshbach resonances. MOLSCAT was then used to characterize these Feshbach resonances.

Recalling from chapter 2, that in the ultracold regime scattering properties can be described in terms of the scattering length, which in general can be complex $a = \alpha - i\beta$.

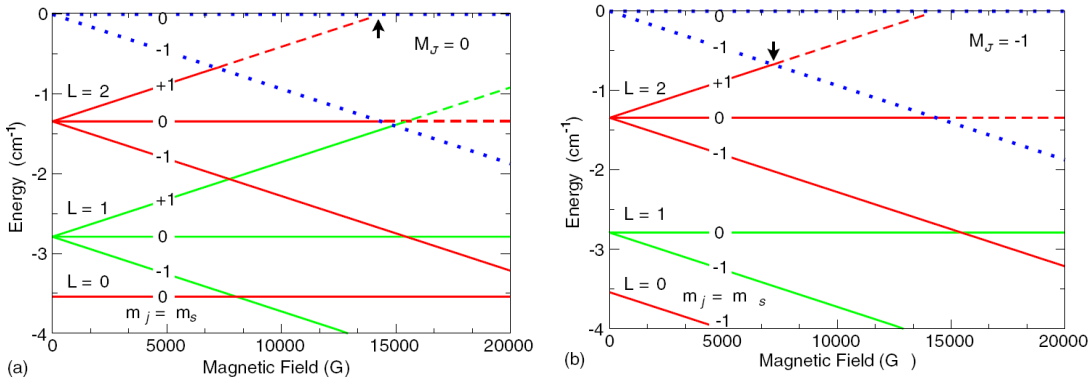

Figure 4.1: Bound-state energy levels for ^{3}He-NH(n=0) for (a) $M = 0$ and (b) $M = -1$ as a function of magnetic field. The NH thresholds are shown as dotted blue lines and bound states of odd parity are shown in red and even parity in green, the dashed lines indicate that the bound state has become quasi-bound. The arrows show positions at which levels cross $L = 0$ thresholds. Images from [52].

The scattering length is defined from the scattering phase shift δ and is therefore for the incident channel 0, related to the diagonal S-matrix element S_{00} by

$$a(k_0) = -\frac{\tan\delta(k_0)}{k_0} = \frac{1}{ik_0}\frac{1 - S_{00}}{1 + S_{00}}, \tag{4.1}$$

where $k_0 = \sqrt{2\mu E}/\hbar$. At a limitingly low energy the scattering length becomes a constant and the elastic and total inelastic cross sections are exactly

$$\sigma_{\mathrm{el}}(k_0) = \frac{\pi}{k_0^2}|1 - S_{00}|^2 = \frac{4\pi|a|^2}{1 + k_0^2|a|^2 + 2k_0\beta} \tag{4.2}$$

and

$$\sigma_{\mathrm{inel}}^{\mathrm{tot}}(k_0) = \frac{\pi}{k_0^2}(1 - |S_{00}|^2) = \frac{4\pi\beta}{k_0\left(1 + k_0^2|a|^2 + 2k_0\beta\right)}. \tag{4.3}$$

It can be seen from (4.3) that inelastic scattering is characterized by the imaginary part of the scattering length β.

If there is only one open channel the phase shift and the scattering length are real, and over a resonance the phase-shift follows the Breit-Wigner form as a function of magnetic field at a constant kinetic energy,

$$\delta(B) = \delta_{\mathrm{bg}} + \tan^{-1}\left[\frac{\Gamma_B(E_{\mathrm{kin}})}{2(B_{\mathrm{res}}(E) - B)}\right], \tag{4.4}$$

where B_{res} is the resonance position and Γ_B the width of the resonance in magnetic field space. The phase-shift changing by π over a resonance causes the corresponding S-matrix

element $S_{00} = \exp[2i\delta(B)]$ to form a circle of radius one in the complex plane and the scattering length follows the form

$$a(B) = a_{\text{bg}}\left[1 - \frac{\Delta_B}{B - B_{\text{res}}}\right], \tag{4.5}$$

going through a pole at resonance. The two widths are related by $\Gamma_B = -2a_{\text{bg}}k_0\Delta_B$. The elastic cross section given by (4.2), thus shows a peak of height $4\pi/k_0^2$ at resonance. MOLSCAT He+NH($^3\Sigma^-$) calculations over the elastic $M = -1$ Feshbach resonance shown in figure 4.1 showed a pole in the scattering length and a peak with a value of $4\pi/k_0^2$ in the elastic cross section.

If there is more than one open channel the scattering length and the phase-shift are in general complex, and the S-matrix eigenphase sum (the sum of S-matrix eigenvalue phase shifts) is now the quantity that follows the Breit-Wigner form. Individual S-matrix elements still form a circle in the complex plane, however an additional phase ϕ_i is required to describe the circle. The scattering length now follows

$$a(B) = a_{\text{bg}} + \frac{a_{\text{res}}}{2(B - B_{\text{res}})/\Gamma_B^{\text{inel}} + i}, \tag{4.6}$$

where a_{res} is a resonant scattering length that characterizes the strength of the resonance,

$$a_{\text{res}} = \frac{2\gamma_{B0}}{\Gamma_B^{\text{inel}}} e^{2i(\phi_0 + k_0\alpha_{\text{bg}})}, \tag{4.7}$$

defined with the phase correction $k_0\alpha_{\text{bg}}$ to ensure that the phase of a_{res} is independent of k_0. In general both a_{res} and the background a_{bg} can be complex.

For the $M = 0$ ^{3}He+NH($^3\Sigma^-$) Feshbach resonance shown in figure 4.1, there is more than one open channel present. Due to the high centrifugal barriers and large rotational constant of NH, the system is weakly inelastic [51] and the background scattering is essentially elastic and therefore a_{bg} and a_{res} are real. In this case over the Feshbach resonance the real part of the scattering length oscillates about α_{bg} by $\pm a_{\text{res}}/2$ and the imaginary part of the scattering length shows a peak of $\beta = a_{\text{res}}$. Figure 4.2 shows the oscillation in the real part of the scattering length and the peak in the imaginary part of the scattering length over the resonance for a collision energy of 10^{-6}K.

To examine the more general case of a complex a_{bg} the collisions of He+NH($^3\Sigma^-$) in its first rotationally excited $n = 1$ state were examined by Rowlands et al. [59]. It was

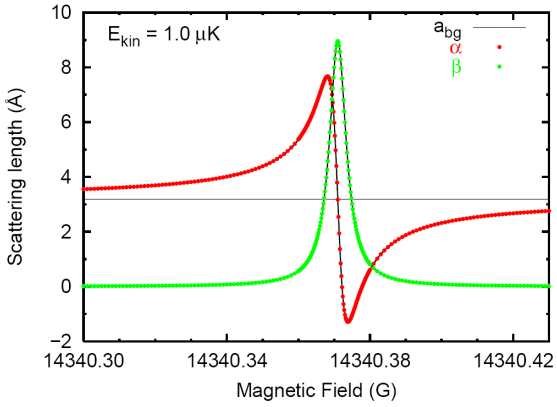

Figure 4.2: Real α (red) and imaginary β (green) parts of the scattering length across a Feshbach resonance in He + NH(n=0). Due to the presence of inelastic scattering the scattering length no longer shows a pole and the real part oscillates by $\pm a_{\text{res}}/2$ about the background scattering length a_{bg}, over the resonance. Image from [59].

shown that a_{res} could indeed be complex and that this allows both peaks and troughs in the real and imaginary parts of the scattering length near a resonance. However this effect was small in He-NH(n=1).

Work by Beyene et al. [60] has shown large peaks and troughs in cross sections near magnetic Feshbach resonances in ^{4}He+^{16}O$_2$($^3\Sigma_g^-$). Performing calculations on the potential of Groenenboom and Struniewicz [63], broad Feshbach resonances were found displaying dramatic troughs in the total inelastic cross section (due to a complex a_{res}). Figure 4.3 shows the elastic and total inelastic cross sections near a Feshbach resonance for various collision energies, in some cases the inelastic cross section is reduced by nearly a factor of 1000. The asymmetric lineshapes were found to be analogous to Fano lineshapes, in which the bound and continuum state contributions to a transition matrix element interfere near a resonance. For a single continuum channel there will always be a point at which the bound and continuum contributions cancel to zero. However, for N continuum channels, there will be one linear combination of the continuum channels coupled to the bound state and $N-1$ orthogonal linear combinations that are not. Thus inelastic scattering is only suppressed in the linear combination coupled to the boundstate at resonance, thus the cross section will not drop to zero. The suppression of inelastic cross sections near Feshbach resonances may be very important in sympathetic and evaporative

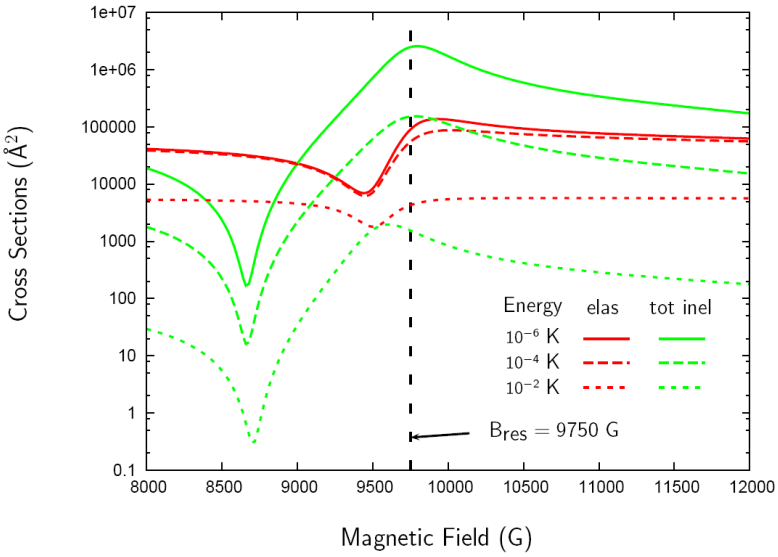

Figure 4.3: ^{4}He+$^{16}O_2(^3\Sigma_g^-)$ elastic (red) and total inelastic (green) cross sections near a Feshbach resonance at collision energies of 10^{-6} (solid), 10^{-4} (dashed), and 10^{-2}K (dotted). Image from [60].

$b_{\rm rot}$ (cm^{-1})	γ_{ns}(cm^{-1})	λ_{ss}(cm^{-1})	d(Debye)
0.7180	-0.0056	5.2788	1.55

Table 4.1: Rotational, spin-rotation and spin-spin constants and the body-fixed electric dipole moment for the ^{32}S^{16}O molecule in its electronic and vibrational ground state, values from [64].

cooling, in which the ratio of the elastic to total inelastic cross sections is important.

4.2 He+SO($^3\Sigma^-$)

Externally applied magnetic fields give a degree of control over ultracold collisions, and the addition of an electric field adds a further degree of control. Calculations for molecules in combined magnetic and electric fields have already produced some interesting results. Friedrich and Herschbach [65] examined the alignment of $^2\Sigma$ molecules, and Boca and Friedrich the alignment of $^3\Sigma$ molecules [66] in congruent electric and magnetic fields.

Finding that electric field induced avoided crossings between Zeeman states of opposite parity strongly orientated molecular states, these induced avoided crossings and some of their consequences are studied in detail in chapters 9 to 13. Krems, Tscherbul and co-workers [53, 54, 67–69] have studied collisions in combined magnetic and electric fields, and have shown that the dynamics of electron spin relaxation can be manipulated by the strength and orientation of the applied fields, especially in the region of an induced avoided crossing, at which point the collision dynamics became extremely sensitive to external fields. The extra degree of control given by combined electric and magnetic fields could also be used to modify Feshbach resonance asymmetries seen in He+NH($^3\Sigma^-$) and He+O_2($^3\Sigma_g^-$).

In order to observe the effect of electric field effects on atom-molecule collisions, the molecule needs to have a large enough electric dipole moment so that electric fields available in the laboratory can be used to alter the collision dynamics, and a rotational constant small enough that states can be brought into degeneracy with accessible magnetic fields. NH has a large rotational constant and a small dipole moment, however SO($X^3\Sigma^-$) has a small rotational constant and a large dipole moment meeting our requirements and it has been proposed that it could be created by the photodissociation of Stark decelerated SO_2 molecules [70], the spectroscopic constants of SO($X^3\Sigma^-$) are given in table 4.1.

The lowest few rovibrational states of SO are shown as a function of magnetic field in figure 4.4. The rovibrational states are best described in the Hund's case (b) coupling limit, in which, n the mechanical rotation of the molecule, couples to s the electron spin, to form j the total angular momentum, with a projection m_j on to the space fixed Z-axis, the resulting case b basis is thus $|n\,s\,j\,m_j\rangle$. The rovibrational states shown in figure 4.4 have been labeled with $|n\,j\rangle$.

It can be seen that the ground state is $|n = 1\,j = 0\rangle$ rather than the more usual $|n = 0\,j = 1\rangle$ ground state, this is due to the large ratio of the spin-spin and rotational constants in SO($X^3\Sigma^-$), which causes the fine structure splitting of the $n = 1$ state to exceed the $b_{\mathrm{rot}}n(n+1)$ rotational splitting of the $n = 0$ and 1 states.

To perform calculations in combined magnetic and electric fields, BOUND and MOLSCAT were generalized to include an electric field parallel to the magnetic field such that the projection of the total angular momentum onto the field axis is conserved. The

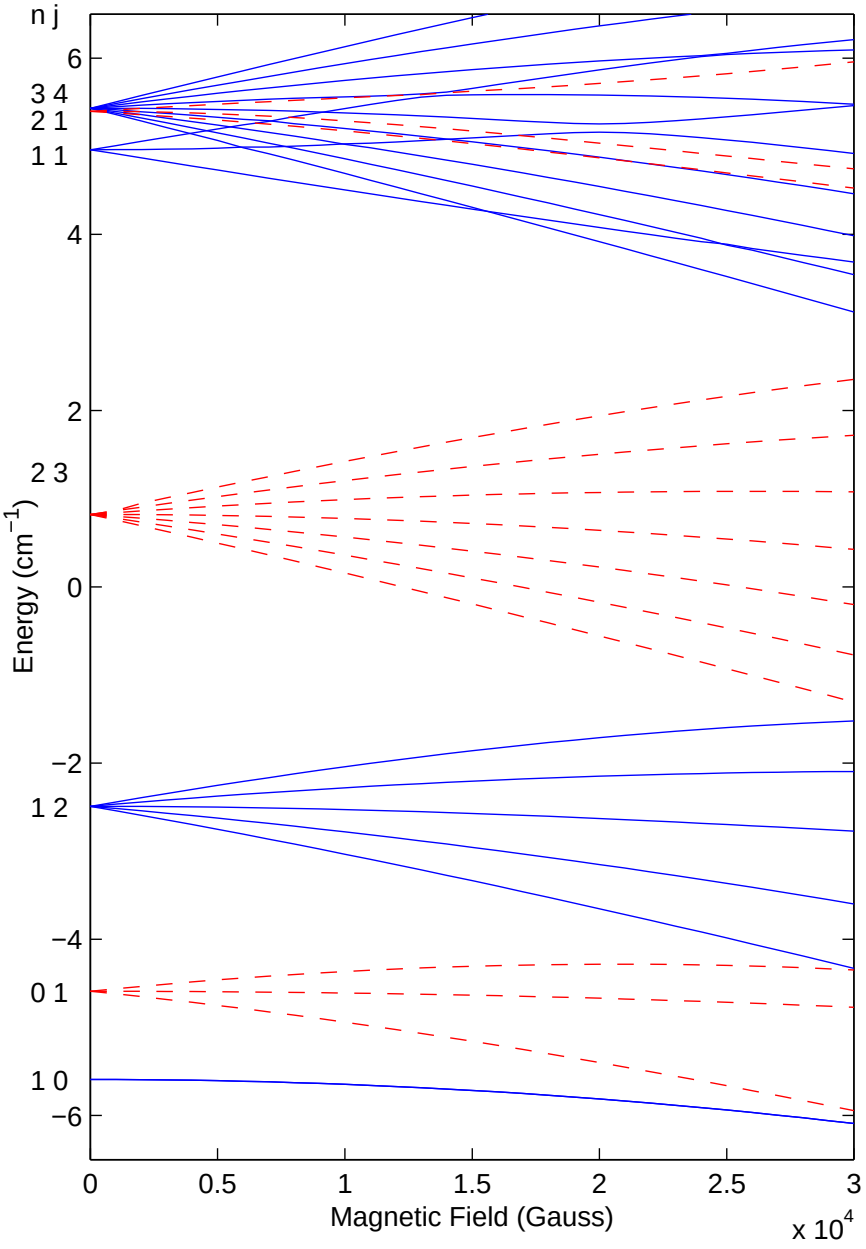

Figure 4.4: Zeeman diagram of the lowest few rovibrational states of SO. States of opposite parities ($(-1)^n$) are shown in red-dashed (+1) and blue-solid (-1).

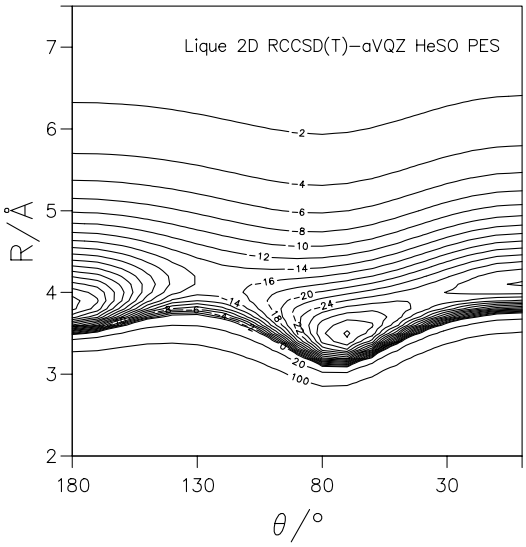

Figure 4.5: He-SO 2D ($\boldsymbol{R}, \theta, \boldsymbol{r}_e$ = 1.48 Å) RCSD(T)/aug-cc-pVQZ potential energy surface, data points originally calculated by [71]. $\theta = 0°$ corresponds to the linear SO-He configuration. Energies given in cm^{-1}.

He(^1S)+SO($^3\Sigma^-$) Hamiltonian and its matrix elements for electric and magnetic fields are identical to those presented in chapter 3.

All of the He+SO calculations presented were performed on the two dimensional ($\boldsymbol{R}, \theta$) intermolecular potential calculated by Lique et al. [71] shown in figure 4.5. It was originally used to examine the rotational excitation of sulphur monoxide via collisions with He in interstellar gas at temperatures in the range of 10 to 50 Kelvin. The surface was calculated by freezing the SO bond length to it equilibrium value $\boldsymbol{r}_e$ = 1.48 Å, and then performing RCCSD(T)/aug-cc-pVQZ calculations over a grid ($4.0 \leq \boldsymbol{R} \leq 16$ a_0 in steps of 0.25 a_0 and $0 \leq \theta \leq 180°$ in steps of 15°) with additional geometries at short range to better describe the repulsive wall, resulting in a total of 668 computed geometries. Correcting for basis set superposition error, a global potential minimum of -38.876 cm^{-1} was found at (R = 3.856 Å, $\theta = 180°$).

4.3 Bound-State Calculations

The bound states were calculated using the coupled-channel method implemented within the BOUND package, as described in chapter 2, using the coupled $|nsjm_j\rangle|LM_L\rangle$ basis.

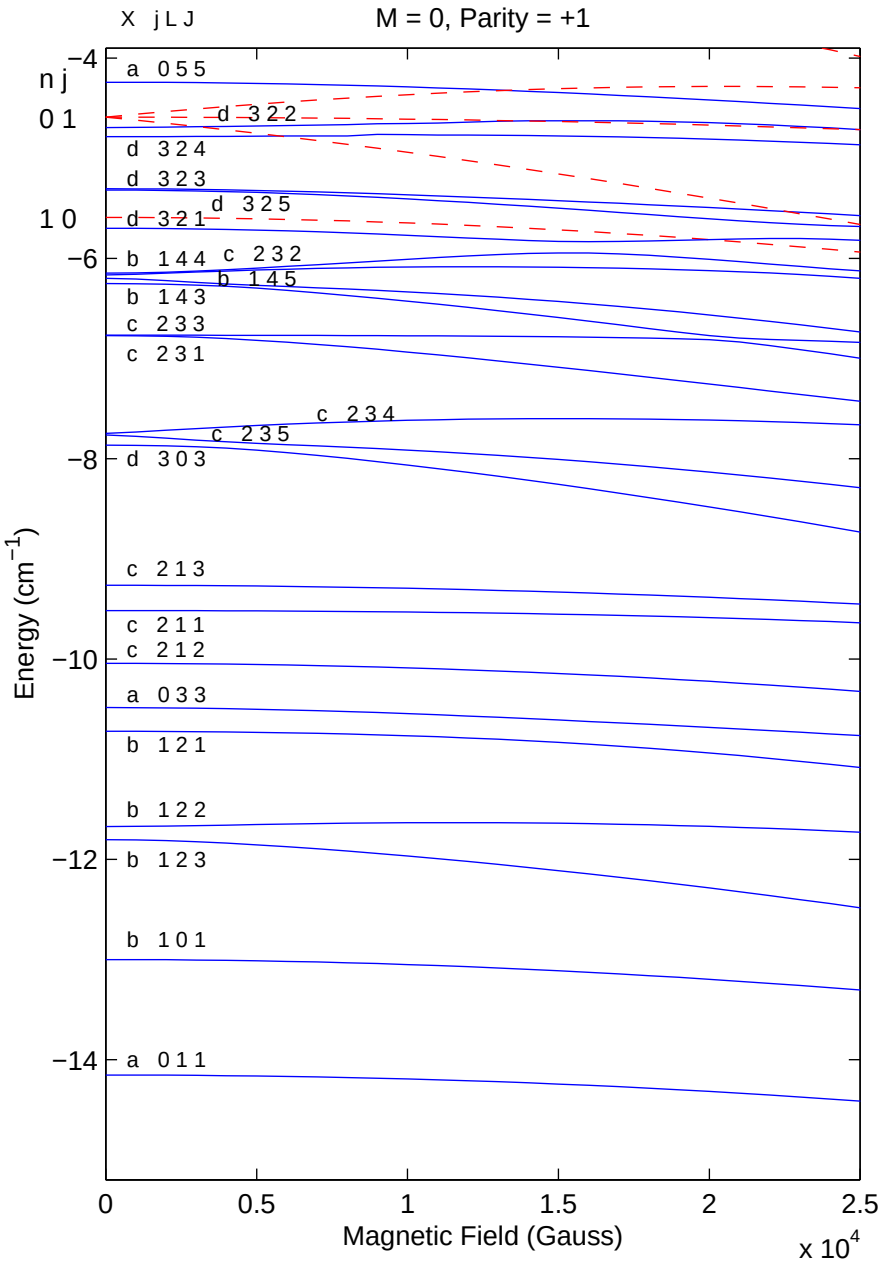

Figure 4.6: Bound states of the He-SO($^3\Sigma^-$) complex shown for even parity as a function of magnetic field, for $M = 0$. The SO thresholds are shown as dashed lines.

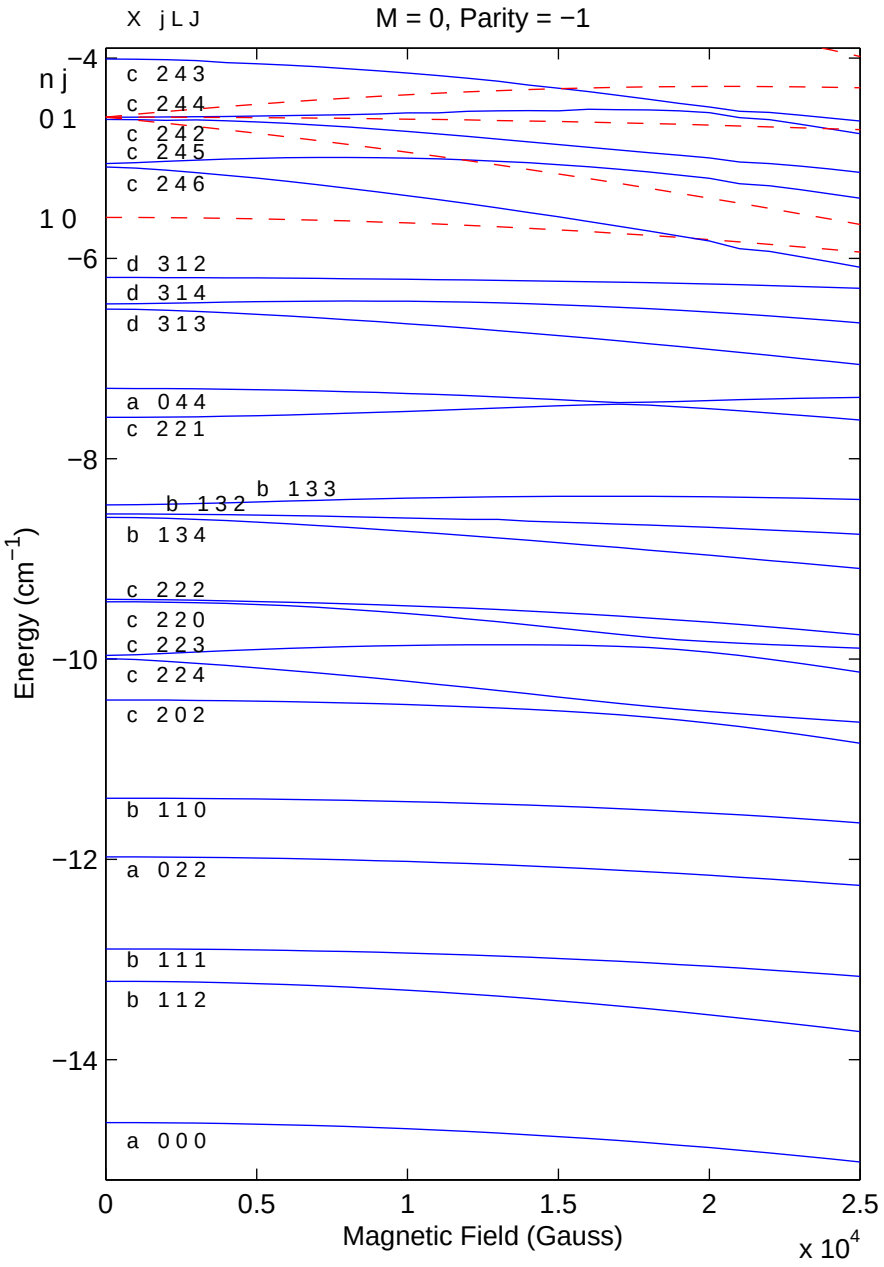

Figure 4.7: Bound states of the He-SO($^3\Sigma^-$) complex shown for odd parities as a function of magnetic field, for $M = 0$. The SO thresholds are shown as dashed lines.

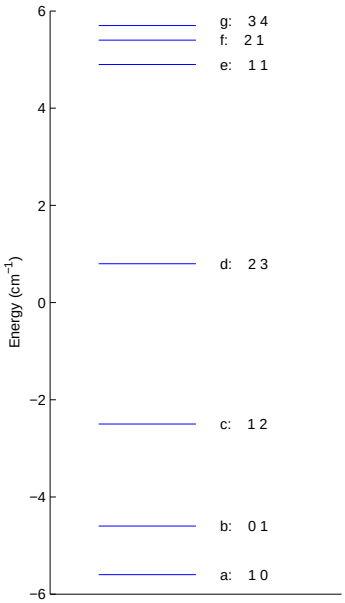

Figure 4.8: Phenomenological quantum numbers for the lowest few SO($^3\Sigma^-$) states, the states have been labeled using the Hund's case b $|\, nj\rangle$ basis.

The bound states with L up to four were converged using all values of n up to $n_{\max} = 5$ and all values of L up to $L_{\max} = 6$, this created 261 and 273 channels for each parity $(-1)^{n+L}$ for $M = 0$ in a magnetic field. In the presence of an additional parallel electric field, parity conservation is removed and only the projection of the total angular momentum M is conserved resulting in 534 channels for $M = 0$. The propagation was performed using the hybrid log-derivative method of Alexander and Manolopoulos [50] with $R_{\text{min/mid/max}} = 1.7, 4.0, 12.0$ Å. The calculated bound states are shown as a function of magnetic field for each parity in figures 4.6 and 4.7; for clarity only the $M = 0$ states are shown.

4.3.1 Zero-Field Quantum Numbers

One approach to making sense of the array of HeSO bound states is to assume that each bound state arises from SO in one of its rovibrational $|nj\rangle$ states with a definite end-over-end rotation L. j and L couple to form the total angular momentum J, which is a conserved quantity at zero-field, resulting in the fully-coupled $|\, (ns)jLJM\rangle$ basis.

The spin-spin interaction mixes states with $\Delta n = 0, \pm 2$, and as $\lambda_{ss} > b_{\text{rot}}$ there is significant mixing states of different n and therefore n in not a good quantum number, thus the HeSO bound states have been labeled x$|jLJ\rangle$ where x is a phenomenological quantum

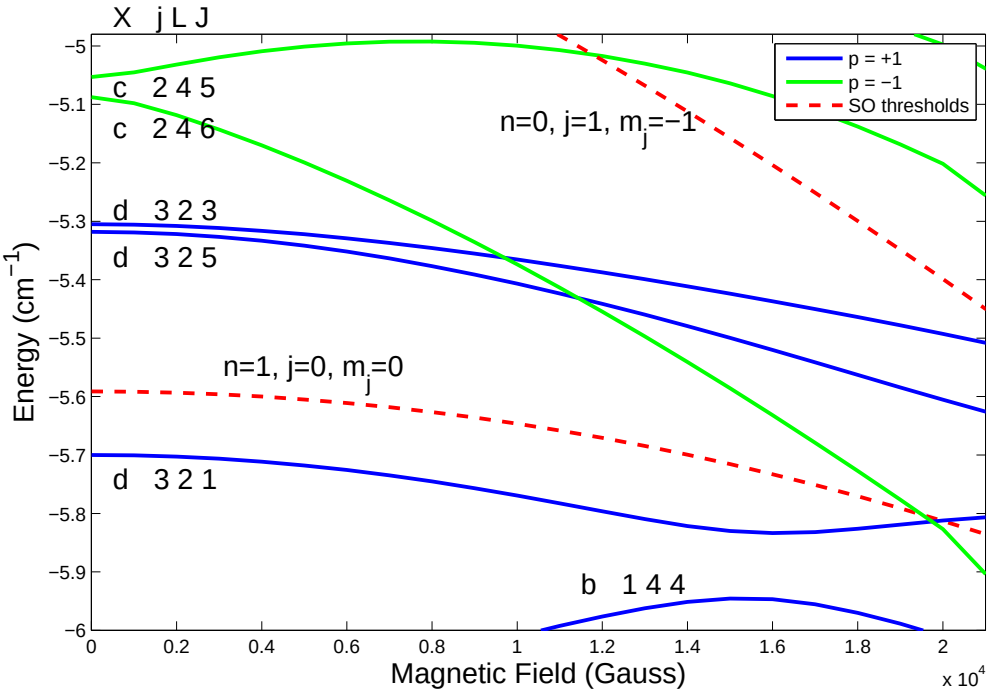

Figure 4.9: HeSO ($M = 0$) bound states near the lowest threshold, zero energy Feshbach resonances are predicted to occur at points at which bound states cross threshold. Odd/even parity states are shown in green/blue and the SO thresholds are shown as red dashed lines.

number representing the rovibrational state of SO. The phenomenological quantum numbers are shown in figure 4.8. The quantum numbers were assigned by performing zero field calculations for a defined L, assigning J and examining the dominant channels in the bound state composition. It can be seen from figures 4.6 and 4.7 that the HeSO potential only supports one vibrational (stretching) state and that all the bound states correspond to rotational states with different possible values of the total angular momentum at zero field.

4.4 Feshbach Resonances

Zero-energy magnetic Feshbach resonances occur at points at which bound states cross a threshold as a function of magnetic field. Figure 4.9, shows the magnetic field dependence

of the $M = 0$ bound states near the lowest $|n = 1, j = 0\rangle$ threshold. $M = 0$ gives the s-wave open channel $|n = 1, j = 0\rangle|L = 0\rangle$ in the lowest threshold. It can be seen that elastic Feshbach resonances should occur when the $d|j = 3, L = 2, J = 1, M = 0\rangle$ and $c|2460\rangle$ bound states cross the $|n = 1, j = 0\rangle$ threshold. Due to the different parity of the bound states the $c|2460\rangle$ bound state will result in an s-wave and the $d|3210\rangle$ bound state will result in a p-wave zero-energy Feshbach resonance.

All scattering calculations were performed using the MOLSCAT package, as described in chapter 2, with $n_{\max} = 5$ and $L_{\max} = 6$, using the hybrid log-derivative method of Alexander and Manolopoulos [50], with $R_{\min/\mathrm{mid}/\max} = 2.4/7.0/100.0$ Å. For each collision energy and applied field values, MOLSCAT produces the S-matrix and its eigenphase sum, the sum of phase shifts obtained from the S-matrix eigenvalues, which follows the Breit-Wigner form in multi-channel scattering, as described in chapter 2. The RESFIT package [72] is then used to fit the calculated eigenphase sum to the Breit-Wigner form, and the diagonal S-matrix elements to equation (2.60) returning the resonance location, width, and the complex quantity g_i that describes the resonant S-matrix circle.

Calculating at a collision energy of $E_k = 1$ μK the $d|3210\rangle$ p-wave resonance was found at $B_{\mathrm{res}} = 19984.629$ G with a width of 0.5413×10^{-05} G. However after extensive calculations the s-wave $c|2460\rangle$ resonance was not found; the situation was further complicated as the resonance appeared upon the application of an electric field, parallel to the magnetic field.

Performing calculations as a function of magnetic field for various values of electric field, the s-wave $c|2460\rangle$ resonance widths at $E_k = 1$ μK were calculated, table 4.2 shows the s-wave magnetic Feshbach resonance locations and widths. In order to find the very narrow resonance at small electric fields extrapolation techniques were required. The differences between eigenphase sums at calculated intervals were fitted to the Breit-Wigner form, from which the resonance location and width could be extrapolated. Using this technique it was possible to locate resonances that were only 1×10^{-7} Gauss wide.

The dominant s-wave resonant partial width (Γ_0) is plotted against the applied electric field on a log-log plot in figure 4.10. The linear nature of figure 4.10 indicates that rather than the resonance being very small it does not exist in the absence of an electric field. The non-integer power dependence of the resonance width $\Gamma_0 \propto E^{4.6}$, does not help in

E (kV/cm)	B_{res}	Γ_0	Γ_1	Γ	$\pm$
0.5	19513.07	1.01E-7	1.84E-9	1.03E-7	4.77E-10
1.0	19517.89	2.68E-6	7.39E-9	2.69E-6	7.49E-10
1.5	19526.50	1.84E-5	2.11E-8	1.83E-5	2.29E-7
2.0	19538.65	5.80E-5	3.62E-8	5.81E-5	1.07E-9
2.5	19554.43	1.67E-4	6.49E-8	1.67E-4	1.16E-9
3.0	19574.07	4.24E-4	1.13E-7	4.24E-4	7.17E-10

Table 4.2: Table of resonance widths as a function of electric field at a collision energy $E_k = 1\ \mu K$. Γ_0 and Γ_1 are the s and p-wave partial widths respectively and Γ is the total resonance width, the error quoted is the error in the eigenphase sum fitting. All values are in Gauss, unless specified otherwise.

determining the cause of the electric field dependence. The presence of an electric field must induce some form of coupling between the threshold and the bound state, possibly by breaking a previously neglected symmetry.

4.4.1 Matrix Elements between the $c|2460\rangle$ bound state and the $|n = 1, j = 0\rangle$ threshold

To evaluate the coupling between the bound state and the threshold, the fully coupled $|\ (ns)jLJM\rangle$ basis is used. The bound state is assumed to be dominated by the $|(11)2460\rangle$ channel, and the lowest threshold can be represented as $|(11)0000\rangle$. From the evaluated matrix elements of the Hamiltonian are given in chapter 3, the Zeeman interaction couples channels with $\Delta J = 0, \pm 1$ and the potential couples channels with; $\Delta L = \pm\lambda, \Delta J = 0, \Delta j = \pm\lambda$, and $\Delta n = 0, \pm\lambda$. Therefore the threshold can be coupled to the bound state via a $((V_{\lambda=2})^2(H_z)^6)$ interaction, as shown in table 4.4.1. The presence of this coupling does not explain the absence of the resonance in the absence of an electric field.

To test the coupling between channels in MOLSCAT, MOLSCAT was modified to calculate asymptotic field dressed eigenvalues and eigenvectors and to transform the potential coupling matrix into a basis of the asymptotic eigenvectors. As predicted from examining the Hamiltonian matrix there existed non-zero matrix elements that would

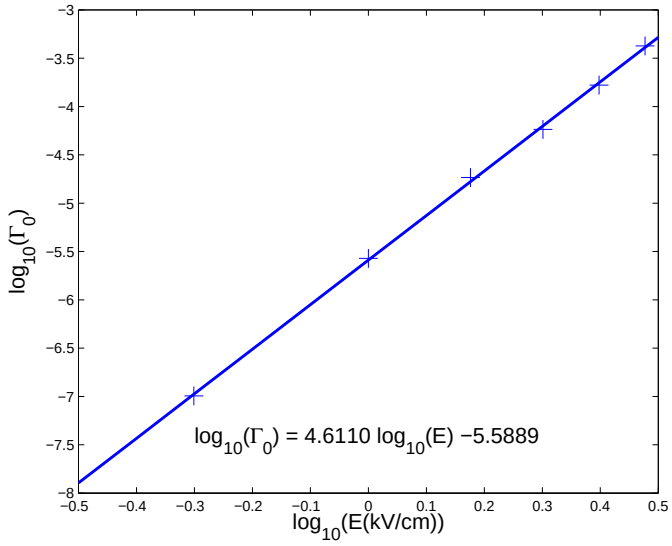

Figure 4.10: Log-log plot of the s-wave Feshbach resonance width (Gauss) against applied electric field strength (kV/cm). The linearity of the plot indicates the resonance has a vanishing width at zero electric field.

couple the bound state to the threshold.

4.4.2 Symmetry Considerations

The absence of a resonance with no applied electric field could be explained by an additional symmetry between the boundstate and the threshold, that has not yet been accounted for. This symmetry would be conserved under a magnetic field and broken by an electric field. For simplicity an uncoupled $|\, nm_n\rangle \,|\, sm_s\rangle \,|\, LM_L\rangle$ basis of;

$$|\, 1\rangle = |\, 1 - 1\rangle \,|\, 11\rangle \,|\, 00\rangle$$
$$|\, 2\rangle = |\, 10\rangle \,|\, 10\rangle \,|\, 00\rangle$$
$$|\, 3\rangle = |\, 11\rangle \,|\, 1 - 1\rangle \,|\, 00\rangle,$$

has been used to observe the effect of the following symmetry operations on terms in the Hamiltonian, in which the field axis is defined along Z.

σ_h

A magnetic field along Z can be envisaged as a point charge circulating in a defined direction (either clockwise or anticlockwise) the XY-plane. A reflection in the XY-plane

$\langle(ns)jLJM\mid$		$\mid(n's)j'L'J'M'\rangle$
$\langle(11)0000\mid$	V_2	$\mid(11)2200\rangle$
$\langle(11)2200\mid$	H_z	$\mid(11)2210\rangle$
$\langle(11)2210\mid$	H_z	$\mid(11)2220\rangle$
$\langle(11)2220\mid$	V_2	$\mid(11)2420\rangle$
$\langle(11)2420\mid$	H_z	$\mid(11)2430\rangle$
$\langle(11)2430\mid$	H_z	$\mid(11)2440\rangle$
$\langle(11)2440\mid$	H_z	$\mid(11)2450\rangle$
$\langle(11)2450\mid$	H_z	$\mid(11)2460\rangle$

Table 4.3: Zeeman and intermolecular potential ($\lambda = 2$) matrix elements between the $|(11)0000\rangle$ threshold and the $|(11)2460\rangle$ bound state.

σ_h leaves the circulating charge, its direction, and the force acting on it unchanged and therefore leaves the magnetic field unchanged [73].

$|nm_m\rangle$ and $|LM_L\rangle$ are described by spherical harmonics $Y_{l,m}(\theta,\phi)$, which under σ_h behave as $\sigma_h Y_{lm} = (-1)^{l-m}Y_{lm}$. Introducing $(-1)^{n-m_n+L-M_L}$ to the basis functions; $\sigma_h|1\rangle = +|1\rangle$, $\sigma_h|2\rangle = -|2\rangle$, and $\sigma_h|3\rangle = +|3\rangle$, indicates that there should be no interaction between state $\mid 2\rangle$ with states $|1\rangle$ and $|3\rangle$. Although this symmetry is conserved in a magnetic field it is broken by the spin-rotation $\hat{H}_{\rm sn}$ and the spin-spin $\hat{H}_{\rm ss}$ terms, as shown in the matrices below, where x represents some general non-zero matrix element.

$\hat{H}_Z$:

	$\mid 1\rangle$	$\mid 2\rangle$	$\mid 3\rangle$
$\langle 1\mid$	x		
$\langle 2\mid$	0	0	
$\langle 3\mid$	0	0	−x

$\hat{H}_{\rm sn}$:

	$\mid 1\rangle$	$\mid 2\rangle$	$\mid 3\rangle$
$\langle 1\mid$	−x		
$\langle 2\mid$	x	0	
$\langle 3\mid$	0	x	−x

σ_v and C_2

σ_v takes all space-fixed projections to their negative, so; $\sigma_v \mid 1\rangle = \mid 3\rangle$, $\sigma_v \mid 2\rangle = \mid 2\rangle$, and $\sigma_v \mid 3\rangle = \mid 1\rangle$. Taking linear combinations $\mid \pm\rangle = \frac{1}{\sqrt{2}}(\mid 1\rangle \pm \mid 3\rangle)$, gives states of opposite symmetries, $\sigma_v \mid +\rangle = \mid +\rangle$, $\sigma_v \mid -\rangle = -\mid -\rangle$.

A C_2 rotation in the plane of the loop has the following effect; $C_2 \mid lm_l\rangle = (-1)^{l-m_l} \mid l - m_l\rangle$ and $C_2 \mid sm_s\rangle = - \mid s - m_s\rangle$. Thus the effect of C_2 on the basis is opposite

	$\hat{E}\cdot\hat{d}$	$\hat{B}\cdot\hat{s}$
Ω	-1	$+1$
σ_v	$+1$	-1
C_2'	$+1$	-1
$\hat{T}$	$+1$	-1
i	-1	$+1$

Table 4.4: Summary of symmetry operations under electric and magnetic fields, where Ω is the general symmetry operation that would explain the absence of the resonance.

to σ_v; $C_2 \mid +\rangle = -\mid +\rangle$, $C_2 \mid -\rangle = \mid -\rangle$ and $C_2 \mid 2\rangle = -\mid 2\rangle$. For both σ_v and C_2 the matrices are the same, and both are conserved under $\hat{H}_{\text{sn}}$ and $\hat{H}_{\text{Stark}}$, but broken by $\hat{H}_Z$.

$$\hat{H}_Z\text{:}\quad \begin{array}{c|ccc} & |-\rangle & |+\rangle & |2\rangle \\ \langle -| & 0 & & \\ \langle +| & \mathrm{x} & 0 & \\ \langle 2| & 0 & 0 & 0 \end{array} \qquad \hat{H}_{\text{sn}}\text{:}\quad \begin{array}{c|ccc} & |-\rangle & |+\rangle & |2\rangle \\ \langle -| & -\mathrm{x} & & \\ \langle +| & 0 & -\mathrm{x} & \\ \langle 2| & 0 & \mathrm{x} & -\mathrm{x} \end{array}$$

The symmetry properties under magnetic and electric fields are summarized in table 4.4, where i is parity and Ω is the symmetry that would explain the absence of the resonance. For completeness, time-reversal symmetry $\hat{T}$ has also been included in table 4.4, however this is conserved by an electric field and broken by a magnetic field [73]. Parity is the only symmetry that meets the requirements, however this has already been accounted for, thus it appears that no additional symmetry exists in the system that would explain the absence of a resonance.

Chapter 5

Sympathetic cooling of NH($X^3\Sigma^-$) with Mg(^1S)

It was noted in section 1.1 sympathetic cooling, the act of putting a warm molecular sample into contact with an ultracold gas, could provide a route to cooling molecules into the sub-mK temperature range. For sympathetic cooling to be an effective method, the rate of thermalizing elastic collisions must be much greater than the rate of inelastic collisions and a commonly stated rule of thumb is that is that the rate of elastic collisions must be at least 100 times greater than the rate of inelastic collisions [74]. However, magnetic and electrostatic traps only trap molecules in low-field seeking states which are not the absolute ground state and therefore inelastic channels are present that can cause heating and trap loss. Thus judicious choices must be made on the molecules and the coolant gas used, in order to keep the rate of inelastic collisions to a minimum. However we are limited to experimentally available species with the most accessible coolants being the alkali-metal atoms, which are easily coolable in large numbers to ultracold temperature [12].

The first to consider sympathetic cooling with alkali-metal atoms was Soldán and Hutson [75] who in 2004, examined the interaction between rubidium atoms with NH($X^3\Sigma^-$), finding that the dispersion bound states of RbNH that correspond to the Rb(^2S)+NH($X^3\Sigma^-$) dissociation threshold were crossed by deeper ion-pair states, that correspond to the $Rb^+(^1S)$ + $NH^-(^2\Pi)$ dissociation threshold at linear geometries. These ion-pair states would introduce mechanisms for inelastic collisions and three-body recombination that

would hamper attempts at sympathetic cooling. Investigation of the Rb(^2S)+OH($^2\Pi_{3/2}$) system [76, 77] also found ion-pair states crossing the RbOH covalent states. More recently in 2007, detailed potential energy surfaces and field free low energy scattering calculations for Rb+NH and Cs+NH have been performed by Tacconi et al. [78–80] finding that the large inelasticity present could be used for rotational cooling of NH into its ground rotational state.

The interaction of NH_3 molecules with alkali-metal and alkaline-earth atoms was surveyed by Żuchowski and Hutson [81], all the systems studied exhibited large anisotropies that would produce strong inelasticity, thus sympathetic cooling is unlikely to be successful for NH_3 in low-field seeking states.

For sympathetic cooling to be successful for atoms and molecules not in their absolute ground state it is desirable to use light atomic cooling partners, that create high centrifugal barriers that can suppress inelastic loss channels, and that the anisotropy of the interaction potential is comparable to or smaller than the rotational constant of the molecule. As closed-shell atomic coolants such as the alkaline-earth atoms are more likely to have more isotropic interaction potentials, there is an increased likelihood that sympathetic cooling will work.

In 2009 Soldán, Żuchowski, and Hutson [82] surveyed the potential energy surfaces for NH interacting with both alkali-metal and alkaline-earth atoms, finding that for Mg and Be the anisotropy of the potential energy surface was small compared to the rotational constant of NH. What follows is a summary of this work, followed by detailed scattering calculations to assess the prospect of sympathetic cooling of NH with Mg.

With its relatively large magnetic moment and the low ratio of the spin-spin to rotational constants, predicted to increase the stability in a magnetic trap, ground state NH($X^3\Sigma^-$) has been the target of buffer gas cooling and magnetic trapping experiments [18, 34, 83], having been cooled and magnetically trapped at 710 mK. The collisions of He with NH have been studied in detail theoretically as experimental work has progressed [51, 57, 58, 62], and the mechanism for spin relaxation is presented in chapter 3. Metastable NH($a^1\Delta$) has also been Stark decelerated and electrostatically trapped [84] and proposals exist to transfer the $a^1\Delta$ molecules into the $X^3\Sigma^-$ ground state [85]. Due to the highly topical nature of NH it was chosen for this work on sympathetic cooling.

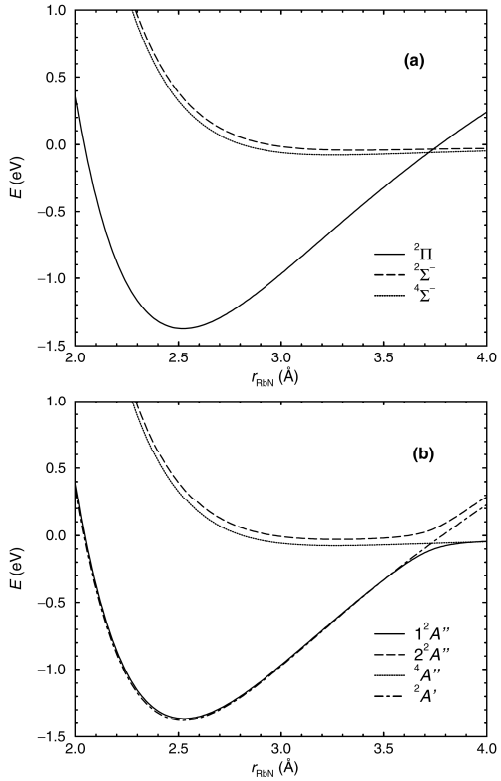

Figure 5.1: CASSCF(10,3)/MRCI potential energy curves of Rb-N-H with a fixed NH bond length $r_{\mathrm{NH}} = 1.0308$Å at linear (a) and non-linear (b) geometries. Image from [75].

5.1 Interaction of an Alkali-metal atom with NH($X^3\Sigma^-$)

For an alkali-metal atom (Alk) interacting with NH, the lowest Alk(^2S)+NH($X^3\Sigma^-$) dissociation threshold forms two electronic $^2\Sigma^-$ and $^4\Sigma^-$ states at collinear geometries with $C_{\infty v}$ point group symmetry. At non-linear geometries the symmetry is reduced to C_s and the two electronic states become $^2A''$ and $^4A''$. Above the Alk(^2S)+NH($X^3\Sigma^-$) threshold there exists the $Alk^+(^1S)$+$NH^-(^2\Pi)$ ion-pair dissociation threshold which forms the deeply bound Alk^+NH^- ionic state, that is $^2\Pi$ at linear geometries. The ion-pair state is subject to the Renner-Teller effect, in which the electronic motion is coupled to nuclear vibrations, splitting the $^2\Pi$ state into two at non-linear geometries with the electron hole either in ($^2A'$) or perpendicular to ($^2A''$) the triatomic plane. The ion-pair and dispersion-bound $^2A''$ states can thus form a conical intersection at linear geometries, for a fixed NH bond length the conical intersection exists at a point, if the NH bound length is allowed to vary there exists a seam of conical intersections along which the two surfaces

	Alk-NH						Alk-HN	
Alk	$R\ ^{4\Sigma}{}_{min}$	$V^{4\Sigma}{}_{min}$	$R^{2\Pi}{}_{min}$	$V^{2\Pi}{}_{min}$	R_x	V_x	$R\ ^{4\Sigma}{}_{min}$	$V^{4\Sigma}{}_{min}$
Li	2.176	-1799.1	1.78	-21073	3.09	-600	4.658	-115.3
Na	2.737	-651.3	2.13	-13287	3.21	-470	4.872	-98.9
K	3.073	-784.7	2.42	-14235	3.84	-432	5.386	-91.1
Rb	3.254	-709.3	2.53	-13918	3.99	-412	5.521	-87.3
Cs	3.435	-737.9	2.65	-15116	4.31	-381	5.761	-85.0

Table 5.1: Geometrically optimized minima (R_{min},V_{min}) and crossing points (R_x,V_x) for the lowest $^4\Sigma^-$ and $^2\Pi$ states of linear Alk-NH complexes. Energies and distances given in cm^{-1} and Å respectively. Tabulated data from [82].

intersect. Figure 5.1 shows the Rb-NH potential energy curves calculated by Soldán and Hutson [75] at linear (a) and non-linear geometries (b), at the non-linear geometry the avoided crossing between the two $^2A''$ states can be seen.

Table 5.1 shows the geometrically optimized linear Alk-NH and NH-Alk energy minima and the crossing points of the $^4\Sigma^-$ and ion-pair $^2\Pi$ states. Examining the $^4\Sigma^-$ quartet state that is unaffected by the ion-pair state and thus more suitable for sympathetic cooling, it can be seen that for all of the alkali-metal atoms the anisotropy of the quartet potential is much greater than the rotation constant of NH ($\approx 16\ cm^{-1}$). This large anisotropy is due to strong *sp* mixing of the alkali-metal orbitals in the Alk-NH arrangements, this mixing is much weaker than Alk-HN arrangement and thus the potential is much shallower. The doublet $^2\Sigma^-$ state is quantitatively higher in energy than the $^4\Sigma^-$ quartet state, thus the $^2\Pi$ ion-pair state crosses the $^2\Sigma^-$ state at distances beyond the $^2\Sigma^-$ minimum. The resultant conical intersection ensures that the lowest adiabatic surface of $^2A'$ or $^2A''$ symmetry will always have a deep ion-pair well.

The large anisotropy in the quartet state and the ion-pair state interacting with the doublet state imply that sympathetic cooling is unlikely to be successful with alkali-metal atoms.

	Ae-NH						Ae-HN	
Ae	$R\ ^{3\Sigma}{}_{min}$	$V^{3\Sigma}{}_{min}$	$R^{3\Pi}{}_{min}$	$V^{3\Pi}{}_{min}$	R_x	V_x	$R\ ^{3\Sigma}{}_{min}$	$V^{3\Sigma}{}_{min}$
Be	3.995	-84.5	1.55	-20240	2.30	2390	4.301	-95.4
Mg	4.157	-106.5	1.95	-10120	2.59	1510	4.636	-103.0
Ca	3.963	-165.7	2.19	-17041	3.19	-146	5.149	-104.5
Sr	3.175	-286.4	2.32	-16734	3.39	-267	5.340	-101.8

Table 5.2: Geometrically optimized minima (R_{min},V_{min}) and crossing points (R_x,V_x) for the lowest $^3\Sigma^-$ and $^3\Pi$ states of linear Ae-NH complexes. Energies and distances given in cm^{-1} and Å respectively. Tabulated data from [82].

5.2 Interaction of an Alkaline-earth atom with NH($X^3\Sigma^-$)

For an alkaline-earth atom (Ae) interacting with NH the Ae(^1S)+NH($X^3\Sigma^-$) dissociation threshold forms only one electronic state, $^3\Sigma^-$ at linear geometries ($C_{\infty v}$) becoming $^3A''$ at non-linear geometries (C_s). The ion-pair $Ae^+(^2S)$+$NH^-(^2\Pi)$ dissociation threshold forms two, $^1\Pi$ and $^3\Pi$, states at linear geometries, and at non-linear geometries the $^3\Pi$ state is split by the Renner-Teller effect into a $^3A'$ state in which the electron hole in is the triatomic plane and a $^3A''$ with the electron hole perpendicular to the triatomic plane. As with the alkali-metal atom case, the ion-pair $^3A''$ state and the dispersion-bound $^3A''$ state form a conical intersection at linear geometries.

Table 5.2 shows the geometrically optimized linear Ae-NH and NH-Ae energy minima and crossing points of the lowest $^3\Sigma^-$ and $^3\Pi$ states. The anisotropy of the alkaline-earth potentials are smaller than anisotropies present in alkali-metal potential, and for Be and Mg the potential anisotropy is smaller than the rotational constant of NH ($\approx 16\ cm^{-1}$). It can also be seen that for Be and Mg, the ion-pair $^3\Pi$ states cross high up on the repulsive wall of the $^3\Sigma^-$ state. For NH-Ae configurations the intersection occurs high on the repulsive wall for all of the alkaline-earth species. Thus for low-energy collisions of Be and Mg with NH the conical intersection occurs in a classical forbidden region and may not have a strong effect on sympathetic cooling collisions.

Recently Mehstäubler et al. [86] succeeded in cooling down magnesium to sub-Doppler temperatures, and as so far no attempt has been made to cool beryllium atoms, magnesium

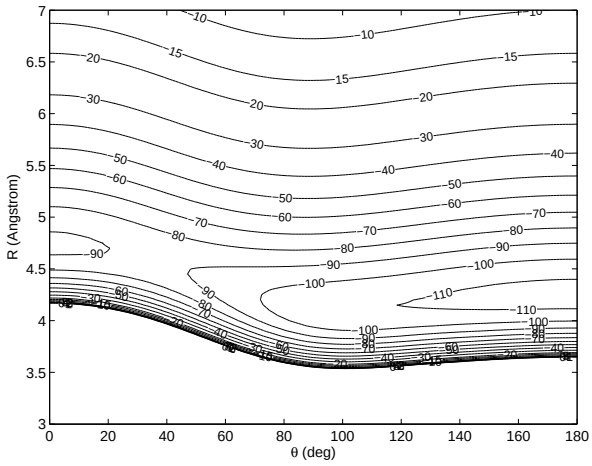

Figure 5.2: MgNH $^3\Sigma^-$ SAPT(DFT) potential energy surface, $\theta = 0$ corresponds to the NH-Mg arrangement. Energy shown in cm^{-1}. Data calculated by [82].

appears to be the best candidate for sympathetic cooling.

5.3 Mg-NH PES

Figure 5.2 shows the SAPT(DFT) potential energy surface for the $^3\Sigma^-$ state of MgNH calculated by Soldán et al. [82]. The ion-pair state does not cross this potential until R = 2.59Å at which point the $^3\Sigma^-$ potential is strongly repulsive. Thus for collision energies that are relevant for sympathetic cooling, $\approx$ 100mK (0.06 cm^{-1}), the barrier appears to be wide and high enough to neglect the MgNH$\rightarrow$Mg$^+$NH$^-$ transition allowing scattering calculations to be performed just on the $^3\Sigma^-$ surface. The long-range coefficients $C_{n,l}$ from the expansion of the potential in terms of the inverse powers of R^{-n} and Legendre polynomials $P_l(\cos\theta)$ are given in table 5.3.

n,l	Dispersion	Induction	Total
6,0	131.33	26.79	158.12
6,2	26.34	59.91	86.25
7,1	181.73	135.63	317.36
7,3	224.16	138.11	362.27
8,0	6517.00	800.49	7317.49
8,2	4346.80	2354.51	6701.31
8,4	539.70	740.60	1280.30
9,1	14855.00	5791.50	20646.50
9,3	21080.00	7982.60	29062.60
9,5	1767.00	2683.60	4450.60
10,0	300670.00	21080.00	321750.00
10,2	306940.00	81017.00	387957.00
10,4	65902.00	39176.00	105078.00
10,6	4529.70	8565.00	13094.70

Table 5.3: Mg+NH($^3\Sigma^-$) long-range dispersion and induction potential coefficients, $C_{n,l}$ for the potential expansion $V(R,\theta) = \sum_n \sum_l C_{n,l} R^{-n} P_l(\cos\theta)$, for the SAPT(DFT) potential presented in [82]. All values are quoted in $E_h\ a_0^n$.

Chapter 6

MgNH Bound States

The zero-field MgNH bound states were calculated using the BOUND package, using the fully-coupled $|(ns)jLJ\rangle$ basis implemented into BOUND for this purpose, the Hamiltonian matrix elements can be found in chapter 3. Calculations were performed with the basis $n_{\max} = 5$ $L_{\max} = 11$ in which states with $L \leq 9$ are converged, and the hybrid log-derivative propagator [50] with $R_{\min/\mathrm{mid}/\max} = 2.5/4.3/20.0$ Å. The NH($X^3\Sigma^-$) molecular constants presented in table 6 are used throughout.

Figure 6.2 shows the calculated bound states as a function of the total angular momentum J for the whole well and 6.3 shows the near threshold bound states. The bound state pattern shown can be rationalized by considering the angular momentum coupling in the Mg-NH complex.

Considering open-shell atom-diatom van der Waals complexes Dubernet et al. [88] presented three angular momentum coupling cases that are analogous to Hund's coupling cases (a), (b) and (c) for diatomic molecules. In case (1) $\boldsymbol{n}$ (the angular momentum of the diatom excluding spin) and $\boldsymbol{s}$ (the spin) are strongly coupled to the intermolecular axis,

b_{rot} (cm^{-1})	γ_{ns}(cm^{-1})	λ_{ss}(cm^{-1})
16.343	-0.0055	5.2788

Table 6.1: Rotational, spin-rotation and spin-spin constants for NH($X^3\Sigma^-$), values from [87].

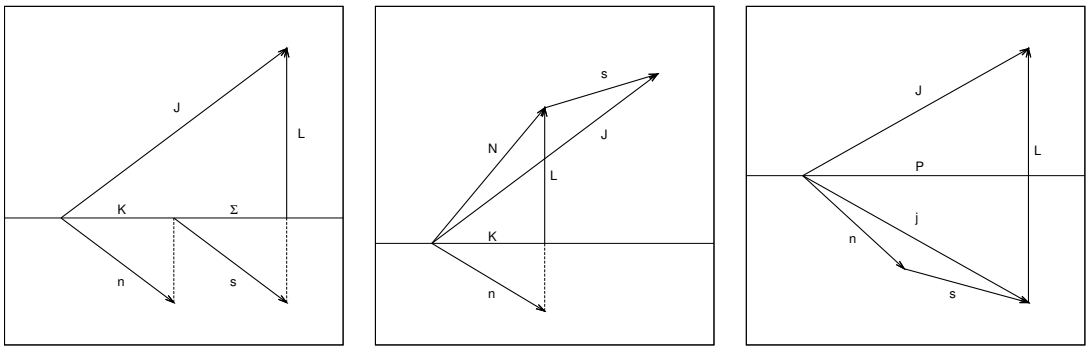

Figure 6.1: Angular momentum coupling cases in open-shell Van der Waals complexes as presented by Dubernet et al. [88]. From left to right cases 1, 2 and 3 ares shown, which are analogous to Hund's cases a, b, and c in diatomic molecules.

with projections K and Σ onto the intermolecular axis respectively. $\boldsymbol{L}$ is perpendicular to the intermolecular axis and thus the body-fixed projection of the total angular momentum $\boldsymbol{J}$ is $K + \Sigma$. In case (2) $\boldsymbol{n}$ but not $\boldsymbol{s}$ is coupled to the intermolecular axis with a well defined projection K, $\boldsymbol{L}$ and K couple to give $\boldsymbol{N}$ (the total angular momentum of the complex excluding spin) which couples with $\boldsymbol{s}$ to form $\boldsymbol{J}$. In case (3) $\boldsymbol{n}$ and $\boldsymbol{s}$ couple to form $\boldsymbol{j}$ with a projection P onto the intermolecular axis, as $\boldsymbol{L}$ is perpendicular to the intermolecular axis P is also the projection of $\boldsymbol{J}$. The three coupling cases are shown in figure 6.1.

The zero-field boundstate pattern in Mg-NH can be rationalized in the limit of the case (2) coupling scheme. MgNH(n = 0,K = 0), forms one J = 0 state $|n = 0, K = 0, N = 1, s = 1, J = 0\rangle$, three J = 1 states (N = 0,1,2), three J = 2 states (N = 1,2,3), and so on. In figures 6.2 and 6.3 these states are labeled by a stretching quantum number v and it can be seen that the potential supports six vibrational states. MgNH(n = 1) states can form bound states with K = 0, 1^e, and 1^f, where 1^e and 1^f are the even and odd linear combinations of the $|K|$ = 1 states, in figure 6.2 two vibrational n = 1 manifolds can be seen and a further vibrational manifold can be seen in figure 6.3. For J = 0, N = 1 and there are three bound states arising from each of the different possible values of K. For J = 1 seven n = 1 bound states are formed three from K = 0 ($N = 0, 1, 2$) and two each from 1^e and 1^f ($N = 1, 2$). For $J \geq 2$ there are nine bound states formed for each value of K with $N = J - 1, J, J + 1$. In figures 6.2 and 6.3 the n = 1 states are labeled by their value of K. Table 6.2 summarizes the assigned quantum numbers for the J = 0, 1, and 2

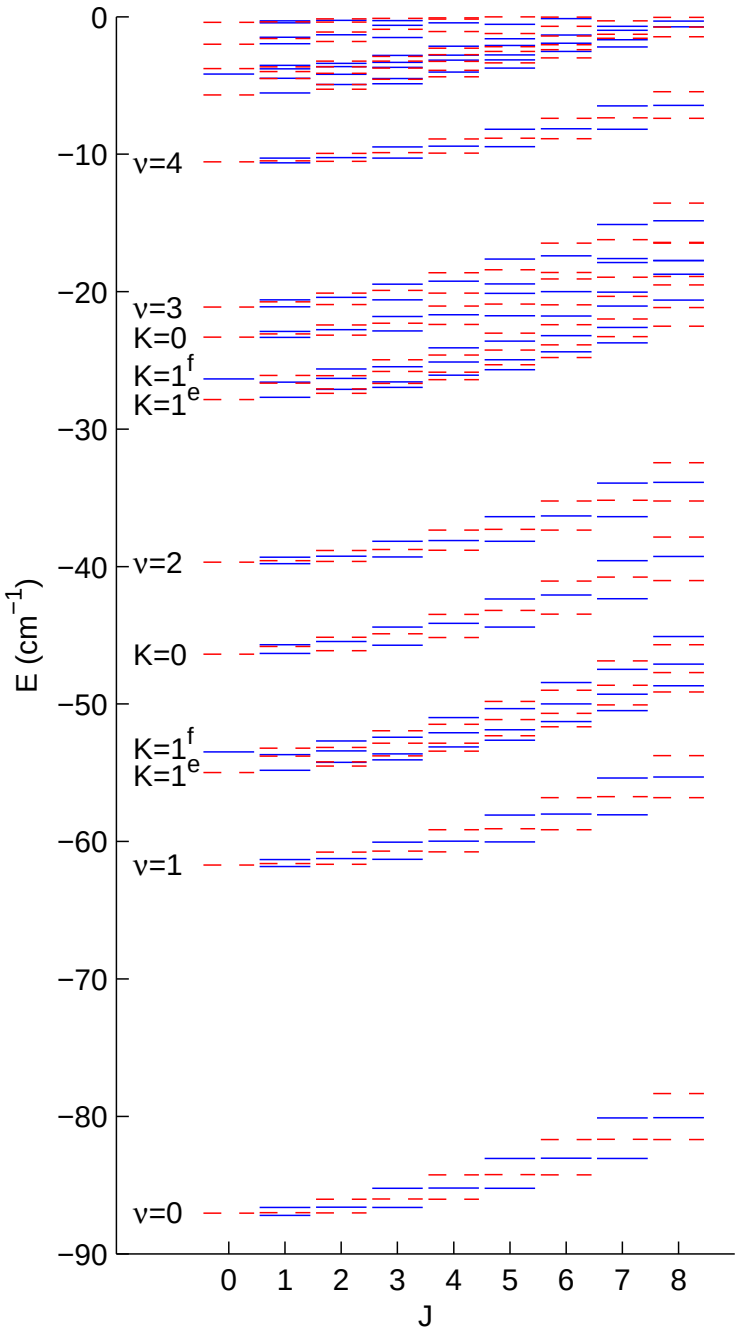

Figure 6.2: MgNH bound states as a function of the total angular momentum J. States of +/- parity ($(-1)^{n+L+1}$) are shown as (red,dashed)/(blue,solid) lines. The $n = 0$ states are labeled by vibrational quantum number v and the $n = 1$ states are labeled by K the projection of n onto the intermolecular axis, two vibrational manifolds can be seen. The near threshold bound states are shown in figure 6.3.

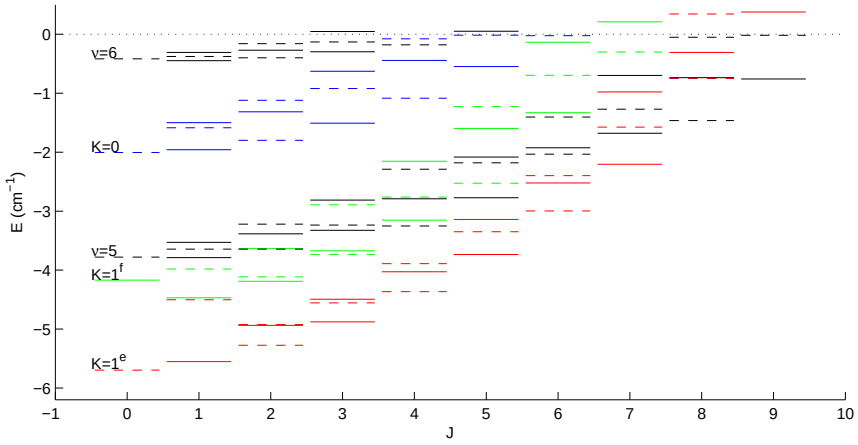

Figure 6.3: MgNH near threshold bound states as a function of the total angular momentum J. States of +/- parity ($(-1)^{n+L+1}$) are shown as (dashed)/(solid) lines, the $n = 1$ states $K = 0$, 1^e, and 1^f have also been indicated by blue, red, and green lines respectively.

cases.

6.0.1 Mg+NH Feshbach Resonances

Feshbach resonances occur when the collision energy is tuned across a boundstate of the colliding complex either via changing the energy or the magnetic field. It can be seen from figure 6.3, which shows the near threshold bound states, that as the lowest $n = 0, m_s = +1$ and $m_s = 0$ NH thresholds are tuned as a function of magnetic field they cross bound states with a large value J. Thus the Feshbach resonances that occur are in a different part of the Hamiltonian than the s-wave ($L = 0$) Feshbach resonances that are discussed in relation to He+SO in chapter 4.

n	K	N	s	J	
0	0	1	1	0	+
0	0	0	1	1	-
0	0	1	1	1	+
0	0	2	1	1	-
0	0	1	1	2	+
0	0	2	1	2	-
0	0	3	1	2	+

n	K	N	s	J	
1	0	1	1	0	+
1	1^e	1	1	0	+
1	1^f	1	1	0	-
1	0	0	1	1	+
1	0	1	1	1	-
1	0	2	1	1	+
1	1^e	1	1	1	-
1	1^e	2	1	1	+
1	1^f	1	1	1	+
1	1^f	2	1	1	-
1	0	1	1	2	-
1	0	2	1	2	+
1	0	3	1	2	-
1	1^e	1	1	2	-
1	1^e	2	1	2	+
1	1^e	3	1	2	-
1	1^f	1	1	2	+
1	1^f	2	1	2	-
1	1^f	3	1	2	+

Table 6.2: The structure of the $n = 0$ and 1, Mg-NH bound states in the case (2) coupling limit for $J = 0$, 1, and 2. Note for $n = 1$ there are three $J = 0$, seven $J = 1$ and nine $J = 2$ states. The parity $(-1)^{n+L+1}$ of each state is indicated in the far right column with ±.

Chapter 7

Mg+NH Scattering Calculations

The collisions that are of most interest for sympathetic are those of NH in its lowest magnetically trappable low-field seeking state $|\ n = 0, s = 1, j = 1, m_j = m_s = +1\rangle$, which may undergo inelastic collisions to the untrapped $m_j = 0$ and -1 states, as shown in figure 7.1.

Neglecting hyperfine structure, scattering calculations have been performed using the MOLSCAT package in the $|nsjm_j\rangle\ |\ LM_L\rangle$ coupled basis with $n_{\max} = 6$ and $L_{\max} = 8$ and using the hybrid log-derivative method [50] with $R_{\min/\mathrm{mid}/\max} = 2.5/50.0/250.0$ Å. Parity $p = (-1)^{n+L+1}$ and $M = m_j + M_L$ are conserved in collisions in a magnetic field, and thus the Hamiltonian is block-diagonalized and calculations are performed separately for each parity and M. Decomposing the integral cross section between NH levels ($|\ \alpha\rangle = |\ nsjm_j\rangle$) into sums of partial cross sections characterized by the value of L in the incident channel, the cross section is [89]

$$\sigma^{L}_{\alpha\to\alpha'} = \frac{\pi}{k^2_\alpha} \sum_{MpL'} |1 - S^{Mp}_{\alpha,LM_L\to\alpha',L'M'_L}|^2, \tag{7.1}$$

where $M_L = M - m_j$, $M'_L = M - m'_j$, and k_α is the wave vector for incoming channel α, defined for a collision energy $E_k = \hbar^2 k^2_\alpha / 2\mu$, and μ is the reduced mass of the colliding system. As we are focusing on transitions between the $n = 0$, $j = 1$ levels, the labels α is abbreviated to just m_j.

MOLSCAT does not automatically calculate partial wave cross sections, instead automatically summing over the partial waves cross sections in the incident and outgoing states to give the cross section $\sigma_{\alpha\to\alpha'}$. The partial wave cross sections were calculated by

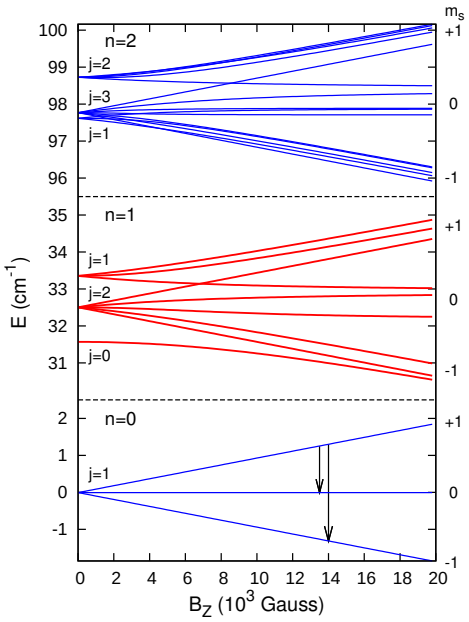

Figure 7.1: NH($^3\Sigma^-$) thresholds as a function of magnetic field. The transitions important for sympathetic cooling are the inelastic collisions from the low-field-seeking magnetically trappable $m_s = +1$ state (as indicated by arrows) which are mediated via the spin-spin interaction and the potential anisotropy.

extracting the S-matrix from MOLSCAT after each calculation and explicitly evaluating (C.0.1), the method used to do this is summarized in appendix C.

The spin relaxation mechanism for $^3\Sigma$ molecules has been presented in chapter 3, in which the coupling between different m_j channels occuring via the interplay of the spin-spin interaction and the potential anisotropy. The spin-spin terms mixes the $n = 0$ and $n = 2$ states with the same j and m_j, and the potential anisotropy then mixes states of different L such that $\Delta m_j + \Delta M_L = 0$.

For s-wave scattering ($L = 0$) from the $m_j = +1$ channel $M_L = 0$ and thus $M = m_j$, and since M is conserved there is no outgoing channel with $L' = 0$ for $m'_j = 0$ or -1 and thus the dominant relaxation channels for s-wave scattering have $L' = 2$ in the outgoing channel, following $|m_s = +1, L = 0\rangle \rightarrow |m_s \neq +1, L = 2\rangle$. At low energies channels with $L > 0$ are suppressed by centrifugal barriers, the heights of which are approximately $E^L_{\rm cf} = (\hbar L(L+1)/\mu)^{\frac{3}{2}}(54C_6)^{-\frac{1}{2}}$, which is 23 mK for MgNH with $L = 2$.

In the absence of a magnetic field the different m_j thresholds are degenerate, and the centrifugal barriers strongly suppresses the inelastic transitions but the spin-relaxation

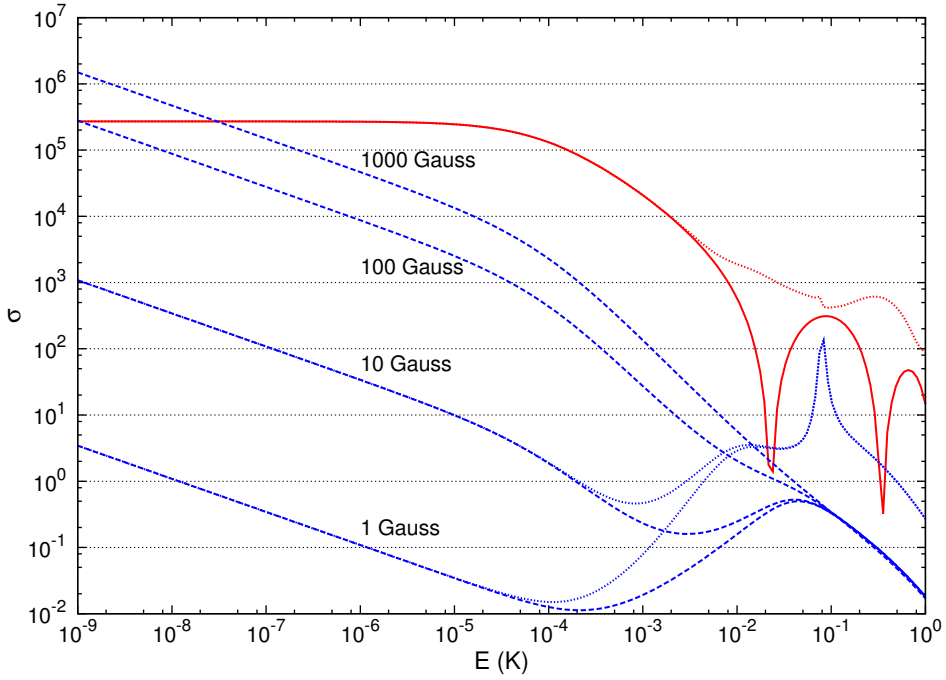

Figure 7.2: Mg+NH elastic $\sigma^0_{\Delta m_j=0}$ (dotted red) and the total inelastic $\sigma^0_{\Delta m_j\neq 0}$ (dotted blue) s-wave cross sections (in Å^2) as a function of collision energy for various magnetic fields. Integral cross sections including p, d and f (L =1, 2, and 3) partial waves are shown for the elastic cross sections (solid red) and the total inelastic cross sections at 1 and 10 G (dashed blue).

cross sections is nevertheless nonzero at finite energy [51, 62]. The application of a magnetic field removes the degeneracy, increasing the kinetic energy in the outgoing channels and reducing the centrifugal suppression. The elastic cross section is dominated by $\Delta L = 0$ and thus the cross section is almost field independent.

Figure 7.2 shows the s-wave elastic cross section $\sigma^0_{\Delta m_j=0}$ (dotted red) and the total inelastic $\sigma^0_{\Delta m_j\neq 0}$ (dotted blue) cross sections for the initial $m_j = +1$ state as a function of energy for varying magnetic field strength. Figure 7.3 shows the s-wave total inelastic cross section as a function of magnetic field for a number of collision energies. It can be seen that the total inelastic cross section increases dramatically as the magnetic field increases.

The general rule for sympathetic cooling to work is that the ratio of elastic to the total inelastic cross section, $\gamma = \sigma_{\rm elas}/\sigma^{\rm tot}_{\rm inelas}$ is greater than 100. It can be seen from figure 7.2 that for low collision energies and small magnetic fields that $\gamma \gg 100$. For collision

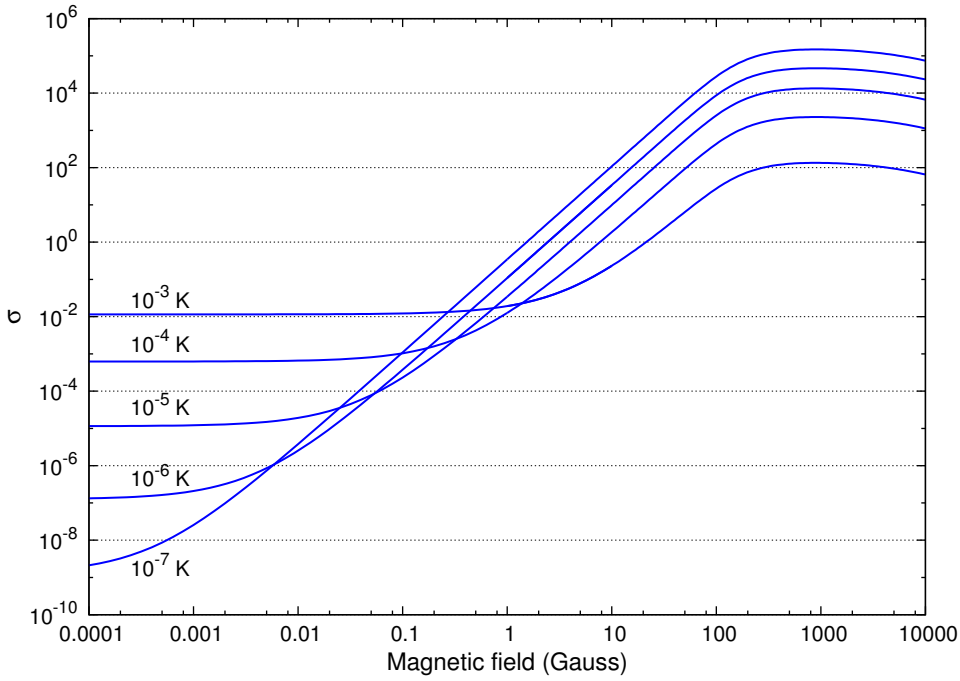

Figure 7.3: Mg+NH total s-wave inelastic cross sections $\sigma^{L=0}_{m_j=+1\to 0} + \sigma^{L=0}_{m_j=+1\to -1}$ as a function of magnetic field strength for various collision energies. The cross sections are given in Å^2.

energies above approximately 10^{-4}K higher partial waves start to contribute to the total cross sections. Figure 7.2 shows the total cross sections including p, d and f (L = 1, 2, and 3) partial waves for 1 and 10 G, with L = 4 partial waves become important above 100 mK. Apart from a sharp resonant peak in the d-wave inelastic cross section around 75 mK, γ remains in excess of 100.

To assess the prospect of sympathetic cooling of NH with Mg, figure 7.4 shows a contour plot of γ as a function of magnetic field strength and collision energy, all partial waves up to f-wave have been included. In a unbiased magnetic trap with a point of zero-field at the center, the density of trapped $m_j = +1$ molecules at a temperature T will be distributed according to the Boltzmann distribution,

$$\rho/\rho_0 = \exp\left(\frac{-m_j g \mu_0 B}{k_B T}\right). \tag{7.2}$$

At any given temperature only about 0.1% of molecules will experience fields greater than $B = 6k_BT/g\mu_0$, which is shown as a solid red line in figure 7.4. When trapped atoms and molecules pass close to the zero-field point at the trap center, they experience a very fast change in the field direction that can cause spin-flip transitions [35, 90] resulting in trap

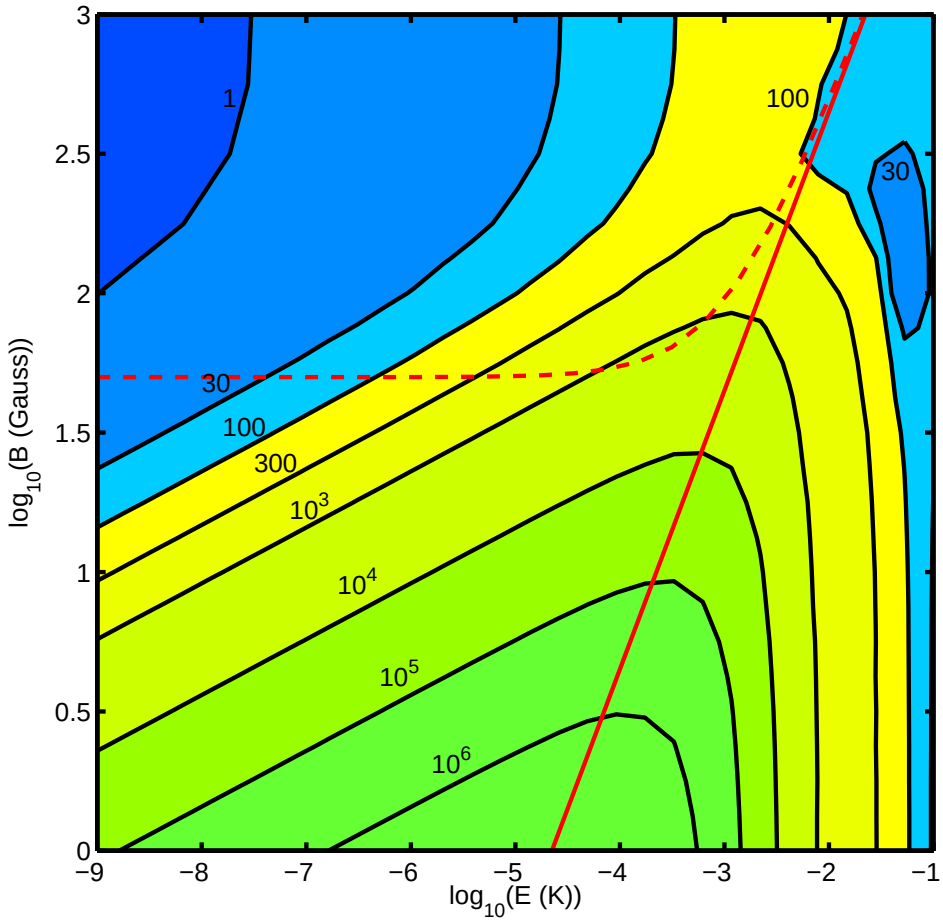

Figure 7.4: Contour plot of γ the ratio of elastic to total inelastic cross sections as a function of magnetic field and collision energy. The red lines show the maximum field sampled by trapped NH in the $m_j = +1$ state ($B = 6kT/g\mu_0$) in a unbiased trap (solid) and for a trap with an additional bias field of 50 G (dashed).

loss. Adding a bias field to the trap creates a non-zero field at the trap center, removing the possibility for this trap loss mechanism. For ^{14}NH there are six magnetically trappable hyperfine levels, the lowest three of these cross untrapped states at fields below 32 G. Thus a bias field larger than 32 G is required to avoid spin-flip losses. The dashed red line on figure 7.4 shows the upper limit of the fields explored by trapped molecules when a bias field of 50 G is applied.

It is important to precool the molecules as far as possible before starting sympathetic cooling, ideally to a temperature on the order of tens of milliKelvin. It can be seen that for temperatures up to around 10 mK γ is always greater than 100 in the allowed region. As the sample is cooled below a milliKelvin the field sampled by the molecules decreases, γ increases and the trapped NH becomes increasingly stable to spin-relaxation. Even with a bias field the temperature at which sympathetic cooling occurs changes very little and it is still possible to cool NH to temperatures below 1 μK.

7.0.2 Potential Dependence

Low energy scattering depends strongly on the details of the potential energy surface and the MgNH surface used is probably accurate to around 5%. To explore the potential sensitivity of the calculations, a scaling factor $\lambda_{\rm scl}$ is introduced to the potential energy surface

$$V^{\rm scaled}(R,\theta) = \lambda_{\rm scl} V(R,\theta). \tag{7.3}$$

Figure 7.5, shows the s-wave elastic and total inelastic cross section as a function of $\lambda_{\rm scl}$ for E_k=1 μK and B = 10 G. Both the elastic and total inelastic cross sections show strong resonance structures as bound states and quasi-bound states cross the $m_j = +1$ threshold as $\lambda_{\rm scl}$ is varied, though away from resonance the ratio γ remains large.

Further contour plots of γ as a function of magnetic field and collision energy have been calculated for a near resonant $\lambda_{\rm scl} = 1.004$ and a non-resonant $\lambda_{\rm scl} = 1.04$ potential, shown in figure 7.6. It can be seen from figure 7.6 that the contour plots are broadly similar, indicating that the conclusions are broadly independent of the details of the potential energy surface, confirming that Mg is a good candidate for sympathetic cooling of magnetically trapped NH.

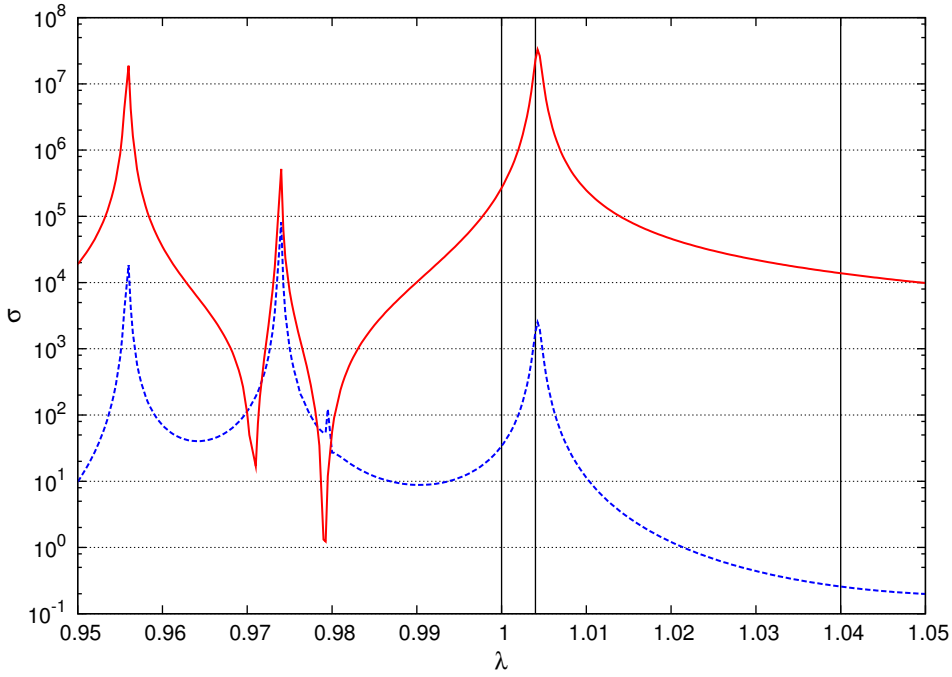

Figure 7.5: s-wave elastic (solid, red) and total inelastic (dashed, blue) cross sections (in Å^2) as a function of a potential scaling factor λ_{scl}, at a collision energy of 10^{-6} K and a magnetic field of 10 G. Values of $\lambda_{\text{scl}} = 1$, 1.004, and 1.04 are indicated.

7.1 Near Threshold Cross Section Dependence

Near thresholds cross sections have well defined collision energy dependencies, the *Wigner threshold laws* [91,92]. For fields small enough that the NH splitting does not exceed the centrifugal barrier height, the inelastic threshold behaviour as a function of energy and magnetic field can be understood in terms of a simple one-parameter formula, derived by Volpi and Bohn [93]

$$\sigma_{\alpha L\to\alpha' L'}(E,B) = \sigma_{\alpha\alpha'}^{LL'} E^{L-\frac{1}{2}} \left(E + \Delta m_j g \mu_B B\right)^{L'+\frac{1}{2}}, \tag{7.4}$$

where the factor $\sigma_{\alpha\alpha'}^{LL'}$ is independent of energy and magnetic field, $\Delta m_j g\mu_B B$ is the linear Zeeman shift with $\Delta m_j = m_j - m_j'$, g is the electron g-factor, and μ_B is the Bohr magneton.

The distorted-wave Born approximation (DWBA) [40,94] is in the first-order is a two-state perturbation theory applicable when the inelastic scattering is small compared to the elastic scattering. In the DWBA the integral for an off-diagonal K-matrix element depends on the *distortion* of the diagonal (elastic) scattering wavefunctions for the incoming $f(R)$

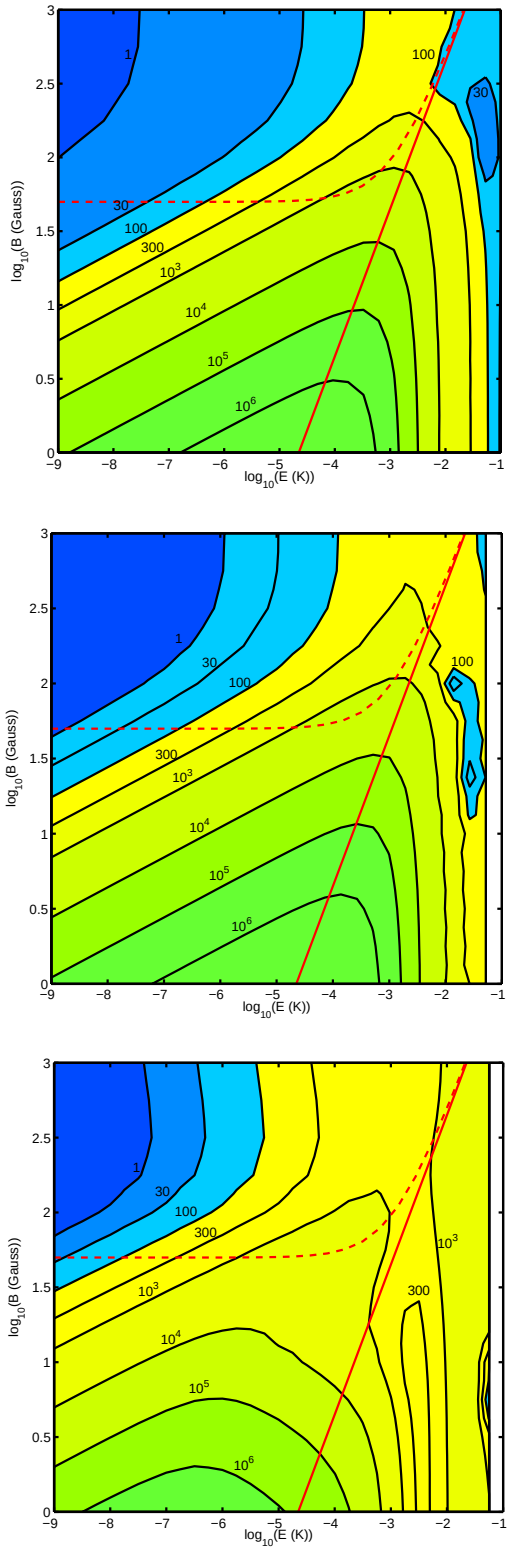

Figure 7.6: γ contour plots, including s, p, d, and f-wave partial cross sections, as a function of magnetic field and collision energy for different values of λ_{scl}. Top: The original $\lambda_{\text{scl}} = 1$ contour plot. Middle: Near resonant $\lambda_{\text{scl}} = 1.004$. Bottom: non-resonant $\lambda_{\text{scl}} = 1.04$. The red lines are as given in figure 7.4

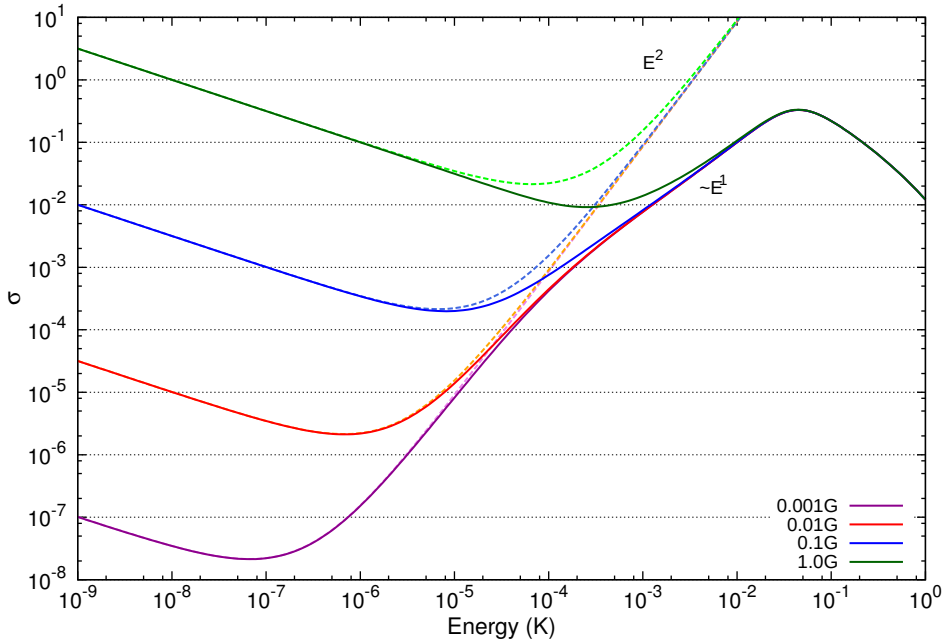

Figure 7.7: ($m_j = +1 L = 0 \rightarrow m_j = -1 L = 2$) inelastic cross sections (in Å^2) (solid lines) and their predicted profiles from (7.4) (dashed lines) as a function of collision energy for various small magnetic fields .

and outgoing $f'(R)$ channels, due to an off-diagonal coupling term $U_{\alpha L,\alpha' L'}$,

$$K_{\alpha L,\alpha' L'} = -\pi \int_0^\infty f(R) U_{\alpha L,\alpha' L'}(R) f'(R) dR. \tag{7.5}$$

If the collision energy and magnetic field are small enough such that the energy in the outgoing channel does not exceed the height of its centrifugal barrier the wavefunctions $f(R)$ and $f'(R)$ can be approximated by the small-argument limit of spherical Bessel functions,

$$\begin{aligned} f(R) &\propto \sqrt{k} j_L(kR) \propto (kR)^{L+1/2}, \\ f'(R) &\propto \sqrt{k'} j_{L'}(k'R) \propto (k'R)^{L'+1/2}, \end{aligned} \tag{7.6}$$

where k and k' are the incident and final wavevectors ($E = \hbar^2 k^2 / 2\mu$) and L and L' are the incident and final partial waves. The energy dependence of the K-matrix element is thus

$$K_{\alpha L,\alpha' L'} \propto k^{L+1/2} k'^{L'+1/2}. \tag{7.7}$$

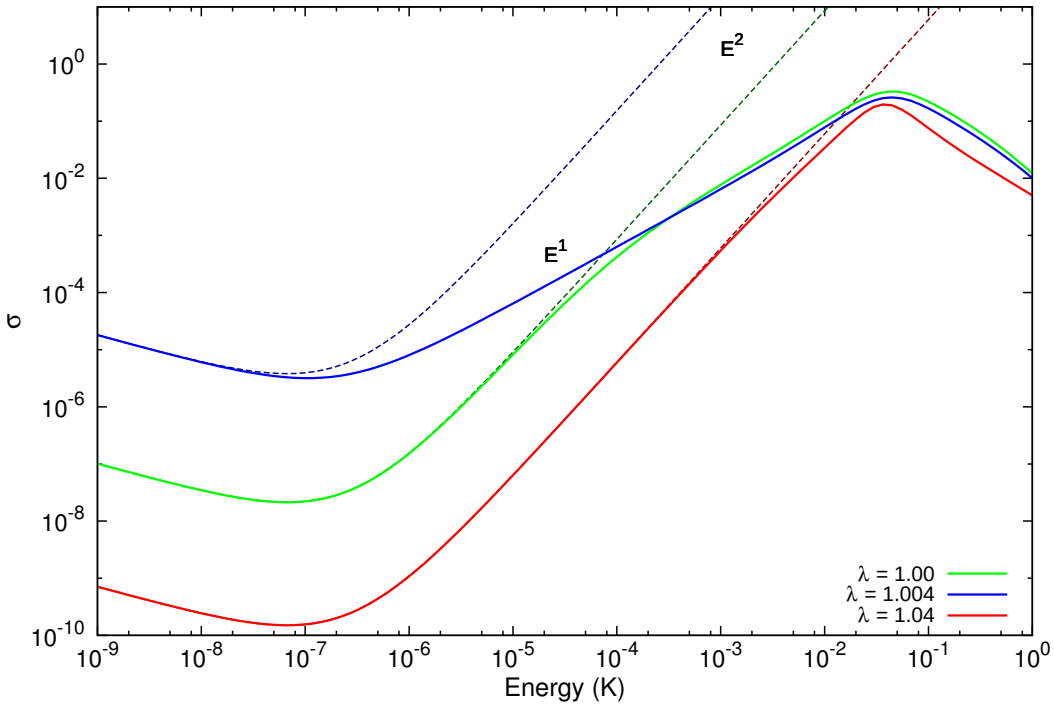

Figure 7.8: ($m_j = +1L = 0 \rightarrow m_j = -1L = 2$) inelastic cross sections (in Å^2) (solid lines) and their predicted profiles from (7.4) (dashed lines) as a function of collision energy at a magnetic field of 0.001 G for the scaled potentials: $\lambda_{\mathrm{scl}} = 1.004$ (near resonant), $\lambda_{\mathrm{scl}} = 1.04$ (far from resonant), and $\lambda_{\mathrm{scl}} = 1$ (original potential).

Relating the K-matrix to the cross section gives

$$\sigma_{\alpha L\to\alpha' L'} \propto k^{-2}k^{2L+1}k'^{2L'+1}$$
$$\sigma_{\alpha L\to\alpha' L'}(k,k') = \left(\frac{\hbar^2}{2\mu}\right)^{L+L'} \sigma^{LL'}_{\alpha\alpha'}k^{2L-1}k'^{2L'+1}, \tag{7.8}$$

and thus

$$\sigma_{\alpha L\to\alpha' L'}(E,B) = \sigma^{LL'}_{\alpha\alpha'}E^{L-\frac{1}{2}}\left(E+\Delta m_j g\mu_B B\right)^{L'+\frac{1}{2}}.$$

For the ($L = 0 \to 2$) process; when the collision energy is less than the Zeeman shift ($\Delta m_j g\mu_B B$) $E^{L-1/2}$ will dominate and the s-wave cross section is proportional to $E^{-1/2}$. For higher collision energies, the second term in (7.7) also contributes and cross section will go as E^2. Figure 7.7 shows the inelastic $|m_j = +1, L = 0\rangle \to |m_j = -1, L = 2\rangle$ cross section for the original ($\lambda_{\rm scl}$) potential, as a function of collision energy for various small magnetic fields compared to the single-parameter formula (7.4). It can be seen that at energies around 10^{-5}K the cross sections deviate from the predicted E^2 dependence and display an approximate E^1 dependence.

Examining the threshold behaviour for a near resonant scaled potential ($\lambda_{\rm scl} = 1.004$) and a far from resonant scaled potential ($\lambda_{\rm scl} = 1.04$), figure 7.8 shows the $\lambda_{\rm scl} = 1$, 1.004, and 1.04 cross sections as a function of energy at a magnetic field of 0.001 G. It can been seen that away from resonance the cross section closely follows the form of (7.4) displaying a clear E^2 dependence and that near a resonance (7.4) fails to describe cross section behaviour with a clear E^1 behaviour. The original potential $\lambda_{\rm scl} = 1$ lies somewhere in between the near and far from resonant cases, with the behaviour switching from E^2 to E^1.

The discrepancy between (7.4) and the cross sections can be understood by examining the approximations made. It was assumed that the wavefunctions $f(R)$ and $f'(R)$ could be approximated by the small argument limit of spherical Bessel functions which are the solutions of the free-particle ($V(R,\theta) = 0$) radial Schrödinger equation,

$$\left[\frac{d^2}{dR^2} + k^2 - \frac{L(L+1)}{R^2}\right] f(R) = 0. \tag{7.9}$$

In reality $V(R,\theta) \neq 0$ and the centrifugal barrier has a finite width, thus when a quasi-boundstate behind the barrier occurs close to the collision energy resonance effects will occur and the approximation that $f(R)$ has the form of a spherical Bessel function will

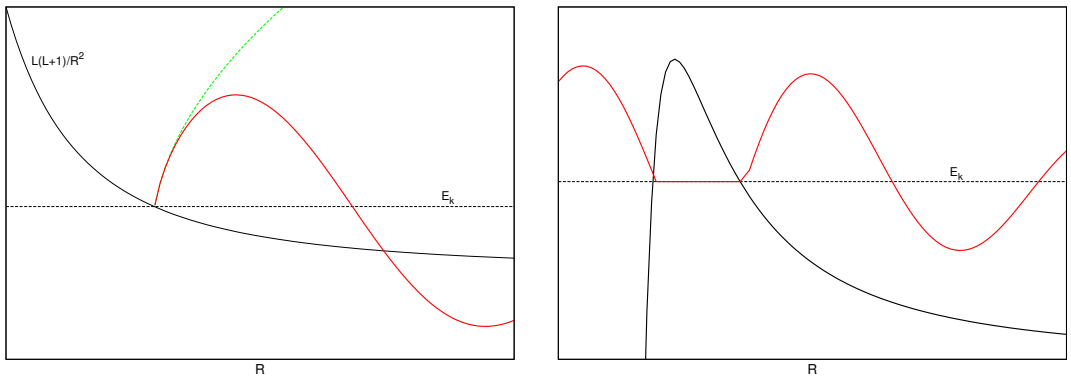

Figure 7.9: Left: Schematic diagram of the small argument limit of a spherical Bessel function which is applicable for small collision energies far away from resonance, the Bessel function is shown in red and the small argument limit in green. Right: If a quasi-bound state exists behind the centrifugal barrier at an energy close to the collision energy E_k the scattering wavefunction can no longer be approximated by the small argument limit of a Bessel function.

break down. Figure 7.9 shows schematic diagrams of the free-particle Bessel function situation and the situation in which a quasi-boundstate occurs behind the centrifugal barrier.

Although (7.4) breaks down near a resonance, it offers the hope that the field dependence of the near threshold cross sections can be found by performing only one field-free calculation to evaluate the constant $\sigma_{\alpha\alpha'}^{LL'}$. This would allow the field dependence to be understood in systems that are to large for full coupled channel calculations to be performed at a large number of points for example in molecule+molecule collisions. A more complete analysis of the near threshold cross section dependence that includes resonance effects can be obtained from a multichannel quantum defect theory (MQDT) approach.

Chapter 8

Multichannel Quantum Defect Theory

Quantum defect theory was initially developed to describe atoms in Rydberg states, in which an electron moves predominately outside of an ion core under the influence of a simple coulomb potential. As the time spent by the electron in the region of the ionic core is relatively small, its effect on the electron motion can be characterized by only a few quantum-defect theory (QDT) parameters. For the simplest case of an electron moving in an attractive Coulomb potential z/R the energy eigenvalues are

$$E_n = -\frac{1}{2}\frac{z^2}{n^2}, \tag{8.1}$$

where n is an integer. For a modified potential $V(R)$, containing an ionic core of finite size that asymptotically tends to the Coulomb form, the energy eigenvalues can be expressed in terms of an effective quantum number ν_n

$$E_n = -\frac{1}{2}\frac{z^2}{\nu_n^2}, \tag{8.2}$$

where the quantum defect $\mu_n = n - \nu_n$ provides a measure of the difference of $V(R)$ from z/R and is a slowly varying function of energy [95]. The techniques developed to separate the scattering problem into the short-range (ionic core) and long-range (Coulomb) regions have been developed into a more general multi-channel quantum defect theory (MQDT) for atomic collisions, in which atoms spend most of there time in the long-range $-C_n/R^n$ part of the potential and a short time in the short-range chemically bonding region of the potential. The MQDT presented here follows that developed by Mies and Julienne [96–98] and is presented predominantly for a potential with a long-range van der Waals form, $-C_6/R^6$.

In the channel state representation the total wavefunction for a total of N_T channels can be written as

$$\Psi_i(E;\boldsymbol{r},\boldsymbol{R}) = \sum_j^{N_T} \psi_j(\boldsymbol{r},\boldsymbol{R}) F_{ji}(E;\boldsymbol{R})/\boldsymbol{R}, \tag{8.3}$$

where the channel states $\{\psi_j(\boldsymbol{r},\boldsymbol{R})\}$ are a set of N_T electronic-rotational states that are explicit functions of the electronic $\boldsymbol{r}$ and internuclear $\boldsymbol{R}$ coordinates. This expansion generates a set coupled equations for the radial functions $F_{ji}(E;\boldsymbol{R})$,

$$\left[-\frac{\hbar^2}{2\mu}\frac{\partial^2}{\partial R^2} - E\right] F_{ji} + \sum_k W^{\infty}_{jk} F_{ki} = 0. \tag{8.4}$$

The interaction matrix $W^{\infty}_{ji}(\boldsymbol{R})$ is obtained from the total Hamiltonian,

$$W^{\infty}_{ji}(\boldsymbol{R}) - \frac{\hbar^2}{2\mu R}\frac{\partial^2}{\partial R^2} R\delta_{ji} = \langle \psi_j \mid \hat{H} \mid \psi_i \rangle, \tag{8.5}$$

and obeys the asymptotic condition,

$$W^{\infty}_{ji}(\boldsymbol{R}) \xrightarrow[R\to\infty]{} \left[E^{\infty}_i + \frac{\hbar^2 L(L+1)}{2\mu R^2}\right]\delta_{ji} + O(\boldsymbol{R}^{-3}). \tag{8.6}$$

The coupled equations (8.4), yield N_T solution vectors that vanish as $R \to 0$, forming a $(N_T \times N_T)$ matrix of radial functions $\mathbf{F}(E,\boldsymbol{R})$ that define N_T independent solutions of the total Hamiltonian. If there are N_o open and N_c closed channels such that $N_T = N_\mathrm{o} + N_\mathrm{c}$, the number of well behaved normalizable solutions is N_o, and the physically meaningful set of radial solutions is an $(N_T \times N_\mathrm{o})$ matrix. Similarly the S-matrix is reduced from a $(N_T \times N_T)$ when all channels are open to a $(N_\mathrm{o} \times N_\mathrm{o})$ matrix as channels become closed.

The philosophy of multichannel quantum defect theory (MQDT) is to obtain an energy insensitive quantum-defect matrix $\mathbf{Y}(N_T \times N_T)$ which is an entire function of E such that it can be analytically continued across threshold as the number of open and closed channels change. Thus, given exact solutions of the coupled equations (8.4) at a number of energies above threshold such that $N_T = N_\mathrm{o}$, $\mathbf{Y}(N_T \times N_T)$ can be obtained. Exact relationships developed in the framework of MQDT can then be used to obtain $S_{\mathrm{oo}}(N_\mathrm{o} \times N_\mathrm{o})$ below threshold when a subset of N_c channels become closed [96].

8.1 Single Channel Theory

MQDT is not a unique theory and a reference potential $\mathcal{V}_i(R)$ is assigned to each channel. The reference potential needs to reproduce the asymptotic form of the real potential,

$$\mathcal{V}_i(R) \xrightarrow[R\to\infty]{} E_i^\infty + \frac{\hbar^2 L(L+1)}{2\mu R^2} + O(R^{-3}), \tag{8.7}$$

but other than that it is arbitrary and can be chosen to simplify problems. The following analysis assumes that $\mathcal{V}_i(R)$ is attractive and supports a number of bound states, and that there is a classically accessible region for each channel, such that an *effective channel wave number*

$$K_i(E,R) = \sqrt{2\mu[E-\mathcal{V}_i(R)]}/\hbar, \tag{8.8}$$

is real and positive. For an open channel with $E > E_i^\infty$, this region extends from an inner turning point $R = a$, where $K_i(E,a) = 0$ to $R = \infty$. For a closed channel, $E < E_i^\infty$ there is a finite region with an outer turning point $R = b$ defined at $K_i(E,b) = 0$ where $b > a$. For $R > b$, $K_i(E,R)$ is purely imaginary approaching $i|k_i|$ as $R \to \infty$, where $k_i = \sqrt{2\mu[E-E_i^\infty]}/\hbar$ is the *channel wave number*.

As the choice of channel reference potential only needs to meet the asymptotic conditions (8.7), the obvious choice for the single channel case is $\mathcal{V}_i(R) = W_{ii}(R)$, which reduces the coupled channel equation (8.4) to

$$\left[-\frac{\hbar^2}{2\mu}\frac{\partial^2}{\partial R^2} - E + \mathcal{V}_i(R)\right]F_i(R) = \left[\frac{\partial^2}{\partial R^2} + K_i^2(E,R)\right]F_i(R) = 0. \tag{8.9}$$

Above threshold ($E > E_i^\infty$) two independent solutions of (8.9) normalized at long-range are

$$\begin{aligned} f_i(E,R) &\xrightarrow[R\to\infty]{} k_i^{-1/2}\sin(k_iR - L\pi/2 + \xi_i(E)) \\ g_i(E,R) &\xrightarrow[R\to\infty]{} k_i^{-1/2}\cos(k_iR - L\pi/2 + \xi_i(E)), \end{aligned} \tag{8.10}$$

where ξ_i is the scattering phase shift associated with the reference potential, that yields the elastic scattering cross section

$$\sigma_i(E) = \frac{4\pi}{k_i^2}(2L+1)\sin^2\xi_i(E). \tag{8.11}$$

Below threshold f_i and g_i become asymptotically divergent and to allow calculation of bound states the well-behaved function,

$$\phi_i(E,R) \xrightarrow[R\to\infty]{} \frac{e^{-|k_i|R}}{2\sqrt{|k_i|}}, \tag{8.12}$$

is defined.

In MQDT the aim is to find a set of solutions to the coupled channel equations that can be analytically continued across threshold and although the three functions f_i, g_i, and ϕ_i, all satisfy (8.9), they are non-analytic at $E = E_i^\infty$ due to the boundary conditions imposed at $R \to \infty$. Thus we need to find an additional pair of independent solutions $\hat{f}_i$, $\hat{g}_i$, that are analytic across threshold.

8.2 WKB formulation

Before examining the addition pair of MQDT functions required to be analytic across threshold, we first need to examine the semi-classical WKB approximation. In the WKB method we search for a solution of the time-independent Schrödinger equation,

$$\frac{d^2}{dR^2}\psi(R) = \frac{2\mu}{\hbar^2}(V(R) - E)\psi(R), \tag{8.13}$$

of the form

$$\psi(R) = A(R)\exp\left[\frac{i}{\hbar}B(R)\right]. \tag{8.14}$$

Substitution of this wavefunction into the Schrödinger equation results in

$$\left(A'' - \frac{A(B')^2}{\hbar^2} + \frac{i}{\hbar}(2A'B' + AB'')\right)e^{iB/\hbar} = \frac{2\mu}{\hbar^2}\left(V(R) - E\right)Ae^{iB/\hbar}. \tag{8.15}$$

Collecting like terms gives

$$2A'B' = -AB'', \tag{8.16}$$

which has solutions $A = \text{const} \times (B')^{-1/2}$ and

$$\hbar^2 A'' - A(B')^2 = 2\mu\left(V(R) - E\right)A, \tag{8.17}$$

solutions of which can approximated semi-classically ($\hbar \to 0$) [41] as

$$B = \pm\int^R \sqrt{2\mu\left(E - V(R')\right)}dR'. \tag{8.18}$$

The WKB wavefunction is thus

$$\psi^{\mathrm{WKB}}(R) = K^{-1/2} \exp\left[\pm i \int^{R} K(R) dR'\right], \tag{8.19}$$

where $K = \sqrt{2\mu\,(V(R') - E)}/\hbar$. Due to the semi-classical approximation made the WKB wavefunction is valid in regions in which the potential changes slowly over a distance comparable to the wavelength.

Assuming a van der Waals potential, a characteristic potential length [99],

$$R_{\mathrm{vdW}} = \frac{1}{2}\left(\frac{2\mu C_6}{\hbar^2}\right)^{1/4}, \tag{8.20}$$

and an average scattering length, first introduced by Gribakin and Flambaum [100],

$$\bar{a} = 4\pi/\Gamma(1/4)^2 R_{\mathrm{vdW}} \approx 0.956\ldots R_{\mathrm{vdW}}, \tag{8.21}$$

can be defined, corresponding to the scaled energies $E_{\mathrm{vdW}} = \hbar^2/(2\mu R_{\mathrm{vdW}}^2)$ and $\bar{E} = \hbar^2/(2\mu\bar{a}^2)$. For distances $R > R_{\mathrm{vdW}}$ the potential takes on its asymptotic van der Waals form

$$V(R) = \frac{\hbar^2 L(L+1)}{2\mu R^2} - \frac{C_6}{R^6}, \qquad R > R_{\mathrm{vdW}}. \tag{8.22}$$

The scaled energy E_{vdW} and distance R_{vdW}, can be used to give an idea of the form of the scattering wavefunction. For collision energies $E \ll E_{\mathrm{vdW}}$, the wavefunction in the long-range region $R > R_{\mathrm{vdW}}$ is characterized by a large local de Broglie wavelength $2\pi/K$ oscillating slowly with R. In the short-range chemical bonding region $R < R_{\mathrm{vdW}}$, the colliding particles are accelerated by the potential, the energy becomes much greater than E_{vdW} and the local de Broglie wavelength becomes small, the wavefunction oscillates rapidly, and it can be approximated semi-classically.

The short-range, near threshold bound and scattering wavefunctions have, with an appropriate short-range normalization, a common amplitude and phase. Thus a pair of short-range normalized semi-classical WKB wavefunctions $\hat{f}_i(E,R)$ and $\hat{g}_i(E,R)$ that are analytic across threshold can be defined at energies that exceed the reference potential minimum $E > \mathcal{V}_i(R_e)$. Due to the short de Broglie wavelength in this region the approximation that $\hat{f}_i(E,R)$ and $\hat{g}_i(E,R)$ have the semi-classical WKB-like phase-amplitude form $\hat{f}_i = A_i(R,E)\sin B_i(R,E)$ is an excellent one, where $A_i^{\mathrm{WKB}}(R,E) = c/K_i(R,E)^{1/2}$ and

$$B_i^{\mathrm{WKB}} = \int^{R} K_i(R',E) dR'. \tag{8.23}$$

The WKB wavefunctions are valid in regions in which the local de Broglie wavelength varies slowly with distance. Thus at energies well above threshold the WKB functions are a good approximation over the whole range of R and $\hat{f}(E,R) = f(E,R)$. However as the collision energy approaches threshold, the energy in the long-range region becomes $E < E_{\rm vdW}$ and the WKB solutions fail to go smoothly to the long range and further MQDT parameters are required to connect the short-range $\hat{f}_i(E,R)$ and $\hat{g}_i(E,R)$ functions to the long-range normalized functions f_i, g_i, and ϕ_i, that have the correct asymptotic form,

$$f_i(E,R) = C_i^{-1}(E)\hat{f}_i(E,R), \qquad E \geq E_i^\infty \tag{8.24}$$

$$g_i(E,R) = C_i(E)\left[\hat{g}_i(E,R) + \tan\lambda_i(E)\hat{f}_i(E,R)\right], \qquad E \geq E_i^\infty \tag{8.25}$$

$$\phi_i(E,R) = \mathcal{N}_i(E)\left[\cos\upsilon_i(E)\hat{f}_i(E,R) - \sin\upsilon_i(E)\hat{g}_i(E,R)\right], \qquad E \leq E_i^\infty. \tag{8.26}$$

The two-parameters $C_i^{-1}(E)$ and $\tan\lambda_i(E)$ defined above threshold thus contain the full threshold behaviour as $E \to E_i^\infty$, with the limiting values well above threshold

$$C_i^{-1}(E) \xrightarrow[E\gg E_i^\infty]{} 1 \tag{8.27}$$

$$\tan\lambda_i(E) \xrightarrow[E\gg E_i^\infty]{} 0, \tag{8.28}$$

and for a van der Waals potential have the following threshold behaviour [101] for $L = 0$

$$C_i^{-2}(E) \xrightarrow[E\to E_i^\infty]{} k\bar{a}\left(1 + \left(\frac{a}{\bar{a}} - 1\right)^2\right) \tag{8.29}$$

$$\tan\lambda_i(E) \xrightarrow[E\to E_i^\infty]{} 1 - \frac{a}{\bar{a}}. \tag{8.30}$$

$C_i^{-1}(E)$ modifies the amplitude of $\hat{f}_i$ and $\hat{g}_i$ and $\tan\lambda_i(E)$ relates the relative phases of $\hat{f}_i$ and $\hat{g}_i$. For an attractive potential that supports bound states, υ_i is a continuous energy dependent phase can be defined below threshold such that modular values of π correspond to the potential eigenvalues, $\upsilon_i(E_{i,n}) = n\pi$. $\upsilon_i(E)$ can be interpolated from the eigenvalues except near threshold when accurate WKB techniques can be used.

8.3 Multichannel formulation

Asymptotically the coupled channel radial functions $F(E,R)$ become

$$\mathbf{F}(E,R) = \mathbf{J}(E,R) + \mathbf{N}(E,R)\mathbf{K}(E), \tag{8.31}$$

and can always be expressed in the form

$$\mathbf{F}(E,R) = \left[\hat{\mathbf{f}}(E,R) + \hat{\mathbf{g}}(E,R)\mathbf{Y}(E)\right]\hat{\mathbf{A}}, \tag{8.32}$$

where $\mathbf{Y}$ acts a short-range normalized K-matrix and $\hat{\mathbf{f}}(E,R) \equiv \hat{f}_i(E,R)\delta_{ij}$ and $\hat{\mathbf{g}}(E,R) \equiv \hat{g}_i(E,R)\delta_{ij}$. The matrix $\hat{\mathbf{A}}$ effects the normalization of the radial function and would be required to evaluate the expectation function of the total wavefunction. However all the scattering dynamics are contained in the R independent $\mathbf{Y}$-matrix and thus there is no need to evaluate $\hat{\mathbf{A}}$. When all channels are open well above threshold (8.32) can be equivalently expressed as

$$\mathbf{F}(E,R) = \left[\mathbf{f}(E,R) + \mathbf{g}(E,R)\mathcal{R}(E)\right]\mathbf{A}, \tag{8.33}$$

which can be related to (8.31) to give

$$\mathbf{S}(E) = e^{i\xi(E)}\left[\mathbf{I} + i\mathcal{R}(E)\right]\left[\mathbf{I} - i\mathcal{R}(E)\right]^{-1} e^{i\xi(E)}, \tag{8.34}$$

where $e^{i\xi(E)}$ is a diagonal matrix with elements $e^{i\xi_i(E)}\delta_{ij}$.

Although $\mathcal{R}(E)$ is non-analytic across threshold $\mathbf{Y}(E)$ can be obtained by relating (8.32) and (8.33) resulting in,

$$\mathcal{R}(E) = \mathbf{C}^{-1}\left[\mathbf{Y}^{-1}(E) - \tan\lambda\right]^{-1}\mathbf{C}^{-1}, \tag{8.35}$$

where $\mathbf{C}^{-1}$ and $\tan\lambda$ are diagonal matrices with elements $C_i^{-1}(E)\delta_{ij}$ and $\tan\lambda_i(E)\delta_{ij}$. Away from threshold $\mathbf{C}^{-1} = 1$, $\tan\lambda = 0$ and thus $\mathbf{Y}(E) = \mathcal{R}(E)$.

In the distorted-wave Born approximation for weak inelasticity, the off-diagonal transition matrix elements [94] are given by

$$T_{ij} = 2e^{i(\xi_i+\xi_j)}\int f_i(E,R)U_{ij}f_j(E',R)dR, \tag{8.36}$$

where E' is the energy in the outgoing channel j. In the MQDT framework the channel wavefunctions f_i in the DWBA can be replaced by the short-range normalized reference functions $\hat{f}_i$,

$$T_{ij} = 2e^{i(\eta_i+\eta_j)}C_i^{-1}(E)C_j^{-1}(E')\int \hat{f}_i(E,R)U_{ij}\hat{f}_j(E',R)dR. \tag{8.37}$$

The inelastic cross section is thus

$$\sigma_{i\to j}(E,E') = \frac{\pi}{k_i^2}|T_{ij}|^2 = \frac{4\pi A^2}{k_i^2}C_i^{-2}(E)C_j^{-2}(E'), \tag{8.38}$$

where $A = \int \hat{f}_i(E,R)U_{ij}\hat{f}_j(E',R)dR$, is the MQDT short-range energy independent Y-matrix element.

The DWBA is only valid when the inelasticity caused by the off-diagonal T-matrix element is small. For more strongly coupled cases a two-channel model can be used analyze the T-matrix element [102]. In the two-channel case the MQDT **Y**-matrix has the form

$$\mathbf{Y} = \begin{pmatrix} Y_{11} & Y_{12} \\ Y_{12} & Y_{22} \end{pmatrix}, \tag{8.39}$$

which can be simplified by a judicious choice of reference potentials. Choosing the two reference potentials such that the scattering length of the reference potential is equal to the channel scattering length requires that $Y_{11} = Y_{22} = 0$, while the strength of the inter-channel coupling can be characterized by $Y_{12} \equiv A$. Substitution of

$$\mathbf{Y} = \begin{pmatrix} 0 & A \\ A & 0 \end{pmatrix}, \tag{8.40}$$

into (8.35) and relating to (8.34) gives the off-diagonal T-matrix element as

$$|T_{12}|^2 = |S_{12}|^2 = \frac{4A^2C_1^2C_2^2}{C_1^4C_2^4 + 2A^2C_1^2C_2^2(1 - C_1^2C_2^2t_1t_2) + A^4(1 + C_1^4t_1^4)(1 + C_2^4t_2^4)}, \tag{8.41}$$

where $C_i = C_i(E)$ and $t_i = \tan\lambda_i(E)$. For small A this reduces to the cross section expression (8.38).

8.4 Angular-momentum-insensitive quantum defect theory, AQDT

In Mg+NH it was seen that resonance effects caused the break down of the simple threshold dependence given by (7.4). We can use the separation of scales for $R > R_{\mathrm{vdW}}$ and $R < R_{\mathrm{vdW}}$ in MQDT to provide insight and approximations for the near threshold bound and scattering states in Mg+NH.

Gribakin and Flambaum [100] showed that for a van der Waals potential the energy of the highest s-wave bound state, just below threshold is given by

$$E_{\mathrm{bind}} = -\frac{\hbar^2}{2\mu(a_s - \bar{a})^2}, \tag{8.42}$$

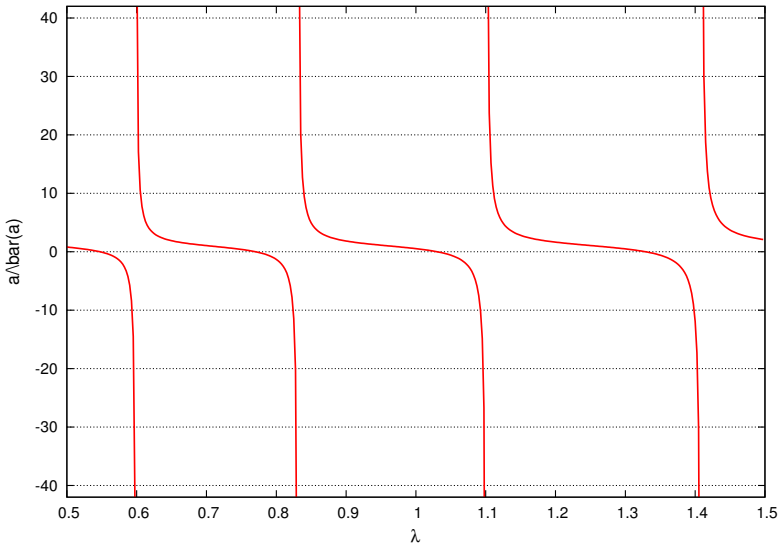

Figure 8.1: The single channel s-wave scattering length as a function of the potential scaling factor λ_{scl}, each time a bound state occurs at threshold the scattering length exhibits a pole. Calculated with the single Mg-NH $|n = 0, m_s = +1, L = 0\rangle$ channel.

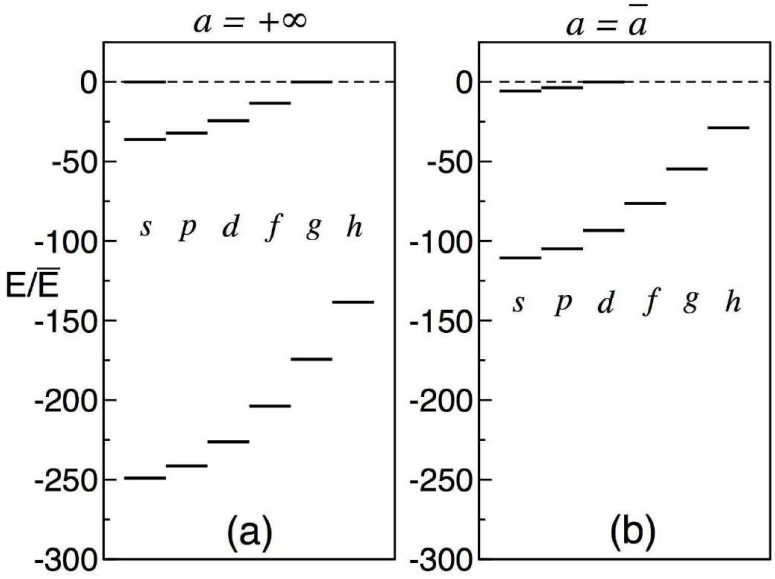

Figure 8.2: AQDT bound state energies for partial waves $L = 0 \ldots 5$ for (a) $a = \pm\infty$ and (b) $a = \bar{a}$. Image from [103].

and the s-wave scattering length follows

$$\frac{a_s}{\bar{a}} = 1 - \tan\left(\Phi - \frac{\pi}{8}\right), \tag{8.43}$$

where,

$$\Phi = \int_{R_0}^{\infty} \sqrt{-2\mu V(R')}/\hbar dR' \tag{8.44}$$

is evaluated at threshold. Thus as the potential is scaled by $\lambda_{\rm scl}$, the scattering length goes through a pole every time an s-wave bound state occurs at threshold. As $\Phi \propto \sqrt{\lambda_{\rm scl}}$, if the potential supports n_b bound states a change in the potential by two parts in n_b will be enough to take the scattering length through a full cycle, from one pole to the next. Figure 8.1 shows the single channel s-wave scattering length as a function of $\lambda_{\rm scl}$ for the single Mg-NH $|n = 0, m_s = +1, L = 0\rangle$ channel.

In the short-range region the rotational energy is small compared to the depth of the electronic potential and the radial wavefunctions are nearly independent of L, with this in mind short-range reference solutions and hence a short-range QDT-matrix can be formulated to be independent of L. Bo Gao [103–110] has derived analytic solutions of the Schrödinger equation for an attractive van der Waals potential and from which has developed an angular momentum independent quantum defect theory (AQDT) approach for van der Waals potentials.

Considering the radial Schrödinger equation

$$\left[\frac{d^2}{dR^2} - \frac{L(L+1)}{R^2} + \frac{\beta_6^4}{R^6} + k^2\right] u_{k,L}(R) = 0, \tag{8.45}$$

where $\beta \equiv (2\mu C_6/\hbar^2)^{1/4}$ and $k^2 = 2\mu E/\hbar^2$. A pair of linearly-independent short-range reference solutions to (8.45) can be defined for energies both above and below threshold as

$$\hat{f}^c_{k,L} \xrightarrow[R\ll\beta_6]{} (2/\pi)^{1/2}(R/\beta_6)\sqrt{R}\cos(y - \pi/4) \tag{8.46}$$

$$\hat{g}^c_{k,L} \xrightarrow[R\ll\beta_6]{} -(2/\pi)^{1/2}(R/\beta_6)\sqrt{R}\sin(y - \pi/4), \tag{8.47}$$

where $y = (R/\beta_6)^{-2}/2$. This pair of solutions is not only energy-insensitive but also angular-momentum independent. In the long-range region the solution to (8.45) can be written as the linear combination

$$u_{k,L}(R) = A_{k,L}\left[\hat{f}^c_{k,L} - K^c\hat{g}^c_{k,L}\right] \tag{8.48}$$

where K^c is the short-range K-matrix, and above threshold ($E > E_i^\infty$) $\hat{f}^c$ and $\hat{g}^c$ have the following asymptotic behaviour

$$\hat{f}^c_{k,L} \xrightarrow[R\to\infty]{} \sqrt{\frac{2}{\pi k}}\left[Z^c_{ff}\sin(kR - L\pi/2) - Z^c_{fg}\cos(kR - L\pi/2)\right] \tag{8.49}$$

$$\hat{g}^c_{k,L} \xrightarrow[R\to\infty]{} \sqrt{\frac{2}{\pi k}}\left[Z^c_{gf}\sin(kR - L\pi/2) - Z^c_{gg}\cos(kR - L\pi/2)\right], \tag{8.50}$$

where the Z-matrix elements contain the analytic solutions to the $1/R^6$ Schrödinger equation first defined by Gao in [104]. The pair of short-range reference solutions can now be related to the long-range normalized solutions of (8.45)

$$f_{k,L} \xrightarrow[R\to\infty]{} \sqrt{\frac{2}{\pi k}}\sin(kR - L\pi/2) \tag{8.51}$$

$$g_{k,L} \xrightarrow[R\to\infty]{} -\sqrt{\frac{2}{\pi k}}\cos(kR - L\pi/2), \tag{8.52}$$

resulting in the matrix equation

$$\begin{pmatrix} \hat{f}^c \\ \hat{g}^c \end{pmatrix} = \begin{pmatrix} Z^c_{ff} & Z^c_{fg} \\ Z^c_{gf} & Z^c_{gg} \end{pmatrix}\begin{pmatrix} f \\ g \end{pmatrix}. \tag{8.53}$$

The full scattering K-matrix, can now be expressed in terms the short-range K-matrix; K^c, and Z-matrix elements

$$K_L \equiv \tan\delta_l = (K^c Z^c_{gg} - Z^c_{fg})^{-1}(Z^c_{ff} - K^c Z^c_{gf}). \tag{8.54}$$

The shape of the centrifugal barrier for $L > 0$ is determined by the long-range part of the potential, and thus the tunneling through it and the form of the shape resonance is fully embedded within the analytic Z-matrix functions. It is important to note that the AQDT formulation is fully valid at energies below threshold ($E < E_i^\infty$) with a corresponding W-matrix, analogous to the Z-matrix, defined from the analytic solutions of the $1/R^6$ Schrödinger equation, details of which can be found in the literature, and that this formulation of MQDT is especially useful for strong long-range potentials, in which the energy-dependencies near threshold are dominated by the long-range interaction for all L.

The power of AQDT is that given just C_6, μ, and a_s the near threshold bound and scattering states can be approximated very accurately. Figure 8.2 shows the near threshold bound states calculated with AQDT, for $a_s = \infty$ and $\bar{a}$. At $a_s = \infty$ a bound state exists at

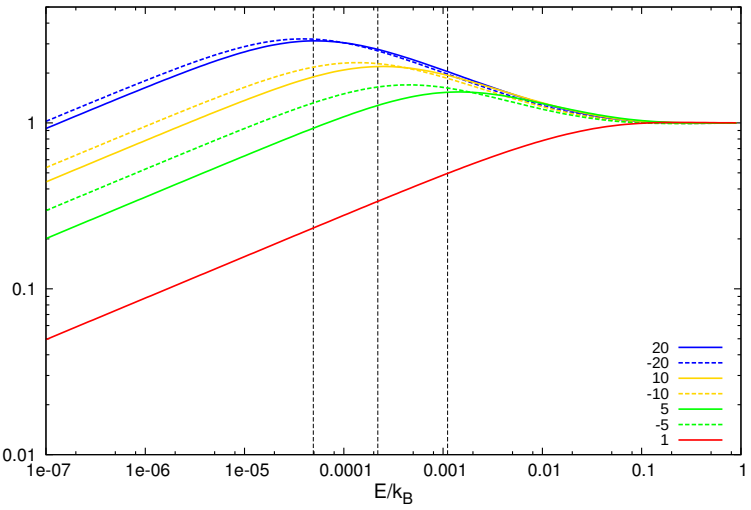

Figure 8.3: AQDT $C^{-1}_{L=0}(E)$ functions for various values of $a_s/\bar{a}$. The location of lowest s-wave bound states $E_{-1} = -\hbar/2\mu(a_s - \bar{a})^2$ for $a_s/\bar{a} = 5$, 10, and 20 are given.

threshold, however the rotational progression also gives $L = 4, 8, \ldots$ partial-wave bound states at threshold and at $a_s = \bar{a}$ an $L = 2$, d-wave bound state exists at threshold.

The MQDT parameters $C^{-2}_L(E)$ and $\tan\lambda_L(E)$ can also be calculated within the AQDT framework. Gao has written a set of $C++$ routines that calculate all the AQDT parameters including $C^{-2}_L(E)$ and $\tan\lambda_L(E)$ for any given C_6, μ, and a_s [111], which was supplied with a FORTRAN wrapper by Paul Julienne. For Mg+NH; C_6=158 $E_{\rm H}a_0^6$, μ = 9.23268 u, and $\bar{a}$ = 12.15 Å, AQDT $C^{-1}_{L=0}$ functions calculated at various values of $a_s/\bar{a}$ are shown in figure 8.3. The energy of the highest bound state $E_{-1} = -\hbar/2\mu(a_s - \bar{a})^2$ have also been plotted for $a_s/\bar{a} = 5$, 10, and 20. It can bee seen that when $a_s/\bar{a} = 1$ the channel is non-resonant, however when $a_s/\bar{a} \neq 1$ a peak occurs in the $C^{-1}_{L=0}(E)$ function when $E = E_{-1}$. As C^{-1} maps the amplitude of the short-range function $\hat{f}$ to the long-range function f a peak in C^{-1} corresponds to an enhancement of the wave function in short-range due to the near-threshold bound state.

8.5 MgNH

The full coupled channel Mg-NH s-wave scattering length is shown in figure 8.4 as a function of $\lambda_{\rm scl}$ at an energy of 10^{-6}K and a magnetic field of 10G. To classify the resonances present in figure 8.4, the zero-field $J = 1$ MgNH bound states have also been

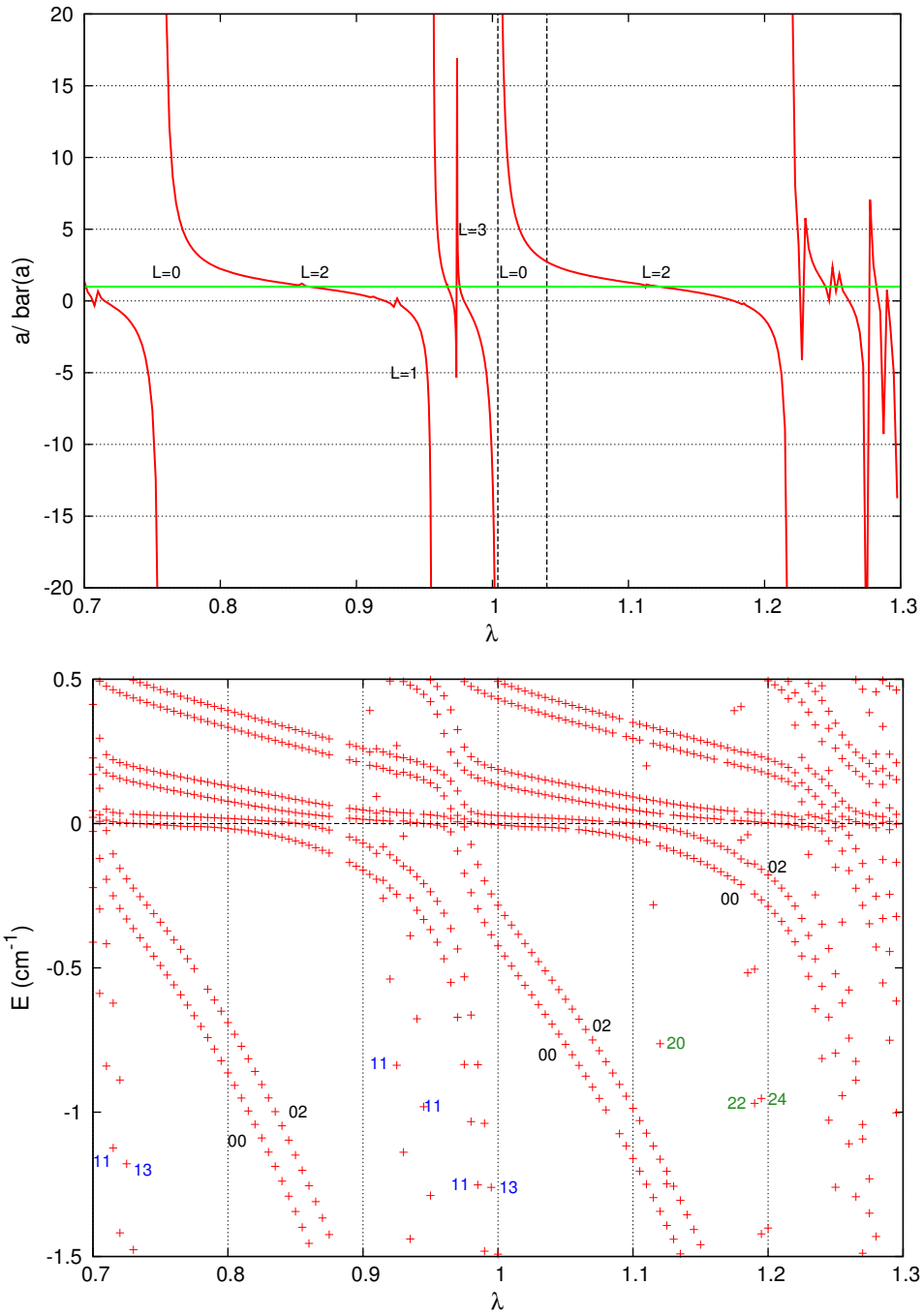

Figure 8.4: Top: Scaled $m_s = +1$ s-wave scattering length as a function of $\lambda_{\rm scl}$ at E=10^{-6}K and B=10G. $\lambda_{\rm scl} = 1.004$ and 1.04 are marked. Bottom: Zero-field $J = 1$ bound states as a function of $\lambda_{\rm scl}$, labeled by nL. From the bound state diagram partial waves can be assigned to each of the resonances in the s-wave scattering length. One the far right, a large number of $n = 1$ and 2 bound states cross threshold resulting in a complicated resonance pattern.

calculated near-threshold as a function of $\lambda_{\rm scl}$, as shown in figure 8.4, where $J = 1$ allows s-wave bound states to exist in the incident $n = 0, m_s = +1, L = 0$ channel. The resonances labeled $L = 0$ and 2 are shape resonances due to s and d-wave bound states that removed from the $n = 0$ potential well as the well depth decreases. It can be seen that d-wave resonances occur near $a = \bar{a}$ in concordance with the angular momentum independent formulation of MQDT. Resonances labeled by $L = 1$ and 3 are Feshbach resonances arising from $n = 1$, p and f-wave bound states being tuned across threshold as a function of $\lambda_{\rm scl}$. On the far right (deeper potential region) of figure 8.4, multiple $n = 1$ and 2 bound states cross threshold forming a complicated resonance structure.

Previously in chapter 7, energy dependent cross sections were shown for $\lambda_{\rm scl} = 1$, 1.004, and 1.04, it can be seen from figure 8.4 that the resonance effects are due to an s-wave shape resonance. To understand the threshold behaviour near the resonance an MQDT approach can be adopted and in regions in which equation (8.31) is valid, away from a Feshbach resonance at which point $\tan\lambda(E)$ can become large and the situation is not as simple [101]. With these limitations in mind the MQDT $C^{-2}(E)$ functions can be backed out of MOLSCAT.

8.5.1 Extraction of $C^{-2}(E)$ functions from MOLSCAT

Transforming the cross section to be a function of $k = \sqrt{2\mu E}/\hbar$ and k' rather than E and E',

$$\sigma_{\alpha,L\to\alpha',L'}(k,k') = 4\pi A^2 k^{-2} C_L^{-2}(k) C_{L'}^{-2}(k'). \tag{8.55}$$

Cross sections can be calculated as a function of k' by fixing k in the incoming channel and varying the magnetic field to vary k' in the outgoing channel, calculated cross sections are shown on the left of figure 8.5. For each fixed value of k,

$$C_{L'}^{-2}(k') \propto \sigma(k_{\rm fixed}, k'), \tag{8.56}$$

and as $C_L^{-2}(k) \to 1$ for large k, $\sigma(k_{\rm fixed}, k')$ can be normalized to 1 at large k' to give $C_L^{-2}(k')$, as shown on the right of figure 8.5, and a value for the ratio $k_{\rm fixed}^2/4\pi A^2 C_L^{-2}(k_{\rm fixed})$ can be obtained. Cross sections can now be calculated as a function of k for a fixed k' by fixing the energy in the outgoing channel and varying the magnetic field, as shown on the left of figure 8.6. As $k' \geq k$, there is a maximum value of k that can be calculated for each

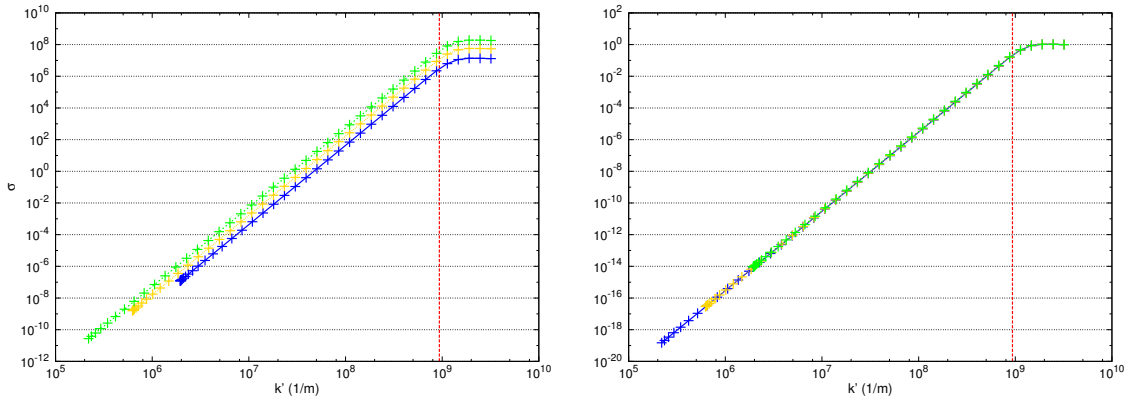

Figure 8.5: Left: Cross sections (in Å^2) as a function of k' for a fixed value of k_{fixed} = 1.95×10^5 (green), 6.17×10^5 (gold), and 1.95×10^6 (blue) m^{-1}. Right: $C_{L'}^{-2}(k')$, normalizing $k^2\sigma(k_{\text{fixed}}, k')$ for each k_{fixed} to 1 at large k' collapses each $k^2\sigma(k_{\text{fixed}}, k')$ onto $C_{L'}^{-2}(k')$. The cross section and $C_{L'}^{-2}(k')$ shown are for the process $|\, m_j = +1, L = 0\rangle \rightarrow |\, m_j = -1, L = 0\rangle$ at $\lambda = 1.004$, the vertical dashed-red line gives the height of the centrifugal barrier.

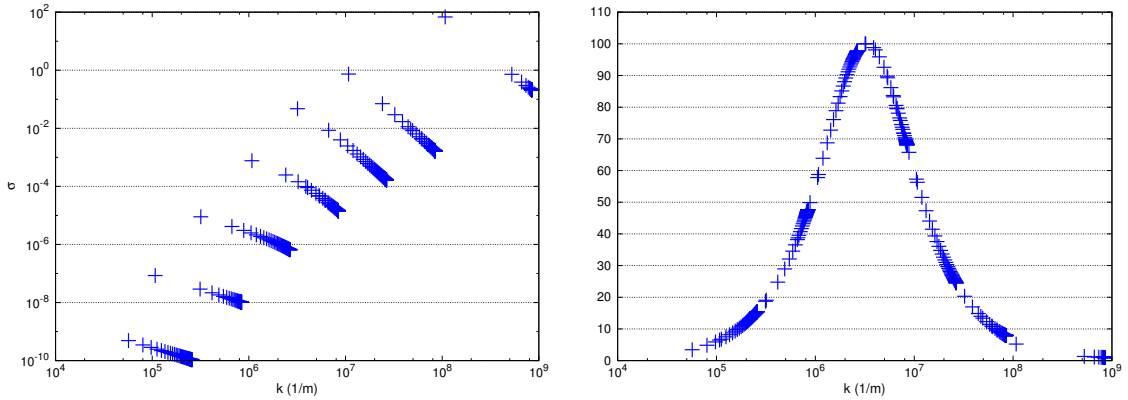

Figure 8.6: Left: Calculated cross section (in Å^2) as a function of k for various values of k'_{fixed}. Right: $C_{\text{L}}^{-2}(k)$ extracted by normalizing $k^2\sigma(k, k'_{\text{fixed}})/C_{L'}^{-2}(k'_{\text{fixed}})$ to 1 at large k. The cross sections and $C_L^{-2}(k)$ shown are for the process $|\, m_j = +1, L = 0\rangle \rightarrow |\, m_j = -1, L = 0\rangle$ at $\lambda = 1.004$.

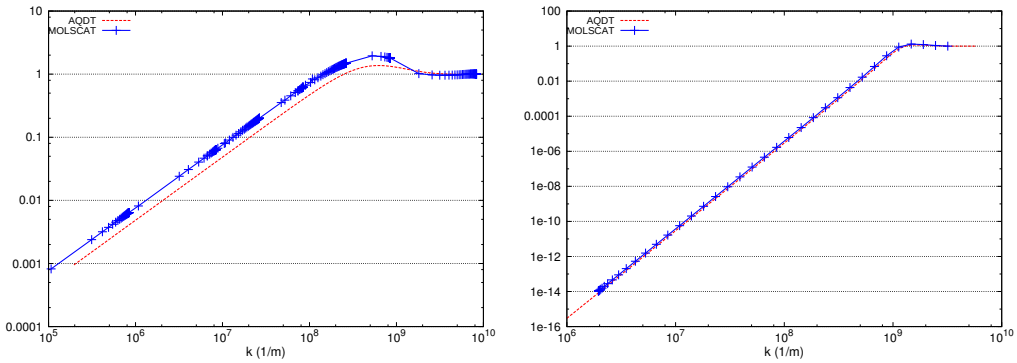

Figure 8.7: $C^{-2}(k)$ L=0 (left) and L=2 (right) functions from Gao's AQDT routines and those backed out of MOLSCAT for the non-resonant $\lambda_{\mathrm{scl}} = 1.04$. Energy given in terms of $k = \sqrt{2\mu E_i^{\infty}}/\hbar$.

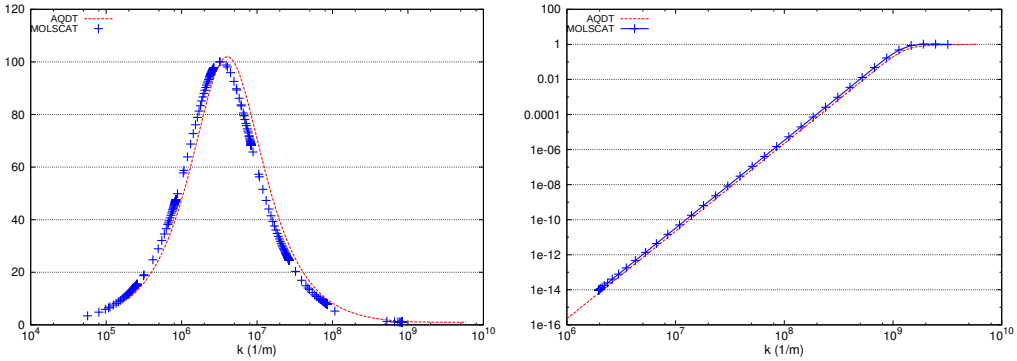

Figure 8.8: $C^{-2}(k)$ L=0 (left) and L=2 (right) functions from Gao's AQDT routines and those backed out of MOLSCAT for the near-resonant $\lambda_{\mathrm{scl}} = 1.004$. Energy given in terms of $k = \sqrt{2\mu E_i^{\infty}}/\hbar$.

fixed k', therefore calculations need to be performed for various values of k'. C_L^{-2} can now be extracted by normalizing the right-hand side of

$$C_L^{-2}(k) \propto k^2 \sigma(k, k'_{\mathrm{fixed}}) / C_{L'}^{-2}(k'_{\mathrm{fixed}}) \tag{8.57}$$

to one at large k, where $C_{L'}^{-2}(k'_{\mathrm{fixed}})$ is extrapolated from $C_{L'}^{-2}(k')$ in figure 8.5. A^2 can now be simply found by comparing both of C^{-2} functions to the calculated cross section.

$C^{-2}(k)$ functions extracted from MOLSCAT and those obtained from AQDT for the non-resonant ($\lambda_{\mathrm{scl}} = 1.04$, $a_s = 33.189$ Å) and resonant ($\lambda_{\mathrm{scl}} = 1.004$, $a_s = -2470$ Å) cases are shown in figures 8.7 and 8.8 respectively. It can be seen that the AQDT $C^{-2}(k)$ functions have the form but not the magnitude of those extracted from MOLSCAT. It can

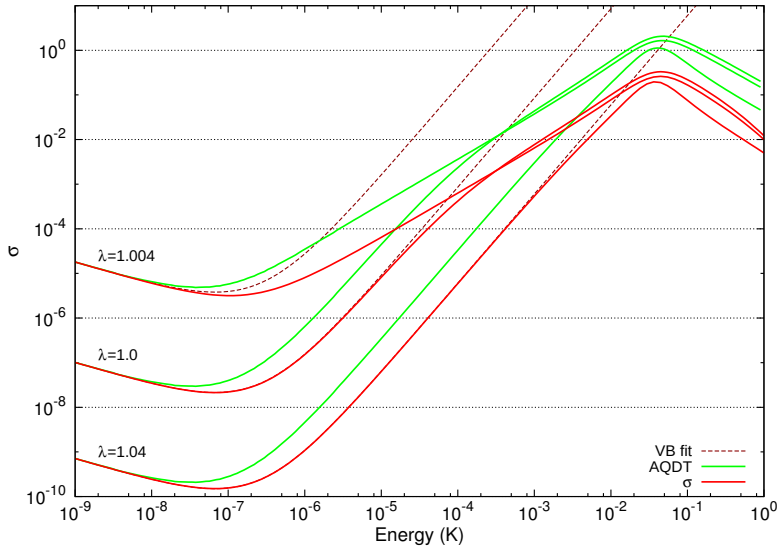

Figure 8.9: The coupled channel cross section $\sigma^{CC}_{m_s=+1,L=0\rightarrow m_s=-1,L=2}(E)$ (shown in red) compared to the corresponding AQDT cross section, σ^{AQDT} (shown in green) for the three values of λ_{scl}, also shown is the predicted functional form of (7.4) (shown in dark-red, dashed).

also be seen that in the near resonant $\lambda_{\mathrm{scl}} = 1.004$ case the $C^{-2}_{L=0}(k)$ decays as k'^{-1} rather than increasing as k^1 in the non-resonant case, which gives the near resonant cross section dependence as $k^2k^{-1}k'^5 = E^{-3/2}E'^{5/2} = E^1$, explaining the change in the cross section dependence near the resonance.

Using the AQDT $C^{-2}(k)$ functions with equation (8.38) we can compare the *exact* coupled channel cross section σ^{CC} to the AQDT cross section σ^{AQDT}. Figure 8.9 shows $\sigma^{\mathrm{CC}}_{m_s=+1,L=0\rightarrow m_s=-1,L=2}(E)$ and $\sigma^{\mathrm{AQDT}}_{m_s=+1,L=0\rightarrow m_s=-1,L=2}(E)$, along with the function form of (7.4) both fitted at low energy to the coupled channel cross section.

The AQDT cross section obtains the correct form of the coupled channel cross section both near and far from resonance. However turning point from the $E^{-1/2}$ region occurs in σ^{AQDT} before σ^{CC}. AQDT is for a pure C_6 van der Waals potential and the potential energy surface of Mg+NH is far from an ideal van der Waals potential with large C_8 and C_{10} coefficients, thus we would not expect σ^{AQDT} to completely reproduce σ^{CC}.

A σ^{MQDT} that should fit σ^{CC} much more accurately than σ^{AQDT} could be obtained by numerically calculating the $C^{-2}(E)$ functions on the actual MgNH potential. This could be done by propagating the scattering wavefunction out to long-range and matching

to the correct boundary conditions to obtain $f(E,R)$, matching to the short-range WKB normalized wavefunction $\hat{f}$ would then yield $C^{-1}(E)$. Propagating back inwards from the boundary conditions for the irregular solution $g(E,R)$ and thus $\tan\lambda(E)$ can be obtained.

Chapter 9

The Born-Oppenheimer approximation

Conical intersections appear all over chemistry as a function of intermolecular separations in polyatomic systems [112] and in the following chapters, the Born-Oppenheimer approximation and its break down in the vicinity of a conical intersections is examined. A new type of conical intersection as a function of externally applied fields is then introduced, before some of its consequences in ultracold gases are investigated.

9.1 The Born-Oppenheimer Approximation and Gauge Invariance

9.1.1 Born-Oppenheimer Expansion

Considering a general molecular system, the total Schrödinger equation,

$$\hat{H}\Psi(\boldsymbol{r},\boldsymbol{R}) = E\Psi(\boldsymbol{r},\boldsymbol{R}), \tag{9.1}$$

has the Hamiltonian,

$$\hat{H} = \hat{T}_n + \hat{T}_e + U(\boldsymbol{r},\boldsymbol{R}), \tag{9.2}$$

where $\hat{T}_n$ and $\hat{T}_e$ are the nuclear and electronic kinetic energy operators respectively, $U(\boldsymbol{r},\boldsymbol{R})$ is the total potential energy, and the vectors $\boldsymbol{r}$ and $\boldsymbol{R}$ denote the complete set of electronic and nuclear coordinates respectively. In this section *mass-scaled coordinates*, that are general to any polyatomic molecule are used, in which all distances are scaled to the same reduced mass M. In the Born-Oppenheimer method [113–115], the electronic

Hamiltonian $\hat{H}_e = \hat{T}_e + U(\boldsymbol{r}, \boldsymbol{R})$ is treated as an operator in electronic space only, depending parametrically on $\boldsymbol{R}$, with electronic eigenfunctions $\Phi_i(\boldsymbol{r}; \boldsymbol{R})$ and eigenvalues $V_i(R)$ that satisfy

$$\hat{H}_e \Phi_i(\boldsymbol{r}; \boldsymbol{R}) = V_i(\boldsymbol{R}) \Phi_i(\boldsymbol{r}; \boldsymbol{R}), \tag{9.3}$$

and the orthonormality condition

$$\int \Phi_i^*(\boldsymbol{r}; \boldsymbol{R}) \Phi_j(\boldsymbol{r}; \boldsymbol{R}) d\boldsymbol{r} \equiv \langle i(\boldsymbol{r}; \boldsymbol{R}) \mid j(\boldsymbol{r}; \boldsymbol{R}) \rangle = \delta_{ij}. \tag{9.4}$$

The total wavefunction $\Psi(\boldsymbol{r}, \boldsymbol{R})$ can now be expanded, in terms of the set of electronic eigenfunctions

$$\Psi(\boldsymbol{r}, \boldsymbol{R}) = \sum_i \chi_i(\boldsymbol{R}) \Phi_i(\boldsymbol{r}; \boldsymbol{R}) \tag{9.5}$$

where the coefficients $\chi_i(\boldsymbol{R})$ are the nuclear wavefunctions. This expansion is known as the Born-Oppenheimer expansion and provides an exact solution to the full molecular Schrödinger equation (9.1). Substituting the expansion into the full Schrödinger equation, projecting onto each electronic eigenfunction in turn, and integrating over $\boldsymbol{r}$ yields a set of coupled equations for the nuclear wavefunctions

$$\left[\hat{T}_n + V_j(\boldsymbol{R})\right] \chi_i(\boldsymbol{R}) - \sum_i \Lambda_{ji} \chi_i(\boldsymbol{R}) = E \chi_i(\boldsymbol{R}), \tag{9.6}$$

where the *non-adiabatic* coupling terms, Λ_{ij}, that describe the interaction between the fast electronic and slow nuclear motions are given by

$$\Lambda_{ji} = \delta_{ji} \hat{T}_n - \langle j(\boldsymbol{r}; \boldsymbol{R}) \mid \hat{T}_n \mid i(\boldsymbol{r}; \boldsymbol{R}) \rangle. \tag{9.7}$$

Given that $\hat{T}_n = -\nabla_{\mathrm{R}}^2 / 2M$, where ∇_{R} is the gradient operator that extends over all the nuclear coordinates, the non-adiabatic coupling term can be divided into

$$\begin{aligned} \Lambda_{ji} =& \frac{1}{2M} \left[2 \langle j(\boldsymbol{r}; \boldsymbol{R}) \mid \nabla_{\mathrm{R}} i(\boldsymbol{r}; \boldsymbol{R}) \rangle \cdot \nabla + \langle j(\boldsymbol{r}; \boldsymbol{R}) \mid \nabla_{\mathrm{R}}^2 i(\boldsymbol{r}; \boldsymbol{R}) \rangle \right] \\ =& \frac{1}{2M} \left[2 \boldsymbol{F}_{ji}(\boldsymbol{r}; \boldsymbol{R}) \cdot \nabla_{\mathrm{R}} + G_{ji}(\boldsymbol{r}; \boldsymbol{R}) \right] \end{aligned} \tag{9.8}$$

where $G_{ji}(\boldsymbol{r}; \boldsymbol{R})$ is known as the *scalar* coupling and $\boldsymbol{F}_{ji}(\boldsymbol{r}; \boldsymbol{R})$ is the *derivative* coupling, which is a vector in $\boldsymbol{R}$.

Differentiating the normalization condition (9.4) and using the definitions in (9.8) the following set of relations can be obtained:

$$\mathbf{F} + \mathbf{F}^{\dagger} = 0 \tag{9.9}$$

$$\mathbf{G} + \mathbf{G}^{\dagger} + 2\mathbf{F}^{\dagger} \cdot \mathbf{F} = 0 \tag{9.10}$$

$$\nabla_{\mathrm{R}} \cdot \mathbf{F} = \mathbf{G} + \mathbf{F}^{\dagger} \cdot \mathbf{F} \tag{9.11}$$

$$(2\mathbf{F} \cdot \nabla_{\mathrm{R}} + \mathbf{G})^{\dagger} = 2\mathbf{F} \cdot \nabla_{\mathrm{R}} + \mathbf{G} \tag{9.12}$$

where $\mathbf{F}$ and $\mathbf{G}$ are matrices with elements $\boldsymbol{F}_{ji}(\boldsymbol{r};\boldsymbol{R})$ and $G_{ji}(\boldsymbol{r};\boldsymbol{R})$ respectively. Using relation (9.10) to eliminate $\mathbf{G}$ from the set of coupled equations (9.6) gives

$$\left\{\frac{1}{2M}\left[\nabla_{\mathrm{R}} + \mathbf{A}\right]^2 + \mathbf{V}\right\}\chi = E\chi, \tag{9.13}$$

where $\mathbf{V}$ is the diagonal matrix of adiabatic potential energies $V_j(R)$, and χ is a column vector with elements χ_j. The advantage of using (9.13) over (9.6) is that in (9.13) the coupling between the electronic and nuclear motion is now confined to only one term $\mathbf{A} = -i\mathbf{F}$.

9.1.2 The Born-Oppenheimer Approximation and Adiabatic Approximation

Taking the gradient ∇_{R} of the electronic Schrödinger equation (9.3) the following result can be obtained for $(i \neq j)$

$$\boldsymbol{F}_{ij} = \frac{\langle i(\boldsymbol{r};\boldsymbol{R}) \mid \nabla_{\mathrm{R}} \hat{H}_e \mid j(\boldsymbol{r};\boldsymbol{R})\rangle}{V_i(\boldsymbol{R}) - V_j(\boldsymbol{R})}. \tag{9.14}$$

For well separated electronic potential energy surfaces, the *off-diagonal* matrix elements of the non-adiabatic coupling given by (9.14) are taken to be small and can be approximated as zero, the *adiabatic approximation*. All the non-adiabatic coupling terms are multiplied by a factor of $1/2M$, thus the adiabatic approximation becomes increasingly accurate with increasing nuclear mass. Furthermore the greater the energetic separation of the electronic state of interest from other electronic states in the system, the weaker the dependence of $\Phi(\boldsymbol{r};\boldsymbol{R})$ on $\boldsymbol{R}$ becomes; thus the *diagonal* non-adiabatic coupling terms can be taken to be small or in the *Born-Oppenheimer approximation*, approximated as zero to

give

$$\left[\hat{T}_n + V_i(\boldsymbol{R})\right]\chi_i(\boldsymbol{R}) = E_i\chi_i(\boldsymbol{R}). \tag{9.15}$$

It can be seen immediately from (9.14) that if the the electronic potential energy surfaces become close or cross the Born-Oppenheimer approximation will break down and $\boldsymbol{F}_{ij}$ will become singular.

9.1.3 Gauge Invariance

The electronic Hamiltonian (9.3) allows the determination of the electronic wavefunction, $\Phi_i(\boldsymbol{r};\boldsymbol{R})$, only up to a $\boldsymbol{R}$-dependent phase factor $g(\boldsymbol{R})$, and the transformation,

$$\tilde{\Phi}(\boldsymbol{r};\boldsymbol{R}) \rightarrow \Phi(\boldsymbol{r};\boldsymbol{R})e^{ig(\boldsymbol{R})}, \tag{9.16}$$

can always be made. Introducing this transformation into equation (9.13), effects only the non-adiabatic parameter $\boldsymbol{A}$

$$\begin{aligned}
\tilde{\boldsymbol{A}}_{ij} &= -i\langle\tilde{j}(\boldsymbol{r};\boldsymbol{R}) \mid \nabla_{\mathrm{R}}\tilde{i}(\boldsymbol{r};\boldsymbol{R})\rangle = -i\langle j(\boldsymbol{r};\boldsymbol{R})e^{-ig(\boldsymbol{R})} \mid \nabla_{\mathrm{R}} i(\boldsymbol{r};\boldsymbol{R})e^{ig(\boldsymbol{R})}\rangle \\
&= -i\langle j(\boldsymbol{r};\boldsymbol{R})e^{-ig(\boldsymbol{R})} \mid e^{ig(\boldsymbol{R})}\nabla_{\mathrm{R}} i(\boldsymbol{r};\boldsymbol{R}) + i(\boldsymbol{r};\boldsymbol{R})\nabla_{\mathrm{R}}e^{ig(\boldsymbol{R})}\rangle \\
&= -i\langle j(\boldsymbol{r};\boldsymbol{R}) \mid \nabla_{\mathrm{R}} \mid i(\boldsymbol{r};\boldsymbol{R})\rangle + \nabla_{\mathrm{R}}g(\boldsymbol{R})\langle j(\boldsymbol{r};\boldsymbol{R}) \mid i(\boldsymbol{r};\boldsymbol{R})\rangle = \boldsymbol{A}_{ij} + \nabla_{\mathrm{R}}g(\boldsymbol{R}),
\end{aligned}$$

which gives

$$\left\{\frac{1}{2M}\left[\nabla_{\mathrm{R}} + \mathbf{A} + \nabla_{\mathrm{R}}g(\boldsymbol{R})\right]^2 + \mathbf{V}\right\}\chi = E\chi. \tag{9.17}$$

The transformation $\mathbf{A} \rightarrow \mathbf{A} + \nabla_{\mathrm{R}}g(\boldsymbol{R})$, is equivalent to a *gauge* transformation in electromagnetic theory with $\mathbf{A}$ playing the role of a vector potential and as $\Phi(\boldsymbol{r};\boldsymbol{R})$ is independent of $g(\boldsymbol{R})$, $\Phi(\boldsymbol{r};\boldsymbol{R})$ is known as gauge invariant. Since the phase introduced is an arbitrary function of $\boldsymbol{R}$, it can be chosen to simplify non-adiabatic problems; the importance of this becomes clear when the crossing of potential energy surfaces are examined.

9.2 Crossing of Potential Energy Surfaces

When electronic potential energy surfaces (PES's) become energetically close or cross, the Born-Oppenheimer approximation breaks down and non-adiabatic coupling terms will become important. In 1936 Teller [116] examined the crossing of potential energy surfaces in diatomic molecules and showed that if the surface is a function of two parameters,

the surfaces will intersect at a point and the surface topology about the point of intersection will be that of a double cone. In 1963, Herzberg and Longuet-Higgins [117] expanded Teller's treatment to polyatomic molecules. Following Herzberg and Longuet-Higgins, we imagine two potential energy surfaces, $\Phi_1(\boldsymbol{r};\boldsymbol{R})$ and $\Phi_2(\boldsymbol{r};\boldsymbol{R})$ that are two orthonormal solutions of the the electronic Hamiltonian with the same symmetry. Solutions of the electronic Hamiltonian can always be expressed in the form

$$\psi(\boldsymbol{r};\boldsymbol{R}) = c_1\Phi_1(\boldsymbol{r};\boldsymbol{R}) + c_2\Phi_2(\boldsymbol{r};\boldsymbol{R}), \tag{9.18}$$

where

$$\begin{bmatrix} H_{11} - E, & H_{12} \\ H_{21} & H_{22} - E \end{bmatrix}\begin{bmatrix} c_1 \\ c_2 \end{bmatrix} = 0. \tag{9.19}$$

For degenerate solutions of (9.19) both of the following independent conditions need to be satisfied,

$$H_{11} = H_{22}, \quad H_{12} = H_{21} = 0,$$

which requires the existence of two independently variable coordinates x and y. Taking the origin at ($H_{11} = H_{22} = W$, $H_{12} = 0$), the following pair of secular equations can be formed

$$\begin{bmatrix} W + h_1x - E & ly \\ ly & W + h_2x - E \end{bmatrix}\begin{bmatrix} c_1 \\ c_2 \end{bmatrix} = 0, \tag{9.20}$$

where $H_{11} = W + h_1x$, $H_{22} = W + h_2x$ and $H_{12} = ly$. (9.20) can be re-expressed as

$$\begin{bmatrix} W + (m + k)x - E & ly \\ ly & W + (m - k)x - E \end{bmatrix}\begin{bmatrix} c_1 \\ c_2 \end{bmatrix} = 0, \tag{9.21}$$

where $m = \frac{1}{2}(h_1 + h_2)$ and $k = \frac{1}{2}(h_1 - h_2)$, the eigenvalues,

$$E_\pm = W + mx \pm \sqrt{k^2x^2 + l^2y^2}, \tag{9.22}$$

are the equations of a double cone, a *conical intersection*, with the vertex at the origin, as shown in figure 9.1. In a diatomic molecule there is only one variable, the interatomic distance, x, thus an intersection between curves in a diatomic molecule can be thought of as a slice through a conical intersection with a non-zero off-diagonal term $ly \neq 0$ mapping out an *avoided crossing*. If the two surfaces had different symmetry, $l = 0$ and

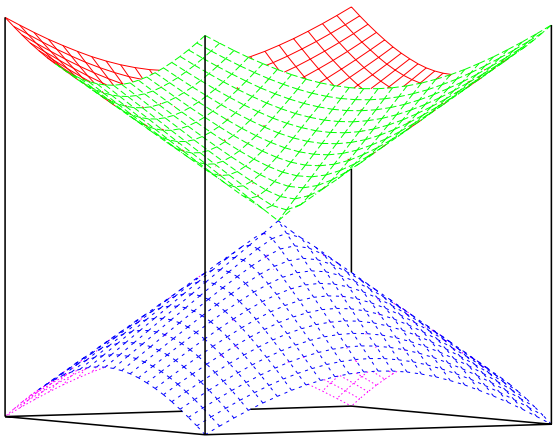

Figure 9.1: The functional form of a conical intersection: $E = \pm\sqrt{x^2 + y^2}$

the states cross. For a polyatomic molecule there are many degrees of freedom and conical intersections can occur at points in two-dimensions or on an (n-1)-dimensional surface in n dimensions.

The result (9.22) was originally obtain by Teller. Herzberg and Longuet-Higgins expanded Teller's result by examining the wavefunctions near the intersection. Firstly an angle θ is defined as,

$$kx = r\cos\theta, \quad ly = r\sin\theta, \tag{9.23}$$

where

$$r = \sqrt{k^2x^2 + l^2y^2} > 0. \tag{9.24}$$

Restricting ourselves to the lower surface of the intersection, the coefficients c_1 and c_2 must satisfy

$$\begin{bmatrix} r + r\cos\theta & r\sin\theta \\ r\sin\theta & r + r\cos\theta \end{bmatrix} \begin{bmatrix} c_1 \\ c_2 \end{bmatrix} = 0, \tag{9.25}$$

from which it follows that

$$\frac{c_1}{c_2} = \frac{-\sin\theta}{1 + \cos\theta} = -\tan\frac{1}{2}\theta. \tag{9.26}$$

Thus if ψ is real

$$c_1 = \pm\sin\frac{1}{2}\theta, \quad c_2 = \mp\cos\tfrac{1}{2}\theta, \tag{9.27}$$

and

$$\psi^- = \begin{pmatrix} \sin\frac{\theta}{2} \\ -\cos\frac{\theta}{2} \end{pmatrix}, \quad \psi^+ = \begin{pmatrix} -\sin\frac{\theta}{2} \\ \cos\frac{\theta}{2} \end{pmatrix}. \tag{9.28}$$

Therefore as we move around the origin with a constant r, θ goes from $0 \rightarrow 2\pi$, c_1, c_2 and thus ψ change sign i.e. $\psi(\theta + 2\pi) = -\psi(\theta)$ and the wavefunction must wind twice around the intersection to return to its initial state $\psi(\theta + 4\pi) = \psi(\theta)$. This change in the number of times the wavefunction must wind around the closed loop to return to its initial state means that somewhere inside the the loop there must be a singular point at which the wavefunction is degenerate. The change in phase of the wavefunction as it winds around the intersection is known as the geometric phase or the Berry phase effect, after Berrys' influential 1984 paper [118], in which it was demonstrated that an eigenstate slowly transported around a closed circuit $\boldsymbol{C}$ can acquire a geometrical phase factor $\exp\{i\gamma(\boldsymbol{C})\}$ upon returning to its initial position.

9.3 The Geometric or Berry Phase

Before examining the consequences of the geometric phase caused by a conical intersection it is important to note that geometric phases and their effects are not unique to conical intersections. More generally the failure of a quantity to return to itself when transported around a closed loop in parameter space is know as an anholonomy. Such anholonomies appear in many diverse areas of physics from the Foucault pendulum to defects in liquid crystals [119]. One famous example of an anholonomy is the Aharonov-Bohm effect [120], in which a charged particle moves around a closed path that encircles a line of magnetic flux; the wavefunction of the charged particle acquires a phase change proportional to the flux encircled even if the magnetic field is zero along the path transversed by the particle.

We have seen that the sign of the electronic wavefunction changes sign when the nuclei encircle a conical intersection. However, the total wavefunction $\Psi(\boldsymbol{r}, \boldsymbol{R}) \approx \chi(\boldsymbol{R})\Phi(\boldsymbol{r}; \boldsymbol{R})$ must remain single-valued. Single-valuedness of Ψ can be achieved in two ways. Method one requires that the nuclear wavefunction $\chi(\boldsymbol{R})$ also changes sign upon completion of a circuit about the intersection, which is achieved by introducing boundary conditions on $\chi(\boldsymbol{R})$. Method two is to introduce a geometric phase factor to the electronic eigenstate [118, 121]

$$\Phi(\boldsymbol{r}; \boldsymbol{R}) \rightarrow \Phi(\boldsymbol{r}; \boldsymbol{R})e^{i\theta/2}, \tag{9.29}$$

which as we have seen is equivalent to the gauge transformation $\mathbf{A} \rightarrow \mathbf{A} + \nabla\theta/2$ in the Born-Oppenheimer expansion (9.13). It is clear then, that the non-adiabatic coupling parameter $\mathbf{A}$ can no longer be treated as a vanishing quantity, therefore the Born-Oppenheimer approximation is not valid in the vicinity of conical intersection.

The two methods outlined are completely equivalent, resulting in a choice between a non-single-valued nuclear wavefunction and a non-vanishing vector potential (gauge) term in the Hamiltonian. This equivalence can be seen, and physical insight gained by examining the effect of the geometric phase on a particle moving on a one-dimensional ring.

9.3.1 States of a Particle on a Ring

Confining a particle to move on a one-dimensional, isotropic ($V(R,\theta) = V(R)$) ring of radius R_0 on the lower surface of the conical intersection, the total wavefunction will have the form

$$\Psi(r,\theta) = \chi(\theta)\psi^{-}(r;\theta). \tag{9.30}$$

In method (i), the single-valuedness of $\Psi(r,\theta)$ is ensured by requiring the nuclear wavefunction $\chi(\theta)$ also undergos a sign change upon completion of a circuit about the intersection. Thus the wavefunctions behave as

$$\chi(\theta) = -\chi(\theta + 2\pi) \tag{9.31}$$

$$\psi^{-}(r;\theta) = -\psi^{-}(r;\theta + 2\pi) \tag{9.32}$$

$$\Psi(r,\theta) = \Psi(r,\theta + 2\pi). \tag{9.33}$$

The Born-Oppenheimer equation for the nuclear motion,

$$\left[-\frac{\hbar^2}{2m}\nabla^2 + V(R_0)\right]\chi(\theta) = \left[-\frac{\hbar^2}{2mR_0^2}\frac{d^2}{d\theta^2} + V(R_0)\right]\chi(\theta) = E\chi(\theta), \tag{9.34}$$

is satisfied by normalized wavefunctions of the form

$$\chi_{m_l}(\theta) = \frac{1}{\sqrt{2\pi}}e^{-im_l\theta} \tag{9.35}$$

where m_l is a dimensionless number that represents the rotational angular momentum of the particle. The multi-valued boundary condition (9.31) implies $e^{im_l\theta} = -e^{im_l\theta}e^{im_l 2\pi}$

which is satisfied by half-integer values of $m_l = \pm\frac{1}{2}, \pm\frac{3}{2}, \ldots = m_l^{\text{half}}$. The eigenvalues follow directly from (9.35),

$$E_{m_l^{\text{half}}} = \frac{\hbar^2}{2mR_0^2}\left(m_l^{\text{half}}\right)^2 + V(R_0). \tag{9.36}$$

Multivalued basis functions, as used in method (i), can be hard to work with and method (ii) introduces a phase factor to electronic wavefunction to compensate for the sign change,

$$\psi^{\text{SV}}(r;\theta) = e^{i\theta/2}\psi^{-}(r;\theta) \tag{9.37}$$

and ensure the singlevaluedness of $\Psi(r,\theta) = \chi(\theta)\psi^{\text{SV}}(r;\theta)$. As we have seen in section 9.1, the phase factor modifies the nuclear momentum operator, introducing a non-vanishing vector potential term

$$\left[\frac{\hbar^2}{2m}\left(-i\nabla + \nabla\frac{\theta}{2}\right)^2 + V(R_0)\right]\chi(\theta) = \left[\frac{\hbar^2}{2mR_0^2}\left(-i\frac{d}{d\theta} + \frac{1}{2}\right)^2 + V(R_0)\right]\chi(\theta) = E\chi(\theta). \tag{9.38}$$

Equation (9.38) is satisfied by wavefunctions of the form (9.35), but as $\chi(\theta) = \chi(\theta + 2\pi)$ m_l is integer quantized $m_l^{\text{int}} = 0, \pm1, \pm2, \ldots$. The eigenvalues are therefore

$$E_{m_l^{\text{int}}} = \frac{\hbar^2}{2mR_0^2}\left(m_l^{\text{int}} + \frac{1}{2}\right)^2 + V(R_0). \tag{9.39}$$

It can be seen that method (i) and (ii) produce the same set of eigenvalues and that the half-integer angular momentum quantization that appeared in $\chi(\theta)$ in method (i) appears in the nuclear momentum operator in method (ii).

9.4 Conical Intersections in Triatomic Systems

The simplest systems in which a conical intersection occur are in triatomic X_3 clusters, which have a conical intersection at the equilateral triangle D_{3h} geometry. One such system is the Na_3 trimer in its electronic ground $Na_3(X)$ state, which has been the subject of a number of experimental and theoretical studies [122–124]. The free pseudorotational mode of Na_3, in which the trimer is in a distorted triangular C_{2v} arrangement, takes the trimer around the conical intersection, resulting in observable half-integer quantization of the vibrational angular momentum.

The H+H_2 reaction has been studied extensively, however the effect of the geometric phase effect on the reaction was less clear. Detailed experimental results up to energies of 2.5 eV, with the conical intersection seam at $E = 2.7$ eV, showed good agreement with calculations in which the geometric phase was neglected. Kuppermann and Wu [125], predicted that the geometric phase effects should have a noticeable effect on state-to-state product distributions. They argued that the apparent absence of geometric phase effects in the experimental results, was due to the effect being confined to a narrow energy range and thus hard to detect. Kendrick [126] performed a set of quantum reactive scattering calculations that included the geometric phase effect via a vector potential approach, predicted that geometric phase effects would appear in the individual state-to-state reaction probabilities, which would cancel when summed to give differential and integral cross sections, although why the effects canceled was not clear. This disagreement was resolved by Althorpe [127–129] who developed a simple and general topological approach to the problem. That takes the product of the topologically different wavefunctions, which encircle the conical intersection an even and odd number of times. Using this approach it was found that small geometric phase effects appeared in individual state-to-state reaction probabilities but that the topologically distinct paths scattered into different regions of space causing the cancelation these small geometric phase effects in the summed differential and integral cross sections; demonstrating that Kendrick was correct.

Chapter 10

Conical Intersection in External Fields

10.0.1 Parity in Electromagnetic Field

The inversion or parity transformation [44] is defined as

$$\hat{P}\begin{pmatrix} x \\ y \\ z \end{pmatrix} = \begin{pmatrix} -x \\ -y \\ -z \end{pmatrix}, \tag{10.1}$$

which has the effect of changing an initial right-handed into a left-handed system. A general vector $\boldsymbol{r} = (x_1, x_2, x_3)$, that transforms under parity as $\hat{P}(x_1, x_2, x_3) = (-x_1, -x_2, -x_3)$ has negative components relative to the transformed axes. Vectors that have this behavior are called *polar* vectors, figure 10.1.

A fundamental difference appears for a vector that is defined as the cross product of two polar vectors. Let $\boldsymbol{C} = \boldsymbol{A} \times \boldsymbol{B}$, where both $\boldsymbol{A}$ and $\boldsymbol{B}$ are polar vectors; when the coordinate axes are inverted under the parity transformation $A_i \rightarrow -A'_i$, and $B_j \rightarrow -B'_j$, but from the definition of $\boldsymbol{C}$, $C_k \rightarrow +C'_k$. Thus C does not behave as a polar vector; it remains unchanged in the parity transformed axes, and is known as an *axial* or pseudo vector, as shown in figure 10.1. In addition an axial vector in a right-handed coordinate system has a sense of rotation associated with it given by the right-hand rule. The difference between polar $\boldsymbol{p}$ and axial $\boldsymbol{q}$ vectors can be seen by a reflection in the xz plane

$$\begin{aligned} \boldsymbol{p} = (p_x, p_y, p_z) &\rightarrow \boldsymbol{p'} = (p_x, -p_y, p_z) \\ \boldsymbol{q} = (q_x, q_y, q_z) &\rightarrow \boldsymbol{q'} = (-q_x, q_y, -q_z). \end{aligned} \tag{10.2}$$

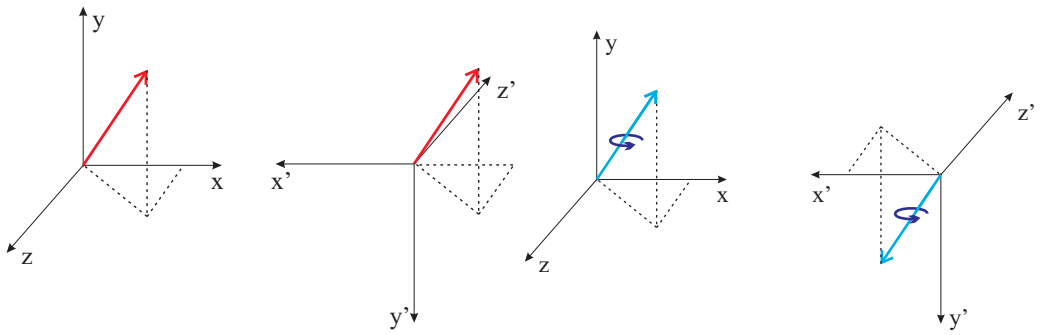

Figure 10.1: Behaviour of a polar (left) and axial (right) vector under inversion of cartesian coordinates (parity transformation). A polar vector transforms as $\boldsymbol{r} = (x, y, z) \rightarrow \boldsymbol{r}' = (x', y', z') = (-x, -y, -z)$ and an axial vector transforms as $\boldsymbol{r} = (x, y, z) \rightarrow \boldsymbol{r}' = (x', y', z') = (+x, +y, +z)$. The sign of a polar vector $\boldsymbol{r}$ reverses with a reversal of the coordinate axes (odd parity), but the sign of a axial vector remained the same with a reversal of the coordinate axes (even parity). Images adapted from [44].

For the physical case of parity in an electric field [73], we can imagine a charge moving in a uniform electric field at a right angle towards a mirror, as shown in figure 10.2, in the reflected situation the electric field $\boldsymbol{E}$, the force acting on the particle $\boldsymbol{F}$, and the particles velocity $\boldsymbol{v}$ are all reversed and therefore we can not tell if we are in reflected world and $\boldsymbol{E}$ is a polar vector and $\hat{P}\boldsymbol{E} = -\boldsymbol{E}$.

Considering a positively charged particle moving in an anti-clockwise direction in a magnetic field $\boldsymbol{B}$ directed into the plane of the paper, as shown in figure 10.2. Applying a parity transformation in a mirror plane parallel to the plane of the paper leaves the force acting on the particle and the direction of the current unchanged and hence leaves the magnetic field unchanged, hence $\boldsymbol{B}$ is an axial vector and $\hat{P}\boldsymbol{B} = \boldsymbol{B}$. In fact, it is immediately apparent that is an axial vector from the Maxwell-Faraday equation $\partial\boldsymbol{B}/\partial t = -\nabla \times \boldsymbol{E}$.

10.0.2 A Conical Intersection as a Function of Electromagnetic Fields

As was shown in section 10.0.1, in the absence of an electric field the parity of atomic or molecular states are conserved, so it is possible to tune the magnetic field so that two levels of different parity cross one another and at some point are exactly degenerate. However, applying a simultaneous electric field will remove parity conservation, mixing the two

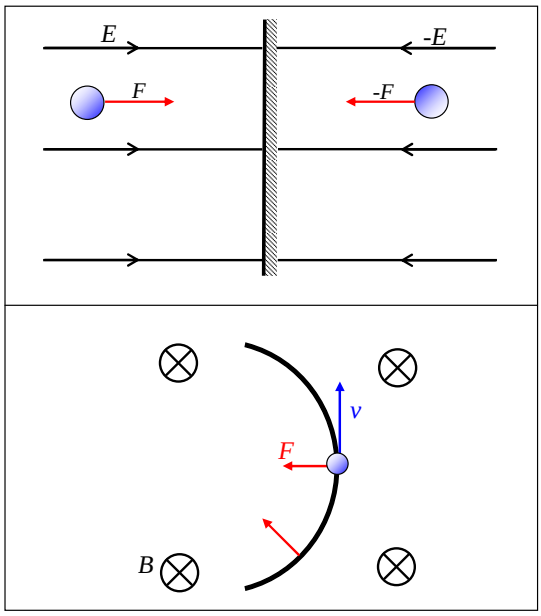

Figure 10.2: Top: motion of a positive charge moving towards a mirror in a uniform electric field (RHS), in the reflect world (LHS), a parity transformation, the field and force have changed sign and the particle is still accelerating towards the mirror, thus we can not tell if we are in a reflected world, $\hat{P}\boldsymbol{E} = -\boldsymbol{E}$. Bottom: Motion of a positively charged particle in a uniform magnetic field (into the paper), a reflection in the plane of the paper leaves the velocity and force acting on the particle and hence the magnetic field unchanged, $\hat{P}\boldsymbol{B} = \boldsymbol{B}$.

states resolving the degeneracy and creating an avoided crossing between the two states [65]. Conical intersections can thus occur at points where the electric field is zero in electromagnetic field space. It is therefore possible to envisage an arrangement of fields that creates conical intersections between two atomic or molecular levels *as a function of external spatial coordinates* rather than the more conventional internal coordinates.

Conical intersections of this type can in principle be observed in any system where two states of opposite parity can be tuned into degeneracy with a magnetic field and can then be coupled with an electric field. However, for atomic systems states of different parity are usually far apart at zero field. More accessible examples are provided by gases of heteronuclear alkali-metals which are the targets of current experiments. To illustrate this effect a gas of KRb molecules in a single vibrational level of the lowest triplet state $a^3\Sigma^+$, which was recently formed experimentally [32], is considered.

Before moving on to examining induced avoided crossings in KRb($a^3\Sigma$), it is worth noting that the proposed electromagnetic field-induced conical intersections differ from conical intersections in diatomic molecules created at very strong magnetic fields that have importance in astrophysical-chemistry [130–132]. These very strong-field intersections occur at magnetic field strengths that are of the order of 10^5 T, which can be found near astrophysical objects such as white dwarfs and neutron stars. In a magnetic field of such strength the rotation to the diatomic molecule about an axis perpendicular to the field is hindered. When the diatomic molecule is parallel to the field direction $\theta = 0$, the point group symmetry is $C_{\infty h}$ and electronic potential energy surfaces can cross as a function of the interatomic distance R. However, when the diatomic molecule is not parallel to the field axis $\theta \neq 0$ the point group symmetry is C_i and thus surfaces that crossed at $\theta = 0$ can avoided cross at $\theta \neq 0$, forming a conical intersection as a function of R and θ. The strong field conical intersections are still a function of an internal coordinate and occur at fields well beyond anything that is currently attainable in a laboratory, whereas the electromagnetic field-induced conical intersections proposed here are independent of internal coordinates and are attainable at laboratory fields.

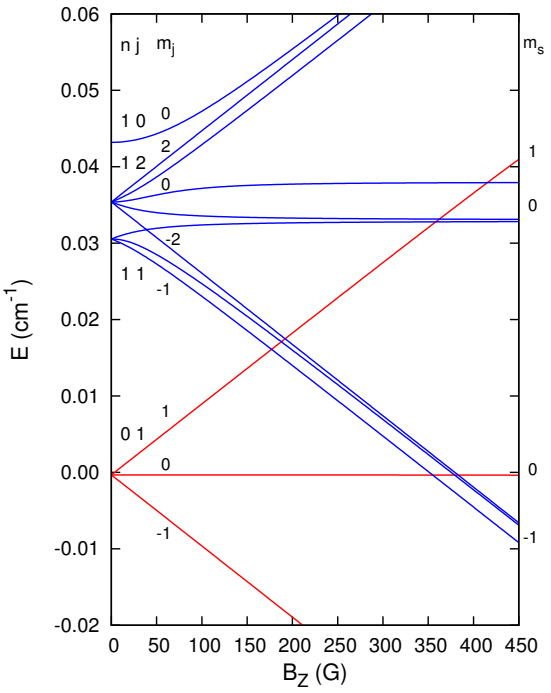

Figure 10.3: The lowest few rovibrational states of KRb as function of magnetic field.

10.1 The Rovibrational States of $^{41}K^{87}Rb$ ($a^3\Sigma^+$)

A simplified Hamiltonian for the $a^3\Sigma$ state of KRb has the form

$$H = B\hat{N}^2 + \frac{2}{3}\lambda\left(\hat{S}^2 - 3\hat{S}_z^2\right) + g_e\mu_B B_Z M_S - \boldsymbol{E}\cdot\boldsymbol{d}, \tag{10.3}$$

where B is the molecular rotational constant, λ is the spin-spin coupling constant, S_z is the projection of S onto the molecular axis, B_Z is the magnetic field orientated along the space-fixed Z axis, and E and d are the electric field and molecular electric dipole moment respectively. KRb has not been characterized in detail spectroscopically, but electronic structure calculations give an equilibrium distance $r_e = 5.901$ Å for the triplet state [133]. This allows B and λ for the lowest vibrational level to be estimated as $B = 0.01813$ cm^{-1} and $\lambda = -0.00632$ cm^{-1}. The dipole moment function has been calculated by Kotochigova, Julienne and Tiesinga [134] and has a value around 0.051 D near r_e.

The Hamiltonian can be conveniently expanded in the fully decoupled basis set $|\, nm_n\rangle \,|\, sm_s\rangle$, where n is the rotational quantum number and s is the electron spin of the molecule; m_n and m_s are the respective projections onto the space-fixed axis. The evaluated matrix elements are identical to those in the monomer Hamiltonian for atom-diatom

nm_nm_s	$\|000\rangle$	$\|100\rangle$	$\|11-1\rangle$	$\|1-10\rangle$	$\|10-1\rangle$	$\|21-1\rangle$
$\langle 000\|$	0	$-\frac{Ed}{\sqrt{3}}\cos\chi$	0	$\frac{Ed}{\sqrt{6}}\sin\chi$	0	$\frac{2}{\sqrt{15}}\lambda$
$\langle 100\|$	$-\frac{Ed}{\sqrt{3}}\cos\chi$	X_1	$\frac{4}{10}\lambda$	0	0	0
$\langle 11-1\|$	0	$\frac{4}{10}\lambda$	X_2	0	0	$-\frac{Ed}{\sqrt{5}}\cos\chi$
$\langle 1-10\|$	$\frac{Ed}{\sqrt{6}}\sin\chi$	0	0	X_3	$\frac{4}{5}\lambda$	0
$\langle 10-1\|$	0	0	0	$\frac{4}{5}\lambda$	X_4	$\frac{Ed}{\sqrt{10}}\sin\chi$
$\langle 21-1\|$	$\frac{2}{\sqrt{15}}\lambda$	0	$-\frac{Ed}{\sqrt{5}}\cos\chi$	0	$\frac{Ed}{\sqrt{10}}\sin\chi$	X_5

Table 10.1: Hamiltonian matrix of relevant basis functions, in the $|nm_nm_s\rangle$, showing the coupling between different KRb Zeeman states caused by an electric field, E at an angle χ to the magnetic field B_Z. X_i are non-zero diagonal matrix elements.

collisions, that are given in chapter 3.

Figure 10.3 shows the lowest few rotational states of KRb($a^3\Sigma^+$), in the absence of an electric field, as a function of magnetic field. The rotational states shown is figure 10.3 are in the limit of Hund's case (b) coupling in which n couples to s forming j, the total molecular angular momentum. At zero field, the $n = 0$ level has a single sublevel with total angular momentum $j = 1$, while the $n = 1$ level is split into 3 sublevels with $j = 0$, 1 and 2. When a magnetic field is applied, each of these sublevels is split into $2j + 1$ components each labeled by m_j.

There are a number of points in figure 10.3 at which states cross as a function of magnetic field, where we would expect to induce avoided crossing by applying a non-zero electric field. However the orientation of the electric field with respect to the magnetic field will affect the avoided crossing.

10.2 Avoided Crossings as a Function of χ

The Stark Hamiltonian $\boldsymbol{E}\cdot\boldsymbol{d}$ can be written as $Ed\cos\chi$ where χ is the angle between the space-fixed Z-axis and the electric field direction $\hat{\boldsymbol{E}}$. Fixing the electric field allows the effect of χ on induced avoided crossings to be examined.

Figure 10.4 shows the effect of χ on the set of $n = 1$ states crossing the $|n = 0 j = 1 m_j = 0\rangle$ states at around 370 Gauss, for an electric field of 2.5 kV cm^{-1}. It can be

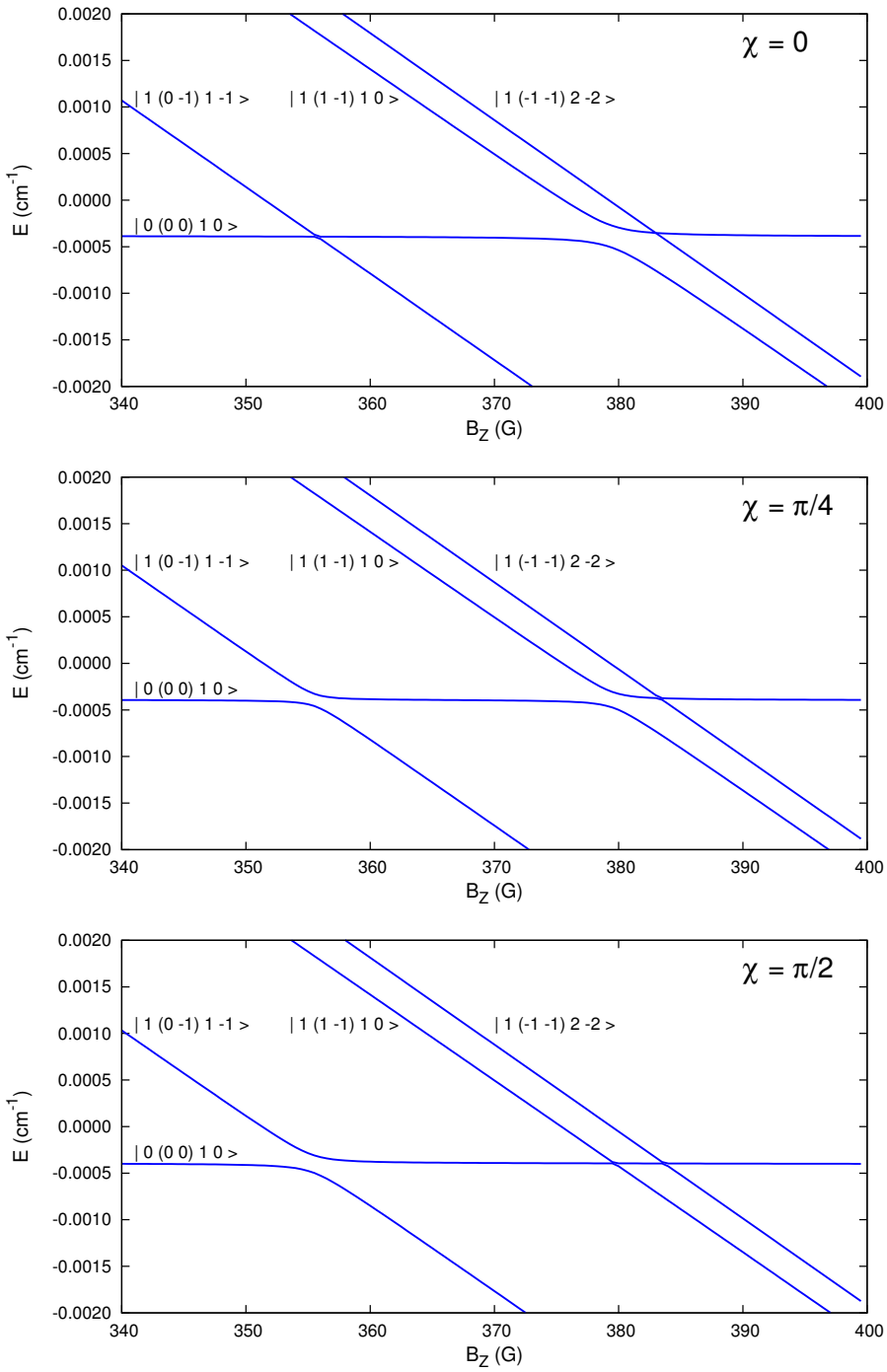

Figure 10.4: The χ dependence of electric field induced avoided crossings at E = 2.5 kV cm^{-1}. The states are labeled $|\, n(m_n m_s)\, j m_j \rangle$

seen clearly in figure 10.4 that as χ is varied the width of induced avoided crossings varies, and at parallel ($\chi = 0$) and perpendicular ($\chi = \pi/2$) field arrangements different avoided crossings exist [54]. This behaviour can be understood by examining the reduced Hamiltonian matrix (shown in table 10.1) that shows the field-induced coupling between the states shown in figure 10.4.

For the case of parallel magnetic and electric fields (figure 10.4(a)), the space-fixed projection of the total angular momentum m_j is conserved and an avoided crossing is only induced between the $|\ n = 1 m_n = 1 m_s = -1\rangle$ and $|\ n = 0 m_n = 0 m_s = 0\rangle$ states. From the matrix elements in table 10.1 we can see that $|\ 000\rangle$ is coupled to $|\ 11-1\rangle$ via an interplay of the spin-spin interaction λ terms and $Ed\cos\chi$ terms. It is clear then, that at perpendicular fields ($\cos\chi = 0$) the coupling between the states is zero and the states cross.

Rotating the electric field away from the parallel configuration removes the m_j conservation, allowing avoided crossings to be induced between states that differ in m_j. The coupling between the $|\ 10-1\rangle$ and $|\ 000\rangle$ states occurs via spin-spin and $Ed\sin\chi$ terms, thus at perpendicular fields the crossing has its maximum width. There is also an avoided crossing between the $|\ 000\rangle$ and $|\ 1-1-1\rangle$ states. However, the coupling between these states is of higher order in λ and $Ed\sin\chi$, thus the width is much smaller, such that the avoided crossing cannot be seen on the scale of figure 10.4 and at $\chi = \pi/2$ it has a width of approximately 5×10^{-6} cm^{-1}.

10.3 Isotropic Conical Intersection and Trapping Potential

In an experimental situation the electromagnetic fields would be applied to a trapped gas of KRb molecules. For the trapped molecules to fully encircle any induced intersection the anisotropy along the path of the molecules needs to be as small as possible. Thus the crossing between the high-field-seeking $|\ n = 0 j = 1 m_j = +1\rangle$ state and the low-field-seeking $|\ n = 1 j = 1 m_j = 0\rangle$ state near $B_Z = 187$ G is examined. As the crossing states differ in m_j, an electric field that is perpendicular, $\chi = \pi/2$, to the magnetic field is considered.

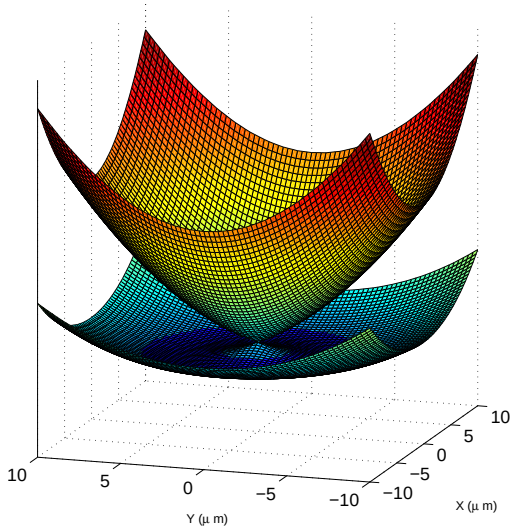

Figure 10.5: Toroidal shaped trapping potential created in the lower surface of a conical intersection formed by perpendicular space-fixed electromagnetic fields, with field gradients $dB_Z/dX = 5$ G cm^{-1} and $d\boldsymbol{E}/dY = 6.723$ kV/cm^2, and an optical trapping potential that has a height of 7 μK at $\rho = 30$ μm.

An experiment may be envisaged in which the KRb molecules are trapped in an cylindrically symmetric optical potential centered at the origin in the space-fixed XY plane, of the form

$$V_{\text{opt}}(\rho, \phi, Z) = \frac{1}{2} M \left(\omega_\rho^2 \rho^2 + \omega_Z^2 Z^2 \right) \tag{10.4}$$

where $\rho^2 = X^2 + Y^2$. The trapped molecules are then subjected to a magnetic field B_Z, orientated along the space-fixed Z axis, which varies along the X axis with field gradient dB_Z/dX. An inhomogeneous electric field $\boldsymbol{E}$ is then oriented along the X axis with a magnitude which varies with Y as $d\boldsymbol{E}/dY$, vanishing on a plane at $Y = 0$. This will create a seam of conical intersections along the line $0, 0, Z$ where $X = 0$ is defined as the position at which the magnetic field brings the two states into degeneracy.

Taking an experimentally feasible optical trapping potential with a height of 7 μK at $\rho = 30$ μm [135], and feasible magnetic and electric field gradients of 5 G/cm and 6.8 kV/cm^2 respectively, creates a doughnut (toroidaly) shaped potential around the conical intersection as shown in figure 10.5.

10.3.1 Removing the anisotropy in the toroidal potential

Despite choosing a more isotropic intersection, the potential shown in figure 10.5 has significant anisotropy (about 10 nK), which is manifested as an asymmetry along a cut with $Y = 0$ as shown schematically in the lower-left panel of figure 10.6. However, the anisotropy of the toroidal trapping potential $V_{\text{trap}}(\phi)$ can be controlled by offsetting the optical trapping potential from the point of intersection. Assuming that the KRb eigenstates are linear as a function of magnetic field over the range of the intersection, with respective gradients a and b, the asymmetry along $Y = 0$ will be zero when the optical trap is centered at $x_0 = (a + b)/(2M\omega_\rho)$. The potential now will have different depths along the X and Y axes. This can be minimized by adjusting the electric field gradient. The right-hand side of figure 10.6 shows the optimized trapping potential with an angular anisotropy on the order of 0.01 nK, where $x_0 = 0.0715\,\mu$m and $d\boldsymbol{E}/dY = 6.723$ kV/cm^2.

10.4 Single Particle States in the Toroidal trapping potential

For a single KRb molecule moving in a toroidal potential such as that shown in figure 10.6, the Hamiltonian is given by

$$\hat{H} = \frac{-\hbar^2}{2m}\left\{\frac{\partial^2}{\partial\rho^2} + \frac{1}{\rho}\frac{\partial}{\partial\rho} + \frac{1}{\rho^2}\frac{\partial^2}{\partial\phi} + \frac{\partial^2}{\partial Z^2}\right\} + V(\rho, Z), \tag{10.5}$$

where the toroidal potential is defined as

$$V(\rho, Z) = \frac{1}{2}k_\rho(\rho - \rho_0)^2 + \frac{1}{2}k_Z Z^2 = V(\rho) + V(Z), \tag{10.6}$$

where k_ρ and k_Z are constants and ρ_0 is the location of the toroidal minimum in the XY-plane. Separating the longitudinal, radial, and rotational degrees of freedom in a trial wave function $\Psi(\rho, \phi, Z) = \psi(\rho)\Phi(\phi)\varphi(Z)$ and substituting into the time-independent Schrödinger equation gives

$$\begin{aligned}\hat{H}\Psi(\rho, \phi, Z) = -\frac{\hbar^2}{2m}\left\{\left[\frac{\partial^2}{\partial\rho^2}\psi(\rho) + \frac{1}{\rho}\frac{\partial}{\partial\rho}\psi(\rho)\right]\Phi(\phi)\varphi(Z) + \psi(\rho)\left[\frac{1}{\rho^2}\frac{\partial^2}{\partial\phi^2}\Phi(\phi)\right]\varphi(Z)\right. \\ \left. + \psi(\rho)\Phi(\phi)\left[\frac{\partial^2}{\partial Z^2}\varphi(Z)\right]\right\} + V(\rho, Z)\psi(\rho)\Phi(\phi)\varphi(Z) = E\psi(\rho)\Phi(\phi)\varphi(Z),\end{aligned} \tag{10.7}$$

which can be rearranged to give

$$E = -\frac{\hbar^2}{2m}\left\{\frac{1}{\psi(\rho)}\left[\frac{\partial^2}{\partial\rho^2}\psi(\rho) + \frac{1}{\rho}\frac{\partial}{\partial\rho}\psi(\rho)\right] + \frac{1}{\rho^2\Phi(\phi)}\frac{\partial^2}{\partial\phi^2}\Phi(\phi)\right\} + V(\rho) - \frac{\hbar^2}{2m}\frac{1}{\varphi(Z)}\left[\frac{\partial^2}{\partial Z^2}\varphi(Z)\right] + V(Z) = E_{\rho,\phi} + E_Z. \tag{10.8}$$

The equation for E_Z is just the one-dimensional harmonic oscillator equation [42], with the eigenvectors

$$\varphi_{v_Z}(Z) = N_{v_Z} H_{v_Z}(\alpha_Z)\, e^{-\alpha_z^2 Z^2/2} \tag{10.9}$$

and the eigenvalues

$$E_{v_Z} = (v_Z + 1/2)\,\hbar\omega_Z, \tag{10.10}$$

where v_Z is an integer, $\omega_Z = \sqrt{k_Z/m}$, $\alpha_Z^2 = \sqrt{mk_Z/\hbar}$, $H_{v_z}(z)$ is a Hermite polynomial, and $N_{v_Z} = \left(\alpha_Z/2^{v_Z} v_Z!\,\sqrt{\pi}\right)^{\frac{1}{2}}$.

Dividing the equation for $E_{\rho,\phi}$ by ρ^2 yields

$$-\frac{1}{\Phi(\phi)}\frac{\partial^2}{\partial\phi^2}\Phi(\phi) = \frac{1}{\psi(\rho)}\left(\rho^2\psi''(\rho) + \rho\psi'(\rho)\right) + \frac{2m\rho^2}{\hbar^2}\left(E_{\rho,\phi} - V(\rho)\right), \tag{10.11}$$

which can be separated to give separate equations in ρ and ϕ

$$\frac{\partial^2}{\partial\phi^2}\Phi(\phi) = -m_l^2\Phi(\phi) \tag{10.12}$$

$$\rho^2\psi''(\rho) + \rho\psi'(\rho) + \frac{2m\rho^2}{\hbar^2}\left(E - V(\rho)\right)\psi(\rho) = m_l^2\psi(\rho). \tag{10.13}$$

Equation (10.12) is just the one dimensional particle on a ring equation, that is satisfied half integer values of $m_l = m_l^{\text{half}} = \pm\frac{1}{2}, \pm\frac{3}{2}, \ldots$, under the geometric phase boundary conditions $\Phi(\phi) = -\Phi(\phi + 2\pi)$ as shown in section 9.3. The radial equation (10.13) can be simplified by substituting in the frequency $\omega_\rho = \sqrt{k_\rho/m}$ and by using the substitution $\psi(\rho) = y(\rho)/\sqrt{\rho}$,

$$-\frac{\hbar^2}{2m}y''(\rho) + \left\{-\frac{\hbar^2}{2m\rho^2}\left(\left(m_l^{\text{half}}\right)^2 + \frac{1}{4}\right) + \frac{1}{2}m\omega^2(\rho - \rho_0)^2 - E_{m_l^{\text{half}}}\right\}y(\rho) = 0. \tag{10.14}$$

First-order perturbation theory allows the separation of the radial hamiltonian into $\hat{H} = \hat{H}^{(0)} + \hat{H}^{(1)}$, where

$$\hat{H}^{(0)}y(\rho) = -\frac{\hbar^2}{2\mu}y''(\rho) - \frac{1}{2}\mu\omega^2(\rho - \rho_0)^2 y(\rho) = E^{(0)}y(\rho), \tag{10.15}$$

and

$$\hat{H}^{(1)}y(\rho) = -\frac{\hbar^2}{2\mu\rho^2}\left(\left(m_l^{\text{half}}\right)^2 + \frac{1}{4}\right)y(\rho) = E^{(1)}y(\rho). \tag{10.16}$$

$\hat{H}^{(0)}y(\rho)$ is the one dimensional harmonic oscillator equation with the eigenvectors

$$y_{v_\rho}(\rho) = N_{v_\rho}H_{v_\rho}\left(\alpha_\rho(\rho-\rho_0)\right)e^{-\alpha_\rho^2(\rho-\rho_0)^2/2} \tag{10.17}$$

and eigenvalues

$$E^{(0)}_{v_\rho} = \left(v_\rho + 1/2\right)\hbar\omega, \tag{10.18}$$

where v_ρ is an integer, $\alpha_\rho^2 = \sqrt{mk_\rho/\hbar}$, $H_{v_\rho}(z)$ is a Hermite polynomial, and $N_{v_\rho} = \left(\alpha_\rho/2^{v_\rho}\right.$ $\left.v_\rho!\,\sqrt{\pi}\right)^{\frac{1}{2}}$. Solutions to $\hat{H}^{(1)}$ can be approximated by taking an equilibrium value for $\rho = \rho_0$ and treating $\hbar^2/2\mu\rho_0^2$ as a constant,

$$E^{(1)}_{m_l^{\text{half}}} = \frac{\hbar^2}{2\mu\rho_0^2}\left(\left(m_l^{\text{half}}\right)^2 + \frac{1}{4}\right) = b_{\text{rot}}\left(\left(m_l^{\text{half}}\right)^2 + \frac{1}{4}\right). \tag{10.19}$$

The total toroidal wave functions are thus

$$\Psi_{v_\rho,m_l,v_Z}(\rho,\phi,Z) = y_{v_\rho}(\rho)\Phi_{m_l}(\phi)\varphi_{v_Z}(Z), \tag{10.20}$$

with the eigenvalues spectrum

$$E_{v_\rho,m_l^{\text{half}},v_Z} = \left(v_Z + \frac{1}{2}\right)\hbar\omega_Z + \left(v_\rho + \frac{1}{2}\right)\hbar\omega_\rho + b_{\text{rot}}\left(\left(m_l^{\text{half}}\right)^2 + \frac{1}{4}\right). \tag{10.21}$$

In order for geometric phase effects to be observed, the angular anisotropy of the toroidal trapping potential $V(\phi)$ must be small enough to allow the wavefunction to fully encircle the intersection. For the potentials shown in Fig. 10.6, $\frac{1}{2}\hbar\omega_\rho \approx 4$ nK and $b_{\text{rot}} \approx 0.5$ nK. For the potential on the left-hand side, the anisotropy is large compared to b_{rot}, so that the single-particle wavefunction will be localized on one side of the trap. However, for the potential on the right-hand side, the anisotropy is small compared to b_{rot} and the single-particle wavefunction will fully encircle the conical intersection and exhibit half-integer quantization.

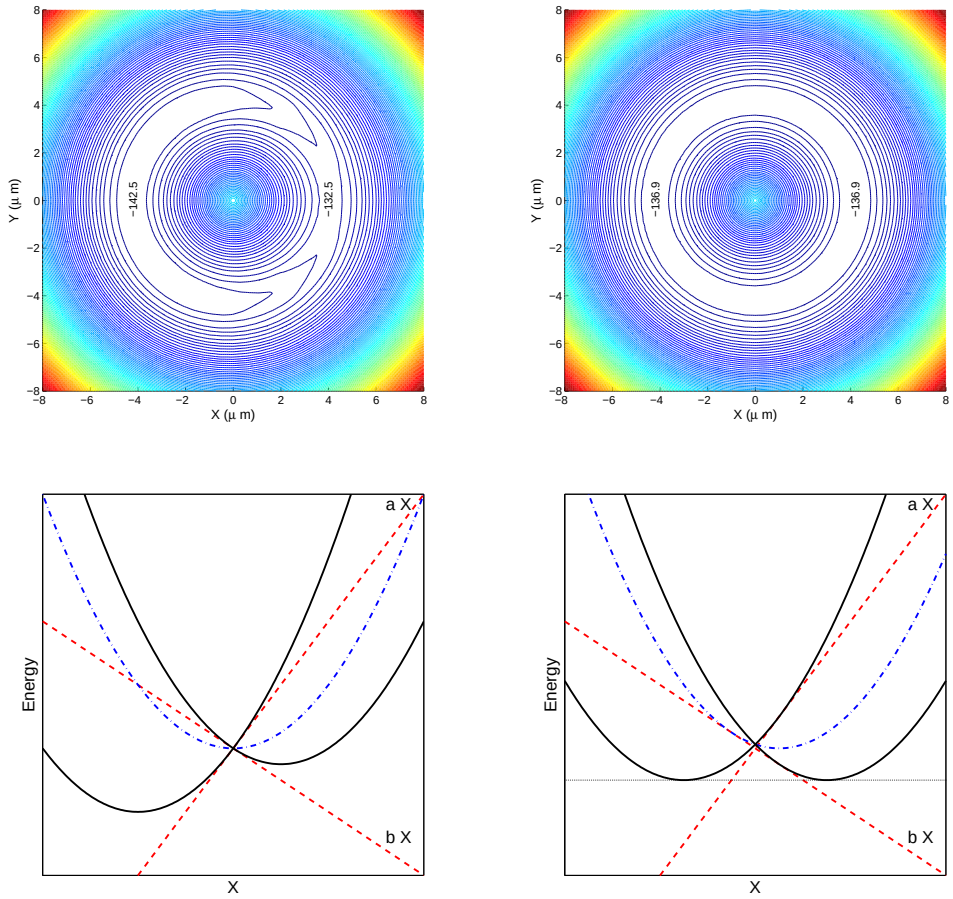

Figure 10.6: Toroidal potentials formed around conical intersections. Left-hand panels: potential formed when the optical trapping potential (7 μK at 30 μm) is centered at the point of intersection (ρ=0), with field gradients 5 G/cm $\hat{\mathbf{X}}$ and 6.8 kV/cm^2 $\hat{\mathbf{Y}}$. Right-hand panels: potential formed when the trapping potential is offset along $\hat{\mathbf{X}}$ by x_0 = 0.0715 μm, with field gradients 5 G/cm $\hat{\mathbf{X}}$ and 6.723 kV/cm^2 $\hat{\mathbf{Y}}$. The electric field gradient is chosen to minimize the anisotropy in each case. The well depths are given in nK relative to the point of intersection. The lower panels show schematic cuts through the potential at $Y = 0$: KRb eigenstates (red, dashed), optical trapping potential (blue, dot-dashed) and the resultant toroidal potential (black, solid).

Chapter 11

Many-Body Physics in Ultracold Gases

In chapter 10 it was shown that a conical intersection could be created in ultracold molecules with externally applied electromagnetic fields and the single-particle energy spectrum was obtained for a molecule in a toroidal trapping potential that encircled the intersection. The presence of the intersection induced half-integer quantization of angular momentum, removing the stationary $m_l = 0$ state and forcing the molecule to rotate in the trap. In reality we are not dealing with isolated molecules but with trapped gases of molecules and therefore an understanding of the many-body interactions between the molecules and their effects on the trapped gas are key.

To go beyond the single-particle states and to start examining many-body effects, we take the simplest case and assume that the toroidal trapping potential is tight, confining the gas to move on a quasi-one-dimensional ring.

11.1 Exact Analysis of a 1D Bose Gas

The physics of one-dimension systems has long been an active area of research, and the recent experimental realization of quasi-one-dimensional Bose-Einstein condensates [136–140] has only served to increase the levels of research in this area. An example of such a one-dimensional system is the Tonks-Girardeau gas of impenetrable bosons, in which the repulsive interactions between particles dominate to such an extent that the bosons cannot exchange places and cannot occupy the same location in space. This effectively mimics the Pauli exclusion principle, forcing the bosons to exhibit fermionic

characteristics. Girardeau [141] showed that in this case, there is a one-to-one mapping between a system of impenetrable bosons and a system of non-interacting fermions, with the two systems showing identical energy spectra. However the bosons don't behave as ideal fermions and the momentum distribution in the two systems differ. Although first considered in 1960 the first experimental realization of a Tonks-Girardeau gas wasn't until 2004 when Paredes et al. [139] observed the effect in a one-dimensional gas of rubidium atoms.

In 1963 Lieb and Liniger [142] generalized Girardeau's result from infinite to finite interaction strengths, deriving a set of $N-1$ exactly soluble coupled equations for N finite spinless bosons in one dimension interacting via a pairwise δ-function interaction. Lieb and Liniger proceeded to explicitly solve this system for two particles and in the thermodynamic limit, in which the length of the one-dimensional box L goes to infinity while the particle density N/L remains constant. However, it wasn't until 1998 that the *exact* solution of the finite-N problem was solved for more than two particles, when Muga and Snider [143] derived the eigenstates and eigenvalues for the three particle problem. So far there has been no exact solutions derived for $N > 3$. However, numerical solutions to the set of coupled equations can be found and in 2005 Sakmann et al. [144] calculated the ground state energy as a function of the interaction strength for $N \leq 50$.

What follows is an outline of Lieb and Liniger's derivation of the $N-1$ coupled equations for a one-dimensional box of length L with periodic boundary conditions, this one-dimensional box is analogous to a ring of circumference L. This is followed by a derivation of the coupled equations with geometric phase boundary conditions applied to the box.

11.2 Exact Analysis with Periodic Boundary Conditions

The Schrödinger equation for N particles in one dimension interacting via a δ-function contact interaction in dimensionless units is

$$\left[-\sum_{i=1}^{N}\frac{\partial^2}{\partial x_i^2}+2c\sum_{<i,j>}\delta(x_i-x_j)\right]\psi=E\psi, \tag{11.1}$$

where $2c$ is the amplitude of the δ-function and for the case of repulsive interactions $c \geq 0$. The δ-function interaction is equivalent to a jump in the derivative of the wavefunction by

$2c$ when the particles touch,

$$\left(\frac{\partial}{\partial x_j} - \frac{\partial}{\partial x_k}\right)\psi|_{x_j=x_k+} - \left(\frac{\partial}{\partial x_j} - \frac{\partial}{\partial x_k}\right)\psi|_{x_j=x_k-} = 2c\psi|_{x_j=x_k}. \tag{11.2}$$

Considering the region, $R : 0 \leq x_i \leq L$, over which ψ is periodic such that

$$\psi(x_1, x_2, \ldots, x_i, \ldots, x_N) = \psi(x_1, x_2, \ldots, x_i + L, \ldots, x_N),$$

a region R_1 can be defined as

$$R_1 : 0 \leq x_1 \leq x_2 \leq \ldots \leq x_N \leq L. \tag{11.3}$$

For identical bosons the knowledge of ψ in R_1 is equivalent to the full knowledge of ψ in R, thus only the region R_1 need be considered. Inside the region R_1 the Schrödinger equation (11.1) and the δ-function boundary conditions (11.2) reduce to

$$-\sum_{i=1}^{N} \frac{\partial^2}{\partial x_i^2}\psi = E\psi \tag{11.4}$$

and

$$\left(\frac{\partial}{\partial x_{j+1}} - \frac{\partial}{\partial x_j}\right)\psi|_{x_{j+1}=x_j} = c\psi|_{x_{j+1}=x_j}. \tag{11.5}$$

Considering the periodic boundary condition for ψ in R, $\psi(x_1 = 0, x_2, \ldots, x_N) = \psi(x_1 = L, x_2, \ldots, x_N)$, it can be seen that the righthand side is not in the region R_1, but by definition $\psi(x_1 = 0, x_2, \ldots, x_N) = \psi(x_2, \ldots, x_N, x_1 = L)$. Therefore the periodic boundary conditions over R are equivalent to

$$\psi(x_1 = 0, x_2, \ldots, x_n) = \psi(x_2, \ldots, x_n, x_1 = L) \tag{11.6}$$

$$\frac{\partial}{\partial x_1}\psi(x_1 = 0, x_2, \ldots, x_n) = \frac{\partial}{\partial x_1}\psi(x_2, \ldots, x_n, x_1 = L), \tag{11.7}$$

in R_1.

11.2.1 The Bethe Ansatz

Lieb and Linigers' solution to the set of equations (11.4,11.5,11.6) was found by by introducing the Bethe ansatz [145, 146] (for an english translation see [147]), which was initially developed by Bethe in 1931 to obtain a solution to the one-dimensional Heisenberg model of magnetism. In the Heisenberg model only pairs of nearest-neighbor spin-$\frac{1}{2}$

particles interact. From the conservation of total angular momentum each eigenstate is a linear combination of all $N!$ states that have the same number of up and down spins. For each of the $N!$ permutated states the ansatz wavefunction is taken as the superposition of single particle plane wave states. Adapting this ansatz to the boson case, we define the ordered set of single particle momenta $\{k\} = (k_1, \ldots, k_N)$, where $k_1 < k_2 < \ldots < k_N$, and take the solution to be a linear combination of all $N!$ permutations of plane wave superpositions

$$\psi(x_1, \ldots, x_N) = \sum_P a(P) P \exp\left(i \sum_{j=1}^{N} k_j x_j \right), \tag{11.8}$$

where $a(P)$ is a coefficient depending on the permutation P.

In order to determine the coefficient $a(P)$ so that ψ satisfies the Schrödinger equation in R_1,

$$E = \sum_{j=1}^{N} k_j^2, \tag{11.9}$$

set $x_1 = x_2$ and let P be the permutation that takes $\{k\}$ into $(p, q, k_3, \ldots, k_N)$ and Q be the permutation that takes $\{k\}$ into $(q, p, k_3, \ldots, k_N)$, where $q = k_1$ and $p = k_2$. Substitution of the P and Q terms of ψ into the R_1 δ-function boundary condition (11.5) gives

$$\begin{aligned} i(q-p)[a(P) - a(Q)] \exp\left(i(p+q)x_1 + \sum_{j=3}^{N} k_j x_j \right) \\ = [a(P) + a(Q)] c \exp\left(i(p+q)x_1 + i \sum_{j=3}^{N} k_j x_j \right), \end{aligned} \tag{11.10}$$

which is satisfied by

$$a(Q) = -a(P) \frac{c - i(q-p)}{c + i(q-p)} = -a(P) \exp(i\theta_{pq}), \tag{11.11}$$

where $\theta_{ij} = \theta(k_i - k_j)$ and

$$\theta(r) = -2 \tan^{-1}(r/c). \tag{11.12}$$

Regarding ψ as a sum of $N!/2$ pairs of P and Q like permutations, (11.11) is substituted back into (11.8) and using the definitions $a(I) = 1$ and $\theta_{kk} = 0$, yields a set of N equations with N unknowns,

$$(-1)^{N-1} e^{-ik_j L} = \exp\left(i \sum_{s=1}^{N} \theta_{sj} \right). \tag{11.13}$$

Taking the product of all N equations in (11.13);

$$((-1)^{N-1})^N \exp\left[-i\sum_{j=1}^{N} k_j L\right] = \exp\left[i\sum_{j=1}^{N}\left(\sum_{s=1}^{N}\theta_{sj}\right)\right], \tag{11.14}$$

and matching exponents gives

$$-\sum_{j=1}^{N} k_j L = \sum_{j=1}^{N}\sum_{s=1}^{N}\theta_{sj}. \tag{11.15}$$

The double summation in (11.15) gives $N^2 - N$ pairs of the form; $\theta_{12} + \theta_{21} + \ldots + \theta_{ab} + \theta_{ba} + \ldots + \theta_{N-1,N} + \theta_{N,N-1}$, and as $\theta_{ij} = -\theta_{ji}$ each of these pairs can be considered independently,

$$\theta_{12} + \theta_{21} = -2\left(\tan^{-1}\left(\frac{k_1 - k_2}{c}\right) + \tan^{-1}\left(\frac{k_2 - k_1}{c}\right)\right) = 0, 2\pi, 4\pi, \ldots, \tag{11.16}$$

and thus considering all pairs, the total momentum is

$$p = \sum_{j=1}^{N} k_j = \frac{2\pi n}{L}, \tag{11.17}$$

where n is an integer. It can also be seen that if $\{k\}$ is a solution to (11.13) then $\{k'\}$ is also a solution where

$$k_i' = k_i + 2\pi n_0/L, \tag{11.18}$$

for any integer n_0. Therefore for any state of momentum p, there exists a state with momentum $p' = p + 2\pi n_0 \rho$ where $\rho = N/L$ and for any state with momentum $|p| \geq \pi\rho$, there is a corresponding state with momentum in the range $-\pi\rho < p \leq \pi\rho$.

11.2.2 The Two-body Solution

To illustrate the above equations, the two-body case is examined in more detail. Starting from the boundary conditions (11.6) and the Bethe ansatz wavefunction (11.8) we have

$$\begin{aligned} \psi(x_1, x_2) &= e^{i(k_1 x_1 + k_2 x_2)} - e^{i\theta_{21}} e^{i(k_1 x_2 + k_2 x_1)} \\ \frac{\partial}{\partial x_1}\psi(x_1, x_2) &= ik_1 e^{i(k_1 x_1 + k_2 x_2)} - ik_2 e^{i\theta_{21}} e^{i(k_1 x_2 + k_2 x_1)} \end{aligned} \tag{11.19}$$

and

$$\begin{aligned} \psi(x_2, x_1) &= e^{i(k_1 x_2 + k_2 x_1)} - e^{i\theta_{21}} e^{i(k_1 x_1 + k_2 x_2)} \\ \frac{\partial}{\partial x_1}\psi(x_2, x_1) &= ik_2 e^{i(k_1 x_2 + k_2 x_1)} - ik_1 e^{i\theta_{21}} e^{i(k_1 x_1 + k_2 x_2)}. \end{aligned} \tag{11.20}$$

Equating the derivatives of the wave functions,

$$\frac{\partial}{\partial x_1}\psi(x_1, x_2)|_{x=0} = \frac{\partial}{\partial x_1}\psi(x_2, x_1)|_{x=L}, \tag{11.21}$$

and matching like terms for k_1 and k_2, gives

$$\begin{aligned} -ik_1 e^{i\theta_{21}} e^{i(k_1 L + k_2 x_2)} &= ik_1 e^{ik_2 x_2} \\ ik_2 e^{i(k_1 x_2 + k_2 L)} &= -ik_2 e^{i\theta_{21}} e^{ik_1 x_2}, \end{aligned} \tag{11.22}$$

which results in equation (11.13) for two particles

$$\begin{aligned} -e^{-ik_1 L} &= e^{i\theta_{21}} \\ -e^{ik_2 L} = e^{i\theta_{21}} &= e^{-i\theta_{12}}. \end{aligned} \tag{11.23}$$

Multiplying both equations in (11.23) and equating exponents gives

$$(k_2 - k_1)\, L = 2\theta(k_2 - k_1) + 2\pi n_1, \tag{11.24}$$

where n_1 is an integer, the second term on the right hand side of (11.24) arises to remove any ambiguity in θ as $\exp(2\pi n_1) = 1$. Defining, $\delta = (k_2 - k_1)L$ and $\gamma = \frac{1}{2}cL$ gives

$$\delta = 2\theta(k_2 - k_1) + 2\pi n_1 = -4\tan^{-1}(\delta/2\gamma) + 2\pi n_1. \tag{11.25}$$

Noting that when $n_1 = 0$ and $\delta = 0$ there is no solution and the allowed values of δ are in the range $2\pi(n_1 - 1) < \delta < 2\pi n_1$, solutions for k_1 and k_2 now can be found from

$$-e^{ik_2 L} = e^{i\frac{\delta}{2}} e^{i\pi n_1} = -e^{-ik_1 L}. \tag{11.26}$$

For odd n_1, $e^{i\pi n_1} = -1$ and

$$\begin{aligned} k_2 L = -k_1 L &= \frac{\delta}{2}, \\ p = \sum_{j=1}^{N} k_j &= 0, \end{aligned} \tag{11.27}$$

for even n_1, $e^{i\pi n_1} = +1$ and

$$\begin{aligned} k_2 L &= \frac{\delta}{2} + \pi \\ k_1 L &= -\frac{\delta}{2} + \pi \\ p &= 2\pi/L. \end{aligned} \tag{11.28}$$

As $n_1 = 0$ has no solution, the two-body ground state corresponds to $n_1 = 1$ and has zero momentum.

11.2.3 N-Body Solution

Having explicitly evaluated the two-body solution, the N-body solution now follows from (11.13). Dividing two successive equations and equating the exponents gives

$$\delta_j \equiv (k_{j+1} - k_j)L = \sum_{s=1}^{N}(\theta_{s,j} - \theta_{s,j+1}) + 2\pi n_j, \tag{11.29}$$

where $j = 1, 2, \ldots, N-1$ and n_j is an integer depending on j, as θ_{kj} is a monotonically increasing function of j, $n_j \geq 1$. It is clear from inspection that

$$k_j = \frac{1}{L}\Big[(k_j - k_{j-1})L - (k_{j-1} - k_{j-2})L - \ldots - (k_2 - k_1)L\Big] + k_1 = k_1 + \frac{1}{L}\sum_{s=1}^{j-1}\delta_s \tag{11.30}$$

and

$$k_\alpha - k_\beta = \frac{1}{L}\sum_{s=\beta}^{\alpha-1}\delta_s, \tag{11.31}$$

where $\alpha > \beta$. From (11.29) and (11.30) it is clear that once the $\delta_{j=1}$ equation for k_1 is satisfied, the rest of the k_j values will follow. Choosing k_1 such that

$$\begin{aligned} k_1 &= -\frac{1}{L}\sum_{s=1}^{N}\theta_{s1} - \frac{2\pi m}{L} + \frac{\epsilon(N)}{L} \\ &= -\frac{1}{L}\sum_{s=1}^{N}\theta\left(\frac{1}{L}\sum_{j=1}^{s-1}\delta_j\right) - \frac{2\pi m}{L} + \frac{\epsilon(N)}{L}, \end{aligned} \tag{11.32}$$

where m is a non-arbitrary integer, $\epsilon(N) = \pi$ for even N and 0 for odd N. The total momentum can be expressed from k_1 as

$$p = \sum_{j=1}^{N}k_j = Nk_1 + \frac{1}{L}\sum_{j=1}^{N-1}(N-j)\delta_j = \frac{1}{L}\sum_{j=1}^{N-1}(N-j)\delta_j - \rho\sum_{j=1}^{N}\theta_{j1} - 2\pi m\rho + \epsilon(N)\rho, \tag{11.33}$$

where $\rho = N/L$ and $-\pi\rho < p \leq \pi\rho$ fixes a value for m.

11.3 Exact Analysis with Geometric Phase Boundary Conditions

Introducing a geometric phase to the ring will impose the following R_1 boundary conditions,

$$\begin{aligned} \psi(x_1 = 0, x_2, \ldots, x_n) &= -\psi(x_2, \ldots, x_n, x_1 = L) \\ \frac{\partial}{\partial x_1}\psi(x_1, x_2, \ldots, x_n)|_{x_1=0} &= -\frac{\partial}{\partial x_1}\psi(x_2, \ldots, x_n, x_1)|_{x_1=L}, \end{aligned} \tag{11.34}$$

but will leave the δ function boundary condition (11.2) unchanged. Starting from the two-body problem the Bethe ansatz wavefunction (11.8) and the boundary conditions (11.34) give

$$\frac{\partial}{\partial x_1}\psi(x_1,x_2)|_{x_1=0} = ik_1 e^{ik_2 x_2} - ik_2 e^{i\theta_{21}} e^{ik_1 x_2}$$
$$\frac{\partial}{\partial x_1}\psi(x_2,x_1)|_{x_1=L} = ik_2 e^{i(k_1 x_2 + k_2 L)} - ik_1 e^{i\theta_{21}} e^{i(k_1 L + k_2 x_2)}$$

which when inserted into the modified geometric phase boundary conditions (11.34) gives

$$e^{-ik_1 L} = e^{i\theta_{21}} = e^{ik_2 L}. \tag{11.35}$$

Similarly, for the three-body problem we have

$$\begin{aligned} -e^{-ik_1 L} &= e^{i(\theta_{21}+\theta_{31})} \\ -e^{-ik_2 L} &= e^{i(\theta_{12}+\theta_{32})} \\ -e^{-ik_3 L} &= e^{i(\theta_{13}+\theta_{23})}. \end{aligned} \tag{11.36}$$

Expanding to the N particle case we find a set of N equation analogous to (11.13)

$$(-1)^N e^{-ik_j L} = \exp\left(i\sum_s \theta_{sj}\right). \tag{11.37}$$

Taking the product of all these N equations in (11.37) and once again matching exponents gives

$$\begin{aligned} N\pi - \sum_j k_j L &= \sum_j \sum_s \theta_{sj}, \\ \sum_j k_j &= \frac{\pi}{L}(2t) - N\pi, \end{aligned} \tag{11.38}$$

where t is an integer, equivalent to n in (11.17). When N is even have simply

$$\sum_j k_j = \frac{\pi}{L} 2t. \tag{11.39}$$

When N is odd, $(-1)^N = -1 = e^{i\pi}$ we have

$$\sum_j k_j = \frac{\pi}{L} 2t + \frac{\pi}{L} = \frac{\pi}{L}(2t+1), \tag{11.40}$$

which can be expressed in a more convenient form for all N as

$$\sum_j k_j = \frac{\pi}{L}(2t + N\mathrm{mod}(2)). \tag{11.41}$$

To examine the nature of this expression for the total momentum, we first observe that for normal boundary conditions (11.6) the system can have zero total momentum (11.17),

$$\sum_j^N k_j = \ldots, -\frac{4\pi}{L}, -\frac{2\pi}{L}, 0, \frac{2\pi}{L}, \frac{4\pi}{L}, \ldots \tag{11.42}$$

for any value of N. In the case of geometric phase boundary conditions the total momentum quantization for N has the form

$$\sum_j^N k_j = \ldots, -\frac{3\pi}{L}, -\frac{\pi}{L}, \frac{\pi}{L}, \frac{3\pi}{L}, \ldots,$$

for odd N, and

$$\sum_j^N k_j = \ldots, -\frac{4\pi}{L}, -\frac{2\pi}{L}, 0, \frac{2\pi}{L}, \frac{4\pi}{L}, \ldots,$$

for even N. As with the case of normal boundary conditions we can once again define

$$\delta_j = (k_{j+1} - k_j)L = \sum_s^N (\theta_{sj} - \theta_{sj+1}) + 2\pi n_j,$$

and as can be easily verified (11.30) still holds, thus k_1 can be chosen as

$$k_1 = -\frac{1}{L}\sum_{s=1}^N \theta_{s1} - \frac{2\pi m'}{L} + \frac{N\pi}{L}, \tag{11.43}$$

where m' is a non-arbitrary integer, and the $N\pi/L$ is just the opposite of $\epsilon(N) = (N-1)\pi$ in (11.32). Lastly the total momentum can again be expressed in terms of k_1 and δ_j's

$$p = \sum_{j=1}^N k_j = Nk_1 + \frac{1}{L}\sum_{j=1}^{N-1}(N-j)\delta_j.$$

Chapter 12

The Properties of a Bose-Einstein Condensate

We have seen in chapter 11 that geometric phase boundary conditions introduce fractionally quantized angular momentum into a one-dimensional gas of bosons. In a truly one-dimensional system Bose-Einstein condensation cannot occur, however in a quasi-one dimensional situation a Bose-Einstein condensate (BEC) can form and toroidaly trapped atomic BECs have been experimentally created [148–150]. Before examining a BEC in a toroidal trap encircling a conical intersection, some of the properties of BECs are examined.

Bose-Einstein condensation was first predicted by Einstein in 1925 [151] using statistical arguments derived by Bose [152] to describe the black-body photon spectrum. Einstein noticed that when a gas of bosons is cooled below a critical temperature T_c, a large fraction of the bosons *condense* into the lowest quantum state. Below this critical temperature the thermal de Broglie wavelength $\lambda_{\mathrm{dB}} = 2\pi/k$ that characterizes the spatial extent of an atom is large enough to overlap with its neighboring atom and the gas becomes a *quantum soup* [4, 5] of indistinguishable particles in the same quantum state.

Despite the predicted existence of a condensate phase in 1925 it wasn't until 1995, 70 years later that the first BECs were observed, when the groups of Cornell and Wieman in JILA, Colorado produced a BEC of rubidium atoms [1] and the group of Ketterle in MIT produced a BEC of sodium atoms [2]. Since then, interest in the field of BECs has exploded and BECs of the all the other alkali metal atoms have been produced:

atomic hydrogen [153], lithium [154], potassium [155], and cesium [156]. Also BECs of: metastable helium [157], chromium [158], and ytterbium [159] have been formed. This year the first BECs of the alkali-earth atoms calcium [160] and strontium [161] have been produced. Even molecular BECs have been produced from BECs and Fermi degenerate gases of alkali metal atoms [25, 162, 163].

12.1 The Gross-Pitaevskii Equation

The Gross-Pitaevskii equation is a mean field theory approach to solving the many-body Schrödinger equation for *N trapped* bosons. In order to develop the theory an effective two-body interaction term is calculated. Which is followed by a derivation of the Gross-Pitaeskii equation from the second quantized Hamiltonian and Heisenberg's equations of motion.

12.1.1 Mean-Field Interaction

Considering the scattering of two particles of equal mass m, with the incoming wave in the Z-direction [13], the wavefunction in coordinate space is given by

$$\psi = e^{ikZ} + \psi_{\text{scat}}(\boldsymbol{r}), \tag{12.1}$$

which for large $\boldsymbol{r}$ becomes

$$\psi = e^{ikZ} + f(\theta)\frac{e^{ikr}}{r}. \tag{12.2}$$

In the low energy limit the scattering amplitude $f(\theta)$ approaches a constant, the s-wave scattering length $-a_s$, and the wave function becomes

$$\psi = 1 - \frac{a_s}{r}. \tag{12.3}$$

Following the derivation given in Pethick and Smith [13], the wavefunction (12.1) in momentum space is

$$\psi(k') = (2\pi)^3\delta(k' - k) + \psi_{\text{scat}}(k'), \tag{12.4}$$

where $\psi_{\text{scat}}(k')$ is the Fourier transform of $\psi_{\text{scat}}(\boldsymbol{r})$. The Fourier transformed Schrödinger equation satisfied by (12.4) is

$$\left(\frac{\hbar^2k^2}{m} - \frac{\hbar^2k'^2}{m}\right)\psi_{\text{scat}}(k') = U(k', k) + \frac{1}{V}\sum_{k''} U(k', k'')\psi_{\text{scat}}(k''), \tag{12.5}$$

where $\hbar^2k^2/m = E$ is the energy eigenvalue and $U(k', k'') = U(k' - k'')$ is the Fourier transform of the bare two-body interaction. The scattering wave is therefore

$$\psi_{\text{scat}}(k') = \left(\frac{\hbar^2k^2}{m} - \frac{\hbar^2k'^2}{m} + i\delta\right)^{-1}\left(U(k', k) + \frac{1}{V}\sum_{k''} U(k', k'')\psi_{\text{scat}}(k'')\right) \tag{12.6}$$

where $i\delta$ has been introduced to ensure that only outgoing waves are present in the scattered wave. This equation can be rewritten in the form,

$$\psi_{\text{scat}}(k') = \left(\frac{\hbar^2k^2}{m} - \frac{\hbar^2k'^2}{m} + i\delta\right)^{-1} T(k', k; \hbar^2k^2/m), \tag{12.7}$$

where the scattering T-matrix satisfies the Lippmann-Schwinger equation,

$$T(k', k; \hbar^2k^2/m) = U(k', k) + \frac{1}{V}\sum_{k''} U(k', k'')\left(E - \frac{\hbar^2k''^2}{m} + i\delta\right)^{-1} T(k'', k; E). \tag{12.8}$$

Using the Fourier transform

$$\int \frac{dk'}{(2\pi)^3}\frac{e^{ik'\cdot r}}{k'^2} = \frac{1}{4\pi r}, \tag{12.9}$$

ψ_{scat} can be found at long range and zero energy ($E = k = 0$)

$$\psi_{\text{scat}} = -\frac{mT(0, 0; 0)}{4\pi\hbar^2 r}. \tag{12.10}$$

Identifying (12.10) with the low energy limit (12.3) implies that,

$$T(0, 0; 0) = \frac{4\pi\hbar^2 a_s}{m}, \tag{12.11}$$

and more generally that the scattering amplitude and the T matrix are related by

$$f(k, k') = -\frac{m}{4\pi\hbar^2}T(k', k; E = \hbar^2k^2/m). \tag{12.12}$$

Dividing the states in the Lippmann-Schwinger equation into states above or below some cutoff value $\epsilon_c = \hbar^2k_c^2/m$, allows the summation over the states in (12.8) to be performed in two stages. Firstly summing over all states above ϵ_c gives the quantity $\tilde{U}(k', k; E)$ that satisfies,

$$\tilde{U}(k', k; E) = U(k', k) + \frac{1}{V}\sum_{k'', k''>k_c} U(k', k'')\left(E - \frac{\hbar^2k''^2}{m} + i\delta\right)^{-1}\tilde{U}(k'', k; E), \tag{12.13}$$

secondly, the correlations from lower-energy states are built in

$$T(k', k; E) = \tilde{U}(k', k; E) + \frac{1}{V}\sum_{k'', k''<k_c} \tilde{U}(k', k; E)\left(E - \frac{\hbar^2k''^2}{m} + i\delta\right)^{-1} T(k', k; E). \tag{12.14}$$

This equation shows that if $\tilde{U}(k', k; E)$ is used as the interaction for a scattering problem in which intermediate states with $k > k_c$ do not appear explicitly, the correct scattering matrix is produced. $\tilde{U}(k', k; E)$ is thus an effective interaction describing interactions between a limited set of states, differing from the bare two-body interaction by the inclusion of high-momentum states. In the limit of $k_c \to 0$, the effective interaction reduces to the scattering T matrix, becoming

$$\tilde{U}(0, 0; 0)|_{k_c \to 0} = \frac{4\pi\hbar^2 a_s}{m} \equiv U_0. \tag{12.15}$$

12.1.2 Heisenberg's Equations of Motion

The Schrödinger equation

$$i\hbar \frac{d}{dt} \mid \psi\rangle = \hat{H} \mid \psi\rangle, \tag{12.16}$$

is satisfied by the general solution

$$\mid \psi(t)\rangle = \exp\left(-\frac{i}{\hbar}\hat{H}(t - t_0)\right) \mid \psi(t_0)\rangle. \tag{12.17}$$

In the Schrödinger description of quantum mechanics the operators are constant and the states evolve in time, whereas in the Heisenberg picture it is the operators that evolve in time and the states that remain constant. The expectation value of a general operator $\hat{A}$ is

$$\langle \hat{A} \rangle = \langle \psi(t) \mid \hat{A} \mid \psi(t) \rangle = \langle \psi(t_0) \mid e^{i\hat{H}t/\hbar} \hat{A} e^{-i\hat{H}t/\hbar} \mid \psi(t_0) \rangle \tag{12.18}$$

from which a general time-dependent operator can be defined as

$$\hat{A}(t) = e^{i\hat{H}t/\hbar} \hat{A} e^{-i\hat{H}t/\hbar}. \tag{12.19}$$

The time-dependence of $\hat{A}(t)$

$$\frac{d}{dt}\hat{A}(t) = \frac{i}{\hbar}\hat{H}e^{i\hat{H}t/\hbar}\hat{A}e^{-i\hat{H}t/\hbar} + \left(\frac{\partial \hat{A}}{\partial t}\right) + \hat{H}e^{i\hat{H}t/\hbar}\hat{A} \cdot \left(-\frac{i}{\hbar}\hat{H}\right)e^{-i\hat{H}t/\hbar} = \frac{i}{\hbar}\left[\hat{H}, \hat{A}\right] + \frac{\partial \hat{A}}{\partial t}, \tag{12.20}$$

is known as Heisenberg's equation of motion and is fully equivalent to the Schödinger equation.

12.1.3 Second Quantization

Following the theory as laid out in [164–167], for N-identical bosons the total symmetric wavefunction can be expanded in a complete basis set formed from all possible tensor

products of the set of single particle eigenstates, $\{\varphi_1(x), \varphi_2(x), \ldots\}$

$$\psi_{N_1 N_2 \ldots}(x_1, x_2, \ldots, x_N) = \sqrt{\frac{N_1! N_2! \ldots}{N!}} \sum_P \varphi_{p_1}(x_1)\varphi_{p_2}(x_2)\ldots\varphi_{p_N}(x_N), \tag{12.21}$$

where there are N_i particles in eigenstate $\varphi_i(x)$. In this basis a one-particle excitation operator that generates the function φ_p for each occurrence of φ_q, can be defined as,

$$\hat{E}_{pq} = \sum_{i=1}^{N} \mid \varphi_p(x_i)\rangle\langle\varphi_q(x_i) \mid . \tag{12.22}$$

Similarly it is possible to define a two-particle excitation operator,

$$\hat{E}_{pq,rs} = \sum_{i\neq j}^{N} \mid \varphi_p(x_i)\rangle\langle\varphi_q(x_i) \mid \quad \mid \varphi_r(x_j)\rangle\langle\varphi_s(x_j) \mid, \tag{12.23}$$

a three-particle excitation operator $\hat{E}_{pq,rs,tu}$, and so on. As the wavefunction Ψ is constructed of an N-fold product of single-particle functions φ_i the following completeness identity is true for all i,

$$\left(\sum_p \mid \varphi_p(x_i)\rangle\langle\varphi_p(x_i) \mid\right)\Psi = \Psi. \tag{12.24}$$

Given a Hamiltonian containing a one-body operator $\hat{h}(x_i)$ and a two-body operator $\hat{U}(x_i, x_j)$,

$$\hat{H} = \sum_i^N \hat{h}(x_i) + \sum_{i<j}^N \hat{U}(x_i, x_j), \tag{12.25}$$

the *second quantized Hamiltonian* can be constructed using (12.24),

$$\begin{aligned}
\hat{H} &= \sum_i^N \sum_{pq} \mid \varphi_p(x_i)\rangle\langle\varphi_p(x_i) \mid \hat{h}(x_i) \mid \varphi_q(x_i)\rangle\langle\varphi_q(x_i) \mid \\
&+ \sum_{i<j}^N \sum_{pqrs} \mid \varphi_p(x_i)\rangle \mid \varphi_r(x_j)\rangle\langle\varphi_r(x_j) \mid \langle\varphi_p(x_i) \mid \hat{U}(x_i, x_j) \mid \varphi_q(x_i)\rangle \mid \varphi_s(x_j)\rangle\langle\varphi_s(x_j) \mid \langle\varphi_q(x_i) \mid \\
&= \sum_{pq} h_{pq}\hat{E}_{pq} + \frac{1}{2}\sum_{pqrs} U_{pq,rs}\hat{E}_{pq,rs},
\end{aligned} \tag{12.26}$$

where

$$h_{pq} = \langle\varphi_p \mid \hat{H} \mid \varphi_q\rangle = \int dx_1 \varphi_p^*(x_1)\hat{h}(x_1)\varphi_q(x_1) \tag{12.27}$$

and

$$\begin{aligned}
U_{pq,rs} &= \langle\varphi_p \mid \langle\varphi_r \mid \hat{U}(x_1, x_2) \mid \varphi_q\rangle \mid \varphi_s\rangle \\
&= \iint dx_1 dx_2 \varphi_p^*(x_1)\varphi_r^*(x_2)\hat{U}(x_1, x_2)\varphi_q(x_1)\varphi_s(x_2).
\end{aligned} \tag{12.28}$$

Fock Space

Combining the excitation-operators with the tensor-product basis (12.21) can make the Hamiltonian independent of the number of particles present. Fock space is the direct sum of the N-fold single-particle tensor-product Hilbert spaces for $N = 0, 1, 2, \ldots$, in which the basis states are uniquely defined by an integer occupation number,

$$\psi_{N_1 N_2 \ldots}(x_1, x_2, \ldots, x_N) = \langle x_1, x_2, \ldots, x_N \mid N_1, N_2, \ldots \rangle. \tag{12.29}$$

$\mid N_1, N_2, \ldots\rangle$ is the Fock (occupation number) representation, that contains states for unlimited and variable numbers of particles. For bosons the occupation number can be any integer but for fermions the occupation number can be either zero or one. Different ranks of the Fock space are connected by the creation $\hat{a}^\dagger$ and annihilation operators $\hat{a}$,

$$\begin{aligned} \hat{a}_p^\dagger \mid N_1, N_2, \ldots, N_p, \ldots\rangle &= \mid N_0, N_1, \ldots, N_p + 1, \ldots\rangle \\ \hat{a}_p \mid N_1, N_2, \ldots, N_p, \ldots\rangle &= \mid N_0, N_1, \ldots, N_p - 1, \ldots\rangle, \end{aligned}$$

and thus the entire Fock space can be constructed from just the zero-particle vacuum state and the creation operator.

In the Fock space representation the second-quantized hamiltonian becomes,

$$\begin{aligned} \hat{H} &= \sum_{pq} \int dx_1 \varphi_p^*(x_1) \hat{h}(x_1) \varphi_q^*(x_1) \hat{a}_p^\dagger \hat{a}_q \\ &\quad + \frac{1}{2} \sum_{pqrs} \iint dx_1 dx_2 \varphi_p^*(x_1) \varphi_r^*(x_2) \hat{U}(x_1, x_2) \varphi_q(x_1) \varphi_s(x_2) \hat{a}_p^\dagger \hat{a}_r^\dagger \hat{a}_q \hat{a}_s \qquad (12.30) \\ &= \int dx_1 \Psi^\dagger(x_1) \hat{h}(x_1) \Psi(x_1) + \iint dx_1 dx_2 \Psi^\dagger(x_1) \Psi^\dagger(x_2) \hat{U}(x_1, x_2) \Psi(x_1) \Psi(x_2), \qquad (12.31) \end{aligned}$$

where $\Psi(x) = \sum_j \hat{a}_j \varphi_j(x)$ is a quantum field operator, annihilating a particle a position x. The many-body Hamiltonian describing N interacting bosons in an external potential V, in second quantized form, is given by

$$\hat{H} = \int d\boldsymbol{r} \hat{\Psi}^\dagger(\boldsymbol{r}) \left[-\frac{\hbar^2}{2m} \nabla^2 + V(\boldsymbol{r}) \right] \hat{\Psi}(\boldsymbol{r}) + \frac{1}{2} \iint d\boldsymbol{r} d\boldsymbol{r}' \hat{\Psi}^\dagger(\boldsymbol{r}) \hat{\Psi}^\dagger(\boldsymbol{r}') U(\boldsymbol{r} - \boldsymbol{r}') \hat{\Psi}(\boldsymbol{r}) \hat{\Psi}(\boldsymbol{r}'), \tag{12.32}$$

where $U(\boldsymbol{r} - \boldsymbol{r}')$ is the two-body interaction potential.

12.1.4 The Gross-Pitaevskii Equation

For a dilute Bose gas it was shown in section 12.1.1 that at low temperatures the interaction potential can be represented by

$$U(\boldsymbol{r}-\boldsymbol{r}') = \frac{4\pi\hbar^2 a_s}{m}\delta(\boldsymbol{r}-\boldsymbol{r}'). \tag{12.33}$$

The Hamiltonian thus takes the form,

$$\hat{H} = \int d\boldsymbol{r}\hat{\Psi}^\dagger(\boldsymbol{r})\left[-\frac{\hbar^2}{2m}\nabla^2 + V(\boldsymbol{r})\right]\hat{\Psi}(\boldsymbol{r}) + \frac{2\pi\hbar^2 a_s}{m}\iint d\boldsymbol{r}\hat{\Psi}^\dagger(\boldsymbol{r})\hat{\Psi}^\dagger(\boldsymbol{r})\hat{\Psi}(\boldsymbol{r})\hat{\Psi}(\boldsymbol{r}), \tag{12.34}$$

and the Heisenberg equation of motion for $\hat{\Psi}$ is

$$i\hbar\frac{d}{dt}\hat{\Psi}(\boldsymbol{r}) = \left[\hat{\Psi}(\boldsymbol{r}), \hat{H}\right] = \left[-\frac{\hbar^2}{2m}\nabla^2 + V(\boldsymbol{r})\right]\hat{\Psi}(\boldsymbol{r}) + \frac{4\pi\hbar^2 a_s}{m}\iint d\boldsymbol{r}\hat{\Psi}^\dagger(\boldsymbol{r})\hat{\Psi}(\boldsymbol{r})\hat{\Psi}(\boldsymbol{r}). \tag{12.35}$$

In general any operator can be spilt into its expectation value plus a fluctuating term,

$$\hat{\Psi}(\boldsymbol{r},t) = \phi(\boldsymbol{r},t) + \hat{\Psi}'(\boldsymbol{r},t), \tag{12.36}$$

where $\phi(\boldsymbol{r},t) = \langle\hat{\Psi}(\boldsymbol{r},t)\rangle$ fixing the condensate density $N_0 =\mid \phi(\boldsymbol{r},t) \mid^2$. $\hat{\Psi}'(\boldsymbol{r},t)$ is the fluctuating term and can be treated as a small perturbation to $\hat{\Psi}(\boldsymbol{r},t)$. The function $\phi(\boldsymbol{r},t)$ is a classical field and its modulus fixes the condensate density through $N_0 =\mid \phi(\boldsymbol{r},t) \mid^2$. $\hat{\Psi}'(\boldsymbol{r},t)$ can be taken to be small when the depletion of the condensate is small, and its neglect gives a non-trivial "zeroth-order" theory for $\phi(\boldsymbol{r},t)$,

$$i\hbar\frac{\partial}{\partial t}\phi(\boldsymbol{r},t) = \left[-\frac{\hbar^2}{2m}\nabla^2 + V(\boldsymbol{r})\right]\phi(\boldsymbol{r},t) + \frac{4\pi\hbar^2 a_s}{m}\left|\phi(\boldsymbol{r},t)\right|^2\phi(\boldsymbol{r},t), \tag{12.37}$$

the time-dependent Gross-Pitaevskii equation (GPE). Its validity is based on the s-wave scattering length being smaller than the average distance between particles in the condensate and that the number of atoms in the condensate N_0 is large. Defining $\psi(\boldsymbol{r},t) = \phi(\boldsymbol{r},t)/\sqrt{N}$, such that $\psi(\boldsymbol{r},t)$ is unit normalized the Gross-Pitaevskii equation becomes

$$i\hbar\frac{\partial}{\partial t}\psi(\boldsymbol{r},t) = \left[-\frac{\hbar^2}{2m}\nabla^2 + V(\boldsymbol{r})\right]\psi(\boldsymbol{r},t) + \frac{4\pi\hbar^2 a_s N}{m}\left|\psi(\boldsymbol{r},t)\right|^2\psi(\boldsymbol{r},t). \tag{12.38}$$

As $\hat{\Psi}$ reduces the number of particles by one, the off-diagonal matrix element $\langle N-1 \mid \hat{\Psi}(\boldsymbol{r}) \mid N\rangle$ oscillates at a frequency corresponding to the chemical potential $\mu \approx E_0(N) - E_0(N-1)$ thus the stationary solutions to (12.37) have the form $\psi(\boldsymbol{r},t) = \psi(\boldsymbol{r})\exp(-i\mu t/\hbar)$,

which when substituted into the time-dependent GPE results in the time-independent GPE,

$$\left[-\frac{\hbar^2}{2m}\nabla^2 + V(\boldsymbol{r})\right]\psi(\boldsymbol{r}) + \frac{4\pi\hbar^2 a_s N}{m}\left|\psi(\boldsymbol{r})\right|^2\psi(\boldsymbol{r}) = \mu\psi(\boldsymbol{r}). \tag{12.39}$$

In the absence of interactions, $a_s = 0$, this equation reduces to the single-particle Schrödinger equation.

In certain cases the GPE can be solved analytically [168, 169], however it can also be solved numerically [170–172]. As an example, the GPE can be solved numerically for the ground state. This involves solving the time-dependent GPE in the absence of non-linear terms, and propagating these solutions through time using the Crank-Nicolson numerical method [171]. The value of the non-linear constant $4\pi\hbar^2 a_s N/m$ is adiabatically increased or decreased at each time step until a desired value for the non-linearity is reached. The resulting solution is the ground state of time-independent GPE corresponding to the desired value of $4\pi\hbar^2 a_s N/m$.

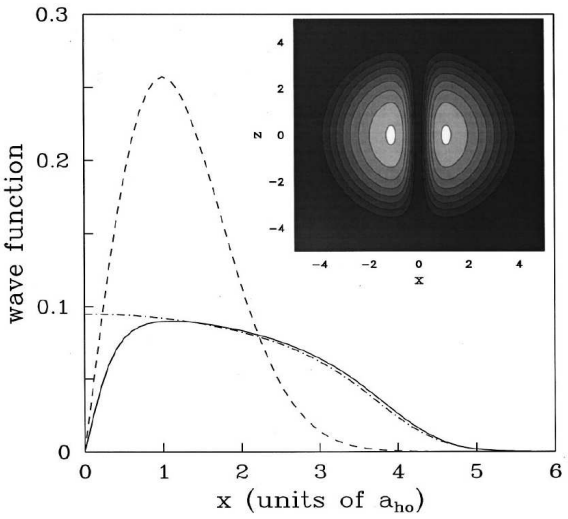

Figure 12.1: Condensate with a quantized vortex along the Z axis. $\psi_v(X, 0, 0)$ calculated for 10^4 Rb atoms in a spherical trap with $a_{\text{ho}} = 0.791$ μm. The dot-dashed line is the solution for $\kappa = 0$, the solid line is for $\kappa = 1$, and the dashed line is the non-interacting $\kappa = 1$ solution. The inset shows the condensate density in the XZ plane. Image from [167].

12.2 Vortices in a BEC

One striking feature of a BEC is its superfluid behaviour, a characteristic sign of which is the formation of quantized vortices in a rotating condensate [167, 173]. The structure of vortices can be investigated by starting from the GPE. The macroscopic wavefunction for a quantized vortex along the Z-axis has the form

$$\psi(\boldsymbol{r}) = \psi_v(r_\perp, Z)e^{i\kappa\phi}, \tag{12.40}$$

where ϕ is the angle around Z, and the angular momentum along Z is $N\hbar\kappa$, where the integer κ is the quantum of circulation characterizing the tangential velocity of the vortex state,

$$v = \frac{\hbar}{mr_\perp}\kappa. \tag{12.41}$$

The circulating velocity gives rise to an extra centrifugal term, $\frac{1}{2}mv^2 = \hbar^2\kappa^2/2mr_\perp^2$, that pushes the condensate away from the Z axis for non-zero κ, the resulting GPE takes on

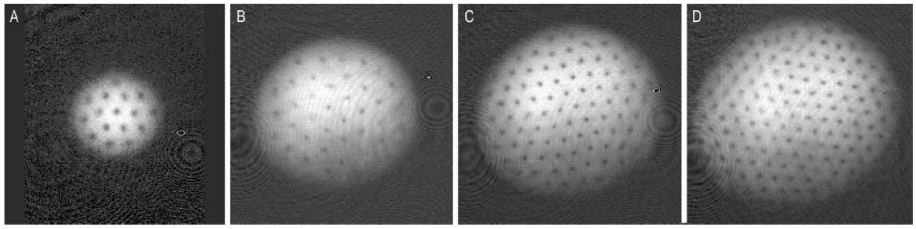

Figure 12.2: Vortex lattices of approximately 16, 32, 80, and 130, vortices in a laser-stirred BEC of Na atoms. Image from [174].

the form

$$\left[-\frac{\hbar^2}{2m}\nabla^2 + \frac{\hbar^2\kappa^2}{2mr_\perp^2} + V(r_\perp, Z)\right]\psi_v(r_\perp, Z) + \frac{4\pi\hbar^2 a_s N}{m}\left|\psi_v(r_\perp, Z)\right|^2\psi_v(r_\perp, Z) = \mu\psi_v(r_\perp, Z). \tag{12.42}$$

For a non-interacting system, $a_s = 0$, (12.42) has analytic solutions, and for $\kappa = 1$ in a harmonic trap

$$\psi_v^{\kappa=1}(r_\perp, Z) \propto r_\perp \exp\left[-\frac{m}{2\hbar}(\omega_\perp r_\perp^2 + \omega_Z Z^2)\right] \tag{12.43}$$

In this case the vortex state corresponds to having all particles in the first rotational single particle state, the energy of which is the ground state energy plus $N\hbar\omega_\perp$. Figure 12.1 shows the non-interacting solution (12.43) (dashed line) in a spherical harmonic trap, as well as the interacting solution with repulsive interactions for $\kappa = 0$ (dot-dashed line) and $\kappa = 1$ (solid line), it can be seen that the repulsive interactions present broaden the condensate.

In a frame rotating with an angular frequency Ω, the energy of the system with angular momentum L_Z is $(E - \Omega L_Z)$ and the creation of a vortex becomes favorable above some critical frequency $\Omega_c = (\hbar/\kappa)^{-1}\left[(E/N)_\kappa - (E/N)_0\right]$ where E_κ is the energy of the system in the presence of a vortex with angular momentum $N\hbar\kappa$. Creating vortices with $\kappa > 1$ is generally unstable with respect to forming κ singly quantized vortices and arrays of multiple vortices can form [174]. In this case the density of vortices is given by,

$$n_v = \frac{N_v}{A_v} = \frac{2\Omega}{\kappa}, \tag{12.44}$$

where N_v is the total number of vortices and A_v is the area of a single vortex. (12.44) is directly analogous to the density of vortices (flux lines) $n_v = B/\Phi_0$ in a type-II superconductor, where B is the magnetic flux density and $\Phi_0 = h/2e$ is the quanta of magnetic flux.

A number of different schemes have been used to create vortices. The first scheme to be used successfully uses laser beams to modify the phase of the condensate and induce a vortex state [175–177]. Applying this scheme to a two-component condensate resulted in the first observation of a vortex in a BEC [178, 179]. Another scheme is to create vortices by physically rotating or *stirring* the trap anisotropy of the condensate with a laser beam [174, 180, 181]. Vortices have also been *topologically imprinted* into a spinor BEC by adiabatically inverting the magnetic field bias along the trapping axis [182–184].

Chapter 13

A BEC in a Toroidal Trap

Atomic BECs have recently been created in toroidal trapping geometries [148–150], and persistent flow around the toroidal trap has been observed [148]. The possibility of forming half-integer quantized vortices within a spinor atomic BEC has been investigated theoretically [185–188], as have a variety of differing consequences of geometric phase effects in atomic BEC systems [189–192]. In this chapter it is shown that in the mean-field approximation of the Gross-Pitaevskii equation, the geometric phase effect creates stable states of persistent flow that are characterized by half-integer quantized angular momentum.

A BEC of a dilute gas may be modeled by the time-independent Gross-Pitaevskii equation (GPE) in a toroidal trap,

$$\left[-\frac{\hbar^2}{2m}\nabla^2 + V(\boldsymbol{r}) + u(\phi)\,|\psi(\rho,\phi,Z)|^2\right]\psi(\rho,\phi,Z) = \mu\psi(\rho,\phi,Z), \tag{13.1}$$

where μ is the chemical potential and $\psi(\boldsymbol{r})$ is the mean-field wavefunction normalized to unity, $\int \psi^*(\boldsymbol{r})\psi(\boldsymbol{r})d\tau = 1$ and the angular dependent effective interaction strength is given by

$$u(\phi) = \frac{4\pi\hbar^2 N a_s(\phi)}{m}. \tag{13.2}$$

The angular dependence of the effective interaction arises if the two states that form the conical intersection have different s-wave scattering lengths. Writing the internal molecular wavefunction, in terms of the individual molecular states ψ_1 and ψ_2 at an angle ϕ as

$$\psi(\phi) = \psi_1 \cos(\phi/2) + \psi_2 \sin(\phi/2). \tag{13.3}$$

The angular dependent scattering length $a_s(\phi)$ is thus

$$a_s(\phi) = \frac{1}{8}(3a_{11} + 3a_{22} + 2a_{12}) + \frac{1}{2}(a_{11} - a_{22})\cos\phi + \frac{1}{8}(a_{11} + a_{22} - 2a_{12})\cos 2\phi, \quad (13.4)$$

where a_{ij} is the scattering length for interaction between molecules in states i and j. An effective 1D GPE can now be obtained by averaging over the radial and vertical wavefunctions, giving

$$\left[-b_{\rm rot}\frac{\partial^2}{\partial\phi^2} + \tilde{u}(\phi)\,|\Phi(\phi)|^2\right]\Phi(\phi) = \tilde{\mu}\Phi(\phi) \quad (13.5)$$

where

$$\tilde{u}(\phi) = \frac{4\pi\hbar^2 N a_s(\phi)}{m}\iint |\psi(\rho)|^4|\varphi(Z)|^4\rho\,d\rho\,dZ \quad (13.6)$$

and $\mu = \tilde{\mu} + \left(\nu_Z + \frac{1}{2}\right)\hbar\omega_Z + \left(\nu_\rho + \frac{1}{2}\right)\hbar\omega_\rho - b_{\rm rot}/4$. For a flat ring the effective 1D GPE has analytical solutions of the form

$$\Phi(\phi) = \frac{e^{im_l\phi}}{\sqrt{2\pi}}, \quad (13.7)$$

with eigenvalues, $\tilde{\mu} = b_{\rm rot}m_l^2 + \tilde{u}/(2\pi)$. With the geometric phase boundary conditions applied, the same set of half-integer quantized solutions are obtained analogous to the single-particle case.

For a slightly anisotropic potential, two classes of solution, for small interactions, exist that satisfy the boundary conditions: flowing solutions $\Phi^{\pm}_{m_l^{\rm half}}(\phi) = (2\pi)^{-1/2}\exp(im_l^{\rm half}\phi)$, and static solutions such as $\Phi^{0}_{m_l^{\rm half}}(\phi) \approx \pi^{-1/2}\cos(m_l^{\rm half}\phi)$. For a trap with a residual anisotropy $V(\phi) = -V_1\cos\phi - V_2\cos 2\phi$ and an angle-dependent effective interaction strength $\tilde{u}(\phi) = u_0 + u_1\cos\phi + u_2\cos 2\phi$, approximate chemical potentials corresponding to these two Ansatzes are obtained: $\tilde{\mu}^{\pm}_{1/2} \approx b_{\rm rot}/4 + u_0/(2\pi)$ and $\tilde{\mu}^{0}_{1/2} \approx b_{\rm rot}/4 - V_1/2 + 3u_0/(4\pi) - u_1/(2\pi) - u_2/(8\pi)$. In this approximation, a flowing state with $m_l^{\rm half} = \pm 1/2$ is the ground state if $2u_1 + u_2/2 + 2\pi V_1 < u_0$. However, for any given $a(\phi)$ and condensate number, an offset can be applied to the optical potential sufficient to compensate for the anisotropy of the interaction term and stabilize the flowing state.

With a conical intersection present, the velocity of the persistent flow can only assume half-integer quantized values compared to the integer quantized circulation that occurs in the more conventional situation. The persistent flow should be observable by releasing the trapped particles and using time-of-flight techniques [148].

An atomic BEC with repulsive interactions would usually be stable in a toroidal trap but the presence of an electric dipole moment in KRb will effect the stability of the BEC.

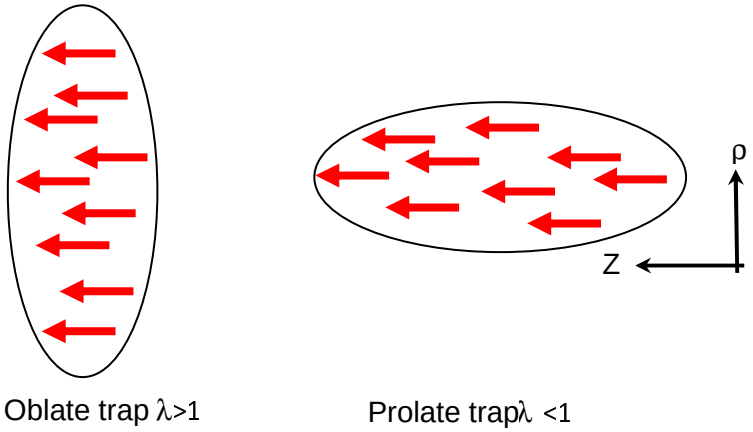

Figure 13.1: Oblate and prolate trapping geometries for dipolar condensates. In an oblate trap the dipoles mainly repel each other stabilizing the condensate and in a prolate trap the interaction is predominately attractive destabilizing the condensate.

13.1 Stability of a Dipolar BEC

Dipolar BECs (a BEC of particles with a magnetic or electric dipole moment) have been the subject of much experimental and theoretical research [193–195]. For a non-polar BEC the stability is dependent on a_s: for $a_s > 0$ the resulting repulsive mean-field interaction accounts for an outward pressure that inflates and stabilizes the condensate against collapse, for $a_s < 0$ the attractive interaction encourages the collapse of the condensate into a high density lump in the center of the trap, the result is that the BEC is stable only up to a critical number of atoms $N_c \approx a_{\text{osc}}/|a_s|$, where a_{osc} is the harmonic oscillator length $a_{\text{osc}} = \sqrt{\hbar/(m\overline{\omega})}$ and $\overline{\omega}$ is the mean trapping frequency.

It is clear that the anisotropic, long-range $(1/r^3)$ dipole-dipole interaction will alter the stability of a BEC. For dipolar particles that are *dipoles are strictly aligned along Z*, the interaction between then is given by

$$V(\boldsymbol{r}) = \frac{d_Z^2(1 - 3\cos^2\theta)}{\boldsymbol{r}^3} + \frac{4\pi\hbar^2 a_s}{m}\delta(\boldsymbol{r}), \tag{13.8}$$

where d_Z is the effective dipole moment for a particle in a field (along Z) with a body-fixed dipole moment d. Considering the particles to be trapped in a cylindrically symmetric harmonic trap

$$V_{\text{trap}}(\rho, Z) = \frac{1}{2}m\left(\omega_\rho^2\rho^2 + \omega_Z^2 Z^2\right) \tag{13.9}$$

the stability of a dipolar BEC depends on a_s and the aspect ratio of the trap $\lambda = \omega_Z/\omega_\rho$. In a pancake-shaped (oblate) trap ($\lambda > 1$) the dipoles repel each other and the BEC is stable, however in a cigar-shaped (prolate) trap ($\lambda < 1$) the dipoles attract one another and the trap is unstable, Figure 13.1 shows schematic diagrams of the two trapping geometries. Thus for the prolate case a positive scattering length is required to stabilize the trap, but in the oblate case a slightly negative scattering length can be afforded. To compare the contact interaction to the dipole-dipole interactions a characteristic length scale of the dipole-dipole interaction can be introduced [194]

$$a_{\mathrm{d}} = \frac{|d_Z^2|m}{12\pi\epsilon_0\hbar^2}. \tag{13.10}$$

If the dipole length a_{d} exceeds a_s the condensate becomes unstable and can undergo dipolar collapse.

The proposed BEC of KRb molecules is only stable if $a_s(\phi) > 0$ for all ϕ. From (13.4), this requires that both a_{11} and a_{22} are positive and that $2a_{12} > -(a_{11} + a_{22})$ and if $a_s(\phi) > a_{\mathrm{d}}$. The molecular wavefunction is given by (13.3) and there is a direct dipole moment matrix element $\langle 1|d|2\rangle$ between the two states the space fixed effective dipole moment is $d_Z = \langle 1|d|2\rangle \sin\phi$. For the two states of KRb considered here, $\langle 1|d|2\rangle \approx 10^{-32}$ Cm, giving $a_{\mathrm{d}} \approx 5 \times 10^{-12}$ m, which is substantially smaller than typical optical scattering lengths so in this case dipolar collapse is unlikely.

13.2 Future Work

Further insight into the effect of a conical intersection on a toroidal BEC could be found by numerically solving Lieb and Liniger's coupled equations for a 1D Bose gas with anti-periodic BC's using similar methods to those developed by Sakmann et al. [144]. Further insight could also be gained into the persistent flow and half-integer vortex formation by solving the hydrodynamic equations for the BEC [13]. There may also be interesting phase and interference effects if the fields were swept in a way to take the molecules around the conical intersection.

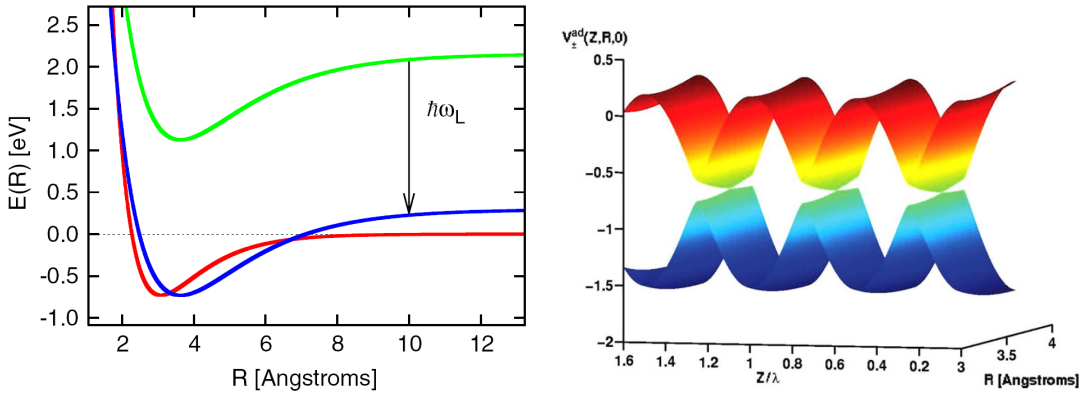

Figure 13.2: Left: Potential energy curves $E_0(R)$ and $E_1(R)$ associated with the electronic states $X^1\Sigma_g^+$ and $A^1\Sigma_u^+$ of Na_2. Also shown is the shifted $E_1(R)-\hbar\omega_L$ curve. Right: Periodic array of conical intersections at $\theta = 0$, the lower crossing point of $E_0(R)$ and $E_1(R) - \hbar\omega_L$ is examined. Images from [196].

13.2.1 Photon Induced Conical Intersections

The electromagnetic field arrangement proposed here; magnetic field orientated along Z with a field gradient dB_Z/dX and an electric field orientated along X with a gradient dE_X/dY, is not the easiest to create experimentally. Therefore rather than using a static electric field the electric field from a standing laser wave could be used.

Recently Moiseyev et al. [196] proposed creating an array of conical intersections between electronic states in a diatomic molecular optical lattice, in which two electronic states ψ_0^{elec} and ψ_1^{elec} with electronic energies $E_0(R)$ and $E_1(R)$, are coupled by the linearly polarized laser light. Taking the laser to be orientated along Z with a frequency ω_L, wave vector $k_L = \omega_L/c$ and maximum field amplitude ϵ_0, the 2×2 matrix Hamiltonian is proportional to,

$$\begin{pmatrix} E_1(R) - \hbar\omega_L & \epsilon_0 \cos\theta \cos(k_L Z) d(R)/2 \\ \epsilon_0 \cos\theta \cos(k_L Z) d(R)/2 & E_0(R) \end{pmatrix}, \tag{13.11}$$

where $d(R)$ is the dipole moment responsible for the light-induced electronic transition and θ is the angle between the diatomic molecule (with bond length R) and Z. The effective Hamiltonian (13.11) gives rise to a conical intersection when

$$\cos\theta \cos(k_L Z) = 0 \tag{13.12}$$

and

$$E_1(R) - E_0(R) = \hbar\omega_L. \tag{13.13}$$

Taking the example of the Na_2 dimer with electronic states $X^1\Sigma_g^+$ and $A^1\Sigma_u^+$ which are coupled with a laser wavelength of 667 nm, figure 13.2 shows the potential energy curves $E_0(R)$ and $E_1(R)$ associated with the electronic states $X^1\Sigma_g^+$ and $A^1\Sigma_u^+$, and the adiabatic potential energy surfaces for $\theta = 0$ exhibiting a periodic array of conical intersections.

There are in fact there are two branches of conical intersections one in the (R, Z)-plane for arbitrary values of θ ($\theta \neq \pi/2$) and one in the (R, θ)-plane for arbitrary values of $Z \neq (n + 1/2)(\pi/k_L)$ (integer n).

The conical intersection proposed by Moiseyev et al. [196] is still dependent on intramolecular properties, namely the interatomic distance. However two arbitrary Zeeman states of opposite parity in a magnetic field could be coupled by the laser field of an optical lattice. A periodic array of conical intersections would then be formed at nodes in the lattice $Z = (n + 1/2)(\pi/k_L)$ (integer n). The clear advantages of using a laser standing wave is that an atomic BEC could be used, removing the experimental inherent in creating a dipolar molecular BEC.

Chapter 14

Conclusions

The field of ultracold molecules is about to explode; ultracold atoms have been produced in large densities for over 15 years, but samples of ultracold molecules are only just starting to be produced in high densities [30–33]. The ability to produce samples of ultracold molecules opens up many new possibilities in atomic and molecular physics, such as the study of many-body physics, high precision spectroscopic measurements, and ultracold collisional and chemical processes.

Magnetic Feshbach resonances are an important feature of ultracold matter and have been used to magnetically associate atoms into diatomic molecules [27]. Asymmetries present in cross sections over these magnetic Feshbach resonances could be used to suppress inelastic loss rates, which would be important for evaporative and sympathetic cooling schemes. Generalizing BOUND and MOLSCAT to incorporate both magnetic and electric fields allowed studies to be performed on He+SO Feshbach resonances in combined electromagnetic fields, as detailed in chapter 4. It was found that a magnetic Feshbach resonance occurred only in the presence of an additional electric field, the cause of this effect is as yet unexplained.

In chapters 5-8, detailed calculations on spin-changing collisions for NH($^3\Sigma^-$)($n = 0$) in a low-field seeking state colliding with Mg atoms are presented. It was found that for a wide range of collision energies and magnetic field strength the ratio of elastic to total inelastic cross sections γ exceeds 100, the factor required for sympathetic cooling to succeed. Thus, if precooled NH molecules are produced at a temperature of around 10 mK can be brought into contact with laser-cooled Mg, there is a good prospect that

sympathetic cooling will succeed. As the temperature decreases the rate of inelastic loss decreases even further, such that once sympathetic cooling begins it will continue. This is the first time that sympathetic cooling of a molecular system that has a good prospect of success has been reported.

Near a resonance the Mg+NH near-threshold inelastic cross sections deviated from a simple single-parameter fitting formula first derived by Volpi and Bohn [93]. However, the form of the inelastic cross section can be understood even in the vicinity of a resonance by using a multichannel quantum defect theory (MQDT) approach. At low temperatures the scattering is dominated by the long-range part of the potential energy surface, and in MQDT the scattering is treated as the scattering by a long-range potential modified by a short-range energy insensitive quantum-defect. Using an analytical angular-momentum insensitive quantum-defect approach for a van der Waals potential, that requires just the reduced mass, C_6, and the s-wave scattering length, the form of the Mg+NH inelastic scattering cross-section is reproduced.

The success of the MQDT approach, offers the hope that the low-energy scattering in applied electromagnetic fields could be understood by numerically calculating the short-range quantum defect from a *small number* of zero-field coupled channel calculations. This would allow scattering properties to be understood without having to perform computationally expensive coupled channel calculations at many different field points. In Mg+NH, the coupled channel calculations were affordable, however in larger or more coupled systems such as NH+NH, in which far more channels are required for convergence, the coupled channel calculations may not be affordable and using an MQDT approach could be the way forward.

For electric field induced avoided crossing between states of the opposite parity that cross as a function of magnetic field, it has been shown that these crossings are in fact a new type of conical intersection in electromagnetic field space. With the correct arrangement of electromagnetic fields applied to an optically trapped molecular Bose-Einstein condensate, a conical intersection of this type can be created within the condensate. The geometric phase effect induced by the conical intersection would create novel superfluid states characterized by half-integer quantized angular momentum, rather than the more usual integer quantized angular momentum. Although polar molecules in static fields

were considered, the effect is more general and it should be possible to induce similar avoided crossings using a laser field to bring two separated states into near degeneracy and a magnetic field to provide a crossing, with conical intersections appearing at nodes in the laser amplitude.

Appendix A

Coupling of Angular Momentum

Before coupling multiple angular momenta terms the general angular momentum operator $\hat{j} = \hat{j}_x + \hat{j}_y + \hat{j}_z$, is defined with the commutative properties

$$[\hat{j}_x, \hat{j}_y] = i\hat{j}_z, \quad [\hat{j}_y, \hat{j}_z] = i\hat{j}_x, \quad [\hat{j}_z, \hat{j}_x] = i\hat{j}_y, \tag{A.0.1}$$

$$[\hat{j}^2, \hat{j}_x] = [\hat{j}^2, \hat{j}_y] = [\hat{j}^2, \hat{j}_z] = 0, \tag{A.0.2}$$

where

$$\hat{j}^2 = \hat{j}_x^2 + \hat{j}_y^2 + \hat{j}_z^2, \tag{A.0.3}$$

and defined to act on the basis $|jm\rangle$, where m is the projection of j on to the space fixed z-axis, as

$$\hat{j}_z \mid jm\rangle = m \mid jm\rangle \tag{A.0.4}$$

$$\hat{j}^2 \mid jm\rangle = j(j+1) \mid jm\rangle. \tag{A.0.5}$$

Classically two angular momentum vectors can be combined to form the total angular momentum $\boldsymbol{j}$, which is given by the vector sum of the two vectors $\boldsymbol{j}_1$ and $\boldsymbol{j}_2$,

$$\boldsymbol{j} = \boldsymbol{j}_1 + \boldsymbol{j}_2. \tag{A.0.6}$$

Quantum mechanically there are two ways of describing the composite system [197,198], the first is using an uncoupled representation with the complete set of commuting angular momentum operators $\hat{j}_1^2$, $\hat{j}_{1z}$, $\hat{j}_2^2$, and $\hat{j}_{2z}$

$$\begin{aligned} \hat{j}_1^2 \mid j_1 m_1, j_2 m_2\rangle &= j_1(j_1+1) \mid j_1 m_1, j_2 m_2\rangle \\ \hat{j}_{1z} \mid j_1 m_1, j_2 m_2\rangle &= m_1 \mid j_1 m_1, j_2 m_2\rangle, \end{aligned} \tag{A.0.7}$$

where the $\mid j_1 m_1, j_2 m_2\rangle$ states span a space of dimension $(2j_1 + 1)(2j_2 + 1)$. The second way is to use another complete set of commuting operators; $\hat{j}_1^2$, $\hat{j}_2^2$, $\hat{j}^2 = \hat{j}_1^2 + \hat{j}_2^2$, and $\hat{j}_z = \hat{j}_{1z} + \hat{j}_{2z}$, in the coupled representation which span a space of dimension $2j + 1$

$$\hat{j}_1^2 \mid j_1 j_2 jm\rangle = j_1(j_1 + 1) \mid j_1 j_2 jm\rangle \quad \hat{j}_2^2 \mid j_1 j_2 jm\rangle = j_2(j_2 + 1) \mid j_1 j_2 jm\rangle$$
$$\hat{j}^2 \mid j_1 j_2 jm\rangle = j(j + 1) \mid j_1 j_2 jm\rangle \qquad \hat{j}_z \mid j_1 j_2 jm\rangle = m \mid j_1 j_2 jm\rangle. \tag{A.0.8}$$

Both representations contain the same number of observables hence the two representations are equivalent

$$\mid j_1 j_2 jm\rangle = \sum_{m_1, m_2} \langle j_1 m_1, j_2 m_2 \mid j_1 j_2 jm\rangle \mid j_1 m_1, j_2 m_2\rangle \tag{A.0.9}$$

where $\langle j_1 m_1, j_2 m_2 \mid j_1 j_2 jm\rangle$ is a Clebsch-Gordan coefficient, which have the following properties

$$\langle j_1 m_1, j_2 m_2 \mid jm\rangle \equiv \langle jm \mid j_1 m_1, j_2 m_2\rangle, \tag{A.0.10}$$

$$\sum_{m_1, m_2} \langle jm \mid j_1 m_1, j_2 m_2\rangle\langle j_1 m_1, j_2 m_2 \mid j'm'\rangle = \delta_{j,j'}\delta_{m,m'} \tag{A.0.11}$$

$$\sum_{j,m} \langle j_1 m_1, j_2 m_2 \mid jm\rangle\langle jm \mid j_1' m_1', j_2' m_2'\rangle = \delta_{m_1,m_1'}\delta_{m_2,m_2'} \tag{A.0.12}$$

and vanish unless the triangle conditions are satisfied

$$m = m_1 + m_2, \quad \mid j_1 + j_2 \mid \geq j \geq \mid j_1 - j_2 \mid . \tag{A.0.13}$$

Similarly Clebsch-Gordan coefficients can be expressed in terms of Wigner 3-j symbols defined as

$$\langle j_1 m_1, j_2 m_2 \mid jm\rangle \equiv (-1)^{j_1 - j_2 + m}(2j + 1)^{\frac{1}{2}} \begin{pmatrix} j_1 & j_2 & j \\ m_1 & m_2 & -m \end{pmatrix}. \tag{A.0.14}$$

A.1 6-j and 9-j Symbols

In much the same way as 3-j symbols arrive from the coupling of two angular momentum vectors 6-j and 9-j symbols arise from the coupling of three and four angular momentum vectors. For the three angular momentum $\mathbf{j}_1$, $\mathbf{j}_2$, and $\mathbf{j}_3$, $\mathbf{j}_1$ and $\mathbf{j}_2$ can be coupled to give $\mathbf{j}_{12}$, which can then be coupled to $\mathbf{j}_3$, to give the resultant total angular momentum $\mathbf{j}$,

$$\mid j_{12} j_3 jm\rangle = \sum_{m_{12}, m_3} \langle j_{12} m_{12}, j_3 m_3 \mid jm\rangle \mid j_{12} m_{12}, j_3 m_3\rangle. \tag{A.1.15}$$

There is also the possibility of coupling j_1 to j_{23} to give

$$\mid j_1 j_{23} jm\rangle = \sum_{m_1,m_{23}} \langle j_1 m_1, j_{23} m_{23} \mid jm\rangle \mid j_1 m_1, j_{23} m_{23}\rangle. \tag{A.1.16}$$

The two representations must be physically equivalent, and thus are connected by the unitary transformation,

$$\mid j_1 j_{23} jm\rangle = \sum_{j_{12}} \langle j_{12} j_3 jm \mid j_1 j_{23} jm\rangle \mid j_{12} j_3 jm\rangle \delta_{jj'} \delta_{mm'}, \tag{A.1.17}$$

where the expansion coefficient $\langle j_{12} j_3 j \mid j_1 j_{23} j\rangle$ is the scalar product between eigenfunctions of the two coupling schemes, which can be explicitly written as

$$\langle j_{12} j_3 j \mid j_1 j_{23} j\rangle = \sum_{m_1 m_{12}} \langle j - 1 m_1, j_2 m_2 - m_1 \mid j_{12} m_{12}\rangle \tag{A.1.18}$$

$$\times \langle j_1 m_1, j_{23} m - m_1 \mid jm\rangle \tag{A.1.19}$$

$$\times \langle j_2 m_{12} - m_1, j_3 m_3 \mid j_{23} m - m_1\rangle \tag{A.1.20}$$

$$\times \langle j_{12} m_{12}, j_3 m - m_{12} \mid jm\rangle \tag{A.1.21}$$

and can be used to explicitly define the Wigner 6-j symbol

$$\left\{ \begin{array}{ccc} j_1 & j_2 & j_{23} \\ j_3 & j & j_{23} \end{array} \right\} = (-1)^{j_1+j_2+j_3+j} [(2j_{12}+1)(2j_{23}+1)]^{-\frac{1}{2}} \langle j_{12} j_3 j \mid j_1 j_{23} j\rangle. \tag{A.1.22}$$

The 9-j symbol results from the coupling of four angular momenta. Possible coupling schemes are $|(j_1 j_4) j_{14} (j_2 j_3) j_{23} jm\rangle$ and $|(j_1 j_2) j_{12} (j_3 j_4) j_{34} jm\rangle$, where $j_{ik} = j_i + j_k$. By analogy to equation (A.1.17), the two coupling schemes can be related

$$\mid (j_1 j_4) j_{14} (j_2 j_3) j_{23} jm\rangle = \sum_{j_{12}} \sum_{j_{34}} \langle (j_1 j_2) j_{12} (j_3 j_4) j_{34} j \mid (j_1 j_4) j_{14} (j_2 j_3) j_{23} j\rangle \tag{A.1.23}$$

$$\times \mid (j_1 j_2) j_{12} (j_3 j_4) j_{34} jm\rangle, \tag{A.1.24}$$

and the 9-j symbol defined,

$$\begin{aligned} &\langle (j_1 j_2) j_{12} (j_3 j_4) j_{34} j \mid (j_1 j_4) j_{14} (j_2 j_3) j_{23} j\rangle \\ &= [(2j_{12}+1)(2j_{34}+1)(2j_{14}+1)(2j_{23}+1)]^{\frac{1}{2}} \left\{ \begin{array}{ccc} j_1 & j_2 & j_{12} \\ j_3 & j_4 & j_{34} \\ j_{14} & j_{23} & j \end{array} \right\}. \end{aligned} \tag{A.1.25}$$

Appendix B

Derivation of Hamiltonian Matrix Elements

Derivations of Hamiltonian matrix elements using angular momentum theory in various basis sets are presented for the matrix elements in chapter 3. The following derivations require the use of the following general results for the matrix elements of spherical tensor operators T^k_q of rank k and order q:

- The Wigner-Eckart theorem

$$\langle \gamma jm \mid T^k_q \mid \gamma' j'm' \rangle = (-1)^{j-m} \begin{pmatrix} j & k & j' \\ -m & q & m' \end{pmatrix} \langle j \parallel T^k \parallel j' \rangle, \tag{B.0.1}$$

  which defines the reduced matrix element $\langle j \parallel T^k \parallel j' \rangle$ that is independent of the projections m and m'.

- The equations for spherical tensor operators in composite systems,

$$\begin{aligned} \langle \gamma j_1 j_2 j \parallel T^k(A_1) \parallel \gamma' j'_1 j'_2 j' \rangle =& \delta_{j_2 j'_2} (-1)^{j_1+j_2+j'+k} \left[(2j'+1)(2j+1)\right]^{\frac{1}{2}} \\ & \times \begin{Bmatrix} j_1 & j & j_2 \\ j' & j'_1 & k \end{Bmatrix} \langle j_1 \parallel T^k(A_1) \parallel j'_1 \rangle \end{aligned} \tag{B.0.2}$$

$$\langle \gamma j_1 j_2 j \parallel T^k(A_2) \parallel \gamma' j'_1 j'_2 j' \rangle = \delta_{j_1 j'_1} (-1)^{j_1+j'_2+j+k_2} \left[(2j'+1)(2j+1)\right]^{\frac{1}{2}} \tag{B.0.3}$$

$$\times \begin{Bmatrix} j_2 & j & j_1 \\ j' & j'_2 & k \end{Bmatrix} \langle \gamma j_2 \parallel T^k(A_2) \parallel \gamma' j'_2 \rangle \tag{B.0.4}$$

$$\langle \gamma j_1 j_2 j \parallel T^k(A_1) \cdot T^{k_2}(A_2) \parallel \gamma' j_1' j_2' j' \rangle = \delta_{jj'}(2j+1)^{1/2}(-1)^{j_1'+j_2+j} \begin{Bmatrix} j_1' & j_2' & j \\ j_2 & j_1 & k \end{Bmatrix} \times \langle j_1 \parallel T^k(A_1) \parallel j_1' \rangle \langle j_2 \parallel T^k(A_2) \parallel j_2' \rangle \tag{B.0.5}$$

in which the tensor operators $T^k(A_1)$ and $T^k(A_2)$ of rank k act only on j_1 and j_2 respectively. For the derivation of these equations see [197] or [198].

- The Racah-Elliott relation,

$$\sum_x (-1)^{a+b+c+d+e+f+g+h+x+j}(2x+1) \begin{Bmatrix} a & b & x \\ c & d & g \end{Bmatrix} \begin{Bmatrix} c & d & x \\ e & f & h \end{Bmatrix} \begin{Bmatrix} e & f & x \\ b & a & j \end{Bmatrix} = \begin{Bmatrix} g & h & j \\ e & a & d \end{Bmatrix} \begin{Bmatrix} g & h & j \\ f & b & c \end{Bmatrix}. \tag{B.0.6}$$

Due to the large number of Kronecker delta functions present the following notation is used $\delta(a, b \ldots) = \delta_{aa'}\delta_{bb'} \ldots$.

B.1 The Spin-Spin Interaction in the Fully Coupled Basis

The spin-spin interaction [51] can be expressed as

$$\hat{H}_{\rm ss} = \frac{2}{3}\lambda_{\rm ss}\sqrt{6}C^2(\hat{r}) \cdot T^2(s, s) \tag{B.1.7}$$

where $T^2(s, s) = [s \otimes s]^2$ is a second order tensor product and $C_q^2(\hat{r}) = (4\pi/2k+1)^{1/2}Y_q^2(\hat{r})$. It is clear that $\hat{H}_{\rm ss}$ is diagonal in L and M_L and thus

$$\begin{aligned}
&\langle (ns) jLJM \mid C^2(\hat{r}) \cdot T^2(s, s) \mid (n's) j'L'J'M' \rangle \\
&= \delta(L, M_L) \sum_{m_j m_j' M_L} \langle (ns) jLJM \mid (ns) jm_j LM_L \rangle \langle (ns) jm_j LM_L \mid C^2(\hat{r}) \cdot T^2(s, s) \mid (n's) j'm_j' L'M_L' \rangle \\
&\times \langle (n's) j'm_j' LM_L \mid (n's) j'LJ'M' \rangle \\
&= \delta(J, M, L, M_L) \langle (ns) jm_j LM_L \mid C^2(\hat{r}) \cdot T^2(s, s) \mid (n's) j'm_j' L'M_L' \rangle \\
&= \delta(J, M, L, M_L, j, m_j)(-1)^{n'+j+s} \begin{Bmatrix} s & n' & j \\ n & s & 2 \end{Bmatrix} \langle n \parallel C^2(\hat{r}) \parallel n' \rangle \langle s \parallel T^2(s, s) \parallel s \rangle.
\end{aligned} \tag{B.1.8}$$

The reduced matrix elements of $T^2(s,s)$ are given by [51]

$$\langle s \parallel T^2(s,s) \parallel s\rangle = \sqrt{5}\,[s(s+1)(2s+1)] \begin{Bmatrix} 1 & 1 & 2 \\ s & s & s \end{Bmatrix}. \tag{B.1.9}$$

The reduced matrix elements of $C^2(\hat{r})$ are given by

$$\langle nm_n \mid C^2_q(\hat{r}) \mid n'm'_n\rangle = (-1)^{m_n}\left[(2n+1)(2n'+1)\right]^{1/2} \begin{pmatrix} n & 2 & n' \\ 0 & 0 & 0 \end{pmatrix} \begin{pmatrix} n & 2 & n' \\ -m_n & q & m'_n \end{pmatrix} \tag{B.1.10}$$

and the Wigner-Eckart theorem

$$\langle nm_n \mid C^2_q(\hat{r}) \mid n'm'_n\rangle = (-1)^{n-m_n} \begin{pmatrix} n & 2 & n' \\ -m_n & q & m'_n \end{pmatrix} \langle n \parallel C^2(\hat{r}) \parallel n'\rangle \tag{B.1.11}$$

to give

$$\langle n \parallel C^2(\hat{r}) \parallel n'\rangle = (-1)^{n}\left[(2n+1)(2n'+1)\right]^{1/2} \begin{pmatrix} n & 2 & n' \\ 0 & 0 & 0 \end{pmatrix}. \tag{B.1.12}$$

Therefore

$$\begin{aligned} &\langle (ns)jLJM \mid C^2(\hat{r}) \cdot T^2(s,s) \mid (n's)j'L'J'M'\rangle = \\ &\delta(J,M,L,M_L,j,m_j)(-1)^{n'+j+n+s}\frac{2\sqrt{30}}{2}\,[s(s+1)(2s+1)]\left[(2n+1)(2n'+1)\right]^{1/2} \\ &\times \begin{pmatrix} n & 2 & n' \\ 0 & 0 & 0 \end{pmatrix} \begin{Bmatrix} 1 & 1 & 2 \\ s & s & s \end{Bmatrix} \begin{Bmatrix} s & n' & j \\ n & s & 2 \end{Bmatrix}. \end{aligned} \tag{B.1.13}$$

B.2 The Zeeman Interaction in the Fully Coupled Basis

The Zeeman Hamiltonian is given by

$$\hat{H}_z = g_e\mu_B\hat{B}\cdot\hat{s} = g_e\mu_B B s_z = g_e\mu_B B T^1_0(s), \tag{B.2.14}$$

which can be evaluated to give

$$\begin{aligned}
&\langle (ns)jLJM \mid T_0^1(s) \mid (n's)j'L'J'M' \rangle \\
&= (-1)^{J-M} \begin{pmatrix} J & 1 & J' \\ -M & 0 & M' \end{pmatrix} \langle (ns)jLJ \parallel T_0^1(s) \parallel (n's)j'L'J' \rangle \\
&= \delta(L)(-1)^{j-M+j+L+J'+1} \left[(2J'+1)(2J+1)\right]^{1/2} \begin{pmatrix} J & 1 & J' \\ -M & 0 & M' \end{pmatrix} \\
&\times \begin{Bmatrix} j & J & L \\ J' & j' & 1 \end{Bmatrix} \langle (ns)j \parallel T_0^1(s) \parallel (n's)j' \rangle
\end{aligned}$$

$$\begin{aligned}
&= \delta(M,L,n)(-1)^{J'-M} \left[(2J'+1)(2J+1)(2j'+1)(2j+1)\right]^{1/2} \begin{pmatrix} J & 1 & J' \\ -M & 0 & M' \end{pmatrix} \\
&\times \begin{Bmatrix} j & J & L \\ J' & j' & 1 \end{Bmatrix} \begin{Bmatrix} s & j & n \\ j' & s' & 1 \end{Bmatrix} \langle s \parallel T_0^1(s) \parallel s \rangle \\
&= \delta(M,L,n)(-1)^{J'-M} \left[(2J'+1)(2J+1)(2j'+1)(2j+1)s(s+1)(2s+1)\right]^{1/2} \\
&\times \begin{pmatrix} J & 1 & J' \\ -M & 0 & M' \end{pmatrix} \begin{Bmatrix} j & J & L \\ J' & j' & 1 \end{Bmatrix} \begin{Bmatrix} s & j & n \\ j' & s' & 1 \end{Bmatrix}
\end{aligned} \tag{B.2.15}$$

B.3 The Stark Interaction in Parallel Fields

The Stark Hamiltonian for a system with parallel electric and magnetic fields orientated along the space fixed Z-axis, is given by

$$\hat{H}_{\text{Stark}} = -E \cdot d = -Ed\cos\theta = -EdC_0^1(\hat{r}), \tag{B.3.16}$$

where θ is the angle between $\hat{r}$ and the field axis.

B.3.1 In the decoupled basis

$$\begin{aligned}
&\langle nm_n \mid \langle sm_s \mid \langle LM_L \mid C_0^1(\hat{r}) \rangle \mid L'M_L' \rangle \mid sm_s' \rangle \mid n'm_n' \rangle \\
&= \delta(LM_Lm_s)\langle nm_n \mid C_0^1(\hat{r}) \mid n'm_n' \rangle = \delta(LM_Lm_s) \int Y_{m_n}^{n*} C_0^1(\hat{r}) Y_{m_n'}^{n'} d\tau
\end{aligned} \tag{B.3.17}$$

The integral over three spherical harmonics is given by [199]

$$\int C^a_\alpha C^b_\beta C^c_\gamma d\tau = 4\pi \begin{pmatrix} a & b & c \\ 0 & 0 & 0 \end{pmatrix} \begin{pmatrix} a & b & c \\ \alpha & \beta & \gamma \end{pmatrix}, \tag{B.3.18}$$

thus

$$\begin{aligned} &\langle nm_n \mid \langle sm_s \mid \langle LM_L \mid C^1_0(\hat{r})\rangle \mid L'M'_L\rangle \mid sm'_s\rangle \mid n'm'_n\rangle = \\ &\delta(LM_Lm_s)\left[(2n+1)(2n'+1)\right]^{1/2}(-1)^{m_n} \begin{pmatrix} a & b & c \\ 0 & 0 & 0 \end{pmatrix} \begin{pmatrix} a & b & c \\ \alpha & \beta & \gamma \end{pmatrix}. \end{aligned} \tag{B.3.19}$$

B.3.2 In the coupled basis

$$\begin{aligned} &\langle nsjm_j \mid C^1_0 \mid n'sj'm'_j\rangle = (-1)^{j-m_j} \begin{pmatrix} j & 1 & j' \\ -m_j & 0 & m'_j \end{pmatrix} \langle nsj \parallel C^1_0 \parallel n'sj'\rangle \\ =&(-1)^{j-m_j+n+s+j'+1}\left[(2j'+1)(2j+1)\right]^{1/2} \begin{pmatrix} j & 1 & j' \\ -m_j & 0 & m'_j \end{pmatrix} \begin{Bmatrix} n & j & s \\ j' & n' & 1 \end{Bmatrix} \langle n \parallel C^1_0 \parallel n'\rangle \\ =&(-1)^{j+j'-m_j+s+1}\left[(2j'+1)(2j+1)(2n+1)(2n'+1)\right]^{1/2} \\ &\times \begin{pmatrix} n & 1 & n' \\ 0 & 0 & 0 \end{pmatrix} \begin{pmatrix} j & 1 & j' \\ -m_j & 0 & m'_j \end{pmatrix} \begin{Bmatrix} n & j & s \\ j' & n' & 1 \end{Bmatrix} \end{aligned} \tag{B.3.20}$$

where $\langle n \parallel C^1_0 \parallel n'\rangle$ has been evaluated with the use of the Wigner-Eckart theorem.

B.3.3 In the fully coupled basis

$$
\begin{aligned}
&\langle (ns)jLJM \mid C_0^1 \mid (n's)j'L'J'M' \rangle \\
&= (-1)^{J-M} \begin{pmatrix} J & 1 & J' \\ -M & 0 & M' \end{pmatrix} \langle (ns)jLJ \parallel C_0^1 \parallel (n's)j'L'J'M' \rangle \\
&= \delta(L)(-1)^{J-M+j+L+J'+1} \left[(2J'+1)(2J+1)\right]^{1/2} \\
&\times \begin{pmatrix} J & 1 & J' \\ -M & 0 & M' \end{pmatrix} \begin{Bmatrix} j & J & L \\ J' & j' & 1 \end{Bmatrix} \langle (ns)j \parallel C_{10} \parallel (n's)j' \rangle \\
&= \delta(L)(-1)^{J-M+j+L+J'+1+n+s+j'} \left[(2J'+1)(2J+1)(2j'+1)(2j+1)\right]^{1/2} \begin{pmatrix} J & 1 & J' \\ -M & 0 & M' \end{pmatrix} \\
&\times \begin{Bmatrix} j & J & L \\ J' & j' & 1 \end{Bmatrix} \begin{Bmatrix} n & j & s \\ j' & n' & 1 \end{Bmatrix} \langle n \parallel C_{10} \parallel n' \rangle \\
&= -\delta(ML)(-1)^{J+J'+j+j'-M+L+s} \left[(2J'+1)(2J+1)(2j'+1)(2j+1)(2n'+1)(2n+1)\right]^{1/2} \\
&\times \begin{pmatrix} J & 1 & J' \\ -M & 0 & M \end{pmatrix} \begin{pmatrix} n & 1 & n' \\ 0 & 0 & 0 \end{pmatrix} \begin{Bmatrix} j & J & L \\ J' & j' & 1 \end{Bmatrix} \begin{Bmatrix} n & j & s \\ j' & n' & 1 \end{Bmatrix}
\end{aligned} \tag{B.3.21}
$$

B.4 Fully Coupled Intermolecular Potential Matrix Elements

Following the derivation from Corey and McCourt [56], n and s are coupled to form j,

$$
\mid (ns)jLJM\rangle = \sum_{m_j M_l} (-1)^{-j+l-M} (2J+1)^{\frac{1}{2}} \begin{pmatrix} j & L & J \\ m_j & M_L & -M \end{pmatrix} \mid (ns)jm_j\rangle \mid LM_L\rangle. \tag{B.4.22}
$$

Another basis can be defined by coupling n to L to form $\mathcal{J}$ with a space-fixed projection $\mathcal{M}$,

$$
\mid (nL)\mathcal{J}sJM\rangle = \sum_{m_n M_L} (-1)^{-\mathcal{J}+s-M} (2J+1)^{\frac{1}{2}} \begin{pmatrix} \mathcal{J} & s & J \\ \mathcal{M} & m_s & -M \end{pmatrix} \mid (nL)\mathcal{J}\mathcal{M}\rangle \mid sm_s\rangle, \tag{B.4.23}
$$

where

$$
\mid (nL)\mathcal{J}\mathcal{M}\rangle = \sum_{m_n M_L} (-1)^{-N+L-\mathcal{M}} (2\mathcal{J}+1)^{\frac{1}{2}} \begin{pmatrix} n & L & \mathcal{J} \\ m_n & M_L & -\mathcal{M} \end{pmatrix} \mid nm_n\rangle \mid LM_L\rangle. \tag{B.4.24}
$$

Relating the two different basis sets yields

$$|\,(ns)jLJM\rangle = \sum_{\mathcal{J}}(-1)^{-s+L-j+\mathcal{J}}\left[(2j+1)(2\mathcal{J}+1)\right]^{\frac{1}{2}}\begin{Bmatrix} s & n & j \\ L & J & \mathcal{J}\end{Bmatrix}|\,(nL)\mathcal{J}sJM\rangle. \tag{B.4.25}$$

Using the fact that V is independent of spin and on the orientation of the space-fixed frame of reference, V can be evaluated in an uncoupled $n+L$ scheme

$$\langle(nL)\mathcal{J}\mathcal{M}sm_s \mid V \mid (n'L')\mathcal{J}'\mathcal{M}'s'm_s'\rangle = \delta_{\mathcal{J}\mathcal{J}'\mathcal{M}\mathcal{M}'ss'm_sm_s'}\langle(nL)\mathcal{J}\mathcal{M} \mid V \mid (n'L')\mathcal{J}'\mathcal{M}'\rangle. \tag{B.4.26}$$

Which in the total J representation becomes

$$\langle(ns)jLJM \mid V \mid (n's')j'L'J'M'\rangle = \delta_{ss'JJ'MM'}\sum_{\mathcal{J}}(-1)^{-L+L'+j-j'}(2\mathcal{J}+1)$$
$$\times\left[(2j+1)(2j'+1)\right]^{\frac{1}{2}}\begin{Bmatrix} s & n & j \\ L & J & \mathcal{J}\end{Bmatrix}\begin{Bmatrix} s & n & j' \\ L' & J & \mathcal{J}\end{Bmatrix}\langle(nL)\mathcal{J}\mathcal{M} \mid V \mid (n'L')\mathcal{J}'\mathcal{M}'\rangle. \tag{B.4.27}$$

Expanding the intermolecular potential in terms of Legendre polynomials

$$V(\hat{r},R) = \sum_{\lambda}V_\lambda(R)P_\lambda(\cos\theta) = \sum_{\lambda}V_\lambda Y^\lambda(\hat{r})\cdot Y^\lambda(\hat{R}), \tag{B.4.28}$$

and evaluating in the uncoupled scheme gives

$$\begin{aligned}\langle(nL)\mathcal{J}\mathcal{M} \mid V \mid (n'L')\mathcal{J}'\mathcal{M}'\rangle = \sum_{\lambda}V_\lambda(R)(-1)^{n'+n+\mathcal{J}}\\ \times\left[(2n+1)(2n'+1)(2L+1)(2L'+1)\right]^{\frac{1}{2}}\\ \times\begin{pmatrix} n & \lambda & n' \\ 0 & 0 & 0\end{pmatrix}\begin{pmatrix} L & \lambda & L' \\ 0 & 0 & 0\end{pmatrix}\begin{Bmatrix} \mathcal{J} & L & n \\ \lambda & n' & L'\end{Bmatrix}.\end{aligned} \tag{B.4.29}$$

Substituting (B.4.29) into (B.4.27) and using the Racah-Elliot relation, gives the potential matrix elements in the fully coupled representation

$$\begin{aligned}\langle(ns)jLJM \mid V \mid (n's)j'L'JM\rangle = \sum_{\lambda}V_\lambda(R)(-1)^{s-\lambda-J}\\ \times\left[(2n+1)(2n'+1)(2j+1)(2j'+1)(2L+1)(2L'+1)\right]^{\frac{1}{2}}\\ \times\begin{pmatrix} n & \lambda & n' \\ 0 & 0 & 0\end{pmatrix}\begin{pmatrix} L & \lambda & L' \\ 0 & 0 & 0\end{pmatrix}\begin{Bmatrix} j' & j & \lambda \\ L & L' & J\end{Bmatrix}\begin{Bmatrix} j' & j & \lambda \\ n & n' & s\end{Bmatrix}.\end{aligned} \tag{B.4.30}$$

Appendix C

Extracting Partial Wave Cross Sections from MOLSCAT

MOLSCAT does not automatically calculate partial wave cross sections, instead automatically sums over the partial waves cross sections in the incident and outgoing states to give the cross section $\sigma_{\alpha\to\alpha'}$, where α is a set of quantum numbers that describe the channel $|\alpha, L, M\rangle$. Thus to calculate partial wave cross sections we need to directly extract the S-matrix from the MOLSCAT output.

MOLSCAT outputs the S-matrix in a unformatted binary file on the ISAVEU channel. For the following to work "KSAVE=0" needs to be set, otherwise the structure of the ISAVEU output is altered and the following fails. The data structure of the ISAVEU file can be found in section 2.5 of the MOLSCAT version 14 documentation.

MOLSCAT calculations for a range of energies and magnetic fields, need to be performed separately for each $MTOT$ (the projection of the total angular momentum of the the space-fixed field axis) and parity, p. A FORTRAN routine ("xsec.f"), using code similar to the RESFIT companion program "SAVER.f", then reads the ISAVEU binary file and writes the $S^{\mathrm{MTOT,p}}$-matrix out in human readable form in format shown in table C. A Python script ("totaliser.py") given an incident partial wave and an outgoing m'_s can then read multiple files of the form shown in table C, to calculate the cross section $\sigma^{L}_{n=0,s=1,m_s=+1\to n'=0,s=1,m'_s}$ using

$$\sigma^{L}_{\alpha\to\alpha'} = \frac{\pi}{k^2_\alpha} \sum_{\mathrm{MTOT}pL'} |1 - S^{\mathrm{MTOT},p}_{\alpha,LM_L\to\alpha',L'M'_L}|^2. \tag{C.0.1}$$

NNRG (number of energies)

EN (list of all energies)

********** (separator)

index number

energy magnetic field electric field

parity MTOT NOPEN (number of open channels)

channel list

channel index, quantum numbers, L, channel wave vector

tabulated channel data (as above)...

" I , J , RE(S(I,J)) , IM(S(I,J)) , $|I - S|^2$, SIG(I→J)"

tabulated cross section data (as above) ...

********** (separator)

index number (2)

...

...

index number (NNRG)

Table C.1: Human readable format for S-matrices extracted from the MOLSCAT ISAVEU file with "xsec.f".

For example to calculate the p-wave ($L = 1$) $n = 0, s = 1, m_s = +1 \rightarrow n = 0, s = 1, m'_s$ cross section, separate MOLSCAT calculations need to be performed with the correct parity for $MTOT = m_s + M_L = 0$, 1, and 2 in different directories. "xsec.f" is then run in each directory creating three output files MTOT0, MTOT1, and MTOT2. "totaliser.py" then needs to be given the three files, and to calculate $\sigma^{L=1}_{n=0,s=1,m_s=+1\rightarrow n'=0,s=1,m'_s=-1}$, the values inL=1 and $m'_s = -1$.

Appendix D

Publications and Conferences

D.1 Publications

- Production of ultracold NH molecules by sympathetic cooling with Mg,
  Alisdair O. G. Wallis and Jeremy M. Hutson, Phys. Rev. Lett. 103, 183201 (2009)

- Conical intersections in laboratory coordinates with ultracold molecules,
  Alisdair O. G. Wallis, S. A. Gardiner, and Jeremy M. Hutson, Phys. Rev. Lett. 103, 083201 (2009)

D.2 Conferences, Meetings and Summer Schools

11 July 2007:	ANUMOCP XVII (Annual Northern Universities Meeting on Chemical Physics), University of Leeds, Leeds
10-13 September 2007:	QuAMP 2007 (Quantum, Atomic, Molecular and Plasma Physics) , University College London, London
7-9 April 2008:	EuroQUAM (Cold Quantum Matter) Inaugural Meeting, Barcelona, Spain
25 June 2008:	ANUMOCP XVIII (Annual Northern Universities Meeting on Chemical Physics) , University of Sheffield, Sheffield
7-19 September 2008:	UK Summer School in Theoretical Chemistry, Oxford University, Oxford
5-7 January 2009:	Annual Conference of the Spectroscopy and Dynamics Group of the RSC Faraday Division, University of Nottingham, Nottingham
15-17 April 2009:	Faraday Discussion 142: Cold and Ultracold Molecules, University of Durham, Durham
17-18 April 2009:	EuroQUAM Satellite Meeting on Cold and Ultracold Molecules, University of Durham, Durham
20-22 April 2009:	EPSRC CoCoChem Summer School: Coherent Control of Molecules, University College London, London
23 April 2009:	Molecular Dynamics and Control Symposium, University College London, London
26-27 October 2009:	CoPoMol (Collisions of Cold Polar Molecules) Annual Meeting, Imperial College London, London
14-15 December 2009:	Aharonov-Bohm Effect and Berry Phase Anniversary 50/25, University of Bristol, Bristol

Visits

21 Sept- 10 Oct 2008:	Visited the research group of Professor R. Krems, University of British Columbia, Vancouver, Canada.

Bibliography

[1] M. H. Anderson, J. R. Ensher, M. R. Matthews, C. E. Wieman, and E. A. Cornell, *Science* **269**, 198 (1995).

[2] K. B. Davis, M. O. Mewes, M. R. Andrews, N. J. VanDruten, D. S. Durfee, D. M. Kurn, and W. Ketterle, *Phys. Rev. Lett.* **75**, 3969 (1995).

[3] B. Schwarzschild, *Phys. Today* **56**, 21 (2003).

[4] W. Ketterle, *Rev. Mod. Phys.* **74**, 1131 (2002).

[5] E. A. Cornell and C. E. Wieman, *Rev. Mod. Phys.* **74**, 875 (2002).

[6] I. Bloch, *Nat. Phys.* **1**, 23 (2005).

[7] H. L. Bethlem and G. Meijer, *Int. Rev. Phys. Chem.* **22**, 73 (2003).

[8] S. Schiller and V. Korobov, *Phys. Rev. A* **71**, 32505 (2005).

[9] H. Bethlem and W. Ubachs, *Faraday Discussions* **142**, 25 (2009).

[10] J. J. Hudson, B. E. Sauer, M. R. Tarbutt, and E. A. Hinds, *Phys. Rev. Lett.* **89**, 023003 (2002).

[11] R. V. Krems, *Int. Rev. Phys. Chem.* **24**, 99 (2005).

[12] W. D. Phillips, *Rev. Mod. Phys.* **70**, 721 (1998).

[13] C. J. Pethick and H. Smith, *Bose-Einstein Condensation in Dilute Gases*, Cambridge University Press, 2002.

[14] R. Grimm, M. Weidem

"uller, and Y. Ovchinnikov, *Adv. at. mol. opt. phys* **42**, 130 (2000).

[15] J. M. Doyle, B. Fredrich, J. Kim, and D. Patterson, *Phys. Rev. A* **52**, R2515 (1995).

[16] J. D. Weinstein, R. deCarvalho, T. Guillet, B. Friedrich, and J. M. Doyle, *Nature* **395**, 148 (1998).

[17] R. Decarvalho, J. Doyle, B. Friedrich, T. Guillet, J. Kim, D. Patterson, and J. Weinstein, *Eur. Phys. J. D* **7**, 289 (1999).

[18] D. Egorov, W. C. Campbell, B. Friedrich, S. E. Maxwell, E. Tsikata, L. D. van Buuren, and J. M. Doyle, *Eur. Phys. J. D* **31**, 307 (2004).

[19] S. E. Maxwell, N. Brahms, R. deCarvalho, D. R. Glenn, J. S. Helton, S. V. Nguyen, D. Patterson, J. Petricka, D. DeMille, and J. M. Doyle, *Phys. Rev. Lett.* **95**, 173201 (2005).

[20] H. L. Bethlem, G. Berden, and G. Meijer, *Phys. Rev. Lett.* **83**, 1558 (1999).

[21] H. L. Bethlem and G. Meijer, *Int. Rev. Phys. Chem.* **22**, 73 (2003).

[22] J. Doyle, B. Friedrich, R. V. Krems, and F. Masnou-Seeuws, *Eur. Phys. J. D* **31**, 149 (2004).

[23] P. F. Weck and N. Balakrishnan, *Int. Rev. Phys. Chem.* **25**, 283 (2006).

[24] J. M. Hutson and P. Soldán, *Int. Rev. Phys. Chem.* **25**, 497 (2006).

[25] M. W. Zwierlein, C. A. Stan, C. H. Schunck, S. M. F. Raupach, S. Gupta, Z. Hadzibabic, and W. Ketterle, *Phys. Rev. Lett.* **91**, 250401 (2003).

[26] E. Bodo and F. A. Gianturco, *Int. Rev. Phys. Chem.* **25**, 313 (2006).

[27] K. E. Strecker, G. B. Partridge, and R. G. Hulet, *Phys. Rev. Lett.* **91**, 080406 (2003).

[28] A. Fioretti, D. Comparat, A. Crubellier, O. Dulieu, F. Masnou-Seeuws, and P. Pillet, *Phys. Rev. Lett.* **80**, 4402 (1998).

[29] J. M. Sage, S. Sainis, T. Bergeman, and D. DeMille, *Phys. Rev. Lett.* **94**, 203001 (2005).

[30] J. G. Danzl, E. Haller, M. Gustavsson, M. J. Mark, R. Hart, N. Bouloufa, O. Dulieu, H. Ritsch, and H.-C. Nägerl, *Science* **321**, 1062 (2008).

[31] F. Lang, K. Winkler, C. Strauss, R. Grimm, and J. Hecker Denschlag, *Phys. Rev. Lett.* **101**, 133005 (2008).

[32] K.-K. Ni, S. Ospelkaus, M. H. G. de Miranda, A. Pe'er, B. Neyenhuis, J. J. Zirbel, S. Kotochigova, P. S. Julienne, D. S. Jin, and J. Ye, *Science* **322**, 231 (2008).

[33] J. G. Danzl, M. J. Mark, E. Haller, M. Gustavsson, R. Hart, J. Aldegunde, J. M. Hutson, and H.-C. Nägerl, *e-print arXiv:0909.4700* (2009).

[34] W. C. Campbell, E. Tsikata, H.-I. Lu, L. D. van Buuren, and J. M. Doyle, *Phys. Rev. Lett.* **98**, 213001 (2007).

[35] W. Petrich, M. H. Anderson, J. R. Ensher, and E. A. Cornell, *Phys. Rev. Lett.* **74**, 3352 (1995).

[36] H. L. Bethlem, G. Berden, F. M. H. Crompvoets, R. T. Jongma, A. J. A. van Roij, and G. Meijer, *Nature* **406**, 491 (2000).

[37] S. Y. T. van de Meerakker, P. H. M. Smeets, N. Vanhaecke, R. T. Jongma, and G. Meijer, *Phys. Rev. Lett.* **94**, 023004 (2005).

[38] T. Rieger, T. Junglen, S. A. Rangwala, P. W. H. Pinkse, and G. Rempe, *Phys. Rev. Lett.* **95**, 173002 (2005).

[39] J. van Veldhoven, H. L. Bethlem, and G. Meijer, *Phys. Rev. Lett.* **94**, 083001 (2005).

[40] J. R. Taylor, *Scattering Theory: The Quantum Theory of Nonrelativistic Collisions*, Wiley, New York, 1972.

[41] C. J. Joachain, *Quantum Collision Theory*, North-Holland, Amsterdam, 1975.

[42] P. W. Atkins and R. Friedman, *Molecular Quantum Mechanics*, Oxford University Press, 4th edition, 2005.

[43] D. Manolopoulos, Quantum Scattering Dynamics Lectures, Coulson Summer School, Oxford, Quantum Scattering Dynamics Lectures, Coulson Summer School, Oxford, 2001.

[44] G. B. Arfken and H. J. Weber, *Mathematical Methods for Physicists*, Acedemic Press Inc., 5th edition, 2001.

[45] J. M. Hutson, *Comput. Phys. Commun.* **84**, 1 (1994).

[46] F. H. Mies, *Mol. Phys.* **41**, 953 (1980).

[47] J. M. Hutson, BOUND computer code, version 16, distributed by Collaborative Computational Project No. 6 of the UK Engineering and Physical Sciences Research Council, 2007.

[48] J. M. Hutson and S. Green, MOLSCAT computer program, version 14, distributed by Collaborative Computational Project No. 6 of the UK Engineering and Physical Sciences Research Council, 1994.

[49] B. R. Johnson, *J. Comput. Phys.* **13**, 445 (1973).

[50] M. H. Alexander and D. E. Manolopoulos, *J. Chem. Phys.* **86**, 2044 (1987).

[51] R. V. Krems and A. Dalgarno, *J. Chem. Phys.* **120**, 2296 (2004).

[52] M. L. González-Martínez and J. M. Hutson, *Phys. Rev. A* **75**, 022702 (2007).

[53] T. V. Tscherbul and R. V. Krems, *Phys. Rev. Lett.* **97**, 083201 (2006).

[54] E. Abrahamsson, T. V. Tscherbul, and R. V. Krems, *J. Chem. Phys.* **127**, 044302 (2007).

[55] J. M. Hutson, An Introduction to the Dynamics of Van der Waals Molecules, in *Advances in Molecular Vibrations and Collision Dynamics*, volume 1A, pp. 1–45, JAI Press, Greenwich, Connecticut, 1991.

[56] G. C. Corey and F. R. McCourt, *J. Phys. Chem.* **97**, 2723 (1983).

[57] H. Cybulski, R. V. Krems, H. R. Sadeghpour, A. Dalgarno, J. Kłos, G. C. Groenenboom, A. van der Avoird, D. Zgid, and G. Chałasiński, *J. Chem. Phys.* **122**, 094307 (2005).

[58] W. C. Campbell, T. V. Tscherbul, H. I. Lu, E. Tsikata, R. V. Krems, and J. M. Doyle, *Phys. Rev. Lett.* **102**, 013003 (2009).

[59] R. A. Rowlands, M. L. González-Martínez, and J. M. Hutson, *arXiv:cond-mat/0707.4397* (2007).

[60] J. M. Hutson, M. Beyene, and M. L. González-Martínez, *arXiv:physics/0908.2065* (2009).

[61] J. M. Hutson, *New J. Phys.* **9**, 152 (2007), Note that there is a typographical error in Eq. (22) of this paper: the last term on the right-hand side should read $-\beta_{\rm res}$ instead of $+\beta_{\rm res}$.

[62] R. V. Krems, H. R. Sadeghpour, A. Dalgarno, D. Zgid, J. Kłos, and G. Chałasiński, *Phys. Rev. A* **68**, 051401(R) (2003).

[63] G. C. Groenenboom and I. M. Struniewicz, *J. Chem. Phys.* **113**, 9562 (2000).

[64] K. P. Huber and G. Herzberg, *Constants of Diatomic Molecules*, Van Nostrand, New York, 1979.

[65] B. Friedrich and D. Herschbach, *Phys. Chem. Chem. Phys.* **2**, 419 (2000).

[66] A. Boca and B. Friedrich, *J. Chem. Phys.* **112**, 3609 (2000).

[67] R. V. Krems, *Phys. Rev. Lett.* **96**, 123202 (2006).

[68] T. V. Tscherbul and R. V. Krems, *J. Chem. Phys.* **125**, 194311 (2006).

[69] T. Tscherbul, G. Groenenboom, R. Krems, and A. Dalgarno, *Faraday Discussions* **142**, 127 (2009).

[70] S. Jung, E. Tiemann, and C. Lisdat, *Phys. Rev. A* **74**, 040701 (2006).

[71] F. Lique, A. Spielfiedel, M. L. Dubernet, and N. Feautrier, *J. Chem. Phys.* **123**, 8134316 (2005).

[72] J. M. Hutson, RESFIT 2007 computer program, 2007.

[73] J. W. Norbury, *Eur. J. Phys.* **11**, 99 (1988).

[74] J. P. Burke, J. L. Bohn, B. D. Esry, and C. H. Greene, *Phys. Rev. Lett.* **80**, 2097 (1998).

[75] P. Soldán and J. M. Hutson, *Phys. Rev. Lett.* **92**, 163202 (2004).

[76] M. Lara, J. L. Bohn, D. Potter, P. Soldán, and J. M. Hutson, *Phys. Rev. Lett.* **97**, 183201 (2006).

[77] M. Lara, J. L. Bohn, D. E. Potter, P. Soldán, and J. M. Hutson, *Phys. Rev. A* **75**, 012704 (2007).

[78] M. Tacconi, E. Bodo, and F. A. Gianturco, *Theor. Chem. Acc.* **117**, 649 (2007).

[79] M. Tacconi, E. Bodo, and F. A. Gianturco, *Phys. Rev. A* **75**, 012708 (2007).

[80] M. Tacconi, L. Gonzalez-Sanchez, E. Bodo, and F. A. Gianturco, *Phys. Rev. A* **76**, 032702 (2007).

[81] P. S. Żuchowski and J. M. Hutson, *Phys. Rev. A* **78**, 022701 (2008).

[82] P. Soldán, P. S. Żuchowski, and J. M. Hutson, *Faraday Discuss.* **142**, 191 (2009).

[83] W. Campbell, G. Groenenboom, H. Lu, E. Tsikata, and J. Doyle, *Phys. Rev. Lett.* **100**, 83003 (2008).

[84] S. Hoekstra, M. Metsala, P. C. Zieger, L. Scharfenberg, J. J. Gilijamse, G. Meijer, and S. Y. T. van de Meerakker, *Phys. Rev. A* **76**, 063408 (2007).

[85] S. Y. T. van de Meerakker, R. T. Jongma, H. L. Bethlem, and G. Meijer, *Phys. Rev. A* **64**, 041401(R) (2001).

[86] T. E. Mehlstäubler, K. Moldenhauer, M. Riedmann, N. Rehbein, J. Friebe, E. M. Rasel, and W. Ertmer, *Phys. Rev. A* **77**, 021402R (2008).

[87] M. Mizushima, *Theory of Rotating Diatomic Molecules*, Wiley, New York, 1975.

[88] M. L. Dubernet, D. Flower, and J. M. Hutson, *J. Chem. Phys.* **94**, 7602 (1991).

[89] J. L. Bohn, *Phys. Rev. A* **62**, 032701 (2000).

[90] E. Majorana, *Nuovo Cimento* **9**, 43 (1932).

[91] E. P. Wigner, *Phys. Rev.* **73**, 1002 (1948).

[92] H. R. Sadeghpour, J. L. Bohn, M. J. Cavagnero, B. D. Esry, I. I. Fabrikant, J. H. Macek, and A. R. P. Rau, *J. Phys. B* **33**, R93 (2000).

[93] A. Volpi and J. L. Bohn, *Phys. Rev. A* **65**, 052712 (2002).

[94] M. S. Child, *Molecular Collision Theory*, Academic Press, London, 1974.

[95] M. J. Seaton, *Proc. Phys. Soc.* **88**, 801 (1966).

[96] F. H. Mies, *J. Chem. Phys.* **80**, 2514 (1984).

[97] F. H. Mies and P. S. Julienne, *J. Chem. Phys.* **80**, 2526 (1984).

[98] P. S. Julienne and F. H. Mies, *J. Opt. Soc. Am. B* **6**, 2257 (1989).

[99] K. M. Jones, E. Tiesinga, P. D. Lett, and P. S. Julienne, *Rev. Mod. Phys.* **78**, 483 (2006).

[100] G. F. Gribakin and V. V. Flambaum, *Phys. Rev. A* **48**, 546 (1993).

[101] P. S. Julienne and B. Gao, Simple Theoretical Models for Resonant Cold Atom Interactions, volume 869, pp. 261–268, AIP, 2006.

[102] Z. Idziaszek, MQDT modeling of atom-molecule and molecule-molecule collisions, MQDT theory developed with P. Julienne (NIST), Warsaw, 2009.

[103] P. S. Julienne, Molecular states near a collision threshold, in *Cold Molecules: Theory, Experiment, Applications*, edited by R. V. Krems, C. Stwalley, and B. Friedrich, pp. 221–244, CRC Press, 2009.

[104] B. Gao, *Phys. Rev. A* **58**, 1728 (1998).

[105] B. Gao, *Phys. Rev. A* **58**, 4222 (1998).

[106] B. Gao, *Phys. Rev. Lett.* **83**, 4225 (1999).

[107] B. Gao, *Phys. Rev. A* **62**, 050702 (2000).

[108] B. Gao, *Phys. Rev. A* **64**, 010701 (2001).

[109] B. Gao, *J. Phys. B* **37**, 4273 (2004).

[110] B. Gao, *Phys. Rev. A* **80**, 012702 (2009).

[111] B. Gao, Routines to calculate the AQDT parameters for an attractive $1/r^6$ potential, Version 2, Universtiy of Toledo, Ohio, Routines to calculate the AQDT parameters for an attractive $1/r^6$ potential, Version 2, Universtiy of Toledo, Ohio. Supplied with Fortran wrapper by P. Julienne (NIST), 2003.

[112] W. Domcke, D. Yarkony, and H. K
"oppel, *Conical intersections: electronic structure, dynamics & spectroscopy*, World Scientific, 2004.

[113] L. S. Cederbaum, Born-Oppenheimer Approximation and Beyond, in *Conical Intersections: Electronic Structure, Dynamics and Spectroscopy*, edited by W. Domcke, D. R. Yarkony, and H. Köppel, Advanced Series in Physical Chemistry, chapter 1, pp. 3–40, World Scientific, 2004.

[114] A. W. Jasper, B. K. Kendrick, C. A. Alden Mead, and D. G. Truhlar, Non-Born-Oppenheimer Chemistry: Potential Surfaces, Coupling, and Dynamics, in *Modern Trends in Chemical Reaction Dynamics: Experiment and Theory (Part 1)*, edited by X. Yang and K. Liu, Advanced Series in Physical Chemistry, chapter 8, pp. 329–391, World Scientific, 2004.

[115] C. Alden Mead, *Rev. Mod. Phys.* **64**, 51 (1992).

[116] E. Teller, *J. Phys. Chem.* **41**, 109 (1936).

[117] G. Herzberg and H. C. Longuet-Higgins, *Disscuss. Faraday Soc.* **35**, 77 (1963).

[118] M. V. Berry, *Proc. Roy. Soc. Lond. A* **392**, 45 (1984).

[119] M. Berry, Bristol anholonomy calendar, in *Sir Charles Frank OBE FRS, an eightieth birthday tribute*, edited by R. G. Chambers, J. E. Enderby, A. Keller, A. R. Lang, and J. W. Steeds, pp. 207–219, Adam Hilger, 1991.

[120] Y. Aharonov and D. Bohm, *Phys. Rev.* **115**, 485 (1959).

[121] C. A. Mead and D. G. Truhlar, *J. Chem. Phys.* **70**, 2284 (1979).

[122] G. Delacrétaz, E. R. Grant, R. L. Whetten, L. Wöste, and J. W. Zwanziger, *Phys. Rev. Lett.* **56**, 2598 (1986).

[123] B. Kendrick, *Phys. Rev. Lett.* **79**, 2431 (1997).

[124] H. von Busch, V. Dev, H.-A. Eckel, S. Kasahara, J. Wang, W. Demtröder, P. Sebald, and W. Meyer, *Phys. Rev. Lett.* **81**, 4584 (1998).

[125] A. Kuppermann and Y. Wu, *Chem. Phys. Lett.* **349**, 537 (2001).

[126] B. K. Kendrick, *J. Phys. Chem. A* **107**, 6739 (2003).

[127] J. C. Juanes-Marcos and S. C. Althorpe, *J. Chem. Phys.* **122**, 204324 (2005).

[128] J. C. Juanes-Marcos, S. C. Althorpe, and E. Wrede, *Science* **309**, 1227 (2005).

[129] S. C. Althorpe, *J. Chem. Phys.* **124**, 084105 (2006).

[130] P. Schmelcher and L. S. Cederbaum, *Phys. Rev. A* **41**, 4936 (1990).

[131] U. Kappes and P. Schmelcher, *Phys. Rev. A* **53**, 3869 (1996).

[132] T. Detmer, P. Schmelcher, and L. S. Cederbaum, *Phys. Rev. A* **57**, 1767 (1998).

[133] S. Rousseau, A. R. Allouche, and M. Aubert-Frécon, *J. Mol. Spec.* **203**, 235 (2000).

[134] S. Kotochigova, E. Tiesinga, and P. S. Julienne, *Eur. Phys. J. D* **31**, 189 (2004).

[135] T. Takekoshi, B. M. Patterson, and R. J. Knize, *Phys. Rev. Lett.* **81**, 5105 (1998).

[136] A. Görlitz, J. M. Vogels, A. E. Leanhardt, C. Raman, T. L. Gustavson, J. R. Abo-Shaeer, A. P. Chikkatur, S. Gupta, S. Inouye, T. Rosenband, and W. Ketterle, *Phys. Rev. Lett.* **87**, 130402 (2001).

[137] M. Greiner, I. Bloch, O. Mandel, T. W. Hänsch, and T. Esslinger, *Phys. Rev. Lett.* **87**, 160405 (2001).

[138] H. Moritz, T. Stöferle, M. Köhl, and T. Esslinger, *Phys. Rev. Lett.* **91**, 250402 (2003).

[139] B. Paredes, A. Widera, V. Murg, O. Mandel, S. Fölling, I. Cirac, G. Shlyapnikov, T. Hänsch, and I. Bloch, *Nature* **429**, 277 (2004).

[140] I. Bloch, J. Dalibard, and W. Zwerger, *Rev. Mod. Phys.* **80**, 885 (2008).

[141] M. Girardeau, *J. Maths. Phys.* **1**, 516 (1960).

[142] E. H. Lieb and W. Liniger, *Phys. Rev.* **130**, 1605 (1963).

[143] J. Muga and R. Snider, *Phys. Rev. A* **57**, 3317 (1998).

[144] K. Sakmann, A. I. Streltsov, O. E. Alon, and L. S. Cederbaum, *Phys. Rev. A* **72**, 033613 (2005).

[145] H. Bethe, *Z. Phys* **71**, 205 (1931).

[146] M. T. Batchelor, *Phys. Today* **60**, 36 (2007).

[147] D. C. Mattis, editor, *The Many-Body Problem*, World Scientific, 1993.

[148] C. Ryu, M. Andersen, P. Clade, V. Natarajan, K. Helmerson, and W. Phillips, *Phys Rev Lett* **99**, 260401 (2007).

[149] A. S. Arnold, C. S. Garvie, and E. Riis, *Physical Review A (Atomic, Molecular, and Optical Physics)* **73**, 041606 (2006).

[150] K. Henderson, C. Ryu, C. MacCormick, and M. G. Boshier, *Arxiv preprint arXiv:0902.2171* (2009).

[151] A. Einstein, *Sitzungsber. Preuss. Akad. Wiss.* , 18 (1925).

[152] S. N. Bose, *Z. Phys.* **26**, 178 (1924).

[153] D. G. Fried, T. C. Killian, L. Willmann, D. Landhuis, S. C. Moss, D. Kleppner, and T. J. Greytak, *Phys. Rev. Lett.* **81**, 3811 (1998).

[154] C. C. Bradley, C. A. Sackett, J. J. Tollett, and R. G. Hulet, *Phys. Rev. Lett.* **75**, 1687 (1995).

[155] G. Modugno, G. Ferrari, G. Roati, R. J. Brecha, A. Simoni, and M. Inguscio, *Science* **294**, 1320 (2001).

[156] T. Weber, J. Herbig, M. Mark, H. C. Nägerl, and R. Grimm, *Science* **299**, 232 (2003).

[157] F. P. Dos Santos, J. Leonard, J. M. Wang, C. J. Barrelet, F. Perales, E. Rasel, C. S. Unnikrishnan, M. Leduc, and C. Cohen-Tannoudji, *Phys. Rev. Lett.* **86**, 3459 (2001).

[158] A. Griesmaier, J. Werner, S. Hensler, J. Stuhler, and T. Pfau, *Phys. Rev. Lett.* **94**, 160401 (2005).

[159] Y. Takasu, K. Maki, K. Komori, T. Takano, K. Honda, M. Kumakura, T. Yabuzaki, and Y. Takahashi, *Phys. Rev. Lett.* **91**, 040404 (2003).

[160] S. Kraft, F. Vogt, O. Appel, F. Riehle, and U. Sterr, *Phys. Rev. Lett.* **103**, 130401 (2009).

[161] S. Stellmer, M. K. Tey, B. Huang, R. Grimm, and F. Schreck, *arXiv:cond-mat/0910.0634* (2009).

[162] M. Greiner, C. A. Regal, and D. S. Jin, *Nature* **426**, 537 (2003).

[163] J. Herbig, T. Kraemer, M. Mark, T. Weber, C. Chin, H. C. Nägerl, and R. Grimm, *Science* **301**, 1510 (2003).

[164] S. A. Gardiner, Lectures on Quantum Field Theory, Lectures on Quantum Field Theory, Durham University, 2006.

[165] P. Knowles, Lectures on Quantum Mechanics, Lectures on Quantum Mechanics: UK Summer School in Theoretical Chemistry, Oxford, 2008.

[166] L. Landau and E. Lifshitz, *Quantum Mechanics Non-Relativistic Theory: Volume 3*, Butterworth-Heinemann, 1981.

[167] F. Dalfovo, S. Giorgini, L. P. Pitaevskii, and S. Stringari, *Rev. Mod. Phys.* **71**, 463 (1999).

[168] L. D. Carr, C. W. Clark, and W. P. Reinhardt, *Phys. Rev. A* **62**, 63610 (2000).

[169] L. D. Carr, C. W. Clark, and W. P. Reinhardt, *Phys. Rev. A* **62**, 63611 (2000).

[170] M. Edwards and K. Burnett, *Phys. Rev. A* **51**, 1382 (1995).

[171] P. A. Ruprecht, M. J. Holland, K. Burnett, and M. Edwards, *Phys. Rev. A* **51**, 4704 (1995).

[172] W. Bao, D. Jaksch, and P. A. Markowich, *J. Comp. Phys.* **187**, 318 (2003).

[173] A. L. Fetter and A. A. Svidzinsky, *J. Phys. Con. Mat.* **13**, R135 (2001).

[174] J. R. Abo-Shaeer, C. Raman, J. M. Vogels, and W. Ketterle, *Science* **292**, 476 (2001).

[175] K. P. Marzlin, W. Zhang, and E. M. Wright, *Phys. Rev. Lett.* **79**, 4728 (1997).

[176] R. Dum, J. I. Cirac, M. Lewenstein, and P. Zoller, *Phys. Rev. Lett.* **80**, 2972 (1998).

[177] K. G. Petrosyan and L. You, *Phys. Rev. A* **59**, 639 (1999).

[178] M. R. Matthews, B. P. Anderson, P. C. Haljan, D. S. Hall, C. E. Wieman, and E. A. Cornell, *Phys. Rev. Lett.* **83**, 2498 (1999).

[179] J. Williams and M. Holland, *Nature* **401**, 568 (1999).

[180] K. Madison, F. Chevy, W. Wohlleben, and J. Dalibard, *Phys. Rev. Lett.* **84**, 806 (2000).

[181] C. Raman, J. Abo-Shaeer, J. Vogels, K. Xu, and W. Ketterle, *Phys. Rev. Lett.* **87**, 21 (2001).

[182] A. E. Leanhardt, A. Gorlitz, A. P. Chikkatur, D. Kielpinski, Y. Shin, D. E. Pritchard, and W. Ketterle, *Phys. Rev. Lett.* **89**, 190403 (2002).

[183] S. I. Ogawa, M. Mttnen, M. Nakahara, T. Ohmi, and H. Shimada, *Phys. Rev. A* **66**, 013617 (2002).

[184] T. Isoshima, M. Nakahara, T. Ohmi, and K. Machida, *Phys. Rev. A* **61**, 63610 (2000).

[185] F. Zhou, *Phys. Rev. Lett.* **87**, 080401 (2001).

[186] J. Ruostekoski and J. R. Anglin, *Phys. Rev. Lett.* **91**, 190402 (2003).

[187] H. Chiba and H. Saito, *Phys. Rev. A* **78**, 043602 (2008).

[188] S. Hoshi and H. Saito, *Phys. Rev. A* **78**, 053618 (2008).

[189] I. Fuentes-Guridi, J. Pachos, S. Bose, V. Vedral, and S. Choi, *Phys. Rev. A* **66**, 022102 (2002).

[190] Z.-D. Chen, J.-Q. Liang, S.-Q. Shen, and W.-F. Xie, *Phys. Rev. A* **69**, 023611 (2004).

[191] C. Zhang, A. M. Dudarev, and Q. Niu, *Phys. Rev. Lett.* **97**, 040401 (2006).

[192] V. M. Kaurov and A. B. Kuklov, *Phys. Rev. A* **73**, 013627 (2006).

[193] D. C. E. Bortolotti, S. Ronen, J. L. Bohn, and D. Blume, *Phys. Rev. Lett.* **97**, 160402 (2006).

[194] T. Koch, T. Lahaye, J. Metz, B. Fröhlich, A. Griesmaier, and T. Pfau, *Nat. Phys.* **4**, 218 (2008).

[195] J. L. Bohn, R. M. Wilson, and S. Ronen, *Laser Phys.* **19**, 547 (2009).

[196] N. Moiseyev, M. Šindelka, and L. S. Cederbaum, *J. Phys. B* **41**, 221001 (2008).

[197] R. N. Zare, *Angular Momentum*, John Wiley & Sons, 1987.

[198] J. Brown and A. Carrington, *Rotational Spectroscopy of Diatomic Molecules*, Cambridge University Press, 2003.

[199] D. M. Brink and G. R. Satchler, *Angular Momentum*, Oxford University Press, 2nd edition, 1975.